

Orthogonal Frequency Division Multiplexing Multiple-Input Multiple-Output Automotive Radar with Novel Signal Processing Algorithms

von der Fakultät Informatik, Elektrotechnik und Informationstechnik
der Universität Stuttgart
zur Erlangung der Würde eines Doktor-Ingenieurs (Dr.-Ing.)
genehmigte Abhandlung

vorgelegt von
Gor Hakobyan
aus Jerewan, Armenien

Hauptberichter:
Mitberichter:

Prof. Dr.-Ing. Bin Yang
Prof. Dr. Friedrich K. Jondral

Tag der mündlichen Prüfung:

07.02.2018

**Institut für Signalverarbeitung und Systemtheorie
der Universität Stuttgart**

2018

Vorwort

Die vorliegende Arbeit entstand während meiner Zeit als Doktorand bei der zentralen Forschung der Robert Bosch GmbH in Kooperation mit der Universität Stuttgart.

Mein besonderer Dank gilt Prof. Bin Yang, dem Leiter des Instituts für Signalverarbeitung und Systemtheorie an der Universität Stuttgart für die Gelegenheit, unter seiner Betreuung zu promovieren. Insbesondere möchte ich mich für das Vertrauen, die stets hervorragende Betreuung, die Freiheit, eigene Wege in Forschung zu gehen, sowie kurzfristige und sorgfältige Korrekturen meiner Veröffentlichungen und der Dissertation recht herzlich bedanken. Prof. Friedrich Jondral vom Institut für Nachrichtentechnik des Karlsruher Instituts für Technologie danke ich herzlich für die Übernahme des Mitberichts.

Ferner möchte ich mich bei den Mitarbeitern der Robert Bosch GmbH und des Instituts für Signalverarbeitung und Systemtheorie bedanken, die zur Entstehung dieser Arbeit beigetragen haben. Insbesondere geht mein Dank an Herrn Siegbert Steinlechner für die fachliche Betreuung, Mentoring, sowie den Freiraum bei der Ausgestaltung der Arbeit. Seine vielseitige und zugleich tiefgründige Kompetenz in fachlichen und außer fachlichen Bereichen diente als Vorbild und hat zu meiner Weiterentwicklung wesentlich beigetragen. Des weiteren geht mein besonderer Dank an Dr. Michael Schoor für die fachlichen Diskussionen, die zur Vertiefung meines Wissens reichlich beigetragen haben, sowie an Herrn Karim Armanious und an Frau Mekdes Girma für die fruchtbare Zusammenarbeit. Mein Dank gilt ferner allen, die die Dissertation mit großer Sorgfalt und in kurzer Zeit Korrektur gelesen haben: Herrn Siegbert Steinlechner, Dr. Vladimir Petkov, Dr. Jo Pletinckx, Dr. Michael Schoor und Tim Poguntke.

Schließlich möchte ich einen ganz besonderen Dank an meine Familie richten, meinen Vater Varazdat Hakobyan, meine Mutter Karine Khachatryan, meinen Bruder Hayk Hakobyan, sowie meine Partnerin Anna Gosk, die mich auf meinem Weg mit stets liebevollen Unterstützung, Ermutigung und Geduld begleitet haben. Ihnen widme ich diese Arbeit.

Stuttgart, April 2018

Gor Hakobyan

Contents

List of Symbols and Abbreviations	9
Abstract	15
Zusammenfassung	17
1. Introduction	19
1.1. Background	19
1.2. Research Objectives	20
1.3. Contributions and Outline of the Work	21
2. Automotive Radar	25
2.1. The Radar Principle	25
2.1.1. Propagation of Radar Signals	25
2.1.2. Distance Estimation	27
2.1.3. Velocity Estimation	28
2.1.4. DOA Estimation	28
2.2. State-of-the-Art Automotive Radar Systems	29
2.2.1. FMCW Radar	29
2.2.2. Fast-Chirp Radar	31
2.3. OFDM Radar	33
2.3.1. OFDM Radar Fundamentals	33
2.3.2. System Parametrization	40
2.3.3. CP-OFDM vs. RS-OFDM	43
2.3.4. Methods for Reduction of PAPR for OFDM Radar	44
2.4. MIMO Radar	45
2.4.1. Improved DOA Estimation Based on MIMO Array Processing	45
2.4.2. Multiplexing of Tx Antennas for MIMO Radar	46
2.4.3. Multichannel Radar Signal Processing	47
2.5. Comparison of Digital OFDM Radar to Traditional Fast-Chirp Radar	48
3. OFDM Radar Signal Model and Signal Processing	51
3.1. Signal Model	52
3.1.1. Continuous-Time Signal Model	52
3.1.2. Discrete-Time Signal Model	54
3.1.3. Signal Model in Matrix Notation	55
3.2. Classical OFDM Radar Signal Processing	56
3.2.1. State-of-the-Art Signal Processing Methods for OFDM Radar	56
3.2.2. Description of the Classical OFDM Radar Processing	58
3.2.3. Performance of the Classical OFDM Radar Processing	61

3.3.	All-Cell Doppler Correction (ACDC) for ICI-Free OFDM Signal Processing . .	64
3.3.1.	Requirements for All-Cell Doppler Correction	65
3.3.2.	ACDC based Distance-Velocity Estimation	65
3.3.3.	ACDC based OFDM Radar and Communication System	69
3.3.4.	Simulative Analysis	71
3.3.5.	Concluding Remarks	74
3.4.	All-Cell Migration Compensation (ACMC) for Migration-Free Range-Doppler Processing	75
3.4.1.	State-of-the-Art Methods for Range and Doppler Frequency Migration Compensation	76
3.4.2.	Range and Doppler Frequency Migration	78
3.4.3.	All-Cell Migration Compensation based Range-Doppler processing . .	79
3.4.4.	ACMC Implementation based on Chirp Z-Transform	81
3.4.5.	Simulative Analysis	82
3.4.6.	Concluding Remarks	85
3.5.	Combination of ACDC and ACMC and Comparison to the Classical Signal Processing	87
4.	OFDM-MIMO Radar	89
4.1.	Conventional Multiplexing Methods Applied to OFDM-MIMO Radar	89
4.1.1.	Time Division Multiplexing	90
4.1.2.	Frequency Division Multiplexing	91
4.1.3.	Code Division Multiplexing	91
4.2.	OFDM-MIMO Radar Multiplexed via Equidistant Subcarrier Interleaving . . .	92
4.3.	OFDM-MIMO Radar Multiplexed via Non-Equidistant Subcarrier Interleaving	93
4.3.1.	Non-Equidistant Subcarrier Interleaving (NeqSI)	94
4.3.2.	Non-Equidistant Dynamic Subcarrier Interleaving (NeqDySI)	96
4.4.	Optimization of the Interleaving Pattern for Non-Equidistant Interleaving Schemes	100
4.4.1.	Genetic Algorithms	100
4.4.2.	Formulation of the Optimization Task	102
4.4.3.	Effect of Windowing on the PSL of Non-Equidistant Sampling	104
4.4.4.	Optimization Results for Non-Equidistant Interleaving Schemes	105
4.5.	Application of Sparse Recovery Methods for OFDM-MIMO Radar	106
4.5.1.	Compressed Sensing Overview	107
4.5.2.	Fundamentals of Compressed Sensing	108
4.5.3.	CS based Distance-Velocity Estimation	114
4.5.4.	Simulative Analysis	119
4.6.	Concluding Remarks	122
5.	Interference Mitigation Techniques for OFDM Radar	125
5.1.	Influence of Interference on OFDM Radar	125
5.2.	A Narrowband Interference Suppression Method for OFDM Radar	128
5.2.1.	Interference Suppression Algorithm	128
5.2.2.	Simulative Analysis	130
5.3.	OFDM Radar Networks and Methods for Mitigation of OFDM Interference . .	132
5.4.	Interference-Aware Cognitive OFDM Radar	133
5.4.1.	Cognitive Radar	134

5.4.2.	Waveform Adaptation Methods for Cognitive Radar	136
5.4.2.1.	Carrier Frequency Hopping – Waveform Adaptation	137
5.4.2.2.	Slow-Time Chirp Waveform Adaptation (STC-WA) with Variable Symbol Repetition Intervals	138
5.4.3.	Spectrum Sensing	145
5.5.	Concluding Remarks	147
6.	OFDM-MIMO Radar Prototype and Experimental Validation of the Proposed Methods	149
6.1.	Description of the System Prototype	149
6.2.	Measurements for Performance Verification of the System Prototype	153
6.2.1.	Measurements in an Anechoic Chamber	153
6.2.2.	Measurements in a Road Scenario	155
6.3.	Experimental Validation of the Proposed Distance-Velocity Estimation Algorithms	156
6.3.1.	Validation of ACDC in a Road Scenario	156
6.3.2.	Validation of APMC in a Road Scenario	159
6.4.	Experimental Validation of the Proposed Multiplexing Methods for OFDM-MIMO Radar	161
6.4.1.	Validation of the NeqDySI Multiplexing	161
6.4.2.	Validation of the NeqSI Multiplexing with Sparse Iterative Multidimensional Frequency Estimation (SIMFE) Based Processing	161
6.5.	Experimental Validation of the Proposed Interference Mitigation Techniques . .	163
6.5.1.	Validation of the Proposed Narrowband Interference Suppression Method	163
6.5.2.	Verification of the Waveform Adaptation Properties of STC-WA for Cognitive Interference Avoidance	164
6.6.	Concluding Remarks	167
7.	Conclusions	169
7.1.	Summary of Key Contributions	169
7.2.	Outlook	171
A.	APMC Description Based on a Frequency Domain Signal Model	173
B.	Estimation Parameters of STC-WA	175

List of Symbols and Abbreviations

Notation

x	Scalar
\underline{x}	Column vector
\mathbf{x}	Matrix
\mathbb{X}	Set

Mathematical Operations

x^*	Complex conjugate
$\underline{x}^T, \mathbf{x}^T$	Transpose of a vector \underline{x} or a matrix \mathbf{x}
$\underline{x}^H, \mathbf{x}^H$	Hermitian transpose of a vector \underline{x} or a matrix \mathbf{x}
$ x $	Amplitude of a scalar, cardinality of a set
$\ \underline{x}\ $	ℓ_2 -norm of a vector
$\ \underline{x}\ _p$	ℓ_p -norm of a vector
\mathbf{x}^{-1}	Inverse of a matrix
\mathbf{x}^+	Moore–Penrose pseudoinverse of a matrix
$\mathbf{x} \odot \mathbf{y}$	Hadamard (elementwise) product of matrices \mathbf{x} and \mathbf{y}
$\mathbf{x} ./ \mathbf{y}$	Elementwise division of matrices \mathbf{x} and \mathbf{y}
$\langle \underline{x}, \underline{y} \rangle$	Scalar (inner) product of vectors \underline{x} and \underline{y}
$\text{diag}(\underline{x})$	Diagonal matrix containing the elements of the vector \underline{x}
$\mathbf{D}_N(\bar{f})$	Diagonal matrix containing elements of $\exp(j2\pi\bar{f}n)$, $n \in [0, N - 1]$
$\mathcal{N}(\mathbf{x})$	Nullspace of the matrix \mathbf{x}
$\text{supp}(\underline{x})$	Support of a vector \underline{x}
$\text{rect}(t/T)$	Rectangular function of the duration T
Σ_K	Set of all K -sparse signals
∇	Nabla operator $\nabla = \left(\frac{\partial}{\partial x_1}, \dots, \frac{\partial}{\partial x_N} \right)$
$\mathcal{F}(\cdot)$	Fourier transform

$\mathcal{F}^{-1}(\cdot)$	Inverse Fourier transform
$\min_x(\cdot)$	Minimum with respect to x
$\max_x(\cdot)$	Maximum with respect to x
$\arg \min_x(\cdot)$	Argument x , for which the minimum is obtained
$\arg \max_x(\cdot)$	Argument x , for which the maximum is obtained
$x \leftarrow y$	Assignment of y to x

Frequently Used Symbols

a, \bar{a}	Real and complex target amplitudes
B	Bandwidth
\underline{B}	Vector of the magnetic field
\mathbf{B}	Doppler scaling matrix
c	Speed of propagation of electromagnetic waves
c_0	Speed of light
d	Distance of the target
d_u	Unambiguous distance range
Δd	Distance resolution
\underline{E}	Vector of the electric field
f_c	Carrier frequency
$f_{c,a}$	Adaptive carrier frequency
f_D	Doppler frequency
\bar{f}_D	Normalized Doppler frequency
f_n	Frequency of the n -th OFDM subcarrier
\mathbf{F}_N	Matrix of the discrete Fourier transform of size $N \times N$
Δf	Subcarrier spacing of OFDM
Δf_c	Adaptation step of the carrier frequency between two consecutive OFDM symbols
\mathbf{I}_N	Identity matrix of size N
N_c	Number of OFDM subcarriers
N_{path}	Number of paths the radar signal traverses from the transmitter to the receiver
N_{Rx}	Number of receive antennas
N_{sym}	Number of OFDM symbols in one measurement cycle

N_{targ}	Number of radar targets
N_{Tx}	Number of transmit antennas
N_{virt}	Number of virtual antennas
\underline{p}	Position vector
\mathbf{P}	Matrix of the target movement that leads to range and Doppler frequency migration
\mathbf{s}	Matrix of complex modulation symbols
t	Continuous time
t_{f}	Fast-time
t_{s}	Slow-time
T	Duration of OFDM symbol
T_{CP}	Duration of cyclic prefix
T_{cycle}	Duration of one measurement cycle
T_{OFDM}	Duration of an OFDM symbol including the cyclic prefix
T_{SRI}	Symbol repetition interval of OFDM radar
\underline{u}	Unit direction vector
v	Velocity of the target
v_{u}	Unambiguous velocity range
Δv	Velocity resolution
\mathbf{w}_N	Diagonal matrix of the window function of size $N \times N$
$x(t)$	Continuous-time OFDM signal at the transmitter
$y(t)$	Continuous-time OFDM signal at the receiver
λ_{c}	Wavelength
σ_{r}	Radar cross section
σ	Noise variance
τ	Delay (time-of-flight)
$\bar{\tau}$	Normalized delay
Φ	Dictionary for compressed sensing
Φ_p	Selection matrix for the p -th transmit antenna
χ	Ambiguity function
Ψ	Sparse basis

Frequently Used Abbreviations

AAF	Anti-aliasing filter
ACDC	All-cell Doppler compensation
ACMC	All-cell migration compensation
ADC	Analog-to-digital converter
AWG	Arbitrary waveform generator
CFAR	Constant false alarm rate
CFH-WA	Carrier frequency hopping waveform adaptation
CP	Cyclic prefix
CP-OFDM	Cyclic prefix OFDM
CRLB	Cramer–Rao lower bound
CS	Compressed sensing
DAC	Digital-to-analog converter
DDS	Direct digital synthesizer
DOA	Direction of arrival
DFT	Discrete Fourier transform
DR	Dynamic range
EqSI	Equidistant subcarrier interleaving
FDM	Frequency division multiplexing
FFT	Fast Fourier transform
FMCW	Frequency modulated continuous wave
ICI	Intercarrier interference
IF	Intermediate frequency
IFFT	Inverse fast Fourier transform
IQ	In-phase–quadrature
ISI	Intersymbol interference
KT	Keystone transform
LO	Local oscillator
LPF	Low pass filter
ML	Maximum likelihood
MIMO	Multiple-input multiple-output

NCI	Non-coherent integration
NeqSI	Non-equidistant subcarrier interleaving
NeqDySI	Non-equidistant dynamic subcarrier interleaving
OFDM	Orthogonal frequency division multiplexing
OMP	Orthogonal matching pursuit
OS-CFAR	Ordered statistics CFAR
PA	Power amplifier
PAPR	Peak-to-average power ratio
PLL	Phase-locked loop
PRR	Peak-to-residue ratio
PSK	Phase shift keying
PSL	Peak-to-sidelobe ratio
QAM	Quadrature amplitude modulation
RCS	Radar cross section
RF	Radio frequency
RMSE	Root mean square error
RS-OFDM	Repeated symbols OFDM
Rx	Receive
SAR	Synthetic aperture radar
SIMFE	Sparse iterative multidimensional frequency estimation
SIR	Signal-to-interference ratio
SNR	Signal-to-noise ratio
SRI	Symbol repetition interval
S-SIMFE	Structured SIMFE
STC-WA	Slow-time chirp waveform adaptation
SW-SS	Stepwise spectrum sensing
TDM	Time division multiplexing
Tx	Transmit
ULA	Uniform linear array
VSRI	Variable symbol repetition intervals

Abstract

Advanced driver assistance systems that actively assist the driver based on environment perception achieved significant advances in recent years. Along with this development, autonomous driving became a major research topic that aims ultimately at development of fully automated, driverless vehicles. Since such applications rely on environment perception, their ever increasing sophistication imposes growing demands on environmental sensors. Specifically, the need for reliable environment sensing necessitates the development of more sophisticated, high-performance radar sensors. A further vital challenge in terms of increased radar interference arises with the growing market penetration of the vehicular radar technology. To address these challenges, in many respects novel approaches and radar concepts are required. As the modulation is one of the key factors determining the radar performance, the research of new modulation schemes for automotive radar becomes essential.

A topic that emerged in the last years is the radar operating with digitally generated waveforms based on *orthogonal frequency division multiplexing* (OFDM). Initially, the use of OFDM for radar was motivated by the combination of radar with communication via modulation of the radar waveform with communication data. Some subsequent works studied the use of OFDM as a modulation scheme in many different radar applications — from adaptive radar processing to synthetic aperture radar. This suggests that the flexibility provided by OFDM based digital generation of radar waveforms can potentially enable novel radar concepts that are well suited for future automotive radar systems.

This thesis aims to explore the perspectives of OFDM as a modulation scheme for high-performance, robust and adaptive automotive radar. To this end, novel signal processing algorithms and OFDM based radar concepts are introduced in this work. The main focus of the thesis is on high-end automotive radar applications, while the applicability for real time implementation is of primary concern.

The first part of this thesis focuses on signal processing algorithms for distance-velocity estimation. As a foundation for the algorithms presented in this thesis, a novel and rigorous signal model for OFDM radar is introduced. Based on this signal model, the limitations of the state-of-the-art OFDM radar signal processing are pointed out. To overcome these limitations, we propose two novel signal processing algorithms that build upon the conventional processing and extend it by more sophisticated modeling of the radar signal. The first method named *all-cell Doppler compensation* (ACDC) overcomes the Doppler sensitivity problem of OFDM radar. The core idea of this algorithm is the scenario-independent correction of Doppler shifts for the entire measurement signal. Since Doppler effect is a major concern for OFDM radar and influences the radar parametrization, its complete compensation opens new perspectives for OFDM radar. It not only achieves an improved, Doppler-independent performance, it also enables more favorable system parametrization. The second distance-velocity estimation algorithm introduced in this thesis addresses the issue of range and Doppler frequency migration due to the target's motion during the measurement. For the conventional radar signal processing, these migration effects set

an upper limit on the simultaneously achievable distance and velocity resolution. The proposed method named *all-cell migration compensation* (ACMC) extends the underlying OFDM radar signal model to account for the target motion. As a result, the effect of migration is compensated implicitly for the entire radar measurement, which leads to an improved distance and velocity resolution. Simulations show the effectiveness of the proposed algorithms in overcoming the two major limitations of the conventional OFDM radar signal processing.

As *multiple-input multiple-output* (MIMO) radar is a well-established technology for improving the direction-of-arrival (DOA) estimation, the second part of this work studies the multiplexing methods for OFDM radar that enable simultaneous use of multiple transmit antennas for MIMO radar processing. After discussing the drawbacks of known multiplexing methods, we introduce two advanced multiplexing schemes for OFDM-MIMO radar based on non-equidistant interleaving of OFDM subcarriers. These multiplexing approaches exploit the multicarrier structure of OFDM for generation of orthogonal waveforms that enable a simultaneous operation of multiple MIMO channels occupying the same bandwidth. The primary advantage of these methods is that despite multiplexing they maintain all original radar parameters (resolution and unambiguous range in distance and velocity) for each individual MIMO channel. To obtain favorable interleaving patterns with low sidelobes, we propose an optimization approach based on genetic algorithms. Furthermore, to overcome the drawback of increased sidelobes due to subcarrier interleaving, we study the applicability of sparse processing methods for the distance-velocity estimation from measurements of non-equidistantly interleaved OFDM-MIMO radar. We introduce a novel sparsity based frequency estimation algorithm designed for this purpose.

The third topic addressed in this work is the robustness of OFDM radar to interference from other radar sensors. In this part of the work we study the interference robustness of OFDM radar and propose novel interference mitigation techniques. The first interference suppression algorithm we introduce exploits the robustness of OFDM to narrowband interference by dropping subcarriers strongly corrupted by interference from evaluation. To avoid increase of sidelobes due to missing subcarriers, their values are reconstructed from the neighboring ones based on linear prediction methods. As a further measure for increasing the interference robustness in a more universal manner, we propose the extension of OFDM radar with cognitive features. We introduce the general concept of cognitive radar that is capable of adapting to the current spectral situation for avoiding interference. Our work focuses mainly on waveform adaptation techniques; we propose adaptation methods that allow dynamic interference avoidance without affecting adversely the estimation performance.

The final part of this work focuses on prototypical implementation of OFDM-MIMO radar. With the constructed prototype, the feasibility of OFDM for high-performance radar applications is demonstrated. Furthermore, based on this radar prototype the algorithms presented in this thesis are validated experimentally. The measurements confirm the applicability of the proposed algorithms and concepts for real world automotive radar implementations.

Zusammenfassung

Moderne Fahrzeuge sind mit Fahrerassistenzsystemen ausgestattet, die den Fahrer basierend auf Umfelderkennung aktiv unterstützen. In Folge der maßgeblichen Weiterentwicklung der Fahrerassistenzsysteme in den letzten Jahren gewinnt das autonome Fahren immer mehr an Bedeutung. Mit zunehmender Komplexität dieser Systeme steigen entsprechend die Anforderungen an die Umfeldsensorik. Im Speziellen erfordert das autonome Fahren für eine zuverlässige Umfelderkennung leistungsfähige Radarsensoren. Im Gegensatz zu den gängigen Radarsystemen sollen die Radarsensoren fürs autonome Fahren wesentlich höhere Anforderungen bezüglich der Auflösung, Zuverlässigkeit, und Flexibilität erfüllen. Des Weiteren entsteht mit zunehmender Anzahl der Radarsensoren im Automobilbereich eine andere grundlegende Herausforderung – die Interferenz zwischen Radarsensoren nimmt zu.

Um den Anforderungen an zukünftige Automobilradare gerecht zu werden, sind neuartige Ansätze und Radarkonzepte erforderlich. Da die Radarmodulation einen wesentlichen Einfluss auf dessen Leistungsfähigkeit hat, spielen für zukünftige Radarsysteme fortgeschrittene Modulationsmethoden eine entscheidende Rolle.

Orthogonal Frequency Division Multiplexing (OFDM) ist eine in der Kommunikationstechnik verbreitete digitale Modulation. Die Anwendbarkeit von OFDM für Radarzwecke ist seit einigen Jahren aus wissenschaftlichen Arbeiten bekannt, die eine Kombination von Radar mit Kommunikation durch die Modulation des Radarsignals mit Kommunikationsdaten erzielen. In weiteren Arbeiten wurden OFDM-Signalformen für verschiedene Radaranwendungen gewinnbringend eingesetzt – von adaptivem Radar bis zum Synthetic Aperture Radar. Diese Untersuchungen legen nahe, dass die Flexibilität der digitalen Signalerzeugung und Verarbeitung der OFDM-Radarsysteme neuartige Radarkonzepte ermöglichen kann, die für die zukünftigen Radarsysteme im Automobilbereich interessant sind.

Diese Dissertation untersucht die Anwendbarkeit der OFDM-Modulation für leistungsfähige, zuverlässige und adaptive Radaranwendungen im Automobilbereich. In diesem Rahmen werden neuartige, leistungsfähige Radarsignalverarbeitungsverfahren und fortgeschrittene Radarkonzepte eingeführt. Dabei spielt die Realisierbarkeit in Echtzeit eine maßgebliche Rolle.

Der erste Teil dieser Arbeit befasst sich mit Signalverarbeitungsalgorithmen für Abstands- und Geschwindigkeitsschätzung mittels OFDM-Radars. Diese Algorithmen werden auf Basis eines neuen und rigorosen Signalmodells vorgestellt. Anhand dieses Signalmodells wird die konventionelle OFDM-Radarsignalverarbeitung erklärt und deren Einschränkungen offenbart. Es werden zwei neue Algorithmen vorgestellt, welche die konventionelle Signalverarbeitung mit komplexeren Signalmodellen verfeinern und somit deren Limitierungen umgehen. Der erste Algorithmus, genannt *All-Cell Doppler Compensation* (ACDC), überwindet die Doppler-Sensitivität des OFDM-Radars durch eine vollständige, szenariounabhängige Korrektur der Dopplerverschiebung für die gesamte Messung. Da die Dopplerverschiebung ein grundlegendes Problem für OFDM-Radar darstellt und Auswirkungen auf die Systemparametrisierung hat, öffnet die

ACDC-basierte Auswertung neue Perspektiven für OFDM-Radar. Zusätzlich zur verbesserten, Doppler-unabhängigen Leistung ermöglicht diese Signalverarbeitung günstigere Systemparametrisierungen. Der zweite Algorithmus zur Abstands- und Geschwindigkeitsschätzung, *All-Cell Migration Compensation* (ACMC) genannt, behandelt das Problem der Abstands- und Dopplerfrequenzmigration, die durch die Bewegung der Ziele während der Messung verursacht wird. Für die konventionelle Radarsignalverarbeitung bestimmen diese Migrationseffekte die maximal gleichzeitig erreichbare Abstands- und Geschwindigkeitsauflösung. Durch die Einbeziehung der Bewegung der Ziele in das Signalmodell ermöglicht der eingeführte ACMC-Algorithmus eine implizite, szenariounabhängige Kompensation der Migrationseffekte, und somit eine hohe Abstands- und Geschwindigkeitsauflösung. Die Fähigkeit der beiden eingeführten Verfahren, zwei maßgeblichen Einschränkungen der klassischen OFDM-Radarsignalverarbeitung zu überwinden, wird mit Simulationen bestätigt.

Im zweiten Teil der Dissertation werden Multiplexingverfahren für OFDM-Radar untersucht, die eine simultane Nutzung mehrerer Sendeantennen zur Verbesserung der Winkelschätzung anhand des MIMO-Radarprinzips (engl. *Multiple-Input Multiple-Output*) ermöglichen. Nach der Einführung der konventionellen Multiplexingverfahren und Erläuterung ihrer Einschränkungen werden zwei neuartige Multiplexingverfahren für OFDM-MIMO Radar eingeführt. Diese Ansätze basieren auf der nicht-äquidistanten Aufteilung der OFDM-Unterträger auf die Sendeantennen. Somit können orthogonale Sendesignale für simultan aktive Sendeantennen erzeugt werden, sodass jeder Sendekanal dabei die ganze Bandbreite belegt. Der Vorteil dieser Multiplexingverfahren besteht darin, dass trotz der Aufteilung der Unterträger auf mehrere Sendekanäle für jeden Kanal die ursprünglichen Radarparameter (d.h. eindeutige Messbereich und Auflösung in Abstand und Geschwindigkeit) weiterhin erreicht werden. Um vorteilhafte Aufteilungsmuster zu erzeugen, wird ein Optimierungsansatz basierend auf genetischen Algorithmen eingeführt. Des Weiteren wird die Anwendbarkeit von Sparsity-basierten Signalverarbeitungsverfahren für die Abstands- und Geschwindigkeitsschätzung mittels OFDM-MIMO Radars mit nicht-äquidistanter Unterträgeraufteilung untersucht. Dabei wird ein neuartiges Verfahren vorgestellt, das eine Sparsity-basierte Frequenzschätzung aus nicht-äquidistant abgetasteten Messungen ermöglicht.

Der dritte Teil der Arbeit untersucht die Störfestigkeit des OFDM-Radars gegenüber Interferenz durch andere Radarsensoren. Die grundsätzlichen Eigenschaften des OFDM-Radars bezüglich der Interferenz-Robustheit werden erläutert und neuartige Ansätze zur Unterdrückung bzw. Vermeidung der Interferenz eingeführt. Als erstes wird ein Algorithmus für OFDM-Radar zur Unterdrückung schmalbandiger Interferenzen vorgestellt. Diesem Algorithmus liegt die Mehrträgerstruktur des OFDMs und daraus resultierende Robustheit gegenüber Schmalbandinterferenz zugrunde. Die Interferenz wird dadurch unterdrückt, dass stark betroffene Unterträger aus der Auswertung ausgenommen und deren Werte mithilfe linearer Prädiktion rekonstruiert werden. Als eine weitere Maßnahme zur Verbesserung der Störfestigkeit wird die Erweiterung des OFDM-Radars mit kognitiven Funktionen eingeführt. Das Gesamtkonzept eines kognitiven OFDM-Radars zur Interferenzvermeidung anhand adaptiver Anpassung auf die spektrale Umwelt wird vorgestellt. Im Fokus stehen Methoden zur adaptiven Signalanpassung, die eine Interferenzvermeidung ermöglichen, ohne dabei die Leistungsfähigkeit der Radarschätzung zu beeinträchtigen.

Abschließend wird die Realisierung eines OFDM-MIMO Radarprototyps vorgestellt. Sowohl die Tauglichkeit als auch die Realisierbarkeit des OFDM-Radars für leistungsfähige Radaranwendungen im Automobilbereich wird anhand realer Messungen mit dem OFDM-MIMO Radarprototyp bestätigt. Darüber hinaus werden die in dieser Dissertation vorgestellten Algorithmen und Radar-konzepte anhand Messungen mit dem OFDM-MIMO Radarprototyp messtechnisch verifiziert.

Chapter 1.

Introduction

1.1. Background

In the light of major advances in the field of advanced driver assistance systems and autonomous driving, demands on the performance of vehicular environmental sensors grow constantly. As radar is a key sensor technology for environment sensing, this development amplifies the need for high-performance, robust and adaptive automotive radars. To meet the increasing requirements on the radar performance, in many respects conceptually new approaches are required — both in terms of signal processing algorithms as well as the overall radar concept. Also, new challenges arise with the ever growing number of automotive radar sensors, which leads to a more severe interference situation and emphasizes the need for interference-robust radar technologies. A crucial ingredient of the radar system that has a paramount impact on its characteristics is the radar modulation. Thus, to achieve performance beyond that of the conventional radar systems operating with analog-generated linear frequency modulated signals, alternative radar modulation schemes including digital modulations are studied. A technology that has emerged over the past few years as a possible alternative to the current radar systems is the radar operating with digitally generated *orthogonal frequency division multiplexing* (OFDM) waveforms. Possible benefits of radar with a higher degree of digitalization are *i*) better accuracy due to replacement of components with analog tolerances by their digital alternatives, *ii*) higher degree of flexibility that can be used to generate new radar features, and *iii*) adaptability which can enable adaptive radar configuration for dynamical performance optimization depending on the scenario or application.

The use of digitally generated multicarrier waveforms for radar was first proposed by Levanon in 2000 [Levanon, 2000a,b]. Since then, numerous publications and several Ph.D. theses studying the topic of digital OFDM radar have appeared in the literature. Owing to the widespread use of OFDM for various communication applications, the subsequent research has mainly focused on combining OFDM radar with communication [Donnet, 2006; Garmatyuk, 2007; Tigrek, 2008; Sturm, 2009, 2013]. This is mainly motivated by the efficient use of limited spectral resources based on a single waveform that combines both applications. Among other sources, one notable contribution to this topic was the work in [Tigrek, 2008, 2010a], where the use of consecutive OFDM waveforms that carry communication data for distance (delay) and velocity (Doppler) estimation was proposed. The authors study correlation based distance processing for estimation of delays from an OFDM symbol and a *fast Fourier transform* (FFT) based Doppler processing for velocity estimation over the consecutive OFDM symbols. These works focused mainly on long range applications, studying accordingly aspects specific to high velocities and

long delays. Almost in parallel, another research group has worked on OFDM based joint radar and communication (RadCom) systems for automotive applications [Sturm, 2009, 2011, 2012b]. Here, the authors adopted a similar approach for distance-velocity processing based on multiple consecutive OFDM symbols carrying communication data. The overall aim of these works was the conception of a network of automotive RadCom systems which act as radar and simultaneously exchange communication data. To this end, the authors studied the joint interference-free operation of such systems using methods for OFDM-based spectrum sharing. Furthermore, these works implemented their OFDM radar concept using a measurement setup operating at 24 GHz and demonstrated the feasibility of OFDM radar for real world applications. A different approach for coexistence of multiple OFDM radar and communication nodes in a network based on more randomized spectrum access was studied in [Braun, 2014]. In the subsequent work, the same research group proposed the extension of OFDM radar to a *multiple-input multiple-output* (MIMO) radar system based on equidistant interleaving of OFDM subcarriers for simultaneous operation (i.e. multiplexing) of multiple transmit antennas [Sturm, 2013]. Further work on this topic includes research of methods for suppression of interference from other nodes operating in a radar network [Sit, 2014a, 2017].

Apart from research that focuses on the use of OFDM waveforms for combination of radar and communication, publications are known that study the use of OFDM radar for different purposes. One example is the use of OFDM signals for passive radar [Berger, 2008, 2010a; Gassier, 2016]. Other research focused on the use of OFDM radar in long range applications such as remote sensing. In [Sen, 2010, 2011, 2014], OFDM based adaptive radar operation for improved detection and tracking performance, e.g. through *space-time adaptive processing* (STAP) in multipath scenarios, was studied. Further research in the context of remote sensing focused on the use of OFDM for *synthetic aperture radar* (SAR) applications [Xia, 2015; Cao, 2015; Zhang, 2014]. Also here, the motivation for OFDM waveforms is the adaptability and flexibility provided by the digital signal generation and processing. One benefit of OFDM waveforms exploited in these works is the advantageous multiplexing of multiple transmit antennas for MIMO radar processing, such that an improved *direction of arrival* (DOA) estimation is achieved. The ability of OFDM to efficiently generate orthogonal radar waveforms was also exploited for multistatic radars in [Paichard, 2010].

This brief survey of the known research on the topic of OFDM radar suggests that the flexibility provided by digitally generated OFDM waveforms opens new possibilities for radar. Thus, OFDM is a modulation method that might enable novel automotive radar concepts superior to the traditional ones.

1.2. Research Objectives

Motivated by the ever increasing demands on automotive radar performance, the main aim of this thesis is to study the feasibility of radar operating with digitally generated OFDM waveforms for high-performance automotive radar applications. As opposed to the known works on the topic of automotive OFDM radar, the focus of this thesis is primarily on radar, whereas the possibility of simultaneous communication plays a secondary role. Consequently, this work aims at developing OFDM radar concepts and signal processing algorithms that achieve performance beyond that of their state-of-the-art counterparts. A more specific description of the main research objectives concerning different aspects of automotive radar is given below:

- (O1) The current automotive radar signal processing algorithms are based on a simplified signal model that approaches its limits for a more demanding parametrization. To achieve a higher performance, one research goal is to develop novel signal processing algorithms that overcome limitations of the state-of-the-art methods.
- (O2) As the use of MIMO radar for improved DOA estimation is an established approach for automotive radar, we aim at combining OFDM with MIMO radar based on advantageous multiplexing methods enabled by the multicarrier structure of OFDM.
- (O3) To ensure high radar performance in the presence of other radar sensors, i.e. in conditions of interference, one research objective is to develop interference mitigation methods for OFDM radar. These methods should facilitate high interference robustness, especially towards the state-of-the-art radar systems.
- (O4) A final research objective is to validate the developed signal processing methods and radar concepts with real world measurements based on a radar prototype. This is to verify their performance and prove their feasibility for real world automotive radar implementations.

For the radar concepts to be considered, the feasibility of realization for real-time automotive radar operation is imperative. This implies high computational efficiency of the signal processing methods and achievable demands on hardware components. Since the considered application is automotive, for the radar concepts in this thesis we consider the automotive frequency band at 77 GHz. Thus, the main research goal of this work is to develop a concept of a high-performance, interference-robust, digital automotive OFDM-MIMO radar at 77 GHz.

1.3. Contributions and Outline of the Work

Below we summarize the main contributions of this thesis and present the structure of the work. The main novelties of this dissertation are as follows:

- A rigorous signal model for OFDM radar that comprises effects arising for high-performance radar parametrization which have been mostly ignored up to now.
- *All-cell Doppler correction* (ACDC) method for overcoming the Doppler sensitivity of OFDM radar (initially reported in [Hakobyan, 2017a], patent application filed [Hakobyan, 2015a]).
- *All-cell migration compensation* (ACMC) algorithm for range and Doppler frequency migration compensation (patent application filed [Hakobyan, 2015b]).
- RS-OFDM operation mode dedicated to radar operation (initially reported in [Hakobyan, 2016f]).
- *Non-equidistant subcarrier interleaving* (NeqSI) based multiplexing for OFDM-MIMO radar (partially reported in [Hakobyan, 2016b], a family of patent applications filed [Hakobyan, 2015c, 2016a]).
- *Non-equidistant dynamic subcarrier interleaving* (NeqDySI) based multiplexing for OFDM-MIMO radar (initially reported in [Hakobyan, 2016d]).
- Method for optimization of non-equidistant interleaving patterns for OFDM-MIMO radar based on *genetic algorithms* (partially reported in [Hakobyan, 2017b]).

- *Sparse iterative multidimensional frequency estimation* (SIMFE) algorithm for sparsity based distance-velocity processing (partially reported in [Hakobyan, 2016b, 2017b]).
- Narrowband interference suppression algorithm for OFDM radar (initially reported in [Hakobyan, 2016c]).
- *Cognitive OFDM radar* concept for interference mitigation.
- *Carrier frequency hopping waveform adaptation* (CFH-WA) and *slow-time chirp waveform adaptation* (STC-WA) methods for adaptive interference avoidance.
- Method for linearization of the Doppler shift via *variable symbol repetition intervals* (VSRI) for STC-WA (patent application filed [Hakobyan, 2016e]).
- OFDM-MIMO radar prototype that outperforms its state-of-the-art counterparts in many key aspects (initially reported in [Hakobyan, 2016f]).

The remainder of this thesis is structured as follows. Chapter 2 introduces the topic of automotive radar. The main radar principles, the current automotive radar types, the concept of MIMO radar and multichannel processing, as well as the OFDM radar theory are presented in this chapter. Its summary provides a comparison between OFDM radar and traditional fast-chirp radar, emphasizing the motivation for automotive OFDM radar.

Chapter 3 presents a novel and rigorous signal model for OFDM radar and signal processing algorithms for distance-velocity estimation. Based on the introduced signal model, first the classical OFDM radar signal processing and its properties are discussed. Then, two novel signal processing methods — ACDC and APMC algorithms — are presented. The former overcomes the Doppler sensitivity problem of OFDM radar based on a scenario independent Doppler correction, whereas the latter achieves an improved distance and velocity resolution via compensation of the range and Doppler frequency migration.

The multiplexing of multiple transmit antennas for OFDM-MIMO radar is the topic of Chapter 4. This chapter presents the conventional multiplexing methods applied to OFDM radar as well as OFDM specific multiplexing approaches based on subcarrier interleaving. After discussion of the state-of-the-art *equidistant subcarrier interleaving* (EqSI), two novel multiplexing methods based on non-equidistant interleaving of subcarriers, namely NeqSI and NeqDySI are introduced. To obtain favorable interleaving patterns, we propose an optimization approach for NeqSI and NeqDySI schemes based on genetic algorithms. Since with these methods the OFDM subcarriers are interleaved over multiple transmit antennas, at each individual MIMO channel an incomplete measurement pattern is obtained. To overcome the limitations due to such subsampling, we introduce the SIMFE algorithm that performs a sparsity based frequency estimation from subsampled measurements. Since the SIMFE algorithm is based on the idea of *compressed sensing* (CS), this chapter provides a brief overview of the CS principles.

The topic of interference is addressed in Chapter 5. We first discuss the impact of OFDM radar signal processing on interfering signals. Then, a narrowband interference suppression method based on dropping the affected OFDM subcarriers and their subsequent reconstruction is presented. To obtain more universal interference robustness by means of adaptive interference avoidance, this chapter introduces the extension of OFDM radar with cognitive features.

Chapter 6 presents an OFDM-MIMO radar prototype realized at 24 GHz. Here, the novel signal processing algorithms and radar concepts introduced in previous chapters are validated with real world measurements.

Finally, Chapter 7 summarizes the main results of this thesis and provides some suggestions for future research.

Chapter 2.

Automotive Radar

This chapter introduces the theoretical basis for automotive radar. First, fundamental principles of distance, velocity and DOA estimation with radar are described in Section 2.1, followed by the description of state-of-the-art automotive radar systems in Section 2.2. OFDM radar principles are described in Section 2.3, along with a discussion of some further aspects regarding the parametrization, typical issues, etc. The principle of MIMO radar as well as some common multichannel signal processing methods are presented in Section 2.4. Finally, a general comparison of the principle and properties of OFDM radar to *fast-chirp radar*, i.e. to the state-of-the-art modulation for automotive radar, is given in Section 2.5.

2.1. The Radar Principle

The primary function of automotive radar is the detection of objects in the vehicle's surroundings and estimation of their parameters such as distance, velocity and direction. Based on this information, environment perception is enabled for higher level functions such as advanced driver assistance systems and autonomous driving. The principle behind radar is the transmission of electromagnetic waves that are reflected from the surrounding objects called radar targets. By reception and processing of the reflected radar signal, the presence of objects in the radar surroundings is identified (detection) and their parameters are estimated. As the name radar (radio detection and ranging) indicates, radar conventionally measures the target ranges (distances). Radar also enables measurement of targets' relative radial velocities based on the Doppler effect. To localize the radar targets, typically also estimation of target directions (angles) is performed. For a three-dimensional (3D) target localization, along with the distances both the azimuth and elevation angles of the targets are required. Fig. 2.1 shows the coordinate system for automotive radar measurements.

Below the principles of distance, velocity and DOA estimation with radar are presented. A more detailed introduction to radar can be found in [Skolnik, 2008; Richards, 2014b].

2.1.1. Propagation of Radar Signals

Radar emits electromagnetic signals, which for a point source are modeled as spherical waves propagating in free space. In terms of Maxwell equations, the free space is characterized by absence of charges ($\rho = 0$) and currents ($\underline{J} = 0$). Based on this, the third and fourth Maxwell's equations can be reduced to a form known as wave equations:

$$\nabla^2 \underline{E} - \frac{1}{c^2} \frac{\partial^2}{\partial t^2} \underline{E} = 0, \quad \nabla^2 \underline{B} - \frac{1}{c^2} \frac{\partial^2}{\partial t^2} \underline{B} = 0, \quad (2.1)$$

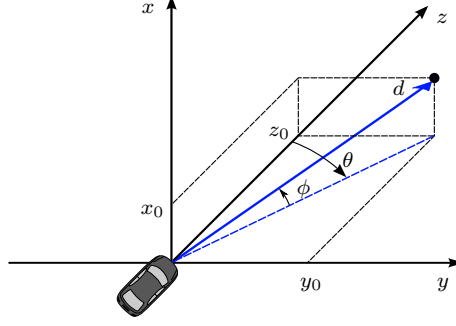


Figure 2.1.: 3D coordinate system for automotive radar: d -distance, θ -azimuth angle, ϕ -elevation angle

which are second order partial differential equations with the electric field \underline{E} and magnetic field \underline{B} . The parameter $c = 1/(\sqrt{\epsilon\mu})$ determined by the permittivity ϵ and permeability μ of the medium is the speed with which the electromagnetic waves propagate; in air it is equal to the speed of light in vacuum c_0 . The calculations in this work assume $c_0 = 299\,792\,458$ m/s.

In far field, electromagnetic waves can be considered as plane waves, i.e. waves for which the surface with equal phases — the wavefront — is a plane [Schoor, 2010]. For a point source to be in the far field of the antenna, the distance to the source d needs to be large in relation to the aperture size D [Balanis, 1997]:

$$d > \frac{2D^2}{\lambda_c}, \quad (2.2)$$

where $\lambda_c = c_0/f_c$ is the wavelength of the signal, with f_c being the carrier frequency. At 77 GHz and for an aperture size D of a few centimeters, the far field of the antenna begins already at several meters [Lange, 2012]. Thus, for the following we will assume targets being in far field.

Since radar signals are typically modulated, each frequency in the signal bandwidth propagates with its own wavelength, i.e. has a different phase progression. In case of narrowband signals, however, over the antenna aperture the wavelength of all frequency components in the signal can be approximated by the wavelength of the carrier frequency [Lange, 2012]. Hence, locally the propagation properties of narrowband signals can be assumed to be modulation independent (narrowband assumption). In the context of antenna (aperture) size, signals are considered narrowband if their bandwidth is much smaller than the inverse of the time it takes for the wave to pass the entire antenna aperture, i.e. $B \ll c_0/D$ [Trees, 2002]. For an aperture size of $D = 7.5 \dots 10$ cm typical for automotive radar, the narrowband assumption is valid for a bandwidth $B \ll 3 \dots 4$ GHz. Since in this work we consider systems with a bandwidth of up to 1 GHz, in the following we will consider the narrowband assumption in the context of the aperture size to be valid.

With both far-field approximation and narrowband assumption, (2.1) can be solved for electric field and plane sinusoidal waves [Balanis, 1997]:

$$\underline{E}(\underline{u}, t) = \underline{E}_0 e^{j2\pi \left(f_c t + \frac{\underline{u}^T \underline{p}}{\lambda_c} \right)}, \quad (2.3)$$

where

$$\underline{u} = \begin{bmatrix} u_x \\ u_y \\ u_z \end{bmatrix} = \begin{bmatrix} \sin \theta \cos \phi \\ \sin \theta \sin \phi \\ \cos \theta \end{bmatrix} \quad (2.4)$$

is a unit vector perpendicular to the wavefront and pointing in its direction, t is the time, $\underline{p} = [p_x, p_y, p_z]^T$ is a point in space, and \underline{E}_0 is the electric field at the origin of the coordinate system. From (2.3) it is apparent that between two points in space \underline{p}_1 and \underline{p}_2 the signal changes only in phase. Consequently, observing the signal at two or more different positions, information about the direction of the wavefront \underline{u} can be obtained. This principle is the basis of the array signal processing for DOA estimation, as we will discuss in more detail in Section 2.1.4.

The received power of the radar signal propagating in the form of spherical waves is given by the radar equation [Skolnik, 2008]:

$$P_{\text{Rx}} = \frac{P_{\text{Tx}} G_{\text{Tx}}}{4\pi d^2} \cdot \frac{\sigma_{\text{r}}}{4\pi d^2} \cdot \frac{G_{\text{Rx}} \lambda_{\text{c}}^2}{4\pi}. \quad (2.5)$$

The product of the three factors in (2.5) represents the physical processes the radar signal undergoes. The numerator of the first factor represents the power P_{Tx} transmitted by an antenna with gain G_{Tx} , and its denominator represents the divergence of the spherical radar waves. This term describes the power density of the radar signal at a distance d [Skolnik, 2008]. The numerator of the second term σ_{r} is the *radar cross section* (RCS) of the target that reflects part of the signal energy back in the direction of the radar. The denominator of the second term denotes analogously the divergence of the spherical radar waves on the return path after reflection from the target. The third term represents the effective aperture area of the receive antenna with gain G_{Rx} that collects a portion P_{Rx} of the reflected energy.

In (2.5), two target-dependent parameters are involved — distance and RCS. Since the received power has a $1/d^4$ dependency due to the path loss, for farther targets a strong decay of the received power takes place. Furthermore, the RCS of the target determines the amount of power reflected back towards the radar. It represents the effective surface of the target that reflects the radar waves back and is measured in square meters. The RCS is determined by the geometry of the target as well as by its reflective properties and can vary strongly with time, e.g. depending on the orientation of the target [Skolnik, 2008]. At 77 GHz, typical RCS values vary from 1 m^2 for a pedestrian to $10\,000 \text{ m}^2$ for a truck [Skolnik, 2008; Schoor, 2010]. Hence, both due to the strong distance dependency of the received power as well as RCS differences of targets, radar reflections exhibit strong amplitude variations. Therefore, automotive radars are typically required to have a large dynamic range, i.e. be able to detect weak signal in the presence of strong ones.

2.1.2. Distance Estimation

Radar uses the time-of-flight principle for distance measurement and the Doppler effect for velocity measurement. That is, by measuring the delay between transmission of the radar signal and reception of radar echoes τ , the distance to the target d can be found with

$$d = \frac{\tau c_0}{2}, \quad (2.6)$$

where c_0 is the velocity of propagation of radar waves that is approximately equal to the speed of light in vacuum. For pulse radar, short pulses are transmitted and the time delay to the reception of pulse-echoes is measured [Skolnik, 2008]. For other radar types that transmit longer signals continuously (parallel to reception of the radar echoes) such as *frequency modulated continuous wave* (FMCW) radar or OFDM radar, the received signal can be correlated with delayed versions of the transmitted waveform to obtain the delays. This is often referred to as pulse compression [Skolnik, 2008]. Since the specific realizations of the distance estimation methods are modulation dependent, we will discuss it in more detail in Chapter 3.

2.1.3. Velocity Estimation

For the relative radial velocity estimation, the Doppler frequency shift of the transmitted signal $f_D = f_{Tx} - f_{Rx}$, i.e. the difference between the transmit (Tx) frequency of the signal f_{Tx} and the receive (Rx) frequency f_{Rx} , is used:

$$v = -\frac{c_0 f_D}{2f_c} = -\frac{\lambda_c f_D}{2}, \quad (2.7)$$

where f_c and λ_c denote the center frequency and the wavelength of the radar signal, respectively. In our work, we define the target velocity such that its relationship to the Doppler shift is with a negative sign. This owes to the fact that for a target e.g. moving away from the radar, the distance $d(t) = d_0 + vt$ increases over the time t , and thus the velocity v is positive, whereas the frequency of the echo decreases, and thus the Doppler shift is negative. For most of the radar systems (pulse-Doppler, fast-chirp, OFDM), the Doppler shift is measured by evaluation of the phase progression over successively transmitted waveforms. From (2.7) it is apparent that the Doppler shift $f_D = -2vf_c/c_0$ depends on the frequency of the radar signal. That is, the higher the carrier frequency, the larger the Doppler shift, and thus the more Doppler sensitive the radar is.

2.1.4. DOA Estimation

For measurement of target directions, the DOA of the reflected electromagnetic waves is estimated. This is typically performed by “scanning” all directions based on the assumption that the antenna or the antenna array has a directive radiation pattern, i.e. receives more power from a certain direction. This dominant direction of the radiation pattern is called main beam. By pointing the main beam subsequently in each possible direction (*beamforming*), the DOA with the maximum power can be identified. Assuming a single main beam in the entire range of DOA from where the antenna is able to receive sufficient power (i.e. no ambiguities called *grating lobes*), the beam with the highest power will point to the DOA of the received signal. The narrower the main beam, the more precise DOA estimation can be performed. As for the beamforming, three possible approaches depending on how the scanning of DOAs is realized exist: mechanical, electronic and digital [Lange, 2012]. State-of-the-art automotive radar uses *digital beamforming* (DBF), and thus in the following we will focus on this approach.

For DBF, signals from all directions are received simultaneously by multiple receive antennas, i.e. antenna array. Due to different antenna positions and through the wave propagation described in Section 2.1.1, phase differences occur between the signals received at different antennas. These phase differences contain the DOA information. Denoting the Rx signal at the origin of the coordinate system by $y_0(t)$, the signals of q -th Rx channel is

$$y_q(t) = y_0(t)e^{j2\pi \frac{\mathbf{u}^T \mathbf{p}_q}{\lambda_c}}, \quad q \in [1, N_{Rx}], \quad (2.8)$$

where $\mathbf{p}_q = [p_{q,x}, p_{q,y}, p_{q,z}]^T$ denotes the position of the q -th Rx antenna, N_{Rx} is the number of Rx channels.

The signals of all Rx antennas are sampled, and the DOA estimation is performed in the digital domain via DBF. For each direction to be scanned, the received signals are combined with phases that direct the beam digitally in this direction. This corresponds to overlapping digitally

the beams of all Rx antennas such that in a certain direction a narrower beam occurs through constructive interference, whereas the other directions overlap destructively. Hence, with this approach Rx antennas are required to have a wide radiation pattern that receives sufficient power from all directions of interest. Then, the DOA estimation becomes a frequency estimation problem, where the antennas represent the sampling points and the waves represent complex exponentials in the spatial domain with frequencies determined by their DOA. Fig. 2.2 illustrates the principle of DOA estimation with an antenna array. This approach has the advantage of simultaneous acquisition of signals from all directions, but due to multiple Rx channels the hardware requirements are increased.

The conventional automotive radar signal processing performs the distance and velocity estimation first, such that the subsequent DOA estimation is carried out for targets already separated in distance and velocity. This significantly reduces the overall computational complexity of the radar estimation, without considerable reduction of estimation performance.

The positions of the array elements have a significant influence on the DOA estimation properties. The array aperture size determines the beam width, i.e. the larger the aperture, the narrower the main beam. The placing of the antenna elements determines the “radiation pattern” of the antenna array during the DBF. For linear arrays, equidistant placing of the array elements is one common array structure called *uniform linear array* (ULA). In the literature also nonuniform antenna arrays (e.g. sparse arrays) are widely studied, since they enable reduction of the number of channels for the same aperture size (see [Lange, 2012] and the references therein). Another widely established array type is the MIMO radar, which uses multiple antennas both on the Rx as well as Tx path. We will discuss this array type in detail in Section 2.4.

Although in our work we consider antenna arrays and MIMO systems in particular, we do not study aspects of DOA estimation related to placement of the antenna elements, since this is a well studied research area. Instead, we focus on modulation related aspects of MIMO radar.

2.2. State-of-the-Art Automotive Radar Systems

In the following, the conventional automotive radar systems operating with FMCW modulation are presented. These radar systems represent the state-of-the-art for automotive radar, and we address them in this work out of two considerations: *i)* for some discussions in the context of OFDM radar we refer to them as the baseline system, *ii)* and in Chapter 5 we propose interference mitigation techniques that are meant primarily for suppression or avoidance of interference from FMCW radars. Two systems are discussed below: the conventional FMCW radar with slow frequency ramps currently integrated in many vehicles, and the fast-chirp radar — the more advanced version of the FMCW radar. The latter has a similar distance-velocity estimation principle as the OFDM radar, and thus will be often referred to for comparisons. Both systems operate with FMCW modulation, i.e. with signal of linearly changing frequency and constant amplitude (frequency chirps, also called ramps). They represent, however, two substantially different approaches in terms of distance-velocity estimation.

2.2.1. FMCW Radar

FMCW radar operates with linear frequency modulated signals as shown in Fig. 2.3a. Over the duration T_{ch} , the frequency of the chirp signal is changing linearly by the chirp bandwidth B .

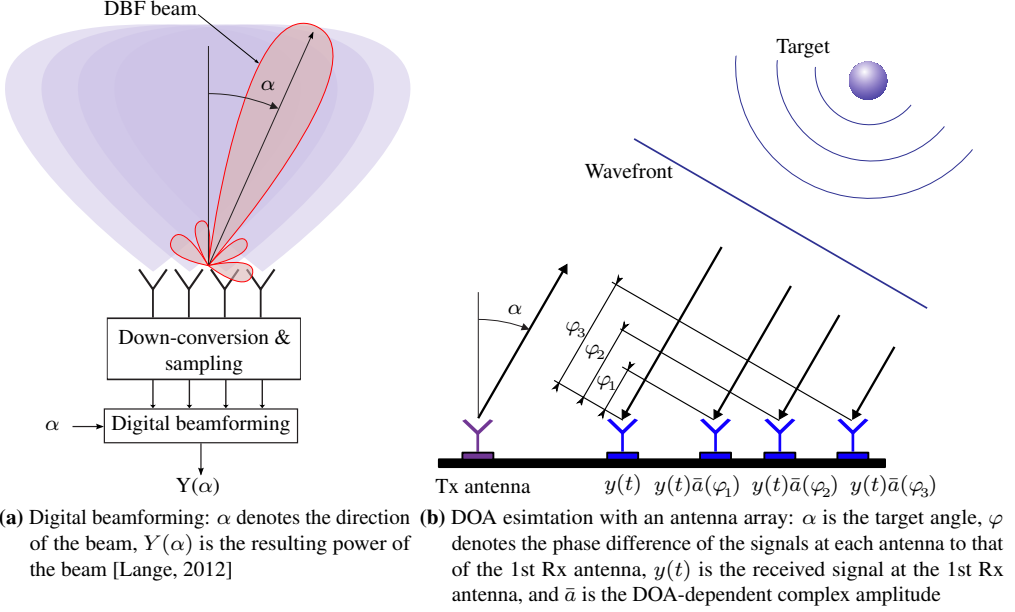


Figure 2.2.: Principle of DOA estimation with 1 Tx and 4 Rx antennas

After reflection from targets, the signal is received back by the radar. Reflections from targets are delayed by τ due to the time-of-flight and shifted in frequency by f_D due to the Doppler effect. The received signal comprising frequency and time shifted chirps is mixed with the transmit chirp. At the time of mixing, the instantaneous frequency of the Tx chirp has progressed compared to that of the reflection due to the time delay. Additionally, the received chirp has a Doppler-induced frequency shift. Thus, the mixing of two chirps yields their frequency difference¹ that is determined both by the delay and Doppler shift [Schoor, 2010]:

$$f_{\text{beat}} = f_{\text{Tx}} - f_{\text{Rx}} = \frac{B}{T_{\text{ch}}} \tau - f_D, \quad (2.9)$$

where f_{beat} represents the frequency difference between the Tx frequency f_{Tx} and Rx frequency f_{Rx} and is called beat frequency, and B/T_{ch} is the slope of the chirp, i.e. the rate of the frequency change. Clearly, mixing in (2.9) cancels the chirp modulation, leaving only the delay and Doppler-induced frequency difference. This frequency difference is measured by sampling the signal and frequency estimation via FFT. In fact, according to this measurement principle both the distance and velocity of the target are projected into a single measurement parameter — the beat frequency. Thus, without further measurements it is not possible to distinguish which portion of the beat frequency is caused by which of the two parameters. More specifically, in the distance-velocity plane the space of all valid solutions is represented by a line (Fig. 2.3b). To resolve this ambiguity in the distance-velocity space, a further chirp is required, which would yield another line in the distance-velocity space. The intersection of these two lines represents the target distance and velocity, i.e. resolves the distance-velocity ambiguity. Consequently, to obtain intersection of two lines, the additional chirp needs to have a different slope.

¹ For real mixers, in addition to the frequency difference, mixing leads to a sum of those frequencies, which is typically filtered out.

For multiple targets, a number of parallel lines representing possible solutions in the distance-velocity space occur for each chirp. For example, for two targets and two ramps of different slope, four intersections occur. Two of them do not represent physical targets, i.e. are ghost targets [Schoor, 2010]. Thus, another chirp is required to resolve the ambiguity. Generally, the number of chirps required for resolving the distance-velocity ambiguity for n targets is $n + 1$ [Reiher, 2008]. With the increasing number of targets and chirps, however, the number of intersections grows disproportionately [Schoor, 2010]. As a result, the distinction between true and ghost targets (so-called matching) becomes more computationally expensive and error-prone. To reduce the matching errors, the results from the previous measurement cycles can be incorporated.

The duration of FMCW ramps are typically in the range of several ms, whereas the chirp bandwidth can be up to few GHz. This results in a moderate chirp slope, and thus in comparably low beat frequencies in the range of several MHz. This is advantageous in terms of hardware cost, since *analog-to-digital converters* (ADCs) with low sampling rates can be used. Furthermore, due to the fact that target distances are projected into the beat frequencies, a distance dependent filtering already in the analog domain is possible. This is advantageous, since the distance dependent power decay due to the path loss can be partially compensated with the help of an analog high pass filter. As a result, the received signal exhibits a lower dynamic range. Furthermore, with a low pass *anti-aliasing filter* (AAF) the beat frequencies can be limited to a desired maximum distance such that overranges² are avoided. Additionally, in case of interference this enables to filter out a portion of the interfering signal that is outside the AAF passband.

A major drawback of this system is, however, the coupling between distance and velocity, which significantly limits the maximum number of detectable targets and necessitates matching which is error-prone. Another shortcoming, albeit not significant for chirps of a long duration, is the reduction of the effective bandwidth due to the time-of-flight (see B_e in Fig. 2.3a). The Tx and Rx chirps have a time shift due to the time-of-flight, and only the portion of the signal where all reflections are present is properly demodulated through mixing of the Rx signal with the Tx chirp. Consequently, not the entire time, and thus bandwidth can be used for the signal processing.

2.2.2. Fast-Chirp Radar

A more advanced radar concept operating with chirp signals is the fast-chirp radar. As the name indicates, this radar type uses chirps of a significantly shorter duration. Specifically, through the use of shorter chirps (i.e. with a higher slope) the portion of the beat frequency in (2.9) induced by the delay (distance) becomes predominant, and the Doppler term can be neglected. This enables Doppler independent distance measurements. For the velocity measurement, chirps are repeated subsequently, and the velocity estimation is performed through Doppler processing over the consecutive chirps — similar to the Doppler processing for pulse-Doppler radar [Skolnik, 2008]. Contrary to the FMCW radar described above, for fast-chirp radar conventionally identical chirps are used. This enables equidistant measurements for the Doppler processing. Hence, fast-chirp radar obtains (in the first approximation) independent distance and velocity measurements through the processing of each chirp and the phases over the consecutive chirps, respectively. In this work we refer to the samples within one chirp as fast-time samples, and to the values of a certain fast-time sample over the chirps as slow-time samples. The processing of these two dimensions spans a two-dimensional (2D) distance-velocity space, such that the error-prone matching step is

² Overranges are the reflections outside the distance range of interest that might lead to a detection of ghost targets due to the aliasing effect

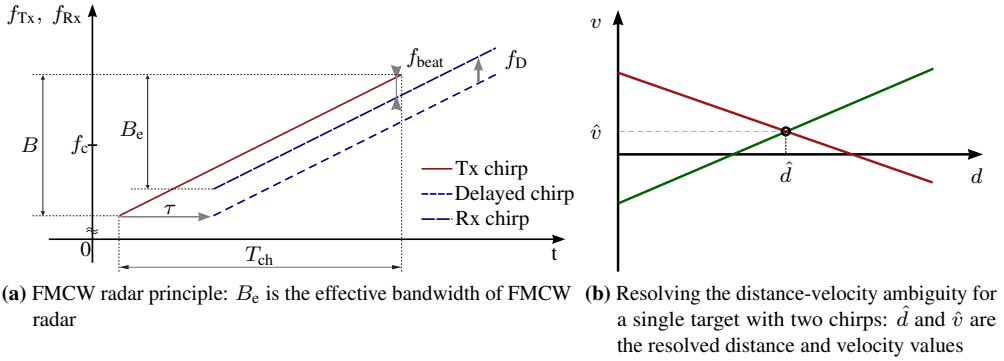


Figure 2.3.: Principle of distance-velocity estimation with FMCW radar [Schoor, 2010]

no longer required. This vastly increases the number of targets that can be processed in one cycle of distance-velocity estimation. The principle of fast-chirp radar is depicted in Fig. 2.4, where the Tx signal of fast-chirp radar (Fig. 2.4a) and the receive signal after the mixing with a chirp as well as after the 2D-FFT is shown (Fig. 2.4b).

According to (2.9), the radar signal of a single reflection after mixing with the Tx chirp is a sinusoid (complex exponential in case of *IQ-sampling*), whereas its Doppler-induced phase progression over the chirps is a complex exponential. Thus, a distance-velocity estimation can be efficiently performed using two-dimensional (2D) FFT processing. This yields a 2D radar image with targets represented by peaks at locations corresponding to their distances and velocities. By means of peak detection, a list of the detected radar targets comprising their distances and velocities is obtained.

The distance-velocity estimation principle of the described fast-chirp radar is similar to that of the OFDM radar described Section 2.3. The major difference of both concepts is the demodulation of the radar signal. Whereas OFDM radar samples the entire signal and performs the demodulation in the digital domain, the fast-chirp radar demodulates the signal prior to the sampling by analog mixing with the Tx chirp. After demodulation, the subsequent signal processing for the distance-velocity estimation is identical for both concepts — conventionally a 2D-FFT over the fast-time and slow-time samples is performed.

To enable unambiguous velocity estimation, the fast-chirp radar requires short chirp repetition intervals T_{CRI} (see Fig. 2.4a), typically in the range of $10\ \mu\text{s}$ to $100\ \mu\text{s}$. That is, for the same bandwidth it requires chirps with much higher slope than the FMCW radar. This results in a larger range of beat frequencies to be sampled, i.e. in ADC rates significantly higher than for FMCW radar but lower than for OFDM radar (sampling of the entire bandwidth). It maintains the advantage of distance-dependent analog filtering of FMCW radar, but the drawback of reduced effective bandwidth becomes more significant. For example, for a chirp duration of $10\ \mu\text{s}$ and a maximum distance of 150 m, the effective bandwidth is reduced by 10 %. Also, the analog filtering of a large portion of interference through AAF becomes less effective due to larger cutoff frequency of the AAF. In terms of interference robustness, a significant issue for fast-chirp radar is the correlation of its signals to the interference of other FMCW or fast-chirp radars. Specifically, interfering chirps of a similar slope are amplified through the 2D-FFT processing and focused into a region of the distance-velocity image, causing detection of ghost targets.

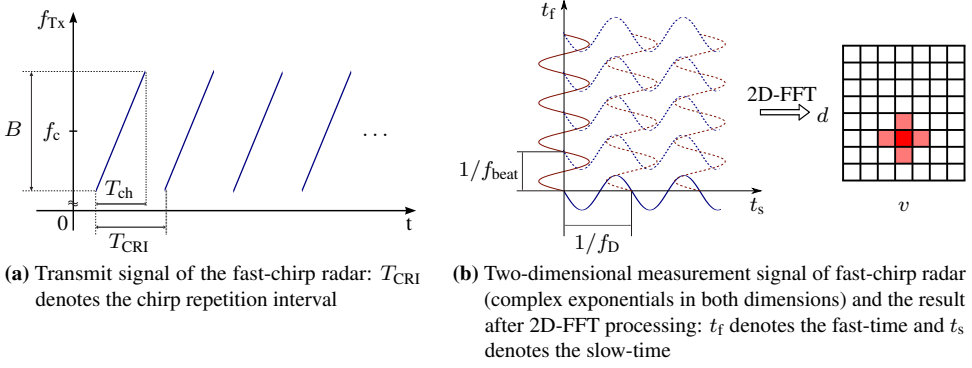


Figure 2.4.: Principle of fast-chirp radar

2.3. OFDM Radar

Digital OFDM radar represents a comparably new research field that attracted the attention of the radar community both in automotive and remote sensing applications. The primary interest to this topic owes to the great degree of flexibility OFDM provides in terms of digital generation and processing of radar waveforms. The freedom of operation with arbitrary OFDM modulated waveforms can be deployed for generation of new radar features not available with the analog signal generation. A well studied example is the combination of radar with communication by modulating the radar signal with communication information [Tigrek, 2010a; Sturm, 2012b; Braun, 2014]. In the following, we introduce the principles of OFDM radar and discuss its advantages as well as characteristic issues in Section 2.3.1, present some guidelines for its parametrization in Section 2.3.2, and describe some measures for reduction of the peak-to-average power ratio (PAPR) of OFDM waveforms in Section 2.3.4. Details of the OFDM radar signal processing are discussed in Chapter 3.

2.3.1. OFDM Radar Fundamentals

OFDM principle

As the name implies, OFDM (orthogonal frequency division multiplexing) is a frequency multiplexing technique based on transmission of multiple parallel data streams on orthogonal frequency subcarriers, i.e. subchannels. Thus, technically speaking OFDM is not a modulation but a multiplexing method based on subcarriers that can be modulated with an arbitrary digital modulation such as phase shift keying (PSK) or quadrature-amplitude modulation (QAM). Splitting of a single high-rate data stream into a number of slower streams by sharing the bandwidth between OFDM subcarriers has several notable advantages, such as robustness to severe channel conditions (e.g. fading due to multipath propagation) and low sensitivity to time synchronization errors. A characteristic feature of OFDM is the placement of orthogonal subcarriers such that they partially overlap in frequency domain, resulting in a high spectral efficiency.

The idea of OFDM was introduced by Chang in 1966 [Chang, 1966]. Some of the subsequent work considered impractical analog implementation for the generation of orthogonal OFDM subcarriers using a bank of oscillators at the required frequencies, until in 1971 a digital implementation using the *discrete Fourier transform* (DFT) was proposed by Weinstein and Ebert [Weinstein,

1971]. Another notable contribution to the development of OFDM was published by Peled and Ruiz in 1980 [Peled, 1980], who proposed the use of a *cyclic prefix* (CP) to convert the linear convolutive channel to a channel performing cyclic convolution, in order to avoid *intersymbol interferences* (ISI). These developments served as the foundation for the widespread use of OFDM for many communication applications including WLAN, LTE, DSL, as well as DVB.

At the very core of OFDM is the notion of overlapping yet orthogonal subcarriers, as illustrated in Fig. 2.5a. In frequency domain, the orthogonality of sinc-shaped OFDM subcarriers means that they are placed such that at the frequency of each subcarrier the remaining subcarriers have their zeros. That is, at the exact subcarrier frequencies the values of the subcarriers have no effect on each other. In time domain, the orthogonality of subcarriers means that over the duration of one complete OFDM sequence called OFDM symbol each subcarrier has a whole number of periods (Fig. 2.5b), i.e. their cross-correlation is zero. With T denoting the duration of the OFDM symbol and $1/f_n$ being the period of the n -th subcarrier, this condition can be mathematically expressed as

$$T \cdot f_n \in \mathbb{Z} \quad \forall n \in [0, N_c), \quad (2.10)$$

where N_c is the number of OFDM subcarriers. For subcarriers $f_n = n\Delta f$ with Δf being the subcarrier spacing, this condition can be simplified to

$$T = \frac{1}{\Delta f}, \quad (2.11)$$

which is the well-known orthogonality condition for OFDM.

A multicarrier signal $x(t)$ comprising a sum of N_c complex exponentials (subcarriers) can be expressed as

$$x(t) = \frac{1}{\sqrt{N_c}} \sum_{n=0}^{N_c-1} s(n) e^{j2\pi f_n t}, \quad (2.12)$$

where $s(n)$ is the complex amplitude, i.e. modulation symbol of the n -th subcarrier. With the orthogonality condition in (2.11), the signal in (2.12) can be represented in discrete-time $t = mT/N_c$, $m \in [0, N_c)$ as

$$x(m) = \frac{1}{\sqrt{N_c}} \sum_{n=0}^{N_c-1} s(n) e^{j2\pi \frac{nm}{N_c}}. \quad (2.13)$$

From (2.13), the similarity of the OFDM symbol structure to the inverse Fourier transform is apparent. This similarity enables efficient generation of digital OFDM signals via an inverse fast Fourier transform (IFFT).

Analogous to the IFFT based generation of the OFDM symbol at the transmitter, signals at the receiver can be demodulated via FFT. To this end, measures are required to guarantee that the orthogonality condition in (2.10) holds for the delayed OFDM signal. Furthermore, to facilitate intersymbol interference free transmission of consecutive OFDM symbols, i.e. such that they do not overlap at the receiver despite different delays of the multipath channel, methods are needed to isolate the consecutive symbols. As a solution to both of these problems, a cyclic prefix, i.e. an end portion of the OFDM symbol is appended before the symbol, as illustrated in Fig. 2.5b. The interval during which the CP is transmitted is called guard interval. To guarantee an ISI free transmission, the guard interval is required to be longer than the longest propagation path, i.e.

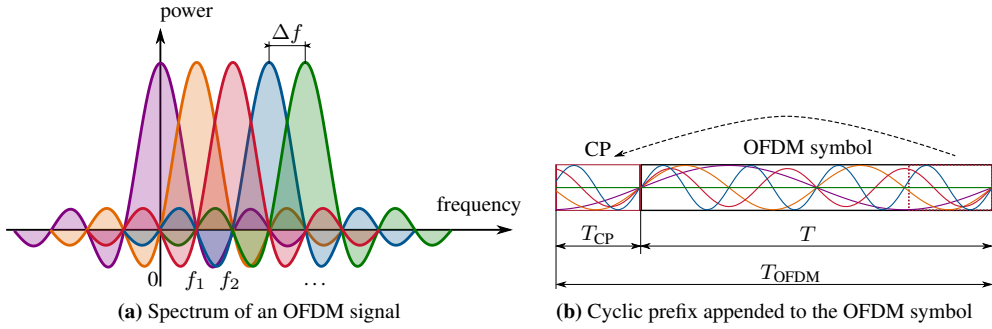


Figure 2.5.: OFDM signal in time and frequency

the longest delay between the transmission and reception. At the receiver, the sampling starts at the end of the guard interval, which guarantees that for each propagation path the complete T -long OFDM symbol is received. This causes the linear convolutive channel to become one that performs a circular convolution of the Tx OFDM symbol with the channel impulse response. Given that the sampling is at Nyquist rate, the resulting signal can be demodulated ISI-free at the receiver via FFT. The mathematical details of the CP based operation are discussed in Chapter 3.

Fig. 2.6 shows the block diagram of an OFDM transmitter and receiver in a homodyne realization with a quadrature modulation. The modulation symbols $s(n)$, $n \in [0, N_c - 1)$ representing the modulated communication data or the complex spectrum of the radar waveform are parallelized and fed to the IFFT. After serialization, the output of the IFFT represents the digital OFDM signal in time domain, i.e. the OFDM symbol. A CP is appended to the OFDM symbol to avoid ISI, after which the real and imaginary parts of the resulting signal are converted to the analog domain with a *digital-to-analog converter* (DAC) and quadrature modulated to the carrier frequency. The resulting signal is transmitted by a Tx antenna and travels through the channel to the receiver. For radar, the channel is the environment with targets reflecting the transmitted signal back to the radar. At the receiver, the Rx signals are analogously quadrature demodulated, sampled with ADCs, and the CP is removed³. For signals sampled at the Nyquist rate, the OFDM demodulation is carried out with FFT, which separates the subcarriers and yields their complex amplitudes $y_r(n)$. These values are determined by both the transmitted modulation symbols as well as the transfer function of the channel, i.e. the environment. Depending on the application, one of these two is of interest. Whereas for communication the unknown complex modulation symbols representing the communication data are primarily of interest, for radar the complex modulation symbols are known, and the goal is to estimate the environment transfer function, i.e. the radar scene.

OFDM radar principle

Similar to the fast-chirp radar described in Section 2.2.2, a block of digitally generated OFDM waveforms according to Fig. 2.6 can be used for distance-velocity estimation. The distance estimation is performed based on delays of OFDM symbols, whereas the velocity estimation is based on evaluation of the Doppler-induced phase progression over consecutive OFDM symbols.

³ Note that typically the sampling will start after the CP, and the block illustrating the removal of the CP is only for clarity of representation

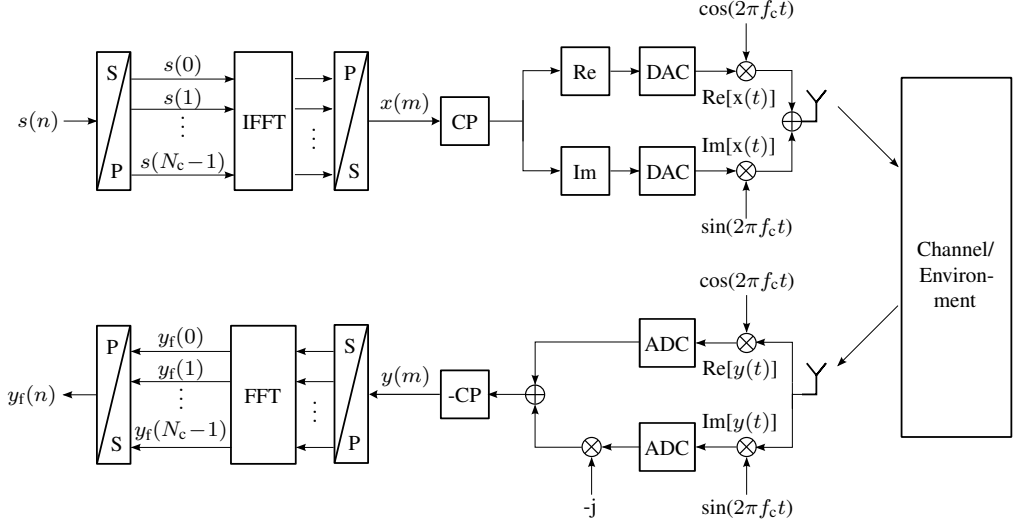


Figure 2.6.: Block diagram of an OFDM transmitter and receiver [Sturm, 2012b]: $s(n)$ denotes the modulation symbol of the n -th subcarrier, $x(m)$, $m \in [0, N_c - 1]$ is the discrete time-domain Tx OFDM symbol, $y(m)$, $m \in [0, N_c - 1]$ is the discrete time-domain Rx OFDM symbol, and $y_f(n)$ is the complex spectrum of the n -th subcarrier at the receiver

Thus, a block of OFDM symbols is used for the distance-velocity processing. Fig. 2.7 illustrates one such block constituting the measurement signal of one processing cycle in a time-frequency representation. Below we describe the basic principle of OFDM radar, while the mathematical foundation of OFDM radar signal processing is given in Chapter 3.

The block diagram in Fig. 2.6 is also applicable to OFDM radar. In this case, the transmitter and the receiver are colocated, and the channel represents the radar targets, i.e. produces a sum of delayed and Doppler shifted replicas of the transmitted OFDM signal. After quadrature demodulation and sampling at Nyquist rate, the received OFDM symbols in time domain are obtained. Thus, the measurement signal comprises a sum of cyclically delayed and Doppler shifted OFDM symbols. The evaluation of target delays is typically performed based on matched filtering efficiently implemented in the frequency domain. To this end, first the signal is transformed to the frequency domain via FFT, which separates the OFDM subcarriers (Fig. 2.7). In frequency domain, a cyclic delay τ of a single reflection $x(t)$ represents a complex exponential over the subcarriers:

$$x(t - \tau) \xrightarrow{\mathcal{F}} X(f) e^{-j2\pi\tau f}, \quad (2.14)$$

where $X(f)$ is the spectrum of $x(t)$. For OFDM radar, through the FFT the spectrum $X(f)$ at the positions of OFDM subcarriers, i.e. the complex modulation symbols $s(n)$ are obtained. These values represent the transmitted OFDM waveform. To process the delay-induced complex exponentials, first these values are canceled out via a complex spectral division of the received signal $y_f(n)$ by the transmitted modulation symbols $s(n)$ [Sturm, 2012b]. This operation can be considered as norming and is performed for all N_{sym} consecutive OFDM symbols individually. Through the spectral division the radar waveform is canceled out from all OFDM symbols, and a sum of delay and Doppler-induced 2D complex exponentials over the subcarriers and over the consecutive OFDM symbols is left — analogous to the measurement signal of fast-chirp radar in Fig. 2.4b. Consequently, the complex exponentials over the subcarriers are processed with IFFT

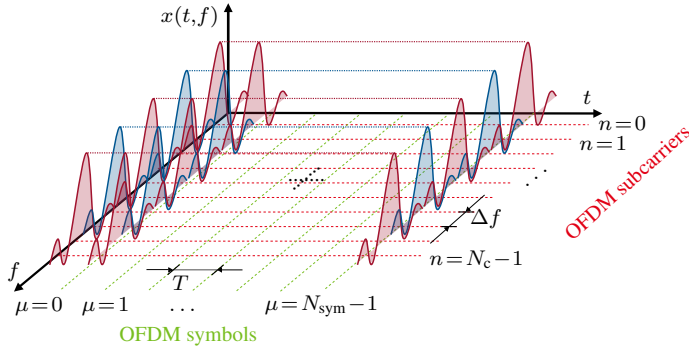


Figure 2.7.: Time-frequency representation of the OFDM radar signal: μ is the index of the OFDM symbol, i.e. in slow-time, N_{sym} denotes the number of OFDM symbols

to create the distance profiles, where each target is represented by a peak. The Doppler processing is analogously performed via FFT over the OFDM symbols, which yields a 2D distance-velocity image analogous to that in Fig. 2.4b.

Evidently, there is a certain similarity between the distance-velocity measurement principle of OFDM radar and fast-chirp radar. Two major differences are that OFDM radar operates with arbitrary OFDM waveforms generated digitally, and that the demodulation of the radar signal takes place in the digital domain, i.e. after sampling at the full Nyquist rate that corresponds to the bandwidth of the OFDM signal. OFDM modulation, demodulation, as well as the subsequent distance-velocity estimation are performed based on FFTs and IFFTs, facilitating efficient radar signal processing and enabling real-time implementation for automotive applications. The ability to perform the radar estimation with arbitrary OFDM waveforms provides room for advanced radar functions and novel features, especially in terms of adaptability and better spectral usage. Some of those features are summarized in Section 2.5.

Nevertheless, there are certain aspects of OFDM radar that have to be taken into account — issues specific either to OFDM modulation or to digital radar generally. These aspects are listed and discussed below.

Typical issues of OFDM radar

Sensitivity to Doppler shift. A fundamental issue of OFDM modulation both in radar and communication is its sensitivity to Doppler shift. More specifically, the orthogonality between OFDM subcarriers applies only at specific frequencies at which they are placed. In case the OFDM signal is Doppler shifted, the points where the orthogonality is given are shifted in frequency, and at the initial frequency points the subcarrier orthogonality deteriorates (see Fig. 2.8a). This leads to intercarrier interference (ICI), i.e. to reduced orthogonality between the OFDM subcarriers, which affects the radar performance. To limit the Doppler-induced ICI to a tolerable level, some works in the literature propose a subcarrier spacing much larger than the maximum possible Doppler shift [Sturm, 2011, 2012a], such that the shift of subcarriers relative to their spacing becomes negligible. This has, however, certain implications on the system parametrization. We will address the topic of Doppler shift in detail in Chapter 3, where we present a signal processing method for scenario-independent Doppler shift compensation.

High peak-to-average-power ratio (PAPR). Another fundamental drawback of OFDM both for radar and communication is the potentially high PAPR. For a time domain signal $x(t)$, PAPR denotes its peak power P_{peak} divided by its mean power P_{avg} :

$$\text{PAPR} = \frac{P_{\text{peak}}}{P_{\text{avg}}} = \frac{\max(|x(t)|^2)}{\frac{1}{T} \int_{n=0}^T |x(t)|^2 dt}, \quad (2.15)$$

In the literature, alternatively the square root of the PAPR called crest factor is used as a measure of the envelope variation. When expressed in dB, both measures are equivalent.

Given that the modulation symbols of the OFDM signal are of a unit amplitude (i.e. phase modulation such as PSK), the frequency domain OFDM signal has a nearly flat (rectangular) spectrum. Its envelope in the time domain, however, largely depends on the complex amplitudes of OFDM subcarriers, i.e. modulation symbols. If these symbols are such that many subcarrier values are added constructively at some point of time, a high peak in the time signal will occur. In fact, depending on these complex amplitudes, the PAPR of an OFDM waveform ranges from an ideal value of 1 for OFDM-generated chirp signals (see Section 2.3.4) to the maximum value of N_c for an OFDM pulse generated from OFDM subcarriers of a constant phase. For random modulation symbols modulated with e.g. quadrature phase shift keying (QPSK), depending on the number of subcarriers the typical PAPR values are in the range of 9 dB to 12 dB [Ochiai, 2001]. As the characteristic PAPR curves for OFDM (see e.g. [Ochiai, 2001]) show, for subcarriers modulated with random phases (e.g. random modulation content) the probability of very high or very low PAPR is negligibly low.

The high PAPR of OFDM has certain implications on hardware components — it imposes linearity demands on the signal chain. Along with the requirements on the resolution of the DACs at the transmitter and ADCs at the receiver, it imposes linearity requirements on the radio frequency (RF) power amplifiers (PA). Non-linearities in the signal chain cause distortion of the OFDM signal, leading to intermodulation terms and harmonics that result in spurious frequency components. The latter typically leads to raise of the noise floor during the radar signal processing as well as to out-of-band spurious radiation. To prevent this, the PAs need to operate in the linear region, which implies a certain back-off from the maximum power level. This leads to a decreased amplifier efficiency, i.e. output power, and as a result, to a lower *signal-to-noise ratio* (SNR) at the receiver.

Since the issue of high PAPR is characteristic of multicarrier signals, it has been studied for several decades. Subsequently, there is a large volume of literature dedicated to this topic — both studying the PAPR of OFDM in different configurations as well as proposing methods for PAPR reduction. For OFDM radar specifically, there are several works studying the waveform optimization with respect to the PAPR as well as the use of PAPR reduction techniques in case the radar waveform is used to carry communication data. We give an overview of these works in Section 2.3.4.

Time and frequency synchronization. For the orthogonality between OFDM subcarriers, the time and frequency synchronization at the receiver is essential. In other words, the synchronization errors both in time and frequency lead to ISI. Considering sampling of the signal for a duration T , a loose time synchronization generally means that some portion of the OFDM symbol will not be sampled, i.e. the orthogonality condition in (2.10) will not hold. Fortunately, in case of operation with CP, the time synchronization errors simply add up to the propagation delay of

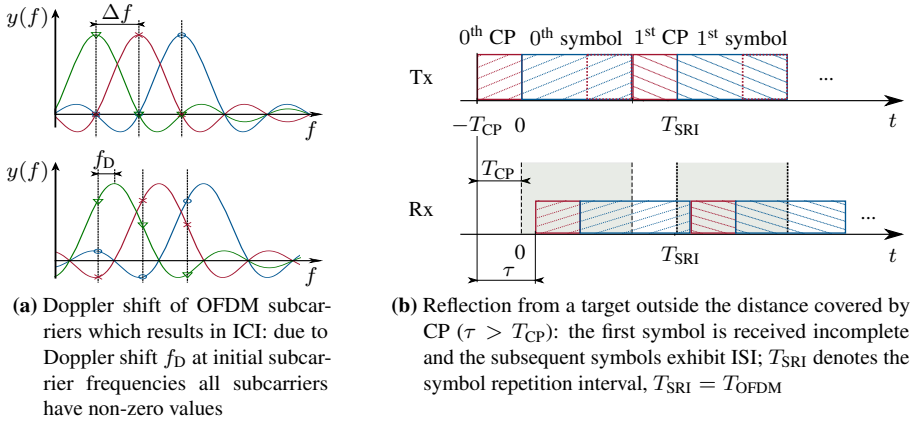


Figure 2.8.: Typical issues of OFDM radar that lead to ICI and/or ISI

the OFDM signal, and thus are efficiently accounted for by the CP. That is, in case a portion of OFDM symbol is used repetitively (e.g. due to CP), the time synchronization errors are less critical for OFDM.

As for the frequency synchronization errors, this type of error leads to a shift of the OFDM spectrum, i.e. to a similar ICI problem as the Doppler shift. Whereas this is a crucial aspect for communication systems where the transmitter and receiver use different (not synchronized) local oscillators (LO), for radar this type of error is typically not of relevance due to the use of the same LO for both the Tx and Rx path.

Inter-Symbol interference and overranges. As opposed to the fast-chirp radar that employs an analog AAF for suppression of reflections from far distances outside the range of interest, for OFDM radar no effective means for distance based analog filtering of the Rx signal is known in the literature. With CP-OFDM, typically the CP duration is chosen such that reflections from the entire distance range of interest can be processed unambiguously and without ISI. That is, the CP duration needs to be longer than the time-of-flight delay of the farthest reflection within the distance range of interest. Nevertheless, targets with a sufficiently high RCS outside the distance range of interest can theoretically result in reception of considerable reflection power. In the literature, such reflections are often referred to as overranges.

In case of OFDM radar, overranges lead to two adverse effects (Fig. 2.8b). For a conventional CP-OFDM, overranges lead to ISI, since they exhibit a longer delay than the CP accounts for. As a result, both the current OFDM symbol and the subsequent one are affected. Furthermore, in case the overranges are outside the unambiguously measurable distance range, they might lead to detections at a wrong distance due to aliasing. In case of changing OFDM symbols, the portion of the overrange OFDM symbol overlapping with the next one fails to focus into a peak due to the spectral division, which to a certain extent is a remedy to the problem of overranges. Nevertheless, for overranges the issue of ISI remains in the form of either ICI or ghost targets. Thus, this is an aspect to be taken into account during the system parametrization of OFDM radar.

Internal coupling and crosstalk between antennas. Another issue characteristic to all radar systems that transmit and receive simultaneously (e.g. FMCW, fast-chirp, OFDM) is the internal coupling inside the radar system that leads to strong input signal at the receiver. A common cause for such coupling is the crosstalk between the antennas. Whereas for FMCW and fast-chirp systems an analog low pass filtering of the internal coupling is possible, for OFDM radar analog filtering of the internal coupling will require more sophisticated approaches such as the ones used for full-duplex systems (see e.g. [Hong, 2014]). Thus, the issue of internal coupling needs to be considered both during the antenna design as well as for the dynamic range of the ADC. The latter has to be configured such that the strong internal coupling does not drive it into saturation, and at the same time weak signals from the range of interest are still detectable. We do not address this topic in the scope of this work, as we consider a proper sampling at the receiver and focus on the aspects concerning the digital domain signal processing. The impact of the properly sampled internal coupling on the radar image can be observed from the measurement results presented in Chapter 6.

Efficiency loss due to the guard interval. While the insertion of a *guard interval* filled with CP is an effective measure for preventing ISI and enables an efficient FFT-based processing at the OFDM receiver, it leads to a certain efficiency loss both in terms of power efficiency as well as effective time of measurement for a single OFDM symbol. Whereas for radar the former means a certain (typically insignificant) SNR loss, the latter determines the lower limit for the *symbol repetition interval* (SRI) denoted by $T_{\text{SRI}} \geq T_{\text{OFDM}}$, and thus the unambiguously measurable velocity range (see Section 2.3.2). To overcome this drawback, we propose in the following an operation mode dedicated to radar, which we name repeated symbols OFDM (RS-OFDM).

2.3.2. System Parametrization

In the following we discuss some key aspects of OFDM radar system parametrization according to [Sturm, 2009, 2012a]. We first give the equations for distance and velocity estimation parameters, and present subsequently an approach for system parametrization that considers the relationship between different radar parameters as well as limitations imposed by the radar signal processing. Based on these considerations, individual system parametrization is made for each concept or signal processing method presented in the subsequent chapters.

Distance estimation parameters

As discussed in Section 2.1.1 and Section 2.3.1, the distance estimation for OFDM radar is performed based on the time-of-flight principle and through processing of delay-induced complex exponentials over the OFDM subcarriers. Consequently, the distance between subcarriers (i.e. the subcarrier spacing) corresponds to the sampling step with which these complex exponentials are sampled, and thus determines the maximum *unambiguously measurable range* of delays that are the frequencies of these exponentials. This follows directly from the Nyquist-Shannon sampling theorem. Keeping in mind that complex valued signals are considered, the maximum unambiguously measurable delay $\tau_u = 2d_u/c_0$ is determined by the “sampling rate” $1/\Delta f$, which leads to

$$d_u = \frac{c_0}{2\Delta f}. \quad (2.16)$$

Analogously, the *resolution* — conventionally determined by the observation time — for the distance estimation is determined by the bandwidth over which the delay-induced complex

exponentials are observed. Thus, the inverse of the bandwidth B determines the resolution with which the delays $\Delta\tau = 2\Delta d/c_0$ are measured, which leads to

$$\Delta d = \frac{c_0}{2B} = \frac{d_u}{N_c} \quad (2.17)$$

for the resolution Δd of the distance processing. For the last identity in (2.17), $B = N_c \Delta f$ is used with N_c being the number of OFDM subcarriers.

Another distance parameter to be configured is the maximum distance of interest d_{\max} . This parameter determines the duration of the CP and typically needs to be set to the maximum distance from which potentially considerable reflection power can be expected. Thus, based on the chosen d_{\max} the CP duration is determined by

$$T_{\text{CP}} = \frac{2d_{\max}}{c_0}. \quad (2.18)$$

As discussed above, this parameter affects both the power efficiency of the OFDM radar as well as the Doppler processing parameters. Evidently, it is reasonable to choose $d_u \geq d_{\max}$, to ensure that the overranges do not lead to ghost targets.

Velocity estimation parameters

Based on the discussion in Section 2.1.1 and Section 2.3.1, the velocity estimation for OFDM radar is performed through estimation of Doppler-induced complex exponentials over the consecutive OFDM symbols. To this end, the OFDM symbols represent the sampling points, and thus the symbol repetition interval corresponds to the sampling step. Hence, according to the Nyquist-Shannon sampling theorem applied to complex signals, the maximum unambiguously measurable Doppler frequency $f_{\text{D,u}} = 2v_u f_c / c_0$ is determined by the sampling rate $1/T_{\text{SRI}}$. The unambiguously measurable velocity range is thus

$$v_u = \frac{c_0}{2f_c T_{\text{SRI}}}. \quad (2.19)$$

As opposed to the distance estimation where physically only positive values occur, the velocity estimation typically exhibits both positive and negative frequencies. That is, the unambiguous velocity range v_u needs to be set such that both positive and negative velocities are detected unambiguously. This, in fact, is a matter of interpretation of the detected Doppler frequencies, since due to the sampling only a limited range of frequencies can be detected unambiguously, and the detected values are assumed to belong to the chosen range. One meaningful choice for the automotive application is the symmetrical choice of the unambiguous velocity range around zero, e.g. $[-80, 80]$ m/s for $v_u = 160$ m/s. Another possibility is the dynamic adjustment of the unambiguous velocity range symmetric around the velocity of the ego vehicle [Sturm, 2012a].

Analogously, the velocity resolution is determined by the observation time of the Doppler-induced complex exponentials. The Doppler resolution $\Delta f_{\text{D}} = 2\Delta v f_c / c_0$ equals to the inverse of the measurement cycle duration $T_{\text{cycle}} = N_{\text{sym}} T_{\text{SRI}}$, which leads the following expression

$$\Delta v = \frac{c_0}{2f_c T_{\text{cycle}}} = \frac{v_u}{N_{\text{sym}}} \quad (2.20)$$

for the velocity resolution.

As (2.19) and (2.20) show, the velocity estimation parameters depend on the carrier frequency. The higher the carrier frequency, the less the unambiguous velocity range and the better the velocity resolution. That is, for the same v_u the higher carrier frequency requires shorter SRI. Another notable aspect from (2.20) is that for a given carrier frequency, Δv depends solely on the measurement cycle duration. This means that the velocity resolution can be simply improved by increasing the measurement duration. However, to obtain a proper pulse compression via the described 2D-FFT based processing, the measurement duration should not exceed the coherence time of the radar scene, i.e. the time during which the scene stays nearly unchanged.

OFDM radar parametrization

For configuration of suitable system parameters, different and sometimes contradictory boundary conditions need to be considered. Whereas some of these boundary conditions are set by the radar parameters and physical effects, others are imposed by the applied signal processing methods. We discuss these aspects below considering the classical OFDM radar signal processing based on the spectral division and 2D-FFT [Sturm, 2012a], while focusing mainly on modulation-related parameters, i.e. on the distance-velocity estimation. We consider an automotive radar parametrization at 77 GHz and start from the given requirements on the distance and velocity estimation, from which we subsequently derive the modulation parameters to satisfy these requirements.

As we will discuss in detail in Chapter 3, the classical OFDM radar signal processing assumes that the Doppler shift of OFDM subcarriers is negligible for all targets. This requires the subcarrier spacing Δf to be much larger than the maximum expected (positive or negative) Doppler shift $f_{D,\max}$, i.e. $\Delta f \gg |f_{D,\max}|$. A common approach is to choose $\Delta f \geq 10|f_{D,\max}|$ [Sturm, 2012a], which sets a lower limit on the subcarrier spacing $\Delta f_{\min} = 10|f_{D,\max}|$. Additionally, according to (2.16) the subcarrier spacing determines the unambiguous distance range, and thus for a given d_u it needs to be $\Delta f \leq c_0/(2d_u)$. This sets an upper limit on the subcarrier spacing $\Delta f_{\max} = c_0/(2d_u)$. Within the range $[\Delta f_{\min}, \Delta f_{\max}]$, the subcarrier spacing can be chosen freely. The smaller Δf , the longer the OFDM symbol $T = 1/\Delta f$. Due to the fact that the portion of the signal energy contained in CP is not received, it is advantageous to maximize the OFDM symbol duration within the given requirements, improving the energy efficiency. This suggests that it is preferable to set $\Delta f = \Delta f_{\min}$. The bandwidth required for the given distance resolution can be directly derived from (2.17), which together with the subcarrier spacing determines the number of OFDM subcarriers required: $N_c = B/\Delta f$. As the OFDM radar distance processing involves multiple FFTs, it is advantageous to choose N_c as a power of two, which may require to slightly adjust Δf or B within the allowed range.

The subcarrier spacing Δf determines the OFDM symbol duration $T = 1/\Delta f$. The duration of the CP T_{CP} is determined solely by the required maximum distance of interest d_{\max} . This completes the derivation of all distance-related parameters, including the duration of the OFDM symbol with CP $T_{\text{OFDM}} = T + T_{CP}$. This is the lower limit of the SRI, i.e. $T_{\text{SRI}} \geq T_{\text{OFDM}}$. The upper limit of the SRI is determined by the required v_u as in (2.19). Within this range, T_{SRI} can be adjusted by adding breaks between consecutive OFDM symbols. Taking into account that the velocity resolution Δv is determined by the measurement time T_{cycle} , this is advantageous for achieving the required $T_{\text{cycle}} = N_{\text{sym}} T_{\text{SRI}}$ with less number of OFDM symbols N_{sym} . However, once the requirement on Δv is satisfied, it is preferable to limit the measurement time in order not to exceed the coherence time of the radar scene. Also here, the choice of N_{sym} as a power of two is preferable due to the FFT processing.

Based on the above considerations, modulation parameters can be derived which satisfy the given radar parameters and enable accurate parameter estimation with the classical OFDM radar signal processing. In case a different signal processing method is used or multiple Tx antennas operate according the MIMO principle, the radar parametrization might need a certain adaptation, as we discuss individually for each method in the following chapters. Refer to Tables 6.1-6.5 for examples.

2.3.3. CP-OFDM vs. RS-OFDM

As discussed above, the use of CP for OFDM prevents ISI and keeps the orthogonality between OFDM subcarriers unaffected by the time delays. This is, however, at a cost of reduced power efficiency, since the signal energy contained in the CP is not captured at the receiver. Also, the use of CP increases the SRI of OFDM radar, resulting in a reduction of the unambiguously measurable velocity range. Whereas for communication the OFDM symbols carry communication data, and thus the consecutive symbols are generally different, in case of radar these are simply waveforms that serve for channel sensing and thus can be fixed to one repeating OFDM symbol. This has the advantage that the CP is no longer needed, and the same waveform can be repeated periodically without breaks. Technically speaking, this leads to ISI between identical symbols, i.e. analogous to CP-OFDM for a duration T the delayed OFDM symbols are a cyclically shifted version of the transmitted symbol. Hence, the advantage of CP-OFDM in terms of orthogonality between OFDM subcarriers is obtained, yet without reduction of the power efficiency. We proposed this radar-dedicated operation mode named *repeated symbols OFDM* (RS-OFDM) in [Hakobyan, 2016f].

The principle of RS-OFDM is illustrated in Fig. 2.9. Clearly, in the shown example where $T_{CP} = T/3$, RS-OFDM enables transmission of four OFDM symbols at a time duration when with CP-OFDM only three symbols are transmitted. With RS-OFDM, CP needs to be used only for the first symbol, and for all subsequent symbols CP is omitted. That is, the energy efficiency is increased from $T/(T + T_{CP})$ to $T_{cycle}/(T_{cycle} + T_{CP})$. This improves, among others, the SNR at the receiver, since more signal energy is received. A further, even more significant advantage of RS-OFDM in the context of radar is the reduction of the SRI to $T_{SRI} = T$, i.e. to its minimum. According to (2.19), this maximizes the unambiguously measurable velocity range v_u . This is a considerable advantage for high carrier frequencies (e.g. at 77 GHz), since for those frequencies the Doppler effect is stronger, and the unambiguous velocity range is accordingly lower.

Evidently, the advantage of RS-OFDM in terms of increased power efficiency and maximized unambiguous velocity range comes at the cost of fixing the consecutive OFDM symbols to a single symbol used for the entire measurement cycle. However, the used OFDM symbol can be arbitrary, e.g. carry communication information at a lower rate or be optimized with respect to PAPR. Even though the use of a fixed OFDM symbol represents a constraint in some respects, it facilitates the use of more advanced signal processing methods, as we present in Chapter 3. Furthermore, in Section 6.2 we give a parametrization example and some measurement results that demonstrate the advantages of RS-OFDM over CP-OFDM for radar. However, it should be noted that these two operation modes have different properties concerning certain effects such as influence of Doppler-induced ICI, as the simulations in Section 3.3 illustrate.

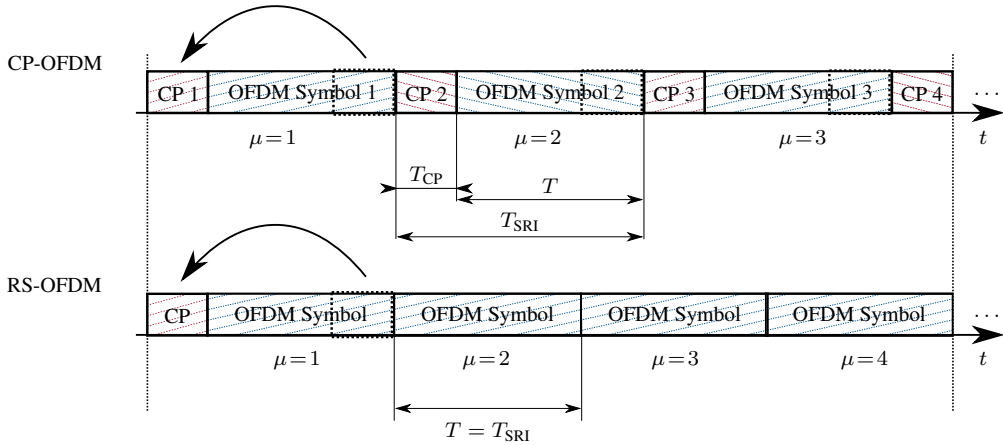


Figure 2.9.: Comparison of RS-OFDM to CP-OFDM for a CP duration $T/3$

2.3.4. Methods for Reduction of PAPR for OFDM Radar

As noted in Section 2.3.1, high PAPR is an issue characteristic for OFDM in general. Below we give an overview of the existing approaches and methods for PAPR reduction as well as point out the existence of certain OFDM generated waveforms that exhibit good PAPR characteristics.

The issue of PAPR has been largely studied in communications, since the problem of high PAPR of multicarrier signals has been known for several decades. There, the communication data to be transmitted are given, and the PAPR of the OFDM signal can only be influenced by the choice of a favorable method to represent the data with an OFDM signal. These methods include amplitude clipping and filtering for elimination of the peaks in the OFDM signal, use of coding to reduce the PAPR by using certain codewords, methods that map the OFDM envelope into the phase of a single carrier, etc. An overview of these methods and further PAPR reduction techniques can be found in [Han, 2005]. Some of these methods have been studied also for OFDM radar and communication systems in [Tigrek, 2010a]. This work investigates the applicability of PAPR reduction techniques such as single carrier OFDM, *Golay complementary codes*, clipping of the peaks of the OFDM signal, etc. for radar and provides some simulation results that demonstrate their influence on the radar performance. The use of constant envelope OFDM for adaptive digital radar is also studied in [Sen, 2011]. The Golay complementary codes were adopted for limiting the PAPR of OFDM radar also in [Paichard, 2010; Braun, 2014].

Another approach for obtaining OFDM waveforms with good PAPR characteristics suitable for radar only is the waveform optimization with respect to PAPR. Typically, such waveform optimization methods do not consider PAPR as the only optimization criterion, but include some further constraints or optimization goals. In [Sen, 2014], for example, a multi-objective PAPR constrained waveform optimization based on multiple optimization goals such as maximizing SNR, minimizing two separate Cramer–Rao bounds, etc. is performed. Other works in [Xia, 2015; Zhang, 2014] propose a joint optimization of OFDM subcarrier amplitudes and the PAPR for OFDM radar in the context of SAR imaging. Note that both of these optimization criteria affect the SNR of the radar image, and thus their joint optimization is meaningful. In [Lellouch, 2015], the use of genetic algorithms for multi-objective optimization of OFDM waveforms including the PAPR reduction is proposed. The author proposes a joint optimization of the

sidelobe level of correlation based distance processing and PAPR, while considering some further constraints such as selective use of the spectrum.

Finally, there are some OFDM waveforms with a closed-form phase dependency between subcarriers that exhibit good to ideal PAPR characteristics. One example of such waveforms is the OFDM-generated linear chirp obtained by quadratic phase dependency of OFDM subcarriers $\phi_n = \phi_0 - \pi n^2 / N_c$, where ϕ_n is the phase of the n -th subcarrier, and ϕ_0 is the phase of the first subcarrier [Schroeder, 1970]. Such an OFDM waveform exhibits a minimal PAPR as well as a flat spectrum, and the OFDM radar operating with it factually resembles a digital fast-chirp radar. Another example of an OFDM waveform with optimal PAPR is obtained by modulating the OFDM subcarriers with *Zadoff-Chu sequences*, as pointed out in [Cao, 2015]. However, it should be noted that such OFDM waveforms with a closed-form phase dependency between the subcarriers lack some of the randomizing and noise-like properties of OFDM radar. Features such as low cross-correlation to other radar waveforms or randomization of interference and distortions during the signal processing (see Chapter 5) are not necessarily maintained.

Based on the above discussion of a large number of remedies to the high PAPR problem of OFDM radar, we consider this topic sufficiently covered by the known research and do not study it in the scope of this work. For the radar prototype presented in Chapter 6, we consider modulation symbols with random phases and unitary amplitudes without a PAPR optimization. This results in performance representative also for simultaneous data transmission, while implying 9 dB to 12 dB back-off from the maximum power level due to linearity considerations.

2.4. MIMO Radar

MIMO radar is a technology for efficiently improving the DOA estimation — a concept meanwhile established in automotive radar applications. Below we present the MIMO radar principle, discuss the multiplexing of multiple Tx antennas, and describe its implications on the radar signal processing due to the multichannel setup as well as multiplexing.

2.4.1. Improved DOA Estimation Based on MIMO Array Processing

MIMO (multiple-input multiple-output) radar measures target reflections through multiple paths between the radar and the target that arise from the use of multiple antennas both at the transmit and receive sides. Contrary to the conventional multichannel DOA estimation based on a single Tx and multiple Rx antennas described in Section 2.1.4, i.e. *single-input multiple-output* (SIMO) system, MIMO radar achieves a number of paths larger than the number of radar antennas used. A single path from a Tx antenna to the target and back to an Rx antenna is called a spatial channel. The number of spatial channels (virtual antennas) is the product of the number of Tx and Rx antennas, i.e. $N_{\text{virt}} = N_{\text{Tx}} \times N_{\text{Rx}}$. Thus, given the same number of physical antennas, the number of spatial channels for MIMO is larger than that of a SIMO system. The paths representing the spatial channels can be arranged into an equivalent array consisting of a single Tx and $N_{\text{Tx}} \times N_{\text{Rx}}$ Rx antennas, which is called virtual array. The principle of MIMO radar and the corresponding virtual array is shown in Fig. 2.10.

From Fig. 2.10 it is evident that the use of multiple antennas both at the Tx and Rx sides results in a (virtual) array constructed efficiently with fewer physical antennas. Besides increasing the number of spatial channels, MIMO radar has additionally the advantage of achieving a larger

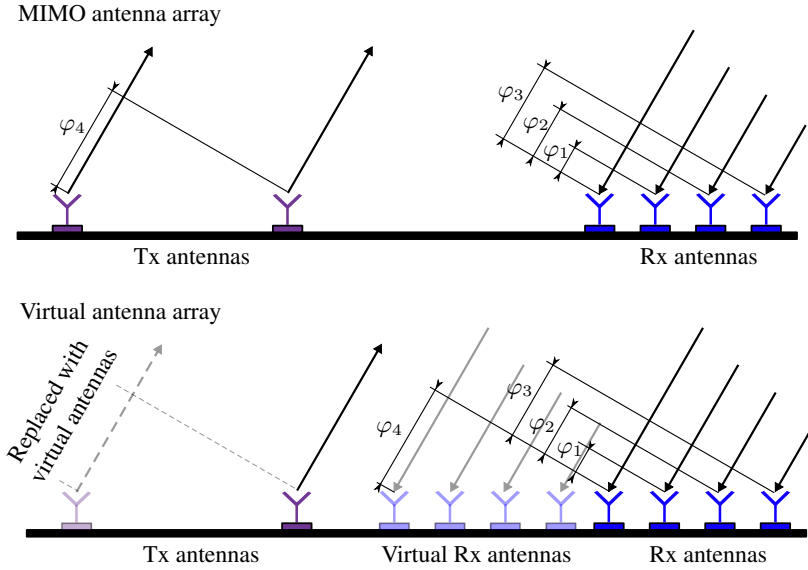


Figure 2.10.: The principle of MIMO radar for $N_{Tx} = 2$ and $N_{Rx} = 4$. The resulting number of array elements of the corresponding virtual array is $N_{virt} = 8$

equivalent aperture and thus a DOA resolution beyond that of the physical radar aperture. This is particularly valuable for automotive applications, since a limited surface is available for the radar aperture and a high DOA resolution is advantageous. Thus, MIMO radar improves efficiently the DOA estimation, both in terms of increasing the number of spatial channels as well as enabling a larger virtual aperture.

2.4.2. Multiplexing of Tx Antennas for MIMO Radar

The simultaneous use of multiple Tx antennas for MIMO radar requires their signals to be distinguishable at the receiver. That is, methods for multiplexing of the Tx antennas are required to ensure that signals from different Tx antennas which traversed different paths do not interfere.

Multiplexing of Tx antennas implies their separation in at least one dimension. To this end, common approaches are time, frequency, or code division multiplexing. In case of time multiplexing, the antennas transmit sequentially in time, such that at each moment only one Tx antenna is active. For frequency multiplexing, each antenna operates at a dedicated frequency, such that a simultaneous operation of all Tx antennas, albeit with a lower bandwidth, is possible. Code multiplexing requires that Tx antennas transmit orthogonal codes such that their signals can be distinguished at the receiver based on their orthogonality. Also hybrid approaches that multiplex the Tx antennas in two dimensions, are possible. An example of such multiplexing is the space-time block codes that represent a code multiplexing stretched over multiple time samples. Furthermore, the multicarrier nature of OFDM enables more sophisticated multiplexing possibilities. Each OFDM subcarrier can individually be assigned to a Tx antenna, which provides multiple degrees of freedom for generation of orthogonal waveforms. This enables advantageous MIMO radar concepts not available for conventional modulation methods.

As multiplexing implies sharing of resources in some dimension, typically it results in fewer resources available for each Tx channel. In case of multiplexing in time, each Tx antenna has

only a portion of the entire measurement time available for its operation. Analogously, in case of frequency division multiplexing only a portion of the complete radar bandwidth is available per Tx antenna. Therefore, depending on the multiplexing method, some of the radar parameters will be affected by the use of the MIMO approach. This means that MIMO radar has certain implications on the radar estimation in general, and on the radar modulation in particular. In our work, we focus on these modulation related aspects of MIMO radar and study advanced multiplexing methods that enable advantageous combinations of OFDM radar with the MIMO concept. In Chapter 4, we study different multiplexing methods for OFDM radar (including the conventional ones) and propose some novel OFDM-MIMO radar concepts based on multiplexing through interleaving of OFDM subcarriers.

2.4.3. Multichannel Radar Signal Processing

DOA estimation requires processing of measurement signals from multiple spatial channels for both SIMO and MIMO radars. This concerns the entire radar signal processing, including the distance-velocity estimation as well as target detection. A common approach for automotive radar systems is to perform the distance-velocity processing first, based on methods described in Section 2.2.2 or Section 2.3 and for each individual spatial channel. In case of MIMO radar, this implies that the signals of different Tx channels are first separated, i.e. demultiplexed. This processing results in a distance-velocity radar image at each spatial channel. These radar images have, however, a DOA-dependent phase difference for each target, based on which a DOA estimation is performed in later processing steps. Intuitively, for better detection and parameter estimation performance it is advantageous to combine the radar images of all spatial channels. However, since these radar images exhibit DOA-dependent phase differences unknown at this processing step, their simple coherent integration is not meaningful. In fact, three common approaches for integration of the radar images from different spatial channels are:

- (I1) Detection and distance-velocity estimation on each channel individually, followed by combination of the detection results. A subsequent DOA estimation is performed for the detected peaks using their complex amplitudes from all spatial channels.
- (I2) *Non-coherent integration* (NCI) of the radar images, a single detection on the non-coherently integrated distance-velocity image, and a subsequent DOA estimation for the detected peaks.
- (I3) A coherent DOA processing for each cell of the distance-velocity image, and a subsequent detection in a three or four dimensional space (distance, velocity, azimuth DOA and when applicable elevation DOA).

The first approach has the drawback that detection needs to be performed on the radar image of each spatial channel individually. This is both computationally expensive and suboptimal regarding the SNR. In contrast, the third method is optimal with respect to the SNR due to coherent processing of the entire multichannel measurement signal. However, the computational cost of such processing are prohibitively high, especially if the DOA estimation involves azimuth and elevation processing. Furthermore, the dynamic range achieved in DOA processing is typically significantly lower than that of the distance-velocity estimation due to the construction tolerances of the antenna array, and thus a decoupling of these estimation problems is advantageous. The second approach based on NCI, i.e. integration of the distance-velocity power spectra of all spatial channels, is significantly superior to the other two methods in terms of computational efficiency. This owes to the fact that a single detection is performed on the NCI radar image,

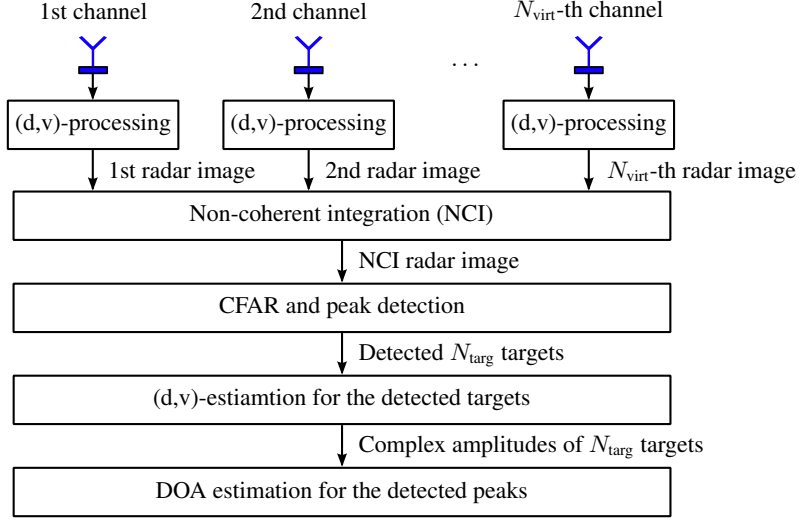


Figure 2.11.: The signal processing flow of multichannel radar processing based on non-coherent integration of the radar images. Inputs are the measurements signals of the spatial channels, i.e. in case of MIMO radar these are the signals after demultiplexing of the Tx channels. N_{targ} denotes the number of detected targets

and the subsequent DOA processing is performed only for the distance-velocity cells detected to contain targets. In terms of SNR, it achieves slightly worse results than the coherent integration [Lange, 2012]. This can, however, be compensated by setting a lower threshold for the detection and discarding the false detections during the DOA estimation, since it obtains the full SNR due to coherent processing. Another advantage of this approach is the decoupling of the distance-velocity estimation from the DOA processing. This, among others, enables the use of parametric methods such as *maximum likelihood* (ML) estimator for the DOA estimation. Due to these advantages this multichannel processing approach will be adopted for the MIMO radar concepts studied in this work.

More specifically, for joint processing of all spatial channels we consider the following signal processing flow: (1) distance-velocity processing for each spatial channel (includes demultiplexing of signals from different Tx channels in case of MIMO radar), (2) a non-coherent integration of these radar images, (3) a *constant false alarm rate* (CFAR) based peak detection on the NCI radar image, (4) distance-velocity estimation for the detected peaks based on their indexes, and (5) a subsequent DOA estimation for the detected peaks based on their complex amplitudes at spatial channels. This signal processing flow is illustrated in Fig. 2.11.

2.5. Comparison of Digital OFDM Radar to Traditional Fast-Chirp Radar

To summarize the discussion of OFDM radar fundamentals and to emphasize the motivation for its application in the automotive area, below we compare the digital radar operating with OFDM waveforms to the traditional fast-chirp radar. A comparison between these two radar types, albeit from a different perspective, has been presented in [Fink, 2015a,b].

Generally, these two radar types have a similar distance-velocity estimation principle. Both systems span two orthogonal measurement dimensions by transmitting a sequence of waveforms, enabling a high-performance distance and velocity estimation for a large number of targets. Two major differences between them — from which most of the secondary differences originate — are *i*) how their signals are generated and *ii*) how the demodulation at the receiver is performed.

For fast-chirp radar, the Tx signals are linear frequency chirps of a short duration generated typically by analog circuits, and the demodulation at the receiver is performed by mixing of the Rx signal with the Tx chirp. The resulting signal consists of sinusoids with beat frequencies proportional to the target ranges and is sampled at a rate lower than the chirp bandwidth. Such analog demodulation of the radar signal projects the target distance into the beat frequency. This enables a distance-dependent analog filtering of the Rx signal, which is advantageous for reducing the requirements on the ADCs in terms of dynamic range. A drawback of such demodulation is the reduction of the effective bandwidth, since only the portion of the received signal that overlaps with the Tx chirp is evaluated. For OFDM radar, the Tx waveform is modulated digitally and converted into the analog domain with DACs. At the receiver, the signal is sampled at a rate corresponding to the OFDM radar bandwidth. The demodulation is then performed in the digital domain. Compared to fast-chirp radar, such processing at the receiver imposes higher demands on the Rx hardware, yet enabling radar operation with arbitrary OFDM generated waveforms.

The flexibility available with OFDM radar due to digital signal generation and demodulation can be exploited for different purposes. One well-studied application that leverages this flexibility is the modulation of OFDM radar waveforms to carry communication information. Another example that benefits from the ability of OFDM radar to operate with various waveforms is the use of waveforms with potentially low cross-correlation or orthogonal to signals of other radar systems. This enhances substantially the interference robustness of OFDM radar.

Some further advantages of OFDM radar originate from the OFDM modulation itself. One such advantage is the robustness of OFDM radar to narrowband interference (see Section 5.2). For MIMO radar, the multicarrier structure of OFDM facilitates advanced multiplexing schemes. Specifically, based on subcarrier interleaving multiple Tx antennas can operate simultaneously using the entire radar bandwidth (see Chapter 4). Among other advantages, such multiplexing schemes provide maximum coherence between the measurements of the MIMO channels, increasing the DOA estimation performance.

A promising perspective for OFDM radar is its further development towards adaptive or ultimately cognitive radar. The fully digital signal generation and processing of OFDM radar provides an ideal platform for implementation of cognitive radar features. As one vitally important application of this idea for future automotive radar systems, in our work we develop the first concept of cognitive OFDM radar for adaptive interference avoidance (Section 5.4).

Among drawbacks of OFDM radar compared to fast-chirp radar are the higher hardware demands, especially on the ADCs, DACs and in the general case on PAs. The lack of means for analog distance-dependent filtering imposes further demands on the hardware components, e.g. the ADCs are required to cover a larger dynamic range, the internal coupling and crosstalk are required to be kept low, etc. As opposed to the fast-chirp radar that filters overranges with the help of an analog AAF, no analog means for suppression of overranges exist for OFDM radar. The same AAF filters a portion of the interference in case of fast-chirp radar, whereas for OFDM radar the interference residing in the radar bandwidth is sampled fully. Finally, OFDM radar is

generally sensitive to Doppler shift. This last point can, however, be overcome with a signal processing approach we introduce in Section 3.3.

Over the course of development of the digital hardware, some of the drawbacks of OFDM radar such as high data rates become less significant, whereas its advantages in terms of flexibility and adaptability gain more importance for high-performance automotive radar applications.

Chapter 3.

OFDM Radar Signal Model and Signal Processing

Since for automotive radar the target detection is conventionally performed on distance-velocity radar images, the distance-velocity estimation is the cornerstone of automotive radar signal processing. For OFDM radar, the classical processing for distance-velocity estimation comprises a pulse compression over two dimensions — for each individual OFDM symbol and along the subsequent OFDM symbols. The pulse compression for an individual OFDM symbol yields the time delays of the radar reflections that correspond to the distances of radar targets. It is typically performed via matched filtering efficiently implemented in the frequency domain, and the output of this operation is commonly referred to as distance (range) profiles. Subsequently, for velocity estimation the Doppler induced phase progression over OFDM symbols is evaluated via a Fourier transform, resulting in a distance-velocity radar image.

The described classical processing assumes decoupling between the distance and velocity estimations, i.e. no Doppler effect within an OFDM symbol and no distance change along the OFDM symbols. The first assumption holds for a system parametrization with a subcarrier spacing much larger than the Doppler shift. Its violation due to large Doppler shifts results in a reduction of orthogonality between OFDM subcarriers, i.e. in inter-carrier-interference (ICI). The second assumption is applicable for systems with small time-bandwidth product. Its violation leads to an effect commonly known as range migration, which results in smearing of peaks in the radar image. This deteriorates the resolution in distance-velocity estimation. Consequently, with the classical signal processing the resolution simultaneously achievable in distance and velocity is limited regardless of the system parametrization.

To overcome the described limitations and to extend the performance of OFDM radar beyond the capabilities of the state-of-the-art signal processing, novel signal processing approaches are presented in this chapter. First, a novel and rigorous signal model for OFDM radar is introduced in Section 3.1. Based on this signal model, the assumptions upon which the classical processing is based are discussed. The classical signal processing is presented in Section 3.2. In Section 3.3, a signal processing method that overcomes the Doppler sensitivity of OFDM radar named all-cell Doppler correction (ACDC) is presented. The proposed method enables an ICI-free processing for any number of targets via a scenario independent correction of Doppler shifts. A range migration compensation method based on the same idea of all-cell correction named all-cell migration compensation (ACMC) is introduced in Section 3.4. This approach enables a simultaneously achievable range and velocity resolution far beyond that of the state-of-the-art OFDM radar signal processing. Thus, the combination of ACDC with ACMC enables maximization of the

unambiguously measurable range as well as resolution in distance and velocity, and thus opens new perspectives for high performance OFDM radar.

To comply with the literature, for the description of the range and Doppler frequency migration and corresponding compensation methods the distance and velocity estimation is referred to as range and Doppler estimation.

3.1. Signal Model

This section introduces a comprehensive signal model for OFDM radar. First, the continuous-time OFDM radar signal model is given, followed by its discrete counterpart. For a concise representation of the signal processing steps in the following sections, a matrix notation of the sampled signal is adopted. Two main novelties of the presented signal model are the additional terms which are commonly ignored in other works as well as the matrix notation that allows two-dimensional representation of signal processing steps.

3.1.1. Continuous-Time Signal Model

An OFDM signal is mathematically described by the following equation [Sturm, 2012b]:

$$x(t) = \frac{1}{\sqrt{N_c}} \sum_{\mu=0}^{N_{\text{sym}}-1} \sum_{n=0}^{N_c-1} s(n, \mu) e^{j2\pi f_n t_i} \text{rect}\left(\frac{t_i + T_{\text{CP}}}{T_{\text{OFDM}}}\right), \quad (3.1)$$

where $x(t)$ is the complex time domain OFDM signal in baseband, N_c is the number of OFDM subcarriers, N_{sym} is the number of OFDM symbols (used for one evaluation cycle), $s(n, \mu)$ is the complex modulation symbol transmitted on n -th subcarrier of μ -th OFDM symbol, $f_n = n\Delta f$ is the frequency of n -th OFDM subcarrier, $\Delta f = 1/T$ is the subcarrier spacing, T is the OFDM symbol duration, $t_i = t - \mu T_{\text{SRI}}$ is the (relative) fast-time for the μ -th OFDM symbol to describe the identical symbol generation and processing¹, T_{CP} is the duration of the cyclic prefix, $T_{\text{SRI}} = T_{\text{OFDM}} + T_0$ is the repetition interval of OFDM symbols, T_0 is the duration of the break between the symbols, and $T_{\text{OFDM}} = T + T_{\text{CP}}$ is the duration of the OFDM symbol including the cyclic prefix. The function $\text{rect}(\cdot)$ describes a rectangular function defined as

$$\text{rect}\left(\frac{t}{T}\right) = \begin{cases} 1 & \text{for } 0 \leq t < T \\ 0 & \text{otherwise} \end{cases}. \quad (3.2)$$

A graphical representation of the OFDM signal from (3.1) is given in Fig. 3.1. Note that as an origin of the absolute time axis the beginning of the first OFDM symbol is defined, which is the starting point of sampling at the receiver. Accordingly, the beginning of each OFDM symbol is the origin of the corresponding fast-time axis.

From (3.1), the representation of a single symbol as in (2.13) can be obtained for $\mu = 0$:

$$x_0(t) = x(t) \cdot \text{rect}\left(\frac{t}{T}\right) = \frac{1}{\sqrt{N_c}} \sum_{n=0}^{N_c-1} s(n, 0) e^{j2\pi f_n t}, \quad 0 \leq t < T. \quad (3.3)$$

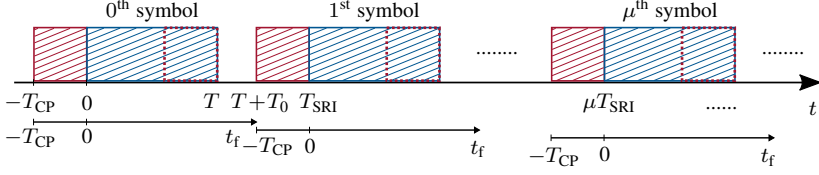


Figure 3.1.: OFDM signal model from (3.1). The dotted portion of the OFDM symbol is used as a CP

Before transmission, the baseband OFDM signal in (3.1) is shifted to the radio frequency (RF) band via quadrature modulation:

$$x_{\text{RF}}(t) = x(t)e^{j2\pi f_c t}, \quad (3.4)$$

where f_c is the carrier frequency. The transmitted signal is reflected from the targets and received back at the receiver. Assuming a constant amplitude and phase change $a_i(n, \mu) = a_i \forall i$ during the wave propagation and reflection on target for each individual propagation path i , the received RF signal can be written as:

$$y_{\text{RF}}(t) = \sum_{i=0}^{N_{\text{path}}-1} a_i x_{\text{RF}}(t - \tau_i(t)) = \sum_{i=0}^{N_{\text{path}}-1} a_i x(t - \tau_i(t)) e^{j2\pi f_c (t - \tau_i(t))}, \quad (3.5)$$

where N_{path} is the number of propagation paths, i is the path index, and $\tau_i(t)$ is the time dependent delay of the i -th reflection. Note that this modelling includes reflections from multiple targets as well as multiple reflections from single targets. Thus, it is not restricted to the point target assumption. Ignoring the third (acceleration) and higher order motion terms, the time dependent delay τ_i at time t is

$$\tau_i(t) = \frac{2(d_i + v_i t)}{c_0} = \tau_{0,i} + \gamma_i t, \quad (3.6)$$

where $\tau_{0,i} = 2d_i/c_0$ is the delay at $t = 0$, d_i is the distance to the i -th target at $t = 0$, and $\gamma_i = 2v_i/c_0$. For simplicity, we skip the index “0” of $\tau_{0,i}$ in the following.

After quadrature demodulation and substituting (3.6) into (3.5), the received baseband signal is:

$$y(t) = y_{\text{RF}}(t) e^{-j2\pi f_c t} = \sum_{i=0}^{N_{\text{path}}-1} a_i x((1 - \gamma_i)t - \tau_i) e^{-j2\pi f_c \tau_i} e^{j2\pi f_D t} \quad (3.7)$$

with $f_D = -\gamma f_c = -2v f_c / c_0$ being the Doppler shift. The term $(1 - \gamma)t$ implies a time stretching/compression of the received signal due to the Doppler effect. Thus, the received radar reflections in (3.7) are the attenuated, stretched or compressed, phase shifted, and Doppler shifted versions of the transmitted radar signal $x(t)$. Since the first exponential term in (3.7) is a constant phase shift, we denote $\bar{a}_i = a_i \cdot \exp(-j2\pi f_c \tau_i)$. Writing $x((1 - \gamma_i)t - \tau_i)$ as

$$x((1 - \gamma_i)t - \tau_i) = \frac{1}{\sqrt{N_c}} \sum_{\mu=0}^{N_{\text{sym}}-1} \sum_{n=0}^{N_c-1} s(n, \mu) e^{j2\pi f_n ((1 - \gamma_i)t - \tau_i - \mu T_{\text{SRI}})} \text{rect}\left(\frac{t_f + T_{\text{CP}} - \tau_i - \gamma_i t}{T_{\text{OFDM}}}\right) \quad (3.8)$$

1 We skip the dependency of t_f from t and μ for the simplicity of notation

and substituting (3.8) into (3.7), in fast-time notation $y(t)$ is:

$$y(t) = \sum_{i=0}^{N_{\text{path}}-1} \frac{\bar{a}_i}{\sqrt{N_c}} \sum_{\mu=0}^{N_{\text{sym}}-1} \sum_{n=0}^{N_c-1} s(n, \mu) e^{j2\pi f_n ((1-\gamma_i)t_f - \tau_i - \gamma_i \mu T_{\text{SRI}})} e^{j2\pi f_{D_i} (t_f + \mu T_{\text{SRI}})} \text{rect}\left(\frac{(1-\gamma_i)t_f + T_{\text{CP}} - \tau_i - \gamma_i \mu T_{\text{SRI}}}{T_{\text{OFDM}}}\right). \quad (3.9)$$

The argument of the rect function in (3.9) reveals the change of the signal form between its transmission and reception. The first term $(1-\gamma)t_f$ denotes the stretching/compression of the fast-time axis of each OFDM symbol. This occurs due to the target movement during the OFDM symbol duration. The term $\gamma\mu T_{\text{SRI}}$ represents the delay of the μ -th OFDM symbol due to the target movement relative to the delay τ of the first symbol. Hence, to ensure the sampling of the complete OFDM symbol for all symbols, T_{CP} has to be chosen properly, i.e. $T_{\text{CP}} \geq \tau_i + \gamma_i T_{\text{cycle}} \forall i$ with $T_{\text{cycle}} = N_{\text{sym}} T_{\text{SRI}}$.

3.1.2. Discrete-Time Signal Model

The received signal in (3.9) is sampled at the receiver. Sampling at the Nyquist rate starting at the end of the cyclic prefix, i.e. $t_f = (m/N_c)T$, $0 \leq m < N_c$, and assuming $\tau_i + \gamma_i T_{\text{cycle}} \leq T_{\text{CP}} \forall i$, the discrete-time received signal is:

$$y(m, \mu) = \sum_{i=0}^{N_{\text{path}}-1} \frac{\bar{a}_i}{\sqrt{N_c}} \sum_{n=0}^{N_c-1} s(n, \mu) e^{j2\pi f_n \frac{m}{N_c} T} e^{-j2\pi f_n \tau_i} e^{-j2\pi f_n \gamma_i \frac{m}{N_c} T} \cdot e^{-j2\pi f_n \gamma_i \mu T_{\text{SRI}}} e^{j2\pi f_{D_i} \frac{m}{N_c} T} e^{j2\pi f_{D_i} \mu T_{\text{SRI}}}, \quad 0 \leq m < N_c, \quad 0 \leq \mu < N_{\text{sym}}, \quad (3.10)$$

where $y(m, \mu)$ denotes the m -th sample of the μ -th OFDM symbol for the received discrete-time signal y . Analogous to the definition of fast-time in continuous-time notation, in discrete-time notation the time samples m within one OFDM symbol will be referred to as fast-time. Consequently, the time samples μ over OFDM symbols will be referred to as slow-time.

Before we continue, the effect of each individual exponential term in (3.10) is discussed below:

1. The first term $\exp(j2\pi f_n m T / N_c)$ represents OFDM subcarriers and can be simplified to $\exp(j2\pi n m / N_c)$ using $f_n = n \Delta f = n / T$.
2. The term $\exp(-j2\pi f_n \tau_i)$ describes the effect of the time delay τ on the OFDM symbol and can be interpreted as a complex exponential over the OFDM subcarriers. It is used for the distance estimation.
3. The third term $\exp(-j2\pi f_n \gamma_i m T / N_c)$ can be simplified to $\exp(-j2\pi n \gamma_i m / N_c)$ and represents a stretching/compression of the fast-time signal due to the target movement during one OFDM symbol. It leads to a compression/stretching of the frequency spectrum, i.e. OFDM subcarriers. This effect is commonly known as Doppler scaling [Tigrek, 2010a]. For most systems with $B \ll f_c$, this frequency stretching can be ignored based on the narrowband assumption.

4. The term $\exp(-j2\pi f_n \gamma_i \mu T_{\text{SRI}})$ denotes the effect of target movement on the OFDM subcarriers over the slow-time, and thus, is closely related to the third term. Whereas for narrowband systems with moderate measurement times this term can be neglected, for radars with high enough time-bandwidth product it may lead to a range and Doppler frequency migration. This effect is studied in detail in Section 3.4.
5. The term $\exp(j2\pi f_{D_i} mT/N_c)$ describes the Doppler shift of OFDM subcarriers due to the target movement. When not compensated, this term may lead to a reduction of orthogonality between OFDM subcarriers, i.e. to ICI. This effect is addressed in Section 3.3.
6. The last term $\exp(j2\pi f_{D_i} \mu T_{\text{SRI}})$ represents the Doppler induced phase change of OFDM symbols and it is used for velocity estimation.

We denote the normalized Doppler shifts by $\bar{f}_{D_i} = f_{D_i}/\Delta f = f_{D_i}T$, the normalized time delays by $\bar{\tau}_i = \tau_i \Delta f = \tau_i / T$ and $T_{\text{SRI}} = \alpha T$. Now we can rewrite (3.10) in a more compact form:

$$y(m, \mu) = \sum_{i=0}^{N_{\text{path}}-1} \frac{\bar{a}_i}{\sqrt{N_c}} \sum_{n=0}^{N_c-1} s(n, \mu) e^{j2\pi \frac{m}{N_c} (n + \bar{f}_{D_i})} e^{-j2\pi n \bar{\tau}_i} e^{-j2\pi n \gamma_i \left(\frac{m}{N_c} + \mu\alpha\right)} e^{j2\pi \bar{f}_{D_i} \mu \alpha}. \quad (3.11)$$

3.1.3. Signal Model in Matrix Notation

For a more concise representation of the signal processing steps, we use matrix notation for the received signal in (3.11):

$$\mathbf{y}_{\text{tf}, \text{ts}} = [y(m, \mu)]_{\substack{0 \leq m < N_c \\ 0 \leq \mu < N_{\text{sym}}}} = \sum_{i=0}^{N_{\text{path}}-1} \bar{a}_i \mathbf{D}_{N_c} \left(\frac{\bar{f}_{D_i}}{N_c} \right) (\mathbf{B}_i \odot \mathbf{F}_{N_c}^{-1}) \mathbf{D}_{N_c}^* (\bar{\tau}_i) (\mathbf{s} \odot \mathbf{P}_i) \mathbf{D}_{N_{\text{sym}}} (\bar{f}_{D_i} \alpha), \quad (3.12)$$

where the index “tf,ts” indicates the columns of \mathbf{y} being in fast-time and rows being in slow-time, \odot denotes the Hadamard (elementwise) product and “*” the complex conjugate, $\mathbf{s} = [s(n, \mu)] \in \mathbb{C}^{N_c \times N_{\text{sym}}}$ is the matrix of transmitted modulation symbols,

$$\mathbf{D}_N(\bar{f}) = \begin{pmatrix} 1 & 0 & \dots & 0 \\ 0 & e^{j2\pi \bar{f}} & \dots & 0 \\ \vdots & \vdots & \ddots & \vdots \\ 0 & 0 & \dots & e^{j2\pi \bar{f}(N-1)} \end{pmatrix} \in \mathbb{C}^{N \times N}, \quad (3.13)$$

\mathbf{B}_i denotes the effect of target movement in fast-time

$$\mathbf{B}_i = \left[e^{-j2\pi \frac{nm}{N_c} \gamma_i} \right]_{\substack{0 \leq m < N_c \\ 0 \leq n < N_c}} \in \mathbb{C}^{N_c \times N_c}, \quad (3.14)$$

\mathbf{P}_i represents the effect of target movement in slow-time

$$\mathbf{P}_i = \left[e^{-j2\pi n \gamma_i \mu \alpha} \right]_{\substack{0 \leq n < N_c \\ 0 \leq \mu < N_{\text{sym}}}} \in \mathbb{C}^{N_c \times N_{\text{sym}}}, \quad (3.15)$$

and \mathbf{F}_N is the DFT matrix defined as

$$\mathbf{F}_N = \frac{1}{\sqrt{N}} \left[e^{-j2\pi \frac{kn}{N}} \right]_{\substack{0 \leq k < N \\ 0 \leq n < N}} \in \mathbb{C}^{N \times N}. \quad (3.16)$$

The matrix notation in (3.12) illustrates clearly different components the signal model consists of. Moreover, in this notation the structure of each component as well as the order of operations during the signal processing are apparent. The terms in the signal model in (3.12) as well as their treatment according to the classical signal processing and in this thesis are summarized in Table 3.1.

Table 3.1.: Summary of terms in the signal model in (3.12)

Matrix	Referred as	Classical OFDM radar signal processing	In this thesis
\mathbf{s}	modulation symbols matrix	communication/waveform definition	waveform definition
$\mathbf{D}_{N_c}^*(\bar{\tau}_i)$	delay term	for range (distance) estimation	for range estimation
$\mathbf{D}_{N_{\text{sym}}}(\bar{f}_{D_i} \alpha)$	Doppler term	for Doppler estimation	for Doppler estimation
$\mathbf{F}_{N_c}^{-1}$	IDFT matrix		
\mathbf{P}_i	Range and Doppler frequency migration matrix	ignored, $\mathbf{P}_i = \mathbf{1}_{N_c} \cdot \mathbf{1}_{N_{\text{sym}}}^T \forall i$	corrected by ACMC
\mathbf{B}_i	Doppler scaling matrix	ignored, $\mathbf{B}_i = \mathbf{1}_{N_c} \cdot \mathbf{1}_{N_c}^T \forall i$	ignored, $\mathbf{B}_i = \mathbf{1}_{N_c} \cdot \mathbf{1}_{N_c}^T \forall i$
$\mathbf{D}_{N_c}(\bar{f}_{D_i} \frac{\alpha}{N_c})$	Doppler shift of OFDM subcarriers	ignored by assuming $I_{N_c} \forall i$	corrected by ACDC

3.2. Classical OFDM Radar Signal Processing

In this section, the state-of-the-art OFDM radar signal processing for distance-velocity estimation is presented based on the signal model in Section 3.1. A brief state-of-the-art review of the distance and velocity estimation methods for OFDM radar is given, followed by the description of the classical signal processing and a discussion of its properties.

3.2.1. State-of-the-Art Signal Processing Methods for OFDM Radar

As the use of multicarrier signals for radar was introduced by Levanon in [Levanon, 2000a,b], only the distance estimation was considered. For the distance estimation, a correlation of the received signal with the transmitted signal was proposed. The correlation-based processing requires, however, signals with a good autocorrelation function to minimize the sidelobe level in distance estimation. Furthermore, whereas these publications consider codes with a favourable periodic autocorrelation function, in the general case for distance estimation a linear and not cyclic correlation has to be performed. This leads to a considerably worse sidelobe level than that of the periodic autocorrelation function. Due to these drawbacks the signals studied in [Levanon, 2000a,b] show sidelobes less than 20 dB below the main peak. To improve the sidelobe level of correlation based processing, a train of OFDM pulses and weighted subcarrier amplitudes to achieve a windowing effect were investigated in [Levanon, 2002]. However, this approach

restricts the choice of the OFDM waveform to certain codes suitable for correlation based processing, significantly limiting the flexibility of the OFDM radar.

Further works in [Donnet, 2006; Garmatyuk, 2007, 2008, 2011] aimed at combining the radar functionality with communication and also considered a correlation based distance estimation. The dynamic range achieved by these concepts is only around 10 dB due to the sidelobes of linear correlation based processing. Note that these concepts do not use cyclic prefix for OFDM symbols as conventionally done in communications, but separate symbols with empty guard intervals.

A joint delay-Doppler (i.e. distance-velocity) processing with OFDM based multifrequency complementary phase coded signals was first briefly discussed in [Levanon, 2002]. Similar to the distance processing, also for the Doppler processing a dynamic range less than 20 dB is achieved. Further works in [Lellouch, 2008b,a] studied the feasibility of OFDM waveforms for Doppler processing and showed its high accuracy for velocity estimation. Eventually, an approach for a joint distance-velocity estimation with OFDM radar signals that carry communication information was presented in [Tigrek, 2008, 2009]. The method for distance estimation proposed in these works is a correlation based processing implemented efficiently in the frequency domain. However, an essential advantage of this approach compared to the previously published methods is the use of a cyclic prefix. At the receiver, the signals sampled at the end of the cyclic prefix are processed. This results in a received signal that contains a sum of cyclically shifted replica of the transmitted signal. Hence, the processing proposed in [Tigrek, 2008, 2009] results in a cyclic and not linear correlation, which significantly reduces the sidelobes in distance estimation. Yet no results of distance estimation are presented in these works, and the dynamic range achieved by this approach is not discussed. The same processing has been used in the context of distance estimation for passive radar with OFDM signals in [Berger, 2010a]. The authors derive the exact formulation of matched filter and show that it is identical with the discussed correlation based processing.

An alternative signal processing method for distance-velocity estimation with OFDM signals has been proposed in [Sturm, 2009, 2011, 2012a]. Also here, a set of OFDM symbols that carry communication information is used for distance and velocity estimation. In most aspects (e.g. CP operation, two-dimensional processing, Fourier analysis for Doppler estimation) the proposed processing is identical to that in [Tigrek, 2008]. There is, however, a difference in distance processing between these two approaches. Instead of correlation, the authors propose a spectral division based processing. The latter is based on the idea of spectral norming of OFDM subcarriers to eliminate the transmitted signal form. This is achieved by a division of the received spectrum by the transmitted modulation symbols for each individual subcarrier. In fact, by this operation not only the phases of OFDM subcarriers are corrected with the transmitted modulation symbols as in [Tigrek, 2008, 2009], but also the amplitudes. Whereas in case of unit amplitudes of OFDM subcarriers this operations are identical, for different subcarrier amplitudes the spectral division based processing shows superior sidelobe characteristics [Sturm, 2012a]. Therefore, this method has been adopted in the further works by other research groups in [Tigrek, 2010a; Zhang, 2014; Xia, 2015; Gassier, 2016], including the authors of [Tigrek, 2008, 2009].

Based on the discussion above it can be concluded that the spectral division based processing is the state-of-the-art method for distance-velocity estimation with OFDM radar. Thus, the OFDM radar concept in [Sturm, 2011, 2012a] will be considered as the baseline system for the

distance-velocity estimation methods presented in this chapter. In the next two sections, this concept and its properties are described in detail.

3.2.2. Description of the Classical OFDM Radar Processing

The classical OFDM radar signal processing from [Sturm, 2011, 2012a] assumes sampling of the received signal as described in Section 3.1, i.e. analogous to communications. Regarding sampling, the following assumption must be satisfied: the sampling is at Nyquist rate, starts at the end of the cyclic prefix, and thus simultaneous to the transmission of the OFDM symbol, and the signal is sampled exactly for the duration of OFDM symbol T . The last two assumptions imply the received discrete signal to be a sum of cyclically shifted replica of the transmitted OFDM symbol as depicted in Fig. 3.2. With these conditions imposed on sampling, the OFDM demodulation of the received signal can be performed efficiently via FFT.

In addition, the following assumptions are made regarding the signal model:

- (A1) The maximum possible Doppler shift $f_{D,\max}$ is much smaller than the subcarrier spacing Δf , and thus the Doppler shift of OFDM subcarriers can be neglected. This can be achieved by a suitable system parametrization, namely by large enough subcarrier spacing.
- (A2) No significant Doppler scaling takes place, i.e. all subcarriers undergo the same Doppler shift. This can be interpreted as narrowband assumption, i.e. assumption that all frequencies in the signal are influenced identically by the channel. This assumption is valid for systems with bandwidth much smaller than the carrier frequency, i.e. $B \ll f_c$.
- (A3) For the moving targets the distance change during the measurement is below the distance resolution of the radar, i.e. no range (distance) migration occurs. Thus, the distance change during the measurement can be ignored.

In terms of the signal model in (3.12), (A1) means that for all targets the effect of Doppler on individual OFDM symbols can be ignored, i.e. $\mathbf{D}_{N_c}(\bar{f}_{D_i}/N_c) = \mathbf{I}_{N_c}$, where \mathbf{I}_{N_c} is the identity matrix of size N_c . Analogously, (A2) and (A3) mean that the matrices \mathbf{B}_i and \mathbf{P}_i representing the target movement in fast-time and slow-time, respectively, can be also ignored for all targets: $\mathbf{B}_i = \mathbf{1}_{N_c} \cdot \mathbf{1}_{N_c}^T \forall i$ and $\mathbf{P}_i = \mathbf{1}_{N_c} \cdot \mathbf{1}_{N_{\text{sym}}}^T \forall i$, where $\mathbf{1}_N$ denotes an all-one column vector of size N , and “ T ” denotes the transpose.

In this thesis, the following short notations are used to describe the steps of the OFDM radar signal processing:

- t_f : fast-time, i.e. samples inside one OFDM symbol
- t_s : slow-time, i.e. successive OFDM symbols
- f : frequency across the OFDM subcarriers
- d : range (distance)
- v : velocity (Doppler)
- $\text{FFT}\downarrow$ and $\text{IFFT}\downarrow$: FFT and IFFT applied to the columns of the input matrix
- $\text{FFT}\rightarrow$ and $\text{IFFT}\rightarrow$: FFT and IFFT applied to the rows of the input matrix

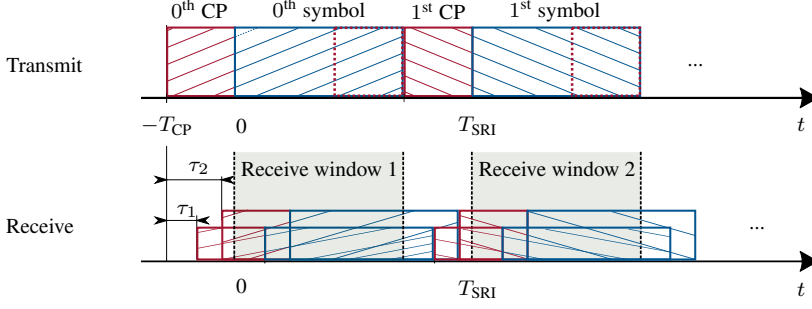


Figure 3.2.: OFDM signal transmission and reception, $T_{\text{SRI}} = T_{\text{OFDM}}$

- S.D.: spectral division, i.e. elementwise division of the received measurement matrix with the transmitted modulation symbols

With the described assumptions, the signal model in (3.12) can be simplified to

$$\mathbf{y}_{\text{f},\text{t}_s} = \sum_{i=0}^{N_{\text{path}}-1} \bar{a}_i \mathbf{F}_{N_c}^{-1} \mathbf{D}_{N_c}^* (\bar{\tau}_i) \mathbf{s} \mathbf{D}_{N_{\text{sym}}} (\bar{f}_{D_i} \alpha). \quad (3.17)$$

Note that for the simplicity of representation the additive noise term is not considered in (3.17). Instead, its effect is studied separately later in this section. An FFT over each OFDM symbol, i.e. column of $\mathbf{y}_{\text{f},\text{t}_s}$, is performed to separate the subcarriers:

$$\mathbf{y}_{\text{f},\text{t}_s} = \mathbf{F}_{N_c} \mathbf{y}_{\text{f},\text{t}_s} = \sum_{i=0}^{N_{\text{path}}-1} \bar{a}_i \mathbf{D}_{N_c}^* (\bar{\tau}_i) \mathbf{s} \mathbf{D}_{N_{\text{sym}}} (\bar{f}_{D_i} \alpha), \quad (3.18)$$

where the index “f,t_s” denotes the frequency domain and the slow-time domain over the first and second matrix dimensions, respectively. Then, the complex modulation symbols in $\mathbf{y}_{\text{f},\text{t}_s}$ can be eliminated via a complex elementwise spectral division of $\mathbf{y}_{\text{f},\text{t}_s}$ by the modulation symbols \mathbf{s} :

$$\begin{aligned} \mathbf{z}_{\text{f},\text{t}_s} &= \mathbf{y}_{\text{f},\text{t}_s} ./ \mathbf{s} = \sum_{i=0}^{N_{\text{path}}-1} \bar{a}_i \mathbf{D}_{N_c}^* (\bar{\tau}_i) (\mathbf{1}_{N_c} \cdot \mathbf{1}_{N_{\text{sym}}}^T) \mathbf{D}_{N_{\text{sym}}} (\bar{f}_{D_i} \alpha) \\ &= \sum_{i=0}^{N_{\text{path}}-1} \bar{a}_i \underline{\mathbf{D}}_{N_c}^* (\bar{\tau}_i) \cdot \underline{\mathbf{D}}_{N_{\text{sym}}}^T (\bar{f}_{D_i} \alpha) \end{aligned} \quad (3.19)$$

where $./$ denotes the elementwise division, $\underline{\mathbf{D}}_N = \mathbf{D}_N \mathbf{1}_N$, and $\underline{\mathbf{D}}_N^T = \mathbf{1}_N^T \mathbf{D}_N$. Note that the division in (3.19) is possible due to the diagonal structure of both \mathbf{D} matrices.

The alternative matched filtering based processing from [Tigrek, 2008] would correspond to an elementwise multiplication of $\mathbf{y}_{\text{f},\text{t}_s}$ with the complex conjugate of \mathbf{s} instead of the spectral division in (3.19): $\mathbf{z}_{\text{MF}} = \mathbf{y}_{\text{f},\text{t}_s} \odot \mathbf{s}^*$. Evidently, in case of unit amplitudes of complex modulation symbols in \mathbf{s} , $y(n,\mu)/s(n,\mu) = y(n,\mu)s(n,\mu)^* \forall n,\mu$, and thus the spectral division based processing corresponds to the matched filtering.

The matrix $\mathbf{z}_{\text{f},\text{t}_s}$ in (3.19) represents a sum of two-dimensional complex exponentials, whose frequencies over the subcarriers and over the OFDM symbols correspond to the distances and

velocities of the targets, respectively. For the Doppler processing, FFT over OFDM symbols (rows of \mathbf{z}_{f,t_s}) is performed in (3.20). In the resulting Doppler spectrum, each reflection is compressed into the corresponding Doppler cell:

$$\begin{aligned} \mathbf{z}_{f,v} &= \mathbf{z}_{f,t_s} \mathbf{w}_{N_{\text{sym}}} \mathbf{F}_{N_{\text{sym}}} = \sum_{i=0}^{N_{\text{path}}-1} \bar{a}_i \underline{D}_{N_c}^*(\bar{\tau}_i) \cdot \left(\underline{D}_{N_{\text{sym}}}^T(\bar{f}_{D_i} \alpha) \mathbf{w}_{N_{\text{sym}}} \mathbf{F}_{N_{\text{sym}}} \right) \\ &= \sum_{i=0}^{N_{\text{path}}-1} \bar{a}_i \underline{D}_{N_c}^*(\bar{\tau}_i) \cdot \underline{u}_{N_{\text{sym}}}^T(\bar{f}_{D_i} \alpha), \end{aligned} \quad (3.20)$$

where $\mathbf{w}_N = \text{diag}([w_N(0), \dots, w_N(N-1)]) \in \mathbb{R}_{\geq 0}^{N \times N}$ is a diagonal matrix of the applied window function, and

$$\underline{u}_N(f) = \frac{1}{\sqrt{N}} \begin{bmatrix} \sum_{n=0}^{N-1} w_N(n) e^{j2\pi(f - \frac{0}{N})n} \\ \vdots \\ \sum_{n=0}^{N-1} w_N(n) e^{j2\pi(f - \frac{N-1}{N})n} \end{bmatrix} \in \mathbb{C}^N \quad (3.21)$$

is the result of the FFT over the slow-time. As (3.20) shows, even though the Doppler spectra of all targets are superimposed, the energy of each reflection is mainly concentrated in the Doppler cell corresponding to its velocity, i.e. at the cell where $\underline{u}_{N_{\text{sym}}}^T(\bar{f}_{D_i} \alpha)$ has its maximum. This is achieved when in $\underline{u}_{N_{\text{sym}}}^T(\bar{f}_{D_i} \alpha)$ the argument of the exponential term yields zero, i.e. for the index l_i that yields $\bar{f}_{D_i} \alpha - l_i/N_{\text{sym}} = 0$. Consequently, by detecting the peaks of the Doppler spectrum, the normalized Doppler of the targets can be estimated by $\bar{f}_{D_i} = l_i/(N_{\text{sym}} \alpha)$ from the corresponding peak indices. According to the definition of the normalized Doppler shift, the target velocities can be calculated by $v_i = -\bar{f}_{D_i} \Delta f c_0 / (2f_c) = -l_i c_0 / (2f_c T \alpha N_{\text{sym}}) = -l_i \Delta v$, where Δv is the velocity resolution in (2.20). That is, the index $l \in [0, N_{\text{sym}})$ corresponds to positive Doppler frequencies in the range $[0, f_{D,u})$ with $f_{D,u} = (2v_u f_c)/c_0$ denoting the unambiguously measurable Doppler range, and thus to the range of velocities $(-v_u, 0]$.

Note that in the automotive application, targets may have both positive and negative velocities. Therefore, the unambiguous velocity range is often chosen symmetrical around zero, i.e. $[-v_u/2, v_u/2)$. Positive velocities in the range $(0, v_u/2)$ lead to negative Doppler shifts, which due to the slow-time sampling are aliased into the positive Doppler range $(f_{D,u}/2, f_{D,u})$. The latter corresponds to the range of indexes $(N_{\text{sym}}/2, N_{\text{sym}})$. Since this can be expressed as a modulo operation with the unambiguous Doppler range, for a symmetric choice of the unambiguous velocity range the Doppler indexes l_i have to be interpreted accordingly. More specifically, for targets with indexes $l_i \in (N_{\text{sym}}/2, N_{\text{sym}})$ corresponding to $v_i \in (0, v_u/2)$, by reversing the aliasing induced modulo operation the following relationship applies: $v_i = (l_i - N_{\text{sym}}/2) \Delta v$. This corresponds to a Doppler processing via a DFT with both positive and negative frequencies. For the sake of simplicity we consider a non-negative or non-positive velocity range for derivations in this chapter. The adjustment to other choices of the unambiguous velocity range is trivial.

Finally, the distance processing is performed via IFFT over the OFDM subcarriers (columns of $\mathbf{z}_{f,v}$), which yields the distance-velocity radar image:

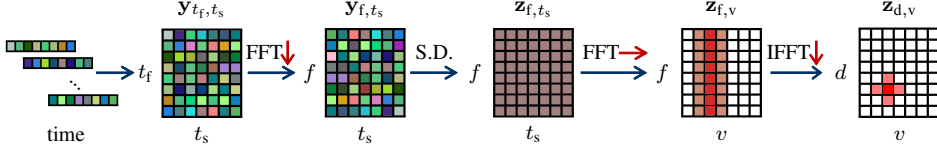


Figure 3.3.: OFDM signal transmission and reception

$$\begin{aligned}
 \mathbf{z}_{d,v} &= \mathbf{F}_{N_c}^{-1} \mathbf{w}_{N_c} \mathbf{z}_{f,v} = \sum_{i=0}^{N_{\text{path}}-1} \bar{a}_i \left(\mathbf{F}_{N_c}^{-1} \mathbf{w}_{N_c} \underline{D}_{N_c}^* (\bar{\tau}_i) \right) \cdot \underline{u}_{N_{\text{sym}}}^T (\bar{f}_{D_i} \alpha) \\
 &= \sum_{i=0}^{N_{\text{path}}-1} \bar{a}_i \underline{u}_{N_c}^* (\bar{\tau}_i) \cdot \underline{u}_{N_{\text{sym}}}^T (\bar{f}_{D_i} \alpha).
 \end{aligned} \tag{3.22}$$

Analogously, $\underline{u}_{N_c}^* (\bar{\tau}_i)$ represents the delay spectrum of the i -th target and has maximum for the index k_i such that $\bar{\tau}_i = k_i / N_c$. Hence, the target distances can be calculated from the normalized delay $\bar{\tau}$ with $d_i = \bar{\tau}_i c_0 / (2\Delta f) = k_i c_0 / (2\Delta f N_c) = k_i \Delta d$, where Δd is the distance resolution in (2.17).

Note that the order of operations in (3.20) and (3.22) is arbitrary and can be exchanged, e.g. for a more efficient practical realization. The described signal processing chain is depicted in Fig. 3.3. Note that the entire signal processing consists of computationally efficient FFT and IFFT operations with a computational complexity of $\mathcal{O}(N \log N)$ and a spectral elementwise division that has a low computational cost.

The properties of the presented signal processing, its performance in presence of noise and its limitations due to the assumptions (A1)-(A3) are discussed in the next section.

3.2.3. Performance of the Classical OFDM Radar Processing

Through the presented signal processing the major part of the signal energy for each reflection is concentrated into a single peak in the distance-velocity radar image. This enables to resolve and process multiple targets with different distances and/or velocities. Note that the result of the presented processing is independent of the OFDM signal form given by the modulation symbols s in (3.17), since the latter is canceled out by the spectral division in (3.19). The choice of s has, however, influence on noise in the radar image, which will be discussed below.

SNR analysis and sidelobe level

In order to analyze the SNR of the radar image, the noise power in each step of the signal processing has to be investigated. Let $\mathbf{W}_{f,t_s} \in \mathbb{C}^{N_c \times N_{\text{sym}}}$ denote the additive complex white Gaussian noise with zero mean and variance σ^2 at the input of the signal processing in (3.17), i.e. $W_{f,t_s}(m, \mu) \sim \mathcal{CN}(0, \sigma^2) \forall m, \mu$. The FFT in (3.18) does not influence the noise power, since FFT is a unitary operation. Thus, the noise matrix at the output of the FFT $\mathbf{W}_{f,t_s} = \mathbf{F}_{N_c} \mathbf{W}_{f,t_s}$ has the same power as \mathbf{W}_{f,t_s} . The spectral division in (3.19), however, has an influence on the noise power, and the (m, μ) -th element of the resulting noise matrix $\bar{\mathbf{W}}_{f,t_s} = \mathbf{W}_{f,t_s} ./ s$ has a variance $\sigma^2 / |s(n, \mu)|^2$ [Zhang, 2014]. Whereas the subsequent FFT and IFFT operations in (3.20) and (3.22) do not influence the noise power, windowing has an impact on the noise. Thus, the noise matrix in the radar image is $\mathbf{W}_{d,v} = \mathbf{F}_{N_c}^{-1} \mathbf{w}_{N_c} \bar{\mathbf{W}}_{f,t_s} \mathbf{w}_{N_{\text{sym}}} \mathbf{F}_{N_{\text{sym}}}$. Consequently, taking into account that the sum of two uncorrelated random variables with variances σ_1^2 and σ_2^2 is a

random variable with a variance $(\sigma_1^2 + \sigma_2^2)$, from (3.22) the SNR in the radar image $\mathbf{z}_{d,v}$ denoted by $\text{SNR}_{\text{Im}}^{(i)}$ for the i -th target peak can be expressed as

$$\begin{aligned} \text{SNR}_{\text{Im}}^{(i)} &= \frac{\left(\left| \frac{\bar{a}_i}{\sqrt{N_c N_{\text{sym}}}} \sum_{n=0}^{N_c-1} \sum_{\mu=0}^{N_{\text{sym}}-1} w_{N_c}(n) w_{N_{\text{sym}}}(\mu) \right| \right)^2}{\left(\frac{1}{\sqrt{N_c N_{\text{sym}}}} \right)^2 \sum_{n=0}^{N_c-1} \sum_{\mu=0}^{N_{\text{sym}}-1} \left(\frac{\sigma w_{N_c}(n) w_{N_{\text{sym}}}(\mu)}{|s(n, \mu)|} \right)^2} \\ &= \frac{|\bar{a}_i|^2 \left(\sum_{n=0}^{N_c-1} \sum_{\mu=0}^{N_{\text{sym}}-1} w_{N_c}(n) w_{N_{\text{sym}}}(\mu) \right)^2}{\sigma^2 \sum_{n=0}^{N_c-1} \sum_{\mu=0}^{N_{\text{sym}}-1} w_{N_c}^2(n) w_{N_{\text{sym}}}^2(\mu) |s(n, \mu)|^{-2}}. \end{aligned} \quad (3.23)$$

As (3.23) shows, the SNR in the radar image depends on both the amplitudes of the modulation symbols \mathbf{s} and the used window functions \mathbf{w}_{N_c} and $\mathbf{w}_{N_{\text{sym}}}$. Moreover, it shows that the radar signal and noise are integrated differently through the FFT and IFFT in (3.20) and (3.22). Whereas the integration of noise yields the sum of variances, i.e. powers of noise samples, the integration of signal results in the squared sum of signal amplitudes, i.e. in coherent integration. Defining the input SNR for the i -th target as

$$\text{SNR}_{\text{In}}^{(i)} = \frac{|a_i|^2}{\sigma^2}, \quad (3.24)$$

and setting $|s(n, \mu)| = 1 \forall n, \mu$, the processing (integration) gain of the two-dimensional Fourier processing is

$$G_{\text{P,2D}} = \frac{\left(\sum_{n=0}^{N_c-1} \sum_{\mu=0}^{N_{\text{sym}}-1} w_{N_c}(n) w_{N_{\text{sym}}}(\mu) \right)^2}{\sum_{n=0}^{N_c-1} \sum_{\mu=0}^{N_{\text{sym}}-1} w_{N_c}^2(n) w_{N_{\text{sym}}}^2(\mu)}. \quad (3.25)$$

Thus, for rectangular windows, i.e. $\mathbf{w}_{N_c} = \mathbf{I}_{N_c}$ and $\mathbf{w}_{N_{\text{sym}}} = \mathbf{I}_{N_{\text{sym}}}$, the maximum processing gain of FFT processing is achieved:

$$G_{\text{P,2D,max}} = \frac{N_c^2 N_{\text{sym}}^2}{N_c N_{\text{sym}}} = N_c N_{\text{sym}}. \quad (3.26)$$

From another perspective, assuming a rectangular window, from (3.23) it can be seen that to maximize SNR_{Im} , the modulation symbols have to be chosen such that $\sum_{n=0}^{N_c-1} \sum_{\mu=0}^{N_{\text{sym}}-1} |s(n, \mu)|^{-2}$ is minimal. For an average unit power of OFDM subcarriers $(1/N_c) \sum_{n=0}^{N_c-1} |s(n, m)|^2 = 1 \forall m \in [0, N_{\text{sym}})$, this condition is satisfied for $|s(n, \mu)| = 1 \forall n, \mu$. Thus, for modulation symbols with constant amplitudes and rectangular window, the SNR improvement through the entire processing is $G_{\text{P,2D,max}}$. Since $G_{\text{P,2D,max}}$ is equal to the number of processed samples $N_c N_{\text{sym}}$, this processing is optimal with regard to the SNR, i.e. it can be seen as an optimal filter. For different window functions and non-unit amplitudes of \mathbf{s} , however, the described signal processing does not achieve the full processing gain. Nevertheless, for typical configurations (e.g. $N_c = 1024$ and $N_{\text{sym}} = 512$) the processing gain of OFDM radar is $G_{\text{P,2D}} > 50$ dB, which enables a significant SNR improvement.

Also regarding the sidelobe level the described processing achieves sound results. The spectral division based processing cancels out the OFDM signal form, and thus corresponds to a correlation based processing for a signal with an ideal periodic autocorrelation function. Moreover, for the subsequent Fourier processing window functions can be applied for suppression of sidelobes due to the finite time duration and bandwidth of the measurement signal. Hence, the sidelobes of the target peaks in the radar image can be effectively suppressed not to limit the dynamic range of the distance-velocity estimation. Typically the window function is chosen such that the sidelobes are suppressed below the noise floor.

Limits of the classical OFDM radar signal processing

Despite the favorable properties of the described signal processing, the signal model behind it is a simplification of the general signal model in (3.12) due to assumptions $\mathbf{D}_{N_c}(\bar{f}_{D_i}/N_c) = \mathbf{I}_{N_c}$, $\mathbf{B}_i = \mathbf{1}$, $\mathbf{P}_i = \mathbf{1}$ with $\mathbf{1}$ being a matrix of ones of the same size as the matrices at the left hand side. In the following, we discuss each of the assumptions that enable this simplification.

According to (A1), the Doppler shift of OFDM subcarriers is neglected based on the assumption $f_{D,\max} \ll \Delta f$. To satisfy this condition, the subcarrier spacing Δf has to be chosen large enough. A design rule for limiting ICI due to the Doppler shift to a tolerable level was proposed in [Sturm, 2011, 2012a], which suggests a subcarrier spacing $\Delta f = 10f_{D,\max}$. Such a parametrization with increased subcarrier spacing reduces, however, the unambiguously measurable distance range of the radar as in (2.16). At the same time, the larger Δf results in a shorter OFDM symbol duration T . In turn, the shorter T results in an increased unambiguous velocity range as in (2.19), assuming $\alpha = T_{\text{SRI}}/T$ is unchanged. However, the targets with a normalized Doppler shift $\bar{f}_D > 0.1$ would lead to a significant ICI level, and therefore the unambiguous velocity range corresponding to $\bar{f}_D > 0.1$ cannot be utilized. This can be seen from the perspective that for a given unambiguously measurable velocity range with a tolerable ICI level, the unambiguous distance range is limited significantly by the discussed design rule. This limitation is more critical for higher carrier frequencies due to the dependency of the Doppler shift on the carrier frequency. Hence, due to this assumption the classical signal processing makes limited use of the unambiguous distance and velocity range available to OFDM radar.

The narrowband assumption (A2) implies that all OFDM subcarriers in the used frequency band are shifted by the same Doppler shift, i.e. no Doppler scaling occurs. Taking into account that in automotive application the radar bandwidth is typically much smaller than the carrier frequency, this assumption is commonly satisfied. For example, for a radar with a bandwidth of $B = 1$ GHz at the carrier frequency of $f_c = 77$ GHz, the maximum Doppler scaling relative to the Doppler shift is $B/f_c \approx 0.013$. If the maximum acceptable subcarrier shift is 0.1 [Sturm, 2011, 2012a], the scaling up to 0.013 is insignificant. Hence, it can be concluded that this assumption is satisfied for automotive radar, and thus will be neglected for algorithms and concepts presented in this thesis.

The third assumption (A3) concerns the range migration due to the target movement during the measurement. Range migration takes place when the target range change during the measurement exceeds the range resolution of the radar, and thus might occur for radars with large bandwidth and long measurement time. Since the bandwidth and measurement time determine the range and velocity resolution of the radar, respectively, this assumption implies a limited simultaneously achievable range and velocity resolution. The violation of this assumption leads to a spread of

the signal energy over multiple adjacent range cells, and thus to smeared peaks in the distance-velocity image. Consequently, for the classical signal processing the simultaneously achievable range and velocity resolution is limited for moving targets.

Novel signal processing methods that overcome the limitations of the classical signal processing resulting from (A1) and (A3) are introduced in Section 3.3 and Section 3.4, respectively.

3.3. All-Cell Doppler Correction for ICI-Free OFDM Signal Processing²

Orthogonality of subcarriers is at the very core of OFDM. This is achieved by placement of subcarriers in a way that at each subcarrier position all other subcarriers have their zeros. In the time domain, this can be interpreted as a use of subcarriers with a whole number of periods during the OFDM symbol duration. This guarantees zero cross-correlation between subcarriers. Due to this principle, an essential drawback of OFDM, both in communication and radar, is its sensitivity to the Doppler effect. The Doppler shift of an OFDM symbol results in a shift of the entire OFDM spectrum such that the initial subcarrier positions correspond neither to the subcarrier peaks nor to the zeros of other subcarriers. This results not only in reduced subcarrier amplitude at its initial position but also in interference from other subcarriers, i.e. ICI. Whereas due to the subcarrier shape the amplitude reduction is not essential for moderate Doppler shifts, ICI might result in a significant performance degradation. The Doppler tolerance of OFDM radar is studied in [Franken, 2006]. To avoid a considerable loss of orthogonality between OFDM subcarriers, the classical OFDM radar signal processing in Section 3.2 requires a subcarrier spacing much larger than the Doppler shift. This limits, however, the parametrization freedom of OFDM radar significantly by imposing a lower limit on the subcarrier spacing.

A Doppler correction method for OFDM radar has been proposed in [Tigrek, 2012], which is based on a detection of the approximate number of subcarriers corresponding to the Doppler shift and a cyclic shift of the columns of the measurement matrix for its compensation. This method, however, does not solve the issue of ICI, since ICI occurs in case of non-integer shift of subcarriers. Moreover, the correction algorithm in [Tigrek, 2012] is only valid for a single target, which strongly limits its practicability.

To avoid these shortcomings, a novel signal processing method that overcomes the Doppler sensitivity of OFDM is presented in this section. We introduce a scenario independent Doppler correction method that enables an ICI-free processing for both OFDM radar and communication. At the core of the proposed method is the principle of correction of Doppler shifts for all cells in a scenario independent manner. We refer to this principle as all-cell correction, and correspondingly name the proposed method all-cell Doppler correction (ACDC). The Doppler robustness of ACDC based processing opens up new perspectives for system parametrization, enabling radar concepts not feasible before. This perspectives are discussed in Section 3.3.3. The effectiveness of ACDC for ICI-free OFDM processing is studied in simulations in Section 3.3.4. The results are validated with real measurements in a road scenario presented in Chapter 6.

² The contributions of this section were partially reported in [Hakobyan, 2017a]. Some of author's own formulations from [Hakobyan, 2017a] are adopted in the text.

3.3.1. Requirements for ACDC

ACDC is applicable for OFDM, if the following requirements are met:

- (R1) A set of OFDM symbols must be available for Doppler processing. Since ACDC is based on Doppler processing in slow-time, multiple consecutive OFDM symbols with the same carrier frequency are required.
- (R2) OFDM symbols used during one measurement cycle must have an inherent linear dependency, i.e. columns of \mathbf{s} in (3.12) must be linearly dependent. This means that \mathbf{s} has to be a rank-one matrix.
- (R3) The range migration must be either negligible or corrected before the application of ACDC.

For OFDM radar capable of distance-velocity estimation, typically (R1) is implicitly given. In contrast, (R2) represents a constraint on the modulation symbol matrix \mathbf{s} . It imposes, however, no limitation on the OFDM symbol itself. Hence, the OFDM symbol can be optimized for radar, e.g. with respect to PAPR, or used to carry communication information. Whereas this constraint has no significant relevance for radar, for communication it limits the data rate considerably. The simplest case that satisfies (R2) is RS-OFDM, i.e. repeated transmission of the same symbol during the entire measurement cycle. Contrary to (R1) and (R2), (R3) is a soft requirement, i.e. in case it is not met, ACDC is still applicable, but its performance degrades with the amount of range migration.

3.3.2. ACDC based Distance-Velocity Estimation

The proposed method is based on the signal model in (3.12) and comprises the operations of the classical processing as well as an additional Doppler correction step.

With (R2), \mathbf{s} can be represented as an outer product of two vectors $\underline{s} \in \mathbb{C}^{N_c}$ and $\underline{s}_s \in \mathbb{C}^{N_{\text{sym}}}$, i.e. $\mathbf{s} = \underline{s} \cdot \underline{s}_s^T$, where \underline{s} and \underline{s}_s denote the complex modulation symbols of OFDM subcarriers and complex amplitudes of OFDM symbols, respectively. Note that out of SNR considerations \underline{s}_s would typically be chosen with unit amplitudes. The simplest case that satisfies (R2) is RS-OFDM, i.e. $\underline{s}_s = \mathbf{1}_{N_{\text{sym}}}$. Ignoring both the range migration \mathbf{P}_i (R3) and the Doppler scaling \mathbf{B}_i (negligible for automotive radar) for all targets, (3.12) can be simplified to

$$\mathbf{y}_{\text{tr}, \text{ts}} = \sum_{i=0}^{N_{\text{path}}-1} \bar{a}_i \mathbf{D}_{N_c} \left(\frac{\bar{f}_{D_i}}{N_c} \right) \mathbf{F}_{N_c}^{-1} \mathbf{D}_{N_c}^* (\bar{\tau}_i) (\underline{s} \cdot \underline{s}_s^T) \mathbf{D}_{N_{\text{sym}}} (\bar{f}_{D_i} \alpha) \quad (3.27)$$

The rank-one structure of \mathbf{s} opens up new possibilities for the signal processing. With this constraint, signal processing steps for distance-velocity estimation can be performed in a different order than for the classical OFDM radar signal processing in Section 3.2. To enable a Doppler shift compensation prior to the distance processing, the Doppler processing is carried out first.

Doppler processing

Before the velocity profiles can be generated, the complex amplitudes of OFDM symbols \underline{s}_s^T have to be corrected:

$$\begin{aligned} \mathbf{y}'_{\text{tr}, \text{ts}} &= \mathbf{y}_{\text{tr}, \text{ts}} \cdot \text{diag}(\underline{s}_s^* / |\underline{s}_s|^2) = \sum_{i=0}^{N_{\text{path}}-1} \bar{a}_i \mathbf{D}_{N_c} \left(\frac{\bar{f}_{D_i}}{N_c} \right) \mathbf{F}_{N_c}^{-1} \mathbf{D}_{N_c}^* (\bar{\tau}_i) (\underline{s} \cdot \underline{1}_{N_{\text{sym}}}^T) \\ &\cdot \mathbf{D}_{N_{\text{sym}}}(\bar{f}_{D_i} \alpha) = \sum_{i=0}^{N_{\text{path}}-1} \bar{a}_i \left(\mathbf{D}_{N_c} \left(\frac{\bar{f}_{D_i}}{N_c} \right) \mathbf{F}_{N_c}^{-1} \mathbf{D}_{N_c}^* (\bar{\tau}_i) \underline{s} \right) \cdot \underline{D}_{N_{\text{sym}}}^T(\bar{f}_{D_i} \alpha), \end{aligned} \quad (3.28)$$

where the $\text{diag}(\cdot)$ operation creates a diagonal matrix with the vector at its argument. Note that this operation is possible due to the diagonal structure of $\mathbf{D}_{N_{\text{sym}}}(\bar{f}_{D_i} \alpha)$. In case of RS-OFDM this step is unnecessary, i.e. $\mathbf{y}'_{\text{tr}, \text{ts}} = \mathbf{y}_{\text{tr}, \text{ts}}$.

As (3.28) shows, $\mathbf{y}'_{\text{tr}, \text{ts}}$ is the outer product of the delayed, attenuated and Doppler shifted transmitted OFDM symbol with a Doppler induced exponential over the slow-time. Thus, FFT over the slow-time will lead to the Doppler spectrum:

$$\mathbf{y}_{\text{tr}, \text{v}} = \mathbf{y}'_{\text{tr}, \text{ts}} \mathbf{w}_{N_{\text{sym}}} \mathbf{F}_{N_{\text{sym}}} = \sum_{i=0}^{N_{\text{path}}-1} \bar{a}_i \left(\mathbf{D}_{N_c} \left(\frac{\bar{f}_{D_i}}{N_c} \right) \mathbf{F}_{N_c}^{-1} \mathbf{D}_{N_c}^* (\bar{\tau}_i) \underline{s} \right) \cdot \underline{u}_{N_{\text{sym}}}^T(\bar{f}_{D_i} \alpha). \quad (3.29)$$

In (3.29), targets are separated in velocity and compressed into the corresponding velocity cells due to $\underline{u}_{N_{\text{sym}}}(\bar{f}_{D_i} \alpha)$.

All-cell Doppler correction

Based on the separation of reflections in velocity through the Doppler processing, the Doppler shift of OFDM subcarriers $\mathbf{D}_{N_c}(\bar{f}_{D_i}/N_c)$ can be corrected prior to the distance processing based on $\mathbf{D}_{N_c}(\bar{\tau}_i)$. Since at this stage of processing pulse compression is performed only in slow-time, the SNR of the reflections is considerably lower than that in the radar image. Hence, any detection based approach will be suboptimal, and for an optimal result detection independent processing is required. Thus, we propose the Doppler correction to be carried out for all velocity cells, since at this point each target is compressed into the corresponding velocity cell. Below we show that through this processing Doppler shifts for all targets are corrected in a scene independent manner and with a high accuracy.

First, the proposed Doppler correction method will be explained for the simplified case of a single target ($N_{\text{path}} = 1, i = 0$) with rectangular window ($\mathbf{w}_{N_{\text{sym}}} = \mathbf{I}_{N_{\text{sym}}}$) and an on-grid velocity, i.e. $\bar{f}_{D_0} \alpha = f_{D_0} \alpha / \Delta f = l_0 / N_{\text{sym}}$ with $l_0 \in \mathbb{Z}$ being the velocity cell index of the target. In this case, the Doppler processing leads to a single velocity peak at $l = l_0$ and zeros at all other velocity cells:

$$\begin{aligned} u_{N_{\text{sym}}}(\bar{f}_{D_0} \alpha) &= \underline{D}_{N_{\text{sym}}}^T(\bar{f}_{D_0} \alpha) \mathbf{w}_{N_{\text{sym}}} \mathbf{F}_{N_{\text{sym}}} = \underline{D}_{N_{\text{sym}}}^T(l_0 / N_{\text{sym}}) \mathbf{F}_{N_{\text{sym}}} = \sqrt{N_{\text{sym}}} \delta_{N_{\text{sym}}}(l_0) \\ &= \sqrt{N_{\text{sym}}} \cdot [\delta(0 - l_0), \delta(1 - l_0), \dots, \delta(N_{\text{sym}} - 1 - l_0)]^T \end{aligned} \quad (3.30)$$

where its l -th element is

$$\frac{1}{\sqrt{N_{\text{sym}}}} \sum_{\mu=0}^{N_{\text{sym}}-1} e^{-j2\pi \frac{l-l_0}{N_{\text{sym}}} \mu} = \sqrt{N_{\text{sym}}} \delta(l - l_0), \quad 0 \leq l < N_{\text{sym}}, \quad l_0 \in \mathbb{Z}, \quad (3.31)$$

with $\delta(l - l_0)$ being the *Kronecker delta function* defined as

$$\delta(l - l_0) = \begin{cases} 1, & l = l_0 \\ 0, & l \neq l_0 \end{cases}. \quad (3.32)$$

For the Doppler correction, $\mathbf{y}_{\text{tr},v}$ in (3.29) is multiplied with a correction matrix \mathbf{C} that compensates the Doppler shift for each velocity cell. Substituting (3.30) into (3.29),

$$\mathbf{y}'_{\text{tr},v} = \mathbf{C} \odot \mathbf{y}_{\text{tr},v} = \mathbf{C} \odot \left(\bar{a}_0 \sqrt{N_{\text{sym}}} \left(\mathbf{D}_{N_c} \left(\frac{l_0}{\alpha N_c N_{\text{sym}}} \right) \mathbf{F}_{N_c}^{-1} \mathbf{D}_{N_c}^* (\bar{\tau}_0) \underline{s} \right) \cdot \underline{\delta}_{N_{\text{sym}}}^T(l_0) \right). \quad (3.33)$$

The Doppler correction matrix \mathbf{C} is chosen as

$$\mathbf{C} = \left[e^{-j2\pi \bar{f}_D(l) \frac{m}{N_c}} \right]_{\substack{0 \leq m < N_c \\ 0 \leq l < N_{\text{sym}}}} \in \mathbb{C}^{N_c \times N_{\text{sym}}}, \quad (3.34)$$

and $\bar{f}_D(l)$ denotes the normalized Doppler correction of the l -th velocity cell. The matrix \mathbf{C} contains complex exponentials in each column, whose frequencies correspond to the Doppler shift of each velocity cell. The elementwise multiplication with \mathbf{C} shifts the signal frequencies in each column of $\mathbf{y}_{\text{tr},v}$ opposite to the Doppler shift, which results in a Doppler shift compensation for the entire measurement matrix.

Note that $\bar{f}_D(l)$ depends on the choice of the unambiguously measurable velocity range. For the range $(-v_u, 0]$ corresponding to $[0, f_{D,u})$, $\bar{f}_D(l) = l/(\alpha N_{\text{sym}})$, analogous to $\bar{f}_{D0} = l_0/(\alpha N_{\text{sym}})$ discussed above. Since only the l_0 -th column of $\mathbf{y}'_{\text{tr},v}$ has non-zero entries, the multiplication in (3.33) has effect only on this column. The l_0 -th column of $\mathbf{y}'_{\text{tr},v}$ can be written as

$$\begin{aligned} y'_{\text{tr},v}(m, l_0) &= e^{-j2\pi \frac{l_0 m}{\alpha N_{\text{sym}} N_c}} \left(\bar{a}_0 \frac{\sqrt{N_{\text{sym}}}}{\sqrt{N_c}} e^{j2\pi \frac{l_0 m}{\alpha N_{\text{sym}} N_c}} \sum_{n=0}^{N_c-1} e^{j2\pi \frac{mn}{N_c}} e^{-j2\pi \bar{\tau}_0 \frac{n}{N_c}} s(n) \right) \\ &= \bar{a}_0 \frac{\sqrt{N_{\text{sym}}}}{\sqrt{N_c}} \sum_{n=0}^{N_c-1} s(n) e^{-j2\pi \bar{\tau}_0 \frac{n}{N_c}} e^{j2\pi \frac{mn}{N_c}}, \quad 0 \leq m < N_c. \end{aligned} \quad (3.35)$$

Clearly, the Doppler correction fully compensates the Doppler shift and the signal left in l_0 -th velocity cell is a delayed and attenuated version of the transmitted OFDM signal. Thus, the succeeding distance processing will be ICI-free. Note that the Doppler correction is carried out in a scene independent manner, i.e. no information about the number of targets, their velocities, distances, etc. is needed. This evidently means that ACDC is analogously applicable for multiple targets with arbitrary on-grid velocities.

Whereas in the discussed simplified case with rectangular window and on-grid target velocities the Doppler shift is corrected completely without residue, in the general case with arbitrary target velocities this operation will correct the Doppler shift of all targets, with a precision comparable to the Doppler shift resolution $\Delta f_D = 2\Delta v f_c / c_0$. The reason behind this is that in case of both off-grid targets and/or windowing, the mainlobe of the target peak will occupy multiple adjacent velocity cells. A residue occurs since the signal in the entire mainlobe has the same Doppler shift, but is corrected with different Doppler values $\bar{f}_D(l)$ at each velocity cell. Thus, assuming

a compression of the signal energy into its mainlobe through the Doppler processing, after the correction all targets will have a Doppler shift up to

$$|\Delta f_{D, \max}| \approx \Delta f_D b_{w,0.5} \ll \Delta f, \quad (3.36)$$

where $b_{w,0.5}$ is the half mainlobe width of the applied window function in FFT bins. As we show in Section 3.3.4, this residue is negligible for any practical parametrization. Consequently, in the general case ACDC is

$$\mathbf{y}'_{f,v} = \mathbf{C} \odot \mathbf{y}_{f,v} \approx \sum_{i=0}^{N_{\text{path}}-1} \bar{a}_i \left(\mathbf{F}_{N_c}^{-1} \mathbf{D}_{N_c}^* (\bar{\tau}_i) \underline{s} \right) \cdot \underline{u}_{N_{\text{sym}}}^T (\bar{f}_{D_i} \alpha). \quad (3.37)$$

Distance processing

After the Doppler shift correction in (3.37), distance estimation is carried out similar to the classical signal processing. First, $\mathbf{y}'_{f,v}$ is transformed to the frequency domain via FFT over the fast-time:

$$\mathbf{y}_{f,v} = \mathbf{F}_{N_c} \mathbf{y}'_{f,v} = \sum_{i=0}^{N_{\text{path}}-1} \bar{a}_i \left(\mathbf{D}_{N_c}^* (\bar{\tau}_i) \underline{s} \right) \cdot \underline{u}_{N_{\text{sym}}}^T (\bar{f}_{D_i} \alpha). \quad (3.38)$$

Next, spectral division is performed to eliminate the complex modulation symbols from the subcarrier values:

$$\begin{aligned} \mathbf{z}_{f,v} &= \mathbf{y}_{f,v} \cdot / (\underline{s} \cdot \underline{1}_{N_{\text{sym}}}^T) = \sum_{i=0}^{N_{\text{path}}-1} \bar{a}_i \left(\mathbf{D}_{N_c}^* (\bar{\tau}_i) \underline{1}_{N_c} \right) \cdot \underline{u}_{N_{\text{sym}}}^T (\bar{f}_{D_i} \alpha) \\ &= \sum_{i=0}^{N_{\text{path}}-1} \bar{a}_i \underline{D}_{N_c}^* (\bar{\tau}_i) \cdot \underline{u}_{N_{\text{sym}}}^T (\bar{f}_{D_i} \alpha). \end{aligned} \quad (3.39)$$

Finally, FFT over subcarriers yields the distance-velocity radar image:

$$\mathbf{z}_{d,v} = \mathbf{F}_{N_c}^{-1} \mathbf{w}_{N_c} \mathbf{z}_{f,v} = \sum_{i=0}^{N_{\text{path}}-1} \bar{a}_i \underline{u}_{N_c}^* (\bar{\tau}_i) \cdot \underline{u}_{N_{\text{sym}}}^T (\bar{f}_{D_i} \alpha) \quad (3.40)$$

In contrast to the classical OFDM radar signal processing in Section 3.2, the results of ACDC based processing in (3.40) are Doppler independent, and no ICI occurs for any target velocity. Hence, the radar image $\mathbf{z}_{d,v}$ has no ICI induced limitation of the dynamic range. The described signal processing chain is depicted in Fig. 3.4. As opposed to Fig. 3.3, the signal processing flow is changed such that the Doppler processing is performed first, followed by the ACDC correction and the subsequent distance processing. The additional Doppler correction step comprises an elementwise multiplication with a predefined correction matrix, and thus its computational overhead is negligible.

Influence of ACDC on noise

Since the Doppler shift is corrected with an all-cell approach, i.e. with a preventive correction everywhere regardless of necessity, not only the velocity cells with targets, but also those with noise only, are influenced. Thus, the noise properties of ACDC based processing have to be

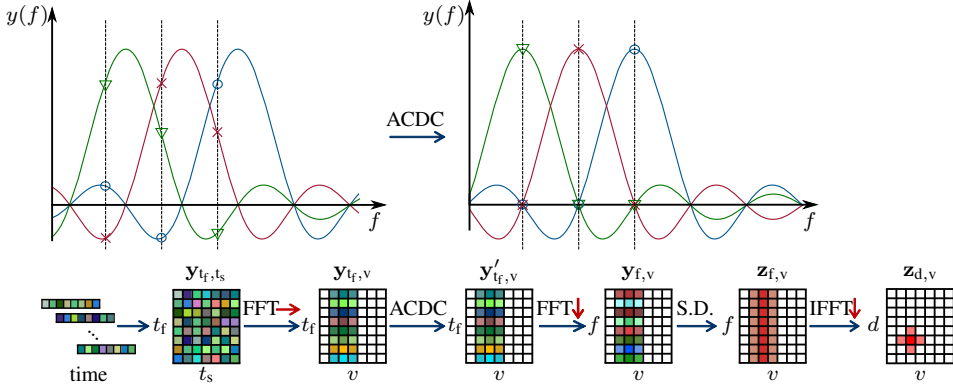


Figure 3.4.: ACDC based signal processing for distance-velocity estimation. $y(f)$ denotes the received frequency domain signal amplitude. The upper illustration shows the spectrum of the Doppler shifted received signal before and after ACDC processing. The lower part of the figure depicts the signal processing chain for ACDC assuming $\underline{s}_s = \frac{1}{N_{\text{sym}}}$

investigated. In case \underline{s}_s has unit amplitudes and no windowing is applied, the described Doppler processing is optimal regarding the SNR (processing gain of N_{sym}), as discussed in Section 3.2.3. The ACDC changes only the noise phases, but not amplitudes. The further processing for distance estimation is optimal in case \underline{s} has unit amplitudes and no windowing (processing gain of N_c). The subsequent detection is based on the amplitudes of the radar image. Thus the phase of the noise is irrelevant. That is, ACDC has no influence on the SNR of the radar image, and its noise behavior is the same as for the classical processing in Section 3.2.

3.3.3. ACDC based OFDM Radar and Communication System

In this section, the effects of ACDC both on radar and communication are discussed and the perspectives it opens for both applications are addressed. For the discussion below RS-OFDM is assumed, since in combination with ACDC it provides additional advantages and simplifies the signal processing.

ACDC based OFDM radar

ACDC enables a scene independent ICI-free distance-velocity estimation for targets within the unambiguously measurable velocity range of OFDM radar. Hence, with ACDC the OFDM radar performance regarding both accuracy and dynamic range is independent from the Doppler shift. Therefore, the constraint on the minimum subcarrier spacing imposed by the Doppler shift [Sturm, 2011] does not apply. In fact, the only requirement for ICI-free processing is now the unambiguous measurement of all target velocities.

For a given OFDM symbol duration T , the unambiguous velocity range $v_u = c_0/(2f_c T_{\text{SRI}})$ is maximized in case of RS-OFDM due to $T_{\text{SRI}} = T$. Since with ACDC the whole unambiguous velocity range can be processed ICI-free, the minimum possible subcarrier spacing resulting from v_u is $\Delta f_{\text{min}} = 1/T$. This is the original subcarrier spacing of OFDM. Thus, ACDC based RS-OFDM radar achieves the maximum unambiguous range both in distance and velocity. This is a valuable feature for applications with highly dynamic targets, long range of interest, high

carrier frequencies, and MIMO architecture. All these criteria apply, for example, for a long range automotive radar.

The increase in unambiguous distance range through ACDC processing compared to the state-of-the-art approach from [Sturm, 2011] is 5-10 times, depending on the choice of the unambiguous velocity range. In case of a symmetric choice $[-v_u/2, v_u/2]$, ICI-free processing is possible for Doppler shifts in the range $[-\Delta f/2, \Delta f/2]$, whereas the state-of-the-art approach recommends the Doppler shift to be restricted to $[-0.1\Delta f, 0.1\Delta f]$. Accordingly, in case of only negative velocity range $(-v_u, 0]$, ACDC enables an ICI-free operation for Doppler shifts $[0, \Delta f]$ instead of the range $[0, 0.1\Delta f]$ for the state-of-the-art approach (see Fig. 3.5). The maximized unambiguous distance range resulting from tighter subcarrier spacing can be used for increasing the radar measurement range. More importantly, it can be used for multiplexing of multiple Tx antennas for MIMO processing. In fact, for some applications certain multiplexing methods for MIMO radar are only feasible with ACDC, as we show in Section 4.2.

ACDC based OFDM Communication

Although primarily designed for radar, ACDC is applicable also for communication. The application of ACDC to communication is especially relevant for OFDM radar and communication systems [Sturm, 2011; Garmatyuk, 2011], since the ACDC based radar operation has implications also for the communication application. Even though the rank-one constraint on the matrix of modulation symbols \mathbf{s} considerably limits the data rate, ACDC still has several attractive features for communication, which are briefly discussed below.

With RS-OFDM, ACDC can be applied to communication analogous to radar. In contrast to radar, the OFDM symbol in communication is unknown at the receiver. Nevertheless, the subsequent transmission of the same symbol enables a Doppler processing at the communication receiver as in (3.29). This means, the communication side gains a new function of a Doppler radar — a feature especially advantageous for automotive systems. Additionally, the multipath reflections from moving objects are separated in velocity, i.e. a separation of spatial channels takes place that is advantageous for communication (e.g. less fading, simpler equalization, etc.). Then, ACDC from (3.37) can be applied, followed by an ICI-free processing of the communication signal. This would enable a Doppler independent performance for communication, since in dynamic scenarios no ICI would occur. Furthermore, by extracting the line-of-sight (LOS) path, the relative distances of the reflecting objects can be estimated. This can be done via matched filtering — similar to distance estimation of passive radar [Berger, 2010a; Gassier, 2016]. With additional information about the distance between the transmit and receive sides (i.e. LOS path), a full radar functionality would be achievable at the communication receiver in addition to the ICI-free communication. The additional passive radar functionality of the communication receiver is an advantageous feature for OFDM radar and communication systems [Tigrek, 2008, 2012; Sturm, 2009, 2011, 2012a], e.g. in automotive application. It would represent a additional means of passive environment sensing for applications that rely on radar.

The effect of ACDC and RS-OFDM on the communication data rate is twofold. On the one hand, restricting the OFDM signal to a single symbol for the whole measurement cycle reduces the data rate by N_{sym} . The higher N_{sym} , the better the radar velocity estimation, and the lower the communication data rate. On the other hand, the Doppler processing increases the SNR of the OFDM symbol by N_{sym} , and thus, larger alphabets can be used for coding of the communication data. Moreover, the separation of the spatial channels through the Doppler FFT is favorable for

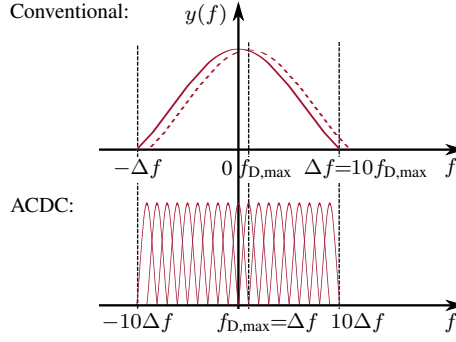


Figure 3.5.: Subcarrier spacing with ACDC vs. the conventional spacing: subcarriers can be placed narrower due to the Doppler correction

communication performance. Furthermore, the ICI-free processing prevents the Doppler induced degradation of the bit error rate (BER). Thus, in highly dynamic scenarios where the Doppler shift leads to a severe performance degradation, the proposed approach might be advantageous even for communication. A deep study of ACDC based OFDM communication, however, is beyond the scope of this thesis.

3.3.4. Simulative Analysis

For performance analysis of ACDC based OFDM radar, the ICI level as a function of the Doppler shift is investigated in simulations. Therefore, the impact of ICI on the distance profiles and the dynamic range in the radar image are analyzed. A bandwidth of $B = 200$ MHz with $N_c = 2048$ OFDM subcarriers is simulated. The number of OFDM symbols is $N_{\text{sym}} = 256$ and the subcarrier spacing is $\Delta f = B/N_c = 97.7$ kHz. This results in an unambiguously measurable distance range of $d_u \approx 1536$ m and velocity range of $v_u \approx 190$ m/s (e.g. $[-95 \text{ m/s}, 95 \text{ m/s}]$). To suppress sidelobes in distance and velocity estimation, a Chebyshev window with 100 dB sidelobe suppression is applied in both dimensions. RS-OFDM with unit subcarrier amplitudes and random phases is used for ACDC. The conventional Fourier processing without ACDC is taken as a reference — both for RS-OFDM and CP-OFDM with randomly changing OFDM symbols. First, simulations are performed in a noiseless setup to observe the effect of ICI solely, followed by analysis in presence of noise. The performance of ACDC in the presence of noise can also be observed from the measurement results in Section 6.3.

First, the distance profiles (a slice of the distance-velocity image for a particular velocity cell) for a target with a normalized Doppler shift $\bar{f}_D = 0.1$ at a distance $d = 25$ m are analyzed. Note that $\bar{f}_D = 0.1$ is the maximum Doppler limit recommended by the design in [Sturm, 2011]. With this configuration \bar{f}_D corresponds to a target velocity of $v = 19$ m/s. For the logarithmic representation the amplitudes of the signal are normalized with the integration gain of the applied window function. The resulting distance profiles for the proposed processing and for the state-of-the-art approach are shown in Fig. 3.6a.

Clearly, the Doppler shift resulting from the movement of the target leads to ICI between the OFDM subcarriers, which, in turn, limits the dynamic range of the radar image. Due to the random modulation symbols, ICI between subcarriers results in a noise-like floor in the corresponding distance profile. For CP-OFDM, the dynamic range is around 57 dB in this configuration. This is due to the fact that the changing OFDM symbols result in changing ICI over the slow-time. Thus,

the Doppler FFT suppresses the ICI by the coherent processing gain, resulting in a comparably high dynamic range. For RS-OFDM, however, the ICI is constant over the slow-time and the Doppler processing integrates it into the corresponding velocity cell. This results in a reduction of the dynamic range down to ≈ 37 dB, which indicates that with the conventional Fourier processing the Doppler induced ICI becomes critical for RS-OFDM. ACDC processing, in contrast, compensates for the Doppler shift, resulting in a high dynamic range (≈ 75 dB in this case). The results show that the residue of the Doppler processing is negligibly small, and for real-world applications will typically be considerably below the noise floor.

Analogously, Fig. 3.6b shows the distance profiles for a target with a normalized Doppler shift $\bar{f}_D = 0.5$. Note that in case of a symmetrical choice of the unambiguous velocity range, $\bar{f}_D = 0.5$ is its limit. In this setup, the dynamic range further degrades for both RS-OFDM and CP-OFDM down to ≈ 22 dB and ≈ 41 dB, respectively. In contrast, the dynamic range for ACDC is around 80 dB — even higher than for $\bar{f}_D = 0.1$. The reason for this somewhat unexpected behavior is the fact that in our case $\bar{f}_D = 0.5$ is very close to a point on the Doppler grid (a grid of Doppler shifts corresponding to the velocity cells), whereas $\bar{f}_D = 0.1$ is between two Doppler grid points. Since the proposed ACDC approach corrects the Doppler shifts in a cell based manner, the residue in the target velocity cell after the correction depends only on the distance between the true target velocity and the closest Doppler cell.

In Fig. 3.7, the dynamic range in distance-velocity estimation in dependence of the normalized Doppler shift is shown for all three approaches discussed above in a noiseless setup. Here the dynamic range is determined by the ratio of the peak to the highest ICI value and is obtained from Monte Carlo simulations with different OFDM symbols. Clearly, RS-OFDM shows a limited dynamic range already for small Doppler shifts, and at the recommended limit $\bar{f}_D = 0.1$ the dynamic range is reduced considerably. Due to the integration gain of the Doppler processing the dynamic range of CP-OFDM is significantly higher. Whereas a sufficiently high dynamic range of ≈ 57 dB is achieved at the limit $\bar{f}_D = 0.1$, the dynamic range degrades considerably at higher Doppler shifts. In contrast, ACDC provides a dynamic range of ≈ 70 dB for any Doppler shift up to $\bar{f}_D = 0.95$.

Note that the dynamic range in the entire distance-velocity image in Fig. 3.7 is almost constant, i.e. independent of whether the target is on a velocity grid or not. The reason is that the highest residue is left in the adjacent cells of the main peak, and not in the same cell. Those cells have a Doppler shift corresponding to the actual velocity of the target, but are corrected according to their cell index. Therefore after the correction a slight frequency shift remains, which leads to the shown residue in the radar image. Since this residue is negligibly small, it can be safely ignored.

Finally, we investigate the performance of ACDC in the presence of noise. Fig. 3.8 shows the dynamic range (the ratio of the highest target peak to the highest noise and sidelobe peak) of the radar image as a function of the SNR at the input of the radar processing for a target with $\bar{f}_D = 0.5$. Results are obtained from Monte-Carlo simulations. The dynamic range is shown only for SNR values that result in a reliable detection performance (detection in all Monte-Carlo runs). Evidently, for all SNR values ACDC achieves a higher dynamic range. This is due to the fact that with ACDC the entire signal energy is focused into the main peak, resulting in a higher peak amplitude as well as no increase of noise due to ICI induced sidelobes. Due to the same reason, ACDC obtains more reliable detection for lower SNR values than the conventional processing. With increasing SNR, the dynamic range for RS-OFDM approaches its limit at

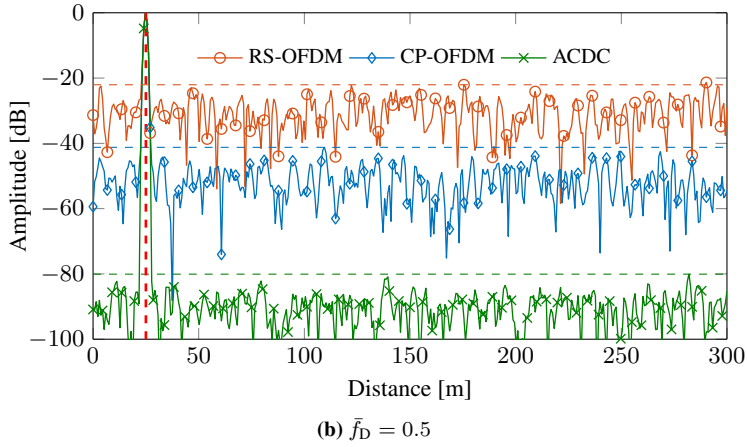
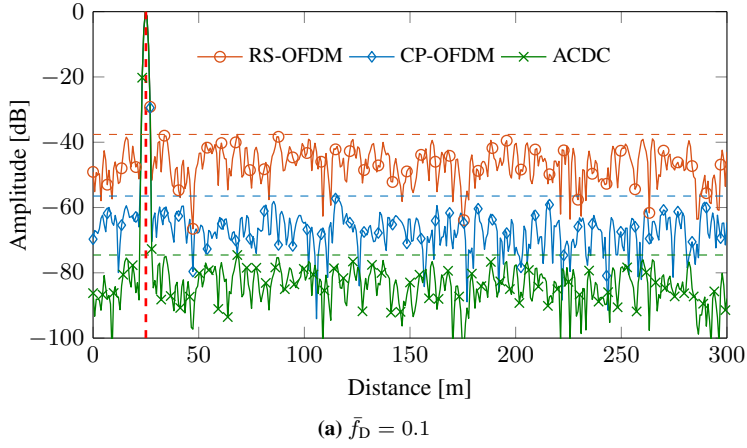


Figure 3.6.: Distance profiles for a moving target at a distance of 25 m, no noise

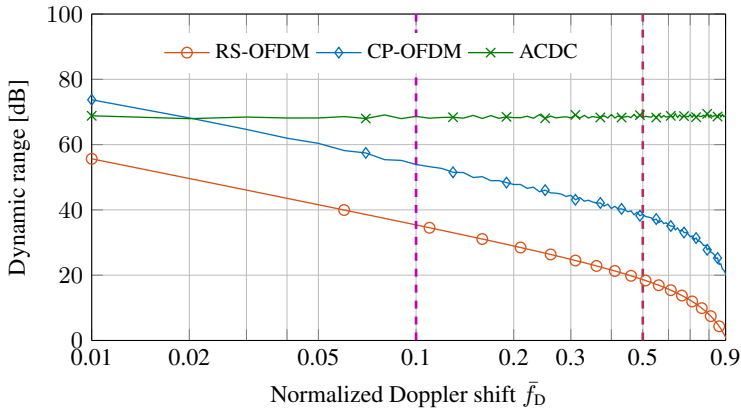


Figure 3.7.: Dynamic range as a function of the normalized Doppler shift for different OFDM radar approaches, no noise

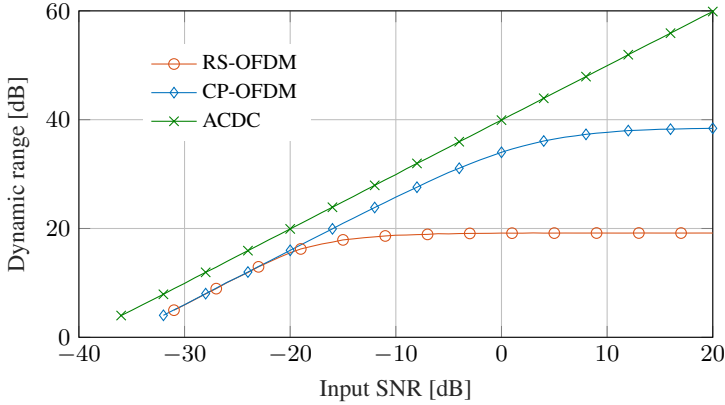


Figure 3.8.: Dynamic range as a function of the input SNR for a normalized Doppler shift $\bar{f}_D = 0.5$

around 19 dB, since for high SNR values the dynamic range is limited predominantly by the ICI induced sidelobes. The same happens for CP-OFDM, although at a higher value of around 38 dB. In contrast, the dynamic range of ACDC grows proportional to the input SNR for all SNR values, since ICI is prevented and the dynamic range is limited solely by noise. For SNR values higher than 20 dB, the dynamic range of ACDC tends asymptotically to its limit, i.e. to the value in a noiseless setup shown in Fig. 3.7.

3.3.5. Concluding Remarks

In this section, a method that overcomes the Doppler sensitivity of OFDM has been presented. To prevent the loss of orthogonality between OFDM subcarriers due to the Doppler shift, a scenario independent Doppler compensation method based on the all-cell correction principle is proposed. The proposed ACDC based processing enables ICI-free distance-velocity estimation for all targets within the unambiguously measurable velocity range of OFDM radar. Since the Doppler correction is performed in a detection independent manner, the correction accuracy is practically independent of the targets' SNR as well as of the scenario in general. Even though performed on all cells including those with noise only, ACDC has no negative influence on target SNR in the radar image, since it is a unitary operation. In fact, through the ACDC based processing the target SNR is even increased, since the target energy is focused in its main peak and not spread to other cells in form of ICI.

The proposed signal processing opens new perspectives both for OFDM radar and communication. For radar, ACDC enables a significant extension of the unambiguously measurable distance range. When used with RS-OFDM, it achieves the maximum unambiguous range both in distance and velocity via ICI-free processing. Simulations show that without ACDC the dynamic range achieved by RS-OFDM is severely limited, and thus the use of ACDC for RS-OFDM is especially advantageous. The increased unambiguous distance range can be shared between multiple Tx antennas via EqSI multiplexing to enable MIMO processing. For communication, ACDC enables a Doppler independent processing, but limits the data rate considerably. A trade-off between the communication data rate and processing accuracy can be achieved by the choice of number of OFDM symbols in one measurement cycle. Additionally, ACDC facilitates the communication receiver to operate as passive radar, which might be a valuable feature for automotive OFDM radar and communication systems.

Simulations show the high dynamic range of ACDC for the entire unambiguously detectable velocity range due to ICI-free processing. The presented results are validated with measurements in Section 6.3.

3.4. All-Cell Migration Compensation for Migration-Free Range-Doppler Processing

The conventional radar signal processing for distance-velocity (range-Doppler) estimation splits the time axis of the measurement signal into two dimensions: fast-time and slow-time. Based on this separation, an efficient two-dimensional parameter estimation via Fourier processing is possible for multiple targets. Such processing yields a two-dimensional spectrum, and with an assumption that these dimensions are independent, i.e. orthogonal, a simple axes scaling results in the range-Doppler radar image. Hence, the assumption that the fast-time and slow-time dimensions are orthogonal is at the very core of the conventional two-dimensional Fourier processing. Since due to the target movement its range changes over the slow-time, in the general case this assumption is not applicable for radar. The range change during the measurement can, however, be assumed negligible, when it is below the range resolution. This is the case for radar systems with sufficiently small bandwidth and short measurement time. Since these two parameters determine the range and Doppler resolution, this implies a certain limit on the simultaneously achievable resolution in range and Doppler.

The violation of this assumption leads to an effect commonly known as *range migration*, when the target migrates from one range cell to another during the coherent processing interval. In this case, the Doppler processing will not compress the signal into a single range-Doppler cell, and the signal energy will be spread over multiple neighboring cells, as illustrated in Fig. 3.9a. This will result in a smeared target peak in the radar image, i.e. lead to a reduced resolution as well as SNR. For range migration to occur, the target movement during the measurement cycle has to exceed one range cell. This happens for radars with large enough time-bandwidth product, since the high bandwidth results in narrow range cells, and the long measurement time leads for moving targets to large range change during the measurement.

For radar systems with a large time-bandwidth product, another effect, known as *Doppler frequency migration* and closely related to the range migration, becomes relevant. Since the Doppler effect is frequency dependent, each frequency in the radar signal undergoes a slightly different Doppler shift. Whereas for small bandwidths this effect is typically ignored based on the narrowband assumption, for a large bandwidth it becomes considerable. For radars with a long measurement time, and thus high Doppler (velocity) resolution, the Doppler frequency might migrate through multiple Doppler cells over the signal bandwidth, analogous to the range migration. Similarly, the range processing will compress the signal into multiple neighboring range-Doppler cells instead of a single cell, as Fig. 3.9b illustrates. As a consequence, the target peak in the radar image will be smeared, resulting in a reduced SNR and resolution.

Both these effects impose a certain limit on the simultaneously achievable range and Doppler resolution for the conventional Fourier processing. To extend the radar range and Doppler resolution beyond the limits of the Fourier processing, methods that account for the range and Doppler frequency migration are needed. To be applicable for the automotive radar, the following conditions have to be satisfied:

- (C1) Applicable for any number of targets. Since multiple targets are typically present in the range-Doppler image of automotive radar, the migration compensation method should be suitable for a high number of targets. Ideally, its performance as well as computational complexity should be independent of the number of targets.
- (C2) High dynamic range. The migration compensation must enable a high dynamic range in the radar image, i.e. have low sidelobes and be free of undesired artefacts.
- (C3) Operate accurately in conditions of low SNR. Ideally, the performance of the migration compensation method should be SNR independent.
- (C4) Computationally efficient. The mitigation compensation method should be feasible for real-time implementation for automotive radar.

In this section, we present a novel signal processing approach for range and Doppler frequency migration compensation that satisfies all the above criteria. The proposed processing is based on the all-cell correction principle already introduced in Section 3.3. Therefore, we name the proposed method all-cell migration compensation (ACMC). In contrast to ACDC that was an additional, separate correction step, ACMC represents a special time-frequency transform that implicitly compensates the range and Doppler frequency migration for all targets. Thus, it is used for the pulse compression over the slow-time instead of the FFT based Doppler processing. The subsequent processing steps are then migration-free. After ACMC, when necessary, a Doppler shift correction with ACDC can be carried out prior to the range processing. Then, the migration and ICI-free range processing can be performed efficiently with the conventional approach described in Section 3.3.2. Note that ACMC is not specific to OFDM radar and is applicable to any other radar with the same measurement principle as for OFDM radar (e.g. fast-chirp radar).

Whereas in the literature both effects of range and Doppler frequency migration are described and treated separately, in the following we point out that these effects have a common origin. In fact, both effects result from the target movement during the measurement and are its consequence in two different domains. Whereas the range migration occurs in the range-slow-time domain, the Doppler frequency migration takes place in the frequency-Doppler frequency domain (see Fig. 3.9). The proposed processing compensates both effects in one step.

Next, a state-of-the-art review of existing migration compensation methods is given, followed by the description of ACMC and a simulative analysis.

3.4.1. State-of-the-Art Methods for Range and Doppler Frequency Migration Compensation

Since range migration is an issue known for several decades, a vast number of publications addressing this topic are known. Particularly, in the area of SAR this topic has been studied extensively and many methods for range migration compensation are known. Considering only the coherent processing methods, the main methods for range migration compensation for moving targets can be classified into three families: *Radon*-based methods [Xu, 2011, 2012; Chen, 2014], *Keystone transform* (KT) [Perry, 1999, 2007; Li, 2006; Huang, 2016, 2017] and joint time-frequency analysis methods [Chen, 1998b, 1999; Jun, 2002].

The joint time-frequency analysis methods typically operate with *short-time Fourier transform* (STFT) and try to recollect the target energy across the time-frequency plane based on tracking of the target range walk. These methods integrate the signal energy from multiple STFTs

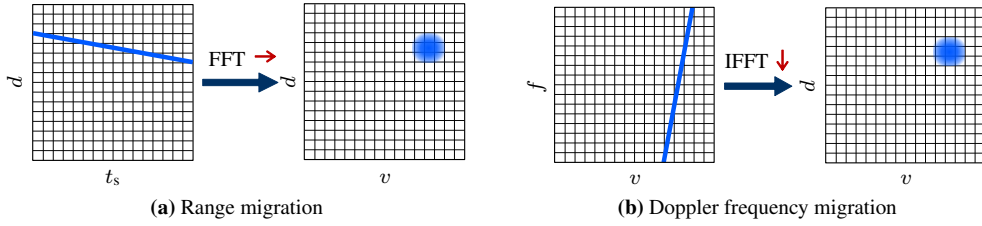


Figure 3.9.: Impact of the range and Doppler frequency migration on the radar image

non-coherently, and thus have a suboptimal performance regarding both SNR and frequency resolution.

Radon-based coherent processing methods, such as *Radon-Fourier transform* [Xu, 2011], *generalized Radon-Fourier transform* [Xu, 2012] and *Radon-fractional Fourier transform* [Chen, 2014] aim at coherently integrating target energy distributed along different range cells. These methods use the relationship between target motion and range and collect coherently the target energy along its movement, i.e. envelope [Xu, 2012]. Whereas the Radon-Fourier transform accounts for target's linear motion, the Radon-fractional Fourier transform extends the initial method to account for target acceleration, and the generalized Radon-Fourier transform formulates the target movement including higher order terms. Whereas theoretically these methods account for the target movement, and thus, overcome the range migration, their essential drawback is that in real application they have to operate on discrete data, i.e. no continuous values between the measurement samples theoretically needed for Radon-Fourier transform are available. The transform accuracy, i.e. the effectiveness of collecting the signal energy, is restricted due to the discrete input. This can be partially compensated e.g. by interpolation [Xu, 2011], which, however, leads to prohibitively high computational costs and additional loss of accuracy. Even without interpolation, the computational complexity of these methods is exhaustively high, especially for automotive applications.

The Keystone transform for range migration compensation was introduced in [Perry, 1999] for SAR. Since then, it has been widely studied in numerous publications and many extensions of this method exist (e.g. [Perry, 2007; Li, 2006; Huang, 2016, 2017]). The principle behind the Keystone formatting is the rearrangement of the measurement signal in frequency-slow-time dimension in form of a keystone (a wedge-shaped piece of stone at the apex of an arch), through which the range migration is implicitly compensated for all targets. Even though not explicitly addressed by authors, the reason the Keystone formatting works is the following: through an individual slow-time stretching/compression for each frequency, the Doppler frequency differences are compensated for each frequency (time stretching/compression reduces/increases the frequency), and thus the Doppler frequency migration is prevented. As we point out in the following, the Doppler frequency migration has the same cause as the range migration. Hence, by Keystone formatting the range migration is corrected. In [Perry, 2007; Li, 2006] the application of KT for pulse-Doppler radar as well as its use for resolving velocity ambiguities is discussed. In [Huang, 2016, 2017], it is extended to higher order motion parameters to enable a long-time coherent integration for SAR.

Since the Keystone formatting is scenario independent, it satisfies (C1) and (C3). However, for the stretching/compression of the slow-time axis interpolation has to be used, and the dynamic range in the radar image depends on the interpolation accuracy. Furthermore, even though KT

is computationally more efficient than most other range migration compensation methods, for most high-accuracy interpolation methods it will still have a high computational complexity. For the analysis in this work we consider an interpolation based on sinc-based kernels [Oppenheim, 2009], which has a computational complexity of $\mathcal{O}(N_{\text{sym}}O_{\text{KT}}^2)$ for each subcarrier, with O_{KT}^2 being the interpolation filter length.

A computationally efficient alternative to KT for SAR based on *chirp Z-transform* has been proposed in [Lanari, 1995]. This approach, however, is not meant for compensation of the target motion induced range migration, but for compensation of range migration due to the range-azimuth coupling and sensor's own velocity in SAR systems. Accordingly, sensor's velocity is assumed to be known, which makes this method inapplicable for target motion compensation — it represents a solution to a different problem. In essence, this method performs a scaling of the range axis to prevent the range migration due to the range-azimuth coupling. Prior to the scaling operation in range, it cancels out the waveform (equivalent of spectral division). As commonly the range migration is accompanied by a non-negligible Doppler shift of the waveform (subcarriers in case of OFDM) that needs to be compensated prior to spectral division (e.g. via ACDC), this sequence of operations is clearly disadvantageous. The performance of Doppler shift compensation via ACDC is affected by the migration effects, and the optimal sequence of operations must first compensate the migration, then the Doppler shift, and perform the spectral division as last — also for SAR processing. Thus, this approach is inapplicable for our purposes.

A method for a range migration compensation described specifically for OFDM radar was presented in [Tigrek, 2010a,b]. However, this method is valid only for one target, and thus inappropriate for our application.

Interestingly, whereas in many publications Doppler frequency migration is not addressed [Tigrek, 2010a; Perry, 1999, 2007; Li, 2006], in others it is referred to as a separate effect and its relationship to range migration is not explicitly discussed (e.g. [Huang, 2016] and the references therein).

Based on the overview given above, KT is the method known from the state-of-the-art which is most suitable for our application. Therefore, it will be considered as a reference method for ACMC. We show that in our application ACMC is superior to KT both in performance as well as computational efficiency.

3.4.2. Range and Doppler Frequency Migration

Intuitively, range migration is caused by the target movement over the slow-time, which is described by the term $\exp(-j2\pi f_n \gamma_i \mu T_{\text{SRI}})$ in (3.10) with $\gamma_i = 2v_i/c_0$. Due to this term, for each consecutive slow-time index the range induced complex exponential over the subcarriers becomes $\exp(-j2\pi f_n(\tau_i + \gamma_i \mu T_{\text{SRI}}))$, and thus, the range changes. Range migration occurs when the range change during the measurement $d_{\text{mig}} = vT_{\text{cycle}}$ exceeds one range cell (resolution) $\Delta d = c_0 / (2B)$, i.e. for a target with velocity

$$|v| \geq \frac{c_0}{2BT_{\text{cycle}}}. \quad (3.41)$$

Consequently, the range migration normalized to a range cell is:

$$\zeta_{\text{RM}} = \frac{d_{\text{mig}}}{\Delta d} = \frac{2vBT_{\text{cycle}}}{c_0}. \quad (3.42)$$

Clearly, the range migration is large for a large time-bandwidth product BT_{cycle} . Analogously, due to the same term $\exp(-j2\pi f_n \gamma_i \mu T_{\text{SRI}})$ the term used for the Doppler processing becomes frequency dependent, i.e. $\exp(j2\pi(f_{D_i} - f_n \gamma_i) \mu T_{\text{SRI}})$. This means, each frequency will yield a different Doppler estimate. The Doppler frequency difference between the first and last frequency within the bandwidth is:

$$f_{\Delta D} = \frac{2v}{c_0} B. \quad (3.43)$$

In order for Doppler frequency migration to occur, this Doppler frequency difference has to exceed one Doppler frequency cell (resolution) $\Delta f_D = 2\Delta v f_c / c_0 = 1/T_{\text{cycle}}$, which happens for target velocities

$$v \geq \frac{c_0}{2BT_{\text{cycle}}}. \quad (3.44)$$

Hence, the Doppler frequency migration can be expressed in unit of a Doppler cell as:

$$\zeta_{\text{DFM}} = \frac{f_{\Delta D}}{\Delta f_D} = \frac{2vBT_{\text{cycle}}}{c_0}. \quad (3.45)$$

From the above discussion it is apparent that not only do the range and Doppler frequency migration both have the same cause described by the term $\exp(-j2\pi f_n \gamma_i \mu T_{\text{SRI}})$, they also appear in the exact same scale in the range-Doppler radar image, i.e. $\zeta_{\text{RM}} = \zeta_{\text{DFM}}$. Thus, as we show in the following, the compensation of this term eliminates both effects.

3.4.3. All-Cell Migration Compensation based Range-Doppler processing

We present ACMC based on the signal model in (3.12), i.e. for OFDM radar. Also for ACMC, the requirements (R1) and (R2) in Section 3.3 have to be satisfied, i.e. multiple coherent OFDM symbols with a rank-one modulation symbol matrix are required. This allows Doppler processing together with migration compensation to be carried out first, i.e. before the spectral division and other processing steps. In addition, ACMC assumes no acceleration and higher order motion terms. This assumption is justified for automotive applications due to coherent processing times in ms range and limited manoeuvring potential of targets. Generally, due to the target acceleration a peak expansion in velocity and — to a smaller scale — in range, takes place. This effect is, however, often negligible for automotive radar parametrization. The signal model in (3.12) implies this assumption. Furthermore, ACMC requires all targets to be within the unambiguously measurable velocity range, i.e. no velocity ambiguities. Also this can be achieved with a suitable system parametrization for automotive radar. Finally, albeit irrelevant for ACMC, based on (A2) from Section 3.2 the Doppler scaling within one OFDM symbol, i.e. the term \mathbf{B}_i in (3.12), is ignored. This means, the narrowband assumption $B \ll f_c$ is still valid despite of a large time-bandwidth product BT_{cycle} .

With the above assumptions, the measurement signal in (3.12) can be written as

$$\mathbf{y}_{\text{tr}, \text{ts}} = \sum_{i=0}^{N_{\text{path}}-1} \bar{a}_i \mathbf{D}_{N_c} \left(\frac{\bar{f}_{D_i}}{N_c} \right) \mathbf{F}_{N_c}^{-1} \mathbf{D}_{N_c}^* (\bar{\tau}_i) ((\underline{s} \cdot \underline{s}_s^T) \odot \mathbf{P}_i) \mathbf{D}_{N_{\text{sym}}} (\bar{f}_{D_i} \alpha). \quad (3.46)$$

First, \underline{s}_s is eliminated analogous to (3.28):

$$\begin{aligned} \mathbf{y}'_{f,t_s} = & \mathbf{y}_{f,t_s} \cdot \text{diag}(\underline{s}_s^* ./ |\underline{s}_s|^2) = \sum_{i=0}^{N_{\text{path}}-1} \bar{a}_i \mathbf{D}_{N_c} \left(\frac{\bar{f}_{D_i}}{N_c} \right) \\ & \cdot \mathbf{F}_{N_c}^{-1} \mathbf{D}_{N_c}^* (\bar{\tau}_i) ((\underline{s} \cdot \underline{1}_{N_{\text{sym}}}^T) \odot \mathbf{P}_i) \mathbf{D}_{N_{\text{sym}}} (\bar{f}_{D_i} \alpha) \end{aligned} \quad (3.47)$$

This is possible because $\mathbf{D}_{N_{\text{sym}}}(\bar{f}_{D_i} \alpha)$ is a diagonal matrix and $\odot \mathbf{P}_i$ is an elementwise multiplication. Since the range migration term \mathbf{P}_i in (3.47)

$$\mathbf{P}_i = \left[e^{-j2\pi n \gamma_i \mu \alpha} \right]_{\substack{0 \leq n < N_c \\ 0 \leq \mu < N_{\text{sym}}}} \in \mathbb{C}^{N_c \times N_{\text{sym}}}, \quad (3.48)$$

is frequency dependent, for the ACMC processing the measurement signal \mathbf{y}_{f,t_s} is transformed to the frequency domain:

$$\begin{aligned} \mathbf{y}_{f,t_s} = & \mathbf{F}_{N_c} \mathbf{y}'_{f,t_s} = \sum_{i=0}^{N_{\text{path}}-1} \bar{a}_i \mathbf{F}_{N_c} \mathbf{D}_{N_c} \left(\frac{\bar{f}_{D_i}}{N_c} \right) \\ & \cdot \mathbf{F}_{N_c}^{-1} \mathbf{D}_{N_c}^* (\bar{\tau}_i) ((\underline{s} \cdot \underline{1}_{N_{\text{sym}}}^T) \odot \mathbf{P}_i) \mathbf{D}_{N_{\text{sym}}} (\bar{f}_{D_i} \alpha). \end{aligned} \quad (3.49)$$

From (3.49), two observations can be made. Due to the Doppler shift of OFDM subcarriers $\mathbf{D}_{N_c}(\bar{f}_{D_i} / N_c)$, the DFT matrix \mathbf{F}_{N_c} does not cancel out the IDFT matrix $\mathbf{F}_{N_c}^{-1}$. Thus, the resulting frequency domain signal does not contain the orthogonal subcarriers, but a mix of those induced by the Doppler shift. This, as we will see in the following, is irrelevant for ACMC. The second observation concerns the rank of the measurement matrix: due to the matrix \mathbf{P}_i , the measurement matrix \mathbf{y}_{f,t_s} is not a sum of rank-one matrices; for moving targets the components of \mathbf{y}_{f,t_s} have a full rank.

Next, ACMC is performed on \mathbf{y}_{f,t_s} . For the migration compensation, each row of \mathbf{y}_{f,t_s} undergoes a special time-frequency transform that accounts for the target movement. This transform comprises a multiplication of y_{f,t_s} with a DFT matrix $F_{N_{\text{sym}}}$ modified by a migration correction matrix $\mathbf{M}_{n'}$, where n' is the row index. For the n' -th row, ACDC can be written as

$$[\mathbf{y}_{f,v}]_{n',:} = ([\mathbf{y}_{f,t_s}]_{n',:} \cdot \mathbf{w}_{N_{\text{sym}}}) \cdot (\mathbf{M}_{n'} \odot \mathbf{F}_{N_{\text{sym}}}), \quad 0 \leq n' < N_{\text{sym}}, \quad (3.50)$$

where $[\mathbf{y}_{f,v}]_{n',:}$ is the n' -th row of the ACMC transformed measurement matrix $\mathbf{y}_{f,v}$, $[\mathbf{y}_{f,t_s}]_{n',:}$ is the n' -th row of \mathbf{y}_{f,t_s} , and

$$\mathbf{M}_{n'} = \left[e^{j2\pi n' \hat{\gamma}(l) \mu \alpha} \right]_{\substack{0 \leq l < N_{\text{sym}} \\ 0 \leq \mu < N_{\text{sym}}}} \in \mathbb{C}^{N_{\text{sym}} \times N_{\text{sym}}}, \quad (3.51)$$

where $\hat{\gamma}(l) = 2\hat{v}(l)/c_0$, and $\hat{v}(l)$ is the velocity value for the l -th velocity cell. For the unambiguous velocity range $[0, v_u)$, $\hat{v}(l) = l\Delta v$. In this case, the phase of the exponential in (3.51) can be simplified to:

$$\begin{aligned} j2\pi n' \hat{\gamma}(l) \mu \alpha &= j2\pi \mu n' \frac{2l\Delta v}{c_0} \alpha = j2\pi \mu n' \frac{l}{f_c T_{\text{cylce}}} \alpha \\ &= j2\pi \mu n' \frac{l}{f_c T N_{\text{sym}}} = j2\pi \frac{\mu l}{N_{\text{sym}}} \cdot \frac{f_{n'}}{f_c} \end{aligned} \quad (3.52)$$

Hence, ACMC modifies the Fourier kernel used for time-frequency transform such that the motion induced migration term is accounted for, i.e. instead of the discrete Fourier kernel

$\exp(-j2\pi\mu l/N_{\text{sym}})$ in $\mathbf{F}_{N_{\text{sym}}}$, a modified kernel $\exp(-j2\pi\mu l\eta(n')/N_{\text{sym}})$ with $\eta(n') = 1 - f_{n'}/f_c$ is used. Consequently, analogous to ACDC the migration compensation is done for the entire measurement regardless of necessity, i.e. in a scenario independent, preventive way.

Even though the discrete modeling of the radar signal is convenient for the representation of signal processing steps, at this point it approaches its limits, as it does not allow exact modelling of simultaneous frequency and time shifts. Specifically, in this case the signal model in (3.46) is exact only for infinite size of the Fourier transform matrix \mathbf{F}_{N_c} , i.e. for a continuous-time and time-unlimited signal. In the opposite case, this model is an approximation of effects such as simultaneous time and frequency shifts. Therefore, the proof of ACMC is given in Appendix A based on a frequency domain signal model that does not have this limitation.

After all rows of \mathbf{y}_{f,t_s} are transformed with ACMC, the measurement signal can be written as

$$\mathbf{y}_{f,v} = \text{ACMC}(\mathbf{y}_{f,t_s}) \approx \sum_{i=0}^{N_{\text{path}}-1} \bar{a}_i \left(\mathbf{F}_{N_c} \mathbf{D}_{N_c} \left(\frac{\bar{f}_{D_i}}{N_c} \right) \mathbf{F}_{N_c}^{-1} \mathbf{D}_{N_c}^* (\bar{\tau}_i) \underline{s} \right) \cdot \underline{u}_{N_{\text{sym}}}^T (\bar{f}_{D_i} \alpha). \quad (3.53)$$

ACMC compensates the range and Doppler frequency migration term \mathbf{P}_i , which enables a full coherent integration during both Doppler and range processing. Analogous to ACDC and according to (A.10), assuming the complete signal energy is concentrated in its mainlobe, the migration residue left after ACMC is:

$$\Delta\zeta_{\text{RM}} = \Delta\zeta_{\text{DFM}} = \frac{b_{w,0.5}B}{f_c}. \quad (3.54)$$

Since for narrowband radar $B \ll f_c$, this residue is negligible for any practical system parametrization. After migration compensation in (3.53), a migration-free ACDC and distance processing can be performed as described in (3.37) to (3.40). A graphical illustration of the ACMC based processing is given in Fig. 3.10.

Note that ACMC has the same noise properties as the conventional Fourier processing, since it only modifies the kernel used for time-frequency transform. As opposed to $F_{N_{\text{sym}}}$, the modified transform matrix is no longer unitary, and thus not an orthogonal basis. So is, however, also the FFT performed with zero-padding, and thus this factor can be considered irrelevant for the result. Accordingly, the noise properties of ACMC are the same as for the classical Fourier based processing.

3.4.4. ACMC Implementation based on Chirp Z-Transform

In terms of computational efficiency, the proposed ACMC based processing is significantly superior to KT, since no potentially computationally expensive interpolation (see Section 3.4.5) is required. Moreover, since after the ACMC based Doppler processing a migration-free distance estimation can be performed efficiently with FFT and IFFT operations, the computational efficiency of the distance estimation is identical to that of the classical signal processing. For the Doppler processing, we apply ACMC instead of FFT, which in case of a straightforward implementation has a computational complexity of $\mathcal{O}(N^2)$ instead of $\mathcal{O}(N \log N)$ of the FFT processing. However, an efficient implementation of ACMC based on the chirp Z-transform [Rabiner, 1969] is possible, which reduces the computational complexity down to $\mathcal{O}(N \log N)$.

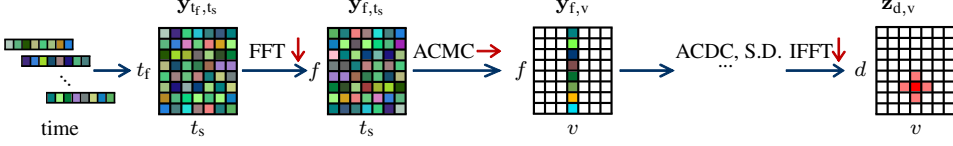


Figure 3.10.: ACMC based signal processing for migration-free range-Doppler estimation assuming $\underline{s}_s = \frac{1}{N_{\text{sym}}}$

Based on the Bluestein's substitution [Bluestein, 1970]

$$\mu l = \frac{\mu^2 + l^2 - (l - \mu)^2}{2}, \quad (3.55)$$

the kernel $\exp(-j2\pi\mu l \eta(n')/N_{\text{sym}})$ used for ACMC can be represented as

$$e^{-j\frac{2\pi\eta(n')}{N_{\text{sym}}}\mu l} = e^{-j\frac{\pi\eta(n')}{N_{\text{sym}}}\mu^2} e^{-j\frac{\pi\eta(n')}{N_{\text{sym}}}l^2} e^{j\frac{\pi\eta(n')}{N_{\text{sym}}}(l-\mu)^2}. \quad (3.56)$$

Considering a rectangular window $\mathbf{w}_{N_{\text{sym}}}$, for the n' -th row of \mathbf{y}_{f,t_s} , ACMC is

$$\begin{aligned} y_{f,v}(n', l) &= \sum_{\mu=0}^{N_{\text{sym}}-1} y_{f,t_s}(n', \mu) e^{-j\frac{2\pi\eta(n')}{N_{\text{sym}}}\mu l} = e^{-j\frac{\pi\eta(n')}{N_{\text{sym}}}l^2} \sum_{\mu=0}^{N_{\text{sym}}-1} \left(y_{f,t_s}(n', \mu) \cdot e^{-j\frac{\pi\eta(n')}{N_{\text{sym}}}\mu^2} \right) \\ &\quad \cdot e^{j\frac{\pi\eta(n')}{N_{\text{sym}}}(l-\mu)^2}, \quad 0 \leq n' < N_c, \quad 0 \leq l < N_{\text{sym}}. \end{aligned} \quad (3.57)$$

Denoting

$$\begin{aligned} g_{n'}(\mu) &= y_{f,t_s}(n', \mu) e^{-j\frac{\pi\eta(n')}{N_{\text{sym}}}\mu^2}, \\ h_{n'}(\mu) &= e^{j\frac{\pi\eta(n')}{N_{\text{sym}}}\mu^2}, \end{aligned} \quad (3.58)$$

the sum in (3.57) can be expressed as a convolution of two sequences $g_{n'}(\mu)$ and $h_{n'}(\mu)$:

$$y_{f,v}(n', l) = h_{n'}^*(l) \sum_{\mu=0}^{N_{\text{sym}}-1} g_{n'}(\mu) h_{n'}(l - \mu), \quad 0 \leq n' < N_c, \quad 0 \leq l < N_{\text{sym}}. \quad (3.59)$$

Hence, ACMC can be implemented efficiently with two complex elementwise multiplications and one convolution. The convolution, in turn, can be efficiently implemented with a pair of FFTs according to the convolution theorem. Thus, albeit factors slower than FFT, with an implementation based on the chirp Z-transform ACMC has the same order of computational complexity as the FFT processing. Since the subsequent processing is performed with FFT and IFFT operations, the computational efficiency of the proposed method is comparable to that of the classical 2D-FFT based processing. Consequently, the computational efficiency of ACMC is significantly higher than that of the state-of-the-art range migration compensation methods including KT.

3.4.5. Simulative Analysis

In the following, the performance of the proposed ACMC based range-Doppler processing is studied in simulations and compared to that of the state-of-the-art methods. For simulations a

bandwidth of $B = 500$ MHz with $N_c = 4096$ subcarriers is considered. With $N_{\text{sym}} = 2048$ a measurement time of $T_{\text{cycle}} = 16.8$ ms is achieved. Note that the time-bandwidth product resulting from these parameters is common for automotive applications. The carrier frequency, defined as the middle of the used frequency band, is $f_c = 77.25$ GHz. Analogously, the target range at the middle of the measurement cycle is chosen as a reference range for the radar images. RS-OFDM is used, i.e. the same OFDM symbol is repeated without breaks throughout the measurement. No window function is applied in order avoid a target peak expansion induced by windowing. To isolate the effects of range migration compensation from that of noise, the simulations are performed in a noiseless setup. As discussed, the noise behavior of ACMC is the same as for conventional Fourier evaluation, which can be observed from measurements presented in Section 6.3. Since for this configuration and high target velocities the Doppler shift is significant, ACDC is applied for Doppler shift compensation for all presented processing methods.

The results of ACMC are compared to two state-of-the-art processing methods: classical OFDM radar signal processing with 2D-FFT, i.e. no migration compensation but with ACDC, and KT based 2D-FFT processing, which we consider the most relevant state-of-the-art migration compensation method. KT is applied on the frequency-slow-time data, i.e. before ACDC, spectral division and 2D-FFT processing. The Keystone formatting is carried out through one-dimensional interpolation of the measurement data in slow-time for each subcarrier. For interpolation sinc-based kernels [Oppenheim, 2009] are used. This is a suitable interpolation method for bandlimited signals. For this method, the order of interpolation, i.e. the length of the interpolation filter, has to be higher than the number of targets in the scene. Thus, the interpolation filter used is of the order $O_{\text{KT}} = 13$. Note, the longer the interpolation filter, the more samples at the beginning and end of the slow-time measurement data are interpolated inaccurately, since for these samples the impulse response of the interpolation filter is longer than the available measurement data. This also reduces slightly the velocity resolution, which becomes considerable for longer interpolation filters [Richards, 2014a]. The computational complexity of the used interpolation is $\mathcal{O}(N_{\text{sym}} O_{\text{KT}}^2)$ for each subcarrier, i.e. it grows quadratically with the interpolation filter length and becomes exhaustive for large O_{KT} .

With this configuration a range and Doppler frequency migration of more than one cell occurs for targets with a velocity $v > 17.9$ m/s ≈ 64 km/h. This makes apparent the practical relevance of migration compensation for automotive application. Nevertheless, for the first simulation a single target with an unrealistically high target velocity of $v = -214.15$ m/s corresponding to $\bar{f}_D \approx -0.9$ is simulated at the range $d = 23.2$ m in order to show distinctly the differences between the discussed processing methods. Note that the target range is irrelevant for the simulations shown below, and thus is chosen arbitrarily, with no claim on practical relevance. The target movement leads to a range and Doppler frequency migration of around 12 cells.

Fig. 3.11 shows the resulting radar images for all three processing methods. The target range and Doppler frequency migration can be observed from the range-slow-time and frequency-velocity images in Fig. 3.11a and Fig. 3.11b, respectively. As a result of range and Doppler frequency migration, the peak in the radar image in Fig. 3.11c is smeared, which significantly reduces its resolution as well as SNR. In contrast, KT is able to compensate both the range and Doppler frequency migration, as Fig. 3.11d and Fig. 3.11e show. Even though the range migration is compensated entirely, the Keystone transformed range-slow-time image exhibits x-formed sidelobes that result from the interpolation. As a result, in the radar image the signal energy is collected into a single peak, but artefacts resulting from interpolation can be seen at approximately

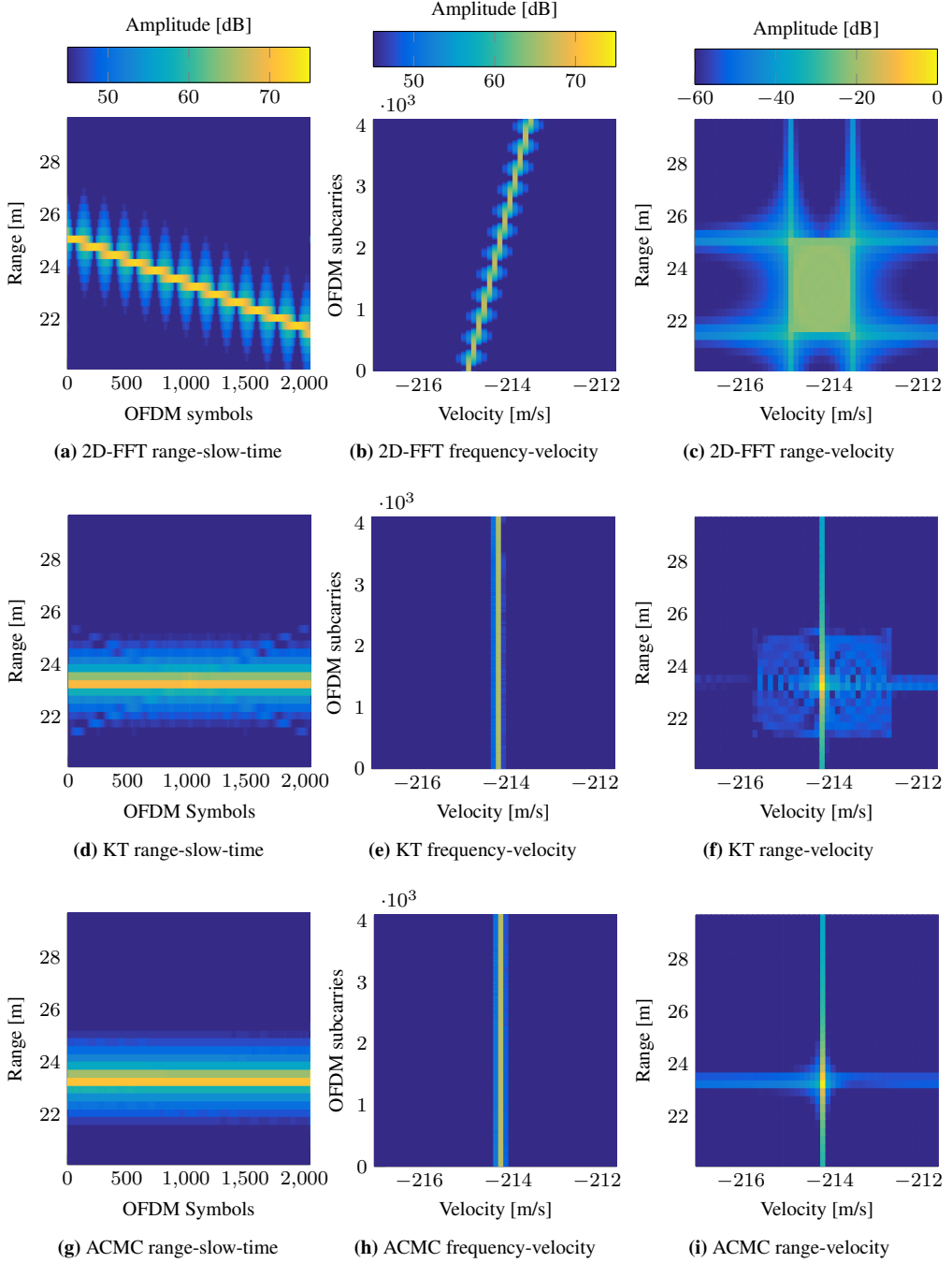


Figure 3.11.: Comparison of ACMC with the state-of-the-art methods in a one-target scenario (the colorbar of (a) applies also to (d) and (g), the same applies to (b), (e), (h) and (c), (f), (i))

45 dB below the main peak (Fig. 3.11f). Thus, the side effects of the range migration correction via KT lead to a limitation of the dynamic range. In contrast, ACMC corrects the range and Doppler frequency migration (Fig. 3.11g and Fig. 3.11h) without any drawbacks for the radar image (Fig. 3.11i). Hence, the full integration of the signal energy into a single peak is achieved, which enables longer integration times, and thus higher SNR and dynamic range. Moreover, ACMC maintains the theoretically achievable resolution in both range and Doppler processing. Note that the vertical and horizontal strips in the radar images in Fig. 3.11 are the sidelobes due to the rectangular window, i.e. the spectral leakage. Through windowing these sidelobes can be effectively suppressed.

To show the performance of the discussed algorithms in a multi-target scenario, three targets with high but realistic velocities are simulated. Two of them are placed close to each other both in range and velocity at ranges 25.1 m and 25.6 m and velocities -58.95 m/s and -58.75 m/s, respectively. A further target with a range 30.2 m and velocity of -57.95 m/s is present in the scene. All three targets have the same amplitude. Note that the theoretical radar range and velocity resolution resulting from the bandwidth and measurement time is $\Delta d = 0.3$ m and $\Delta v = 0.11$ m/s, respectively. Thus, if not for the effect of migration, all three targets are supposed to be clearly resolved in the radar image. For these targets, however, a migration of around 4 cells takes place.

Due to the target migration, the classical 2D-FFT processing is hardly capable of resolving the closely located targets (Fig 3.12b). From Fig. 3.12b, another issue becomes evident. Not only is the SNR reduced and peaks are harder to resolve, but even in case the peaks are resolved and detected properly, the subsequent DOA estimation is affected due to spread of the targets' energy. More specifically, for each target peak in the radar image, the DOA estimation will deliver multiple targets, since considerable amount of energy from the other target is present in the same cell. Since these additional targets do not physically exist, such behavior is to be avoided. In contrast, KT based processing compensates for the migration and resolves clearly all targets. However, some residue resulting from interpolation based Keystone formatting can be seen in the radar image in Fig. 3.12d, which affects the dynamic range. Analogous to KT, ACMC collects the entire target energy into a single peak, and all targets can be clearly resolved. Additionally, since ACMC is based on a modified kernel and not on interpolation, no residue in the radar image occurs, and thus the full dynamic range is maintained.

3.4.6. Concluding Remarks

The issue of range and Doppler frequency migration caused by the target movement was addressed in this section. After pointing out the common cause of both effects, formulas were derived for quantification of the migration amount. The limitations of the conventional OFDM radar signal processing due to migration effects were discussed. Based on a review of the extensive literature on migration compensation, the Keystone transform was identified to be the state-of-the-art migration compensation method most suitable for the automotive application. To overcome its drawbacks both in terms of accuracy and computational complexity, a novel migration compensation method based on all-cell correction was introduced. Instead of the Fourier based processing, ACMC performs the Doppler processing with a modified kernel that accounts for the target movement, and thus compensates the range and Doppler frequency migration. In contrast to KT, ACMC does not require a computationally expensive interpolation that affects the dynamic range.

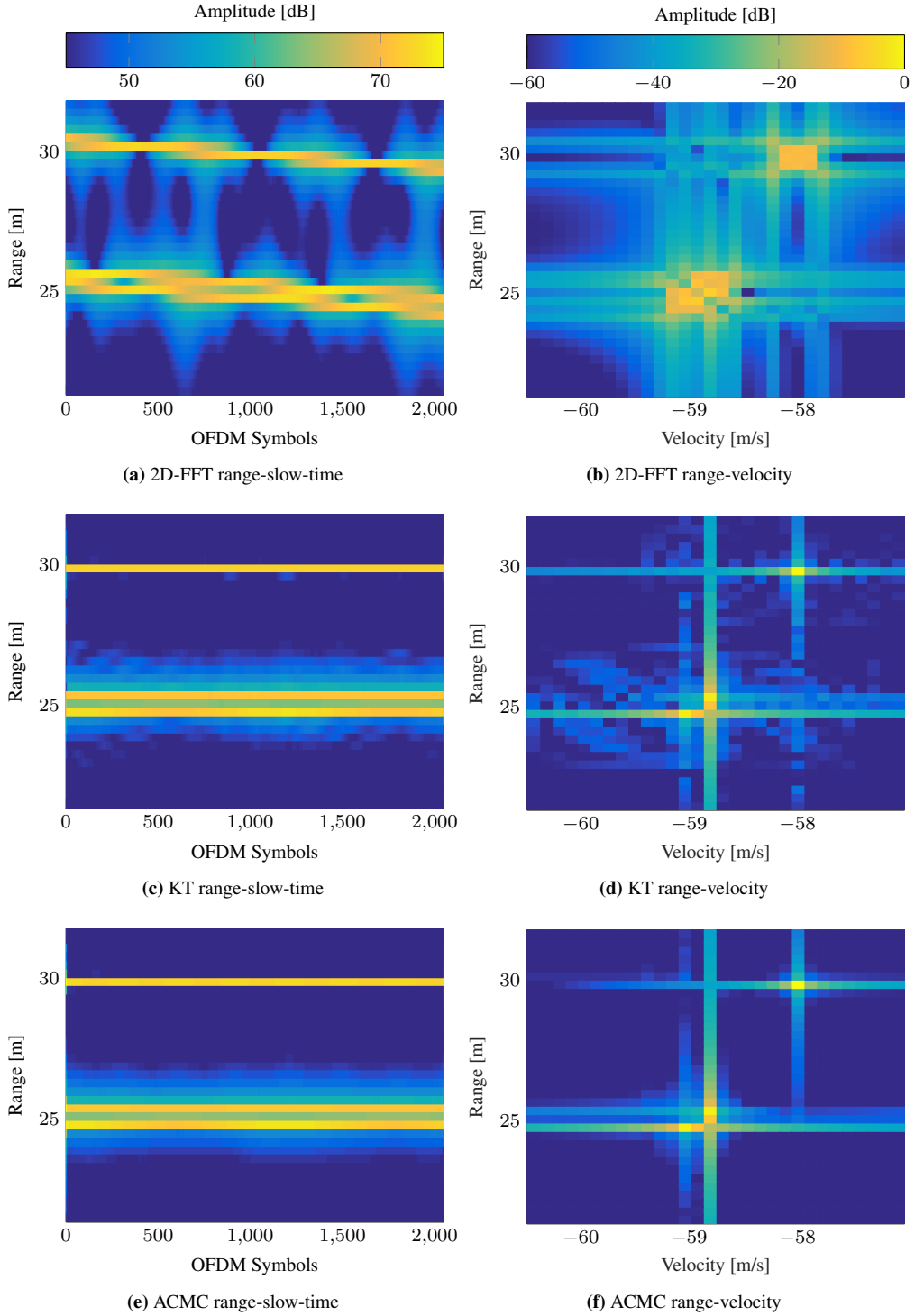


Figure 3.12.: Comparison of ACMC with the state-of-the-art methods in a three-target scenario (colorbar of (a) applies to (c) and (e), and that of (b) to (d) and (f))

Simulations have shown the effectiveness of ACMC in compensating entirely the range and Doppler frequency migration, and thus achieving the theoretical resolution limit both in range and velocity. Moreover, since ACMC enables longer coherent processing times, more data can be integrated coherently, and thus higher SNR can be achieved. This, in turn, enables a higher dynamic range due to lower noise floor, higher accuracy, increased maximum range, etc. Furthermore, an efficient implementation of ACMC based on chirp Z-transform matches the $\mathcal{O}(N \log N)$ computational complexity of the classical FFT based processing. This makes ACMC feasible for real-time implementation in automotive applications that require high distance-velocity resolution. Since ACMC is a transform designed for Doppler processing, it is scenario independent, and thus applicable to multi-target scenarios, needs no a priori information, and its performance is independent of SNR as well as the number of targets. Moreover, as the simulations show, it achieves the full dynamic range in the radar image. Thus, the criteria (C1)-(C4) required for automotive application are all satisfied for ACMC.

Based on the above discussion it can be concluded that ACMC extends the OFDM radar performance both in terms of resolution and SNR far beyond that of the conventional FFT processing, while maintaining the computational complexity of the latter. Thus, it has the potential to replace the conventional Doppler processing for automotive application — not only for OFDM radar, but also for other modulations.

3.5. Combination of ACDC and ACMC and Comparison to the Classical Signal Processing

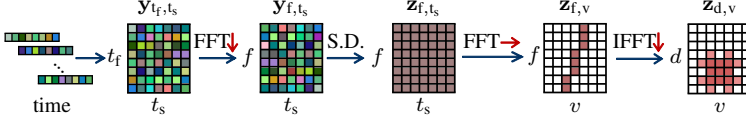
In this section, we summarize the guidelines for application of ACDC and ACMC, present a signal processing chain for joint application of both methods, and discuss their computational efficiency.

As discussed, the classical OFDM radar signal processing in Section 3.2 is based on assumptions that allow a simplification of the signal model. Specifically, the Doppler shift of subcarriers is ignored based on the assumption that it is negligible compared to the subcarrier spacing. Furthermore, assuming a sufficiently small time-bandwidth product, the movement of targets during the measurement and the resulting range and Doppler frequency migration are neglected.

Taking into account that the proposed ACDC and ACMC algorithms incorporate more sophisticated signal models, they are required when the discussed assumptions behind the classical signal processing do not hold. There is, however, no hard limit determining whether the application of the proposed methods is necessary. Instead, a key consideration is how much performance degradation due to ignored terms in the signal model is still tolerable for a particular application and parametrization. For the Doppler induced ICI, Fig. 3.7 provides an orientation whether the application of ACDC is needed on example of one particular configuration. Specifically, ACDC based processing is necessary if for the given subcarrier spacing (determined by the required unambiguous distance range) the required dynamic range is not achievable based on the classical signal processing. A particular parametrization example that demonstrates the limits of the classical signal processing and the need for ACDC to achieve the required radar parameters is provided in Section 4.2.

Analogously, also for the range and Doppler frequency migration there is no hard limit that determines whether the application of ACMC is required. Also here, the amount of migration

2D-FFT processing:



ACDC and ACMC based processing:

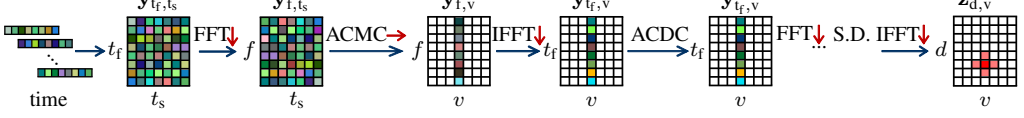


Figure 3.13.: Comparison of the combined ACDC and ACMC based processing with the classical OFDM radar signal processing, assuming $\underline{s}_s = \underline{1}_{N_{\text{sym}}}$ for the former

tolerable for the particular application at hand is the key criterion. As the migration depends on the time-bandwidth product of the radar system, for high time-bandwidth product the ACMC is required to prevent a significant performance degradation due to migration induced smearing of the target peaks. As a rule of thumb, we suggest for automotive applications the following limit: the classical signal processing is applicable up to the limit of time-bandwidth product $BT_{\text{meas}} \leq 2c_0/|v_{\text{max}}|$, with $|v_{\text{max}}|$ being the expected target velocity with the largest absolute value. This simply means that more than one cell migration occurs first for targets with $|v| \geq 0.25|v_{\text{max}}|$. The application of ACMC is recommended if for a given v_{max} the radar time-bandwidth product exceeds the proposed limit.

According to the proposed guidelines, application of both ACDC and ACMC might be necessary for some parametrizations. Since ACDC assumes no migration and is performed after the Doppler processing, its application after the ACMC based Doppler processing is meaningful. This is feasible due to the fact that the Doppler shift of OFDM subcarriers does not affect the ACMC performance. Hence, an advantageous sequence for combined application of both algorithms is: start from ACMC based Doppler processing, followed by ACDC on migration-free measurement data and the subsequent distance processing. Thus, ACDC and ACMC algorithms complement each other, enabling high performance for OFDM radar with demanding system parametrization. Whereas ACDC maximizes the unambiguously measurable range in distance and velocity, ACMC enables high simultaneously achievable distance and velocity resolution as well as long coherence times. The signal processing chain in case of combined ACDC and ACMC processing is depicted in Fig. 3.13 and compared to the classical OFDM radar processing.

As for the computational efficiency, the classical OFDM radar signal processing is based mainly on FFT and IFFT operations that have a computational complexity of $\mathcal{O}(N \log N)$. The proposed ACDC processing comprises an elementwise multiplication with a predefined Doppler correction matrix, and thus its computational overhead is negligible. Since the ACMC applies a more complex transform for the Doppler processing than the FFT, it is computationally more complex. However, in case of an efficient implementation based on chirp Z-transform, its order of computational complexity is the same as for FFT, i.e. $\mathcal{O}(N \log N)$. The distance processing in case of ACMC is unchanged, and thus its computational efficiency is identical to that of the classical processing. In case of combined application of ACDC and ACMC, however, an additional FFT and IFFT is required for the ICI-free distance processing (see Fig. 3.13). Consequently, albeit computationally more complex than the classical FFT based processing, the combined ACDC and ACMC processing is still feasible for real-time implementation for automotive OFDM radar.

Chapter 4.

OFDM-MIMO Radar

DOA estimation for radar can be efficiently improved by the use of MIMO technology. For MIMO radar, multiplexing of Tx antennas is required to guarantee that signals of different Tx paths do not interfere. Due to its multicarrier structure, OFDM offers new multiplexing possibilities for MIMO radar not available for conventional radar systems with analog modulation. Specifically, each individual subcarrier can be assigned to a Tx antenna, which provides a high degree of freedom for generation of orthogonal transmit waveforms via subcarrier interleaving. This chapter focuses on multiplexing concepts for combination of OFDM radar with MIMO and introduces novel multiplexing approaches based on subcarrier interleaving. Furthermore, a signal processing method for MIMO radar that complements the proposed multiplexing schemes is presented.

We start from a discussion of conventional multiplexing methods, such as time, frequency and code division multiplexing. Then, the multiplexing of Tx antennas via equidistant subcarrier interleaving (EqSI) is discussed, which is the state-of-the-art multiplexing method for OFDM-MIMO radar. We point out that EqSI multiplexing approaches its limits for many automotive radar configurations due to the reduction of the unambiguously measurable distance range. As we will see, the application of ACDC partially compensates this drawback through maximizing the unambiguous distance range. This enables EqSI multiplexing in configurations not feasible with the classical signal processing. To overcome the drawbacks of EqSI, we introduce two new multiplexing methods based on non-equidistant interleaving of OFDM subcarriers. This approach enables a full distance and velocity resolution as well as unambiguous range for each individual MIMO channel. To obtain non-equidistant interleaving patterns with high *peak-to-sidelobe ratio* (PSL), an optimization approach based on genetic algorithms is proposed. To further improve the dynamic range in radar images, we present an algorithm for multidimensional frequency estimation from undersampled sparse data, which we name sparse iterative multidimensional frequency estimation (SIMFE). Through iterative processing, the proposed algorithm is able to detect targets entirely masked by sidelobes of more dominant ones, and thus overcomes the drawback of increased sidelobes for proposed non-equidistant interleaving schemes.

Unless stated otherwise, for simplicity the discussions in this chapter assume the classical signal processing described in Section 3.2. Other methods from Chapter 3 are analogously applicable.

4.1. Conventional Multiplexing Methods Applied to OFDM-MIMO Radar

To make the motivation for multiplexing via subcarrier interleaving apparent, conventional multiplexing methods applied to OFDM-MIMO radar are briefly discussed in the following.

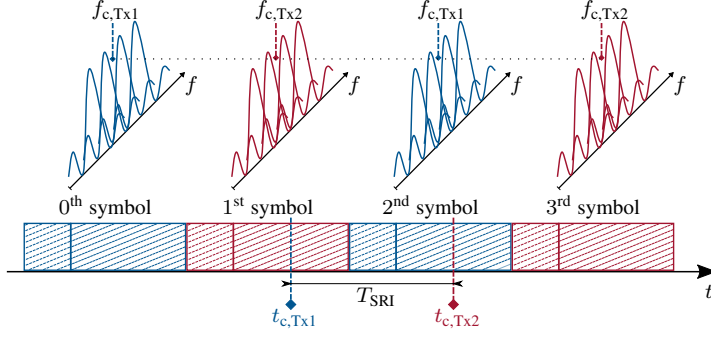


Figure 4.1.: TDM multiplexing for OFDM-MIMO radar (CP is denoted by dashed lines, OFDM symbol is shown by solid lines)

Additionally, the following discussion aims to demonstrate the advantages of OFDM compared to analog modulations in the context of MIMO radar.

4.1.1. Time Division Multiplexing

Time division multiplexing (TDM) is a straightforward multiplexing approach simple to realize. With equidistantly interleaved TDM, OFDM symbols are transmitted subsequently from different Tx antennas, such that different Tx paths are separated in time (Fig. 4.1). The main drawback of TDM is the increase of the time interval between two symbols that belong to the same Tx channel (e.g. the time difference between the first and third symbol in Fig. 4.1) by a factor N_{Tx} , with N_{Tx} being the number of Tx antennas. This leads to a reduction of unambiguous velocity range for radar images of individual Tx-Rx antenna pairs, i.e. spatial channels, by a factor of N_{Tx} . To obtain the original unambiguous velocity range, the SRI (symbol repetition interval) has to be reduced by N_{Tx} . However, for a fixed CP duration T_{CP} this leads to an increase of $\alpha = T_{SRI}/T$, i.e. to shorter OFDM symbols by a factor $N_{Tx}\alpha$. The shorter OFDM symbols for a fixed CP duration result in reduced energy efficiency. Additionally, due to the orthogonality condition shorter OFDM symbols imply wider subcarrier spacing $\Delta f = 1/T$. The latter, in turn, reduces the unambiguous distance range by a factor $T/(T_{SRI}/N_{Tx} - T_{CP})$, since a fixed length CP is required for each OFDM symbol of each Tx channel. This is disadvantageous compared to multiplexing based on subcarrier interleaving, as the latter employs a common CP for OFDM symbols of all Tx channels. Thus, the reduction of unambiguous distance range for the conventional EqSI multiplexing is N_{Tx} only — less than for TDM. Another drawback of TDM is that it cannot be combined with RS-OFDM, since the consecutive OFDM symbols are transmitted from different Tx antennas, and thus have DOA dependent phase differences. This necessitates the use of CP-OFDM for TDM multiplexed OFDM-MIMO radar.

Another issue to take into account in the case of TDM is the time difference between measurements of different spatial channels, as Fig. 4.1 illustrates. More precisely, denoting the center of the slow-time axis for a Tx channel by $t_{c,Tx}$, there is a time difference up to $T_{SRI}(N_{Tx} - 1)$ between center points of slow-time axis of different Tx channels. For moving targets, during this time difference a Doppler induced phase change occurs, which adds to the phase difference induced by the DOA of the target. When not compensated prior to the DOA estimation, such Doppler induced phase dependency (i.e. incoherence) between the Tx channels affects the DOA estimation. This problem is addressed in detail and compensation methods are presented in [Rambach, 2013, 2016].

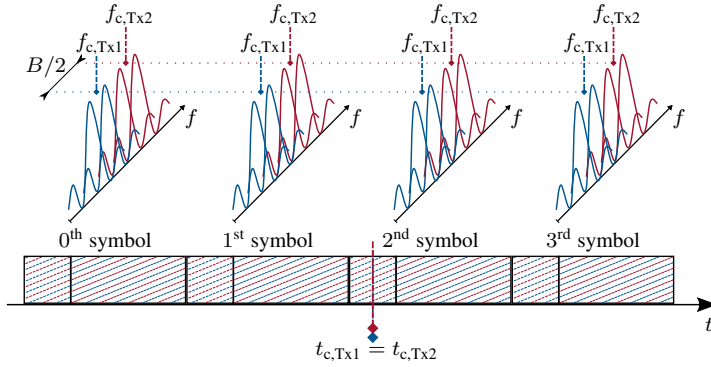


Figure 4.2.: FDM multiplexing for OFDM-MIMO radar

4.1.2. Frequency Division Multiplexing

Another conventional multiplexing method is the *frequency division multiplexing* (FDM), with which the bandwidth is shared between multiple Tx channels such that each channel has its own frequency sub-band. In the context of OFDM, this would mean that each Tx channel uses a block of subcarriers, as illustrated in Fig. 4.2. Whereas FDM enables a simultaneous transmission for all channels, sharing of the available bandwidth leads to a reduction of the distance resolution by N_{Tx} . Since in automotive application bandwidth is a limited resource (e.g. by frequency regulation, ADC-rates, etc.) and a high distance resolution is desired, the reduction of distance resolution due to multiplexing is a significant drawback.

Moreover, since both the distance and velocity terms in the received signal depend on the carrier frequency according to (3.7), different center frequencies of Tx channels lead to different distance and velocity terms in measurement signals of spatial channels. Whereas in the velocity estimation this results in a scaling of the velocity axis, the distance term causes a range dependent phase shift. The latter adds up with the phase differences due to the DOA and is typically much more dominant. This affects considerably the DOA estimation.

4.1.3. Code Division Multiplexing

An OFDM-MIMO radar concept based on multiplexing with *orthogonal space-time block codes* has been proposed in [Xia, 2015], which enables the use of all subcarriers by each Tx antenna. In fact, a similar concept of OFDM-MIMO radar with code division multiplexing has been proposed earlier in [Wu, 2010]. Whereas these approaches might be promising for range (distance) reconstruction in the context of SAR, its application for distance-velocity estimation leads to a reduction of the unambiguous velocity range due to the use of block codes (similar to TDM). Additionally, the orthogonality between the codes degrades in presence of Doppler shift, which is even more severe for block codes stretching over multiple OFDM symbols. A further drawback of code division multiplexing is the predefinition of the transmit signal for each antenna. This complicates the optimization of the former for other purposes such as low PAPR as well as limits its adaptability, e.g. for communication.

4.2. OFDM-MIMO Radar Multiplexed via Equidistant Subcarrier Interleaving

The idea of multiplexing for OFDM-MIMO radar via subcarrier interleaving has first been introduced in [Donnet, 2006]. The authors proposed the step-frequency technique, i.e. any of subcarriers is assigned to one Tx antenna at a time, such that over a certain period all subcarriers are commuted over all Tx channels [Donnet, 2006], forming a full bandwidth occupancy for each Tx channel. Analogous to the code division multiplexing approaches in [Xia, 2015; Wu, 2010], this method has a disadvantage when not only distance but also velocity estimation is performed.

Equidistant interleaving of OFDM subcarriers for multiplexing of Tx antennas has been proposed in [Sturm, 2013] and adopted for OFDM-MIMO radar in some further publications, e.g. [Sit, 2012a, 2013; Cao, 2015]. With this approach each N_{Tx} -th subcarrier is assigned to one Tx antenna, resulting in an equidistant spacing between subcarriers used by one Tx antenna. This ensures that each subcarrier is occupied by only one Tx channel, and thus represents a special type of frequency domain multiplexing. Fig. 4.3 illustrates the principle of EqSI multiplexing.

A substantial advantage of EqSI is the simultaneous use of the nearly entire bandwidth $B - N_{\text{Tx}}\Delta f$ by all Tx antennas. This enables the original unambiguous velocity range and distance resolution for all Tx channels. Moreover, since Tx channels have the same slow-time center and minor to no difference between their center frequencies, there is a very high coherence between Tx channels. Unlike for FDM, the phase differences between Tx channels due to different center frequencies and target distance can be accurately corrected after the distance estimation. Assuming a subcarrier spacing typical for automotive radar in the kHz range and distance estimation accuracy in the cm range, the correction can be performed with an accuracy in the μrad range. Thus, such a correction will ensure that the coupling of the distance and velocity to the DOA estimation is negligible. Alternatively, the same center frequency for different Tx channels can be achieved by leaving one or several subcarriers at the edges of the frequency band unused.

Compared to TDM, EqSI has the advantage that a single CP is used for all Tx channels for one slow-time sample. Moreover, in case of EqSI all Tx antennas radiate power simultaneously. Assuming the limit imposed by frequency regulation is not crossed, this allows more transmit power to be radiated. Furthermore, EqSI is compatible with RS-OFDM, which further improves the energy efficiency and unambiguous velocity range by omitting CP.

EqSI has, however, the drawback of increased spacing between subcarriers assigned to one Tx antenna. Since this means sampling of distance induced frequency domain complex exponentials with a larger sampling step $N_{\text{Tx}}\Delta f$, the unambiguously measurable distance range is reduced by N_{Tx} .

Based on the above discussion it can be deduced that EqSI is the state-of-the-art multiplexing method for OFDM-MIMO radar. Nevertheless, for some automotive applications, especially at higher carrier frequencies, no EqSI based MIMO parametrization is feasible with the classical OFDM radar signal processing due to the large subcarrier spacing imposed by the Doppler shift. Below we present a parametrization at 77 GHz for automotive radar that does not enable EqSI multiplexed MIMO due to the reduction of unambiguous distance range. Furthermore, we show that the application of ACDC significantly increases the unambiguous distance range (see Fig. 3.5), and thus enables multiplexing with EqSI in configurations not possible before.

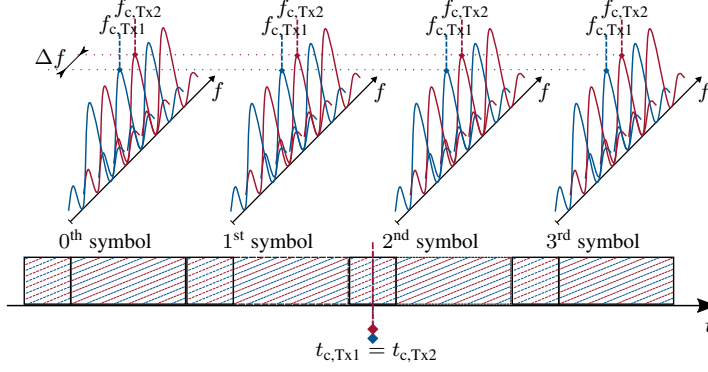


Figure 4.3.: EqsI multiplexing for OFDM-MIMO radar

For this discussion, we assume RS-OFDM for both the conventional approach and ACDC. We start by defining the unambiguous velocity range to be $[-80, +80]$ m/s, i.e. $v_u = 160$ m/s, and derive subsequently the modulation parameters according to the parametrization approach described in Section 2.3.2. The maximal SRI resulting from v_u is $T_{\text{SRI}} = c_0/(2f_c v_u) = 12.175 \mu\text{s}$. Assuming an unambiguous distance range of $d_u = 400$ m is needed to prevent overranges, a minimum subcarrier spacing of $\Delta f_{\text{min}} = c_0/(2d_u) = 375$ kHz is necessary. The subcarrier spacing resulting from the maximal OFDM symbol duration $T_{\text{OFDM,max}} \approx 12.175 \mu\text{s}$ is $\Delta f_{\text{min}} = 1/T_{\text{OFDM,max}} \approx 82.14$ kHz. However, following the design rule $f_{\text{D,max}}/\Delta f \leq 0.1$, with $f_{\text{D,max}} = 41$ kHz the distance between subcarriers should be $\Delta f = 10f_{\text{D,max}} = 410$ kHz to ensure a tolerable ICI level. This translates into an unambiguous distance range of $d_u = 366$ m, i.e. slightly less than the desired value. Hence, the presented requirements on unambiguous range of distance and velocity are hard to fulfil with the conventional parametrization according to [Sturm, 2012a]. The use of MIMO multiplexed with EqsI is not feasible with the presented configuration, since it further reduces the unambiguous distance range.

With ACDC, targets from the entire unambiguous velocity range can be processed without ICI. Thus, the minimum distance between subcarriers resulting from $T = 12.175 \mu\text{s}$ is $\Delta f_{\text{min}} = 82$ kHz. With this subcarrier spacing, a distance of $d_u = c_0/(2\Delta f) \approx 1826$ m can be measured unambiguously. Consequently, with EqsI multiplexing up to 4 Tx antennas can be used for MIMO, while requirements on unambiguously measurable distance range are satisfied for each Tx channel.

4.3. OFDM-MIMO Radar Multiplexed via Non-Equidistant Subcarrier Interleaving

Even though with ACDC based signal processing EqsI becomes feasible for 77 GHz automotive radar, it implies the constraint of rank-one modulation symbol matrix (see Section 3.3) and requires tighter subcarrier spacing to maintain the original unambiguous distance range. This means that for a given bandwidth the overall number of subcarriers is increased. This leads to higher memory demands as well as computational costs, and thus might become challenging for a large bandwidth. To generally overcome the drawback of reduced unambiguous distance range specific to EqsI, we propose the use of non-equidistant subcarrier interleaving (NeqSI) for OFDM-MIMO radar. This multiplexing scheme maintains the original unambiguously measurable range

as well as resolution both in distance and velocity for all Tx channels, but leads to increased sidelobes in the distance dimension. For each individual spatial channel, NeqSI can be interpreted as non-uniform sampling in a grid for the distance induced complex exponentials, i.e. incomplete measurement at the original Nyquist rate. To cope with the sidelobes in the distance dimension due to such subsampling, we propose a frequency estimation algorithm that exploits the sparsity of the measurement signal and is suitable for subsampled measurements (Section 4.5). Furthermore, we introduce a variation of NeqSI we name non-equidistant dynamic subcarrier interleaving (NeqDySI). The latter changes dynamically the interleaving pattern, which for one individual spatial channel can be interpreted as a joint subsampling in the distance-velocity space. Such multiplexing obtains significantly improved PSL compared to NeqSI, which enables a high dynamic range even for conventional 2D-FFT processing. We study the performance of the proposed multiplexing concepts based on the radar *ambiguity function* and point out advantages and drawbacks of each approach.

4.3.1. Non-Equidistant Subcarrier Interleaving¹

The drawback of reduced unambiguous distance range in case of EqSI multiplexing can be overcome by interleaving of subcarriers in a non-equidistant manner. It is well known that in case of non-equidistant sampling in a grid (e.g. subcarrier interleaving), the maximum unambiguously measurable frequency range (e.g. distance) is limited by the grid size (e.g. subcarrier spacing). To achieve this maximum range, the subcarrier interleaving has to be chosen properly. The maximum range can be obtained by choosing the interleaving pattern such that for each Tx antenna the minimum distance between its subcarriers is equal to the original subcarrier spacing. This guarantees that no grating lobes appear in the ambiguity function, and thus, the original unambiguous distance range is maintained. This is, however, not a necessary requirement, and interleaving patterns with larger minimum distance between subcarriers of one Tx antenna but the original unambiguous distance range exist.

Since in case of subcarrier interleaving OFDM subcarriers are transmitted from different Tx antennas, the distance-velocity estimation cannot be performed with all subcarriers at once due to DOA dependent phase differences between the subcarrier sets of different Tx channels. First, subcarriers belonging to different Tx channels have to be separated after the spectral division in (3.19). The spatial channels can be separated via a multiplication of the fully occupied matrix \mathbf{z} from (3.19) with a selection matrix Φ_p :

$$\mathbf{z}_{p,q} = \Phi_p \mathbf{z}_q, \quad (4.1)$$

where $\mathbf{z}_{p,q}$ is the measurement matrix of the spatial channel of p -th Tx and q -th Rx antenna pair, Φ_p is a diagonal matrix of size N_c that has ones only at the diagonal positions corresponding to the subcarriers assigned to the p -th Tx antenna and zeros elsewhere, and \mathbf{z}_q denotes the matrix \mathbf{z} from (3.19) for the q -th Rx antenna.

For the classical signal processing, the measurement matrix of each spatial channel is then processed with a 2D-FFT to generate a distance-velocity radar image according to (3.20) and (3.22):

$$\mathbf{Z}_{p,q} = \mathbf{F}_{N_c}^{-1} \mathbf{w}_{N_c} \mathbf{z}_{p,q} \mathbf{w}_{N_{\text{sym}}} \mathbf{F}_{N_{\text{sym}}}, \quad (4.2)$$

¹ The contributions of this section were partially reported in [Hakobyan, 2016b]. Some of author's own formulations from [Hakobyan, 2016b] are adopted in the text.

where $\mathbf{Z}_{p,q}$ denotes the distance-velocity image of the p -th Tx and q -th Rx antenna pair.

Next, the radar images of all spatial channels are integrated non-coherently for a combined detection and distance-velocity estimation, as described in Section 2.4.3:

$$\mathbf{Z}_{\text{NCI}} = \sum_{p=1}^{N_{\text{Tx}}} \sum_{q=1}^{N_{\text{Rx}}} |\mathbf{Z}_{p,q}|^2 \in \mathbb{R}_{>0}^{N_c \times N_{\text{sym}}} \quad (4.3)$$

where $|\cdot|^2$ denotes the elementwise squared magnitude. For target detection, a 2D peak detection is performed on \mathbf{Z}_{NCI} . Whereas the indices of the detected peaks indicate the distances and velocities of the targets, the complex amplitudes of $\mathbf{Z}_{p,q}$ at the positions of the detected peaks are used for DOA estimation in later steps.

To investigate the properties of NeqSI and its influence on the radar image \mathbf{Z}_{NCI} , the radar ambiguity function is studied. Informally speaking, the ambiguity function of a radar can be interpreted as its “signature” in the frequency domain. In case of distance-velocity estimation it corresponds to the radar image for a zero-distance zero-velocity target.

Given the same interleaving for all OFDM symbols, the ambiguity function in velocity estimation does not depend on the subcarrier interleaving. In contrast, the ambiguity function in the distance dimension is strongly determined by the interleaving scheme. Thus, we study the properties of NeqSI and compare it to EqSI based on the ambiguity function in distance estimation.

In case of EqSI, grating lobes appear in the distance ambiguity function. Hence, the unambiguously measurable distance range is reduced by the interleaving factor N_{Tx} . An example for an ambiguity function with $N_{\text{Tx}} = 4$ and $N_c = 2048$ is shown in Fig. 4.4a². Evidently, for EqSI the unambiguously measurable distance range is reduced by N_{Tx} due to grating lobes.

In contrast to EqSI, in case of NeqSI multiplexing no grating lobes appear within the original unambiguous distance range. However, the level of the sidelobes in the ambiguity function increases (Fig. 4.4a), which limits the dynamic range in the distance dimension. The non-coherent integration of radar images $\mathbf{Z}_{p,q}$ from different spatial channels in (4.3) reduces the sidelobes. In this example with *pseudo-random interleaving*, the PSL, i.e. the power ratio between the peak and the highest sidelobe in the ambiguity function, is reduced by approximately 3 dB due to the NCI (shown by the dashed lines in Fig. 4.4a). The term pseudo-random interleaving refers to random interleaving of an equal number of subcarriers over the Tx antennas. The PSL improvement through NCI occurs due to the fact that the radar images from different Tx channels use different interleaving patterns, and thus have different sidelobes. Their integration reduces the sidelobe peaks, i.e. smoothens the sidelobes. The PSL can be further increased through the use of optimized interleaving schemes instead of pseudo-random ones. For the discussed example, a further improvement of more than 3 dB can be obtained through optimization, as shown in Fig. 4.4b. The optimization of the interleaving pattern is described in Section 4.4.

Since NeqSI leads to increased sidelobes in the distance dimension, the classical Fourier based processing is not suitable for it. Instead, methods that leverage the knowledge about the interleaving pattern for improving the detection performance are required. We present the problem of distance-velocity estimation with NeqSI as a frequency estimation problem from subsampled data, based on which we develop a suitable signal processing method in Section 4.5. In the same

² The distance axis is extended to some negative values for the clarity of representation

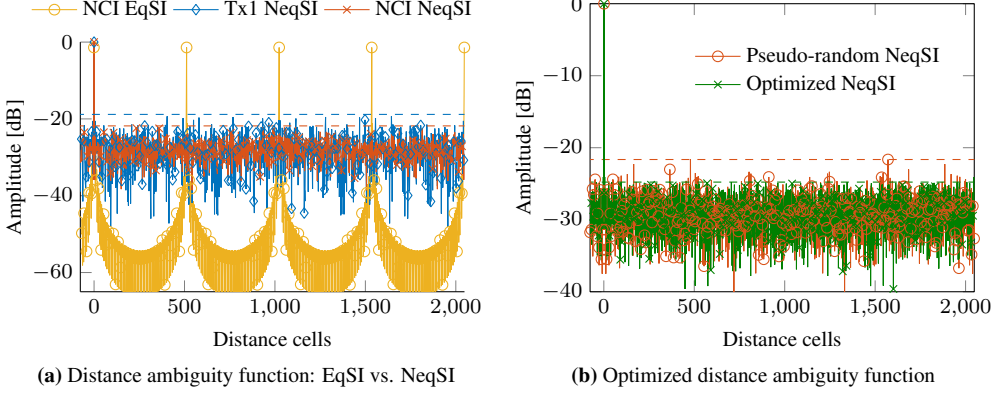


Figure 4.4.: Distance ambiguity function for 4 Tx antennas

section we give simulative analysis of the target detection performance for NeqSI in combination with the proposed signal processing method.

4.3.2. Non-Equidistant Dynamic Subcarrier Interleaving³

As discussed in the previous section, NeqSI enables a full unambiguous range and resolution both in distance and velocity for all Tx channels, overcoming the drawbacks of EqSI multiplexing. However, due to the increased sidelobes in the distance dimension it requires more sophisticated signal processing methods to obtain a high dynamic range in distance estimation. To suppress sidelobes in the distance dimension to an extent that the classical Fourier processing is applicable, we propose an extension of NeqSI we name non-equidistant dynamic subcarrier interleaving (NeqDySI). The idea behind NeqDySI is to change the interleaving pattern dynamically from OFDM symbol to symbol, such that the sidelobes induced by non-equidistant interleaving are different for each OFDM symbol. In this case, the Doppler processing leads to a suppression of sidelobes, i.e. the sidelobes due to non-equidistant sampling are now spread over both distance and velocity dimensions. This results in a high PSL both in distance and velocity, and thus in a high dynamic range with the classical 2D-FFT processing.

For demultiplexing, i.e. separation of the spatial channels, the fully occupied matrix \mathbf{z} from (3.19) is multiplied elementwise with a NeqDySI selection matrix Φ_p , analogous to (4.1):

$$\mathbf{z}_{p,q} = \Phi_p \odot \mathbf{z}_q. \quad (4.4)$$

As opposed to NeqSI, in this case the selection matrix Φ_p is not diagonal but an $N_c \times N_{\text{sym}}$ selection matrix with ones in positions of subcarriers belonging to the p -th Tx antenna and zeros elsewhere. The matrices Φ_p are complementary, i.e. use all subcarriers and each subcarrier is assigned to a single Tx antenna. A simple approach to generate the selection matrices is the pseudo-random NeqDySI, i.e. for each OFDM symbol, N_c/N_{Tx} ones are randomly selected and assigned to each Tx antenna.

³ The contributions of this section were partially reported in [Hakobyan, 2016d]. Some of author's own formulations from [Hakobyan, 2016d] are adopted in this section.

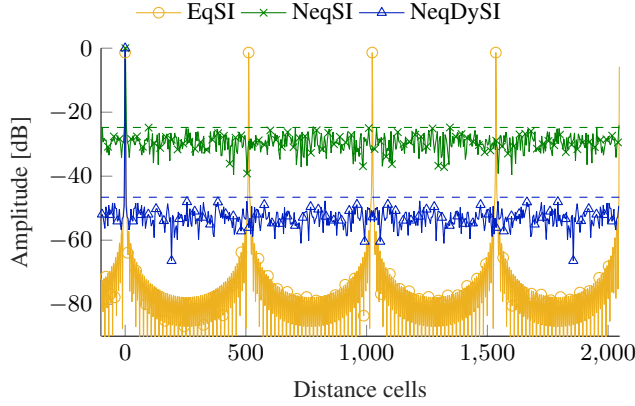


Figure 4.5.: Zero-Doppler cut of the ambiguity function for an OFDM-MIMO radar with 4 Tx antennas (Kaiser window, $\beta = 6.5$).

After demultiplexing, the measurement matrices of all spatial channels are processed with 2D-FFT and integrated non-coherently as in (4.2) and (4.3), followed by peak detection and further processing steps.

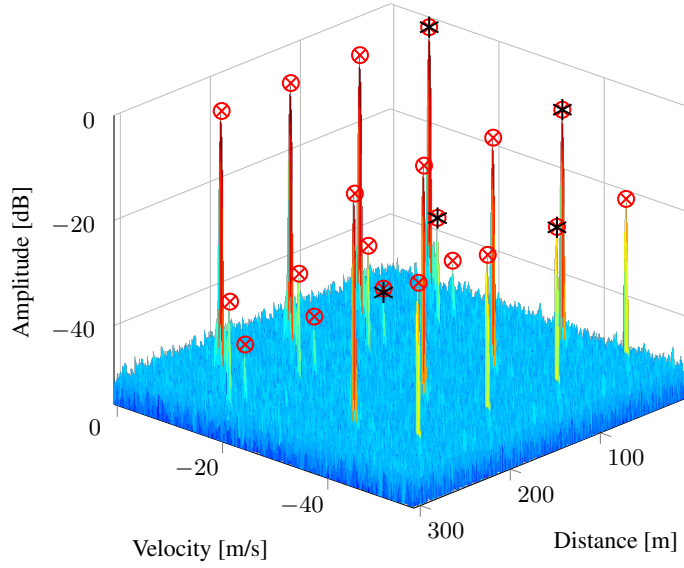
Ambiguity function of NeqDySI

Also here, we study the properties of NeqDySI based on the ambiguity function and compare it to other subcarrier interleaving methods. Even though for NeqDySI the interleaving pattern influences the ambiguity function both in distance and velocity, for the clarity of representation we show the distance ambiguity function of the zero-Doppler cut only, implying that its floor for sidelobes is the same as for the 2D ambiguity function. The non-coherently integrated distance ambiguity functions for EqSI, NeqSI and NeqDySI are shown in Fig. 4.5 for an example with $N_{Tx} = 4$, $N_c = 2048$ and $N_{sym} = 512$. For both NeqSI and NeqDySI the optimized interleaving patterns are shown.

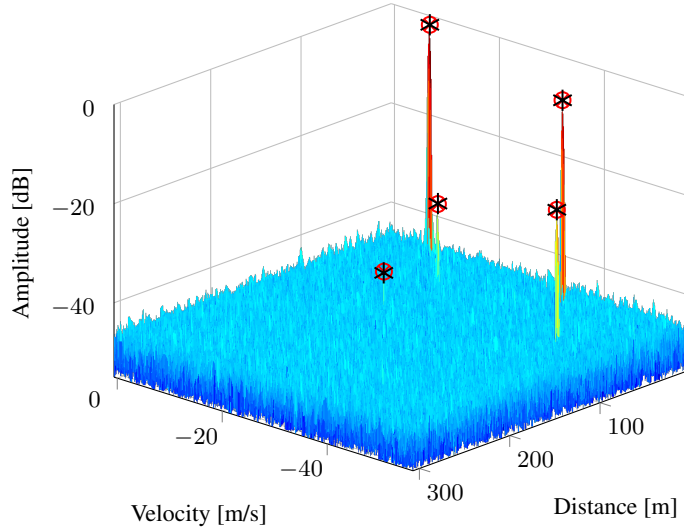
Clearly, by varying the interleaving pattern from OFDM symbol to symbol an increase of PSL is achieved. The PSL improvement over NeqSI depends on the number of slow-time samples N_{sym} , which is 27 dB in the discussed example. Thus, the PSL for NeqDySI generally depends on the overall number of samples, i.e. $N_c \times N_{sym}$. Furthermore, it is influenced by the window function, as we point out in Section 4.4. In the same section, an approach for optimization of the interleaving pattern for NeqDySI is presented.

Effect of NeqDySI on distance-velocity estimation

To illustrate the performance of the presented concept in distance-velocity estimation, simulations with $N_{Tx} = 4$ Tx antennas are performed. The OFDM radar has a bandwidth of 1 GHz with $N_c = 2048$ subcarriers and $N_{sym} = 512$ symbols. That is, each Tx antenna uses $N_c/N_{Tx} = 512$ subcarriers. The carrier frequency is $f_c = 77$ GHz. A Kaiser window with $\beta = 6.5$ is used in both dimensions. For peak detection from the non-coherently integrated distance-velocity image \mathbf{Z}_{NCI} a 2D ordered statistics CFAR (OS-CFAR) [Rohling, 1983] detector and a 2D Kaiser window based peak interpolation are applied. The interleaving scheme is optimized as described in Section 4.4 and has a PSL of 46.05 dB. The simulated scenario comprises five targets of



(a) EqSI



(b) NeqDySI

Figure 4.6.: Radar images in a scenario with 5 targets: * – true position, \otimes – detection

different amplitudes (Table 4.1). A white Gaussian noise with power of 0 dB is added to the measurement signal.

Since for a proper performance NeqSI needs special signal processing algorithms, for performance evaluation we compare NeqDySI to EqSI — both using the conventional 2D-FFT processing. Fig. 4.6a and Fig. 4.6b show the non-coherently integrated distance-velocity images for the EqSI and optimized NeqDySI schemes, respectively. Fig. 4.6a illustrates clearly that in case of EqSI grating lobes occur, resulting in multiple, equally high peaks for each target. If the distance evaluation is limited to the unambiguously measurable range, the targets outside this range (e.g.

Table 4.1.: Targets in simulation

Targets	1	2	3	4	5
Distance [m]	15	30	90.3	60	120
Velocity [m/s]	-9.3	-37.15	-46.44	-18.6	-18.57
Amplitude [dB]	0	-5	-20	-30	-40

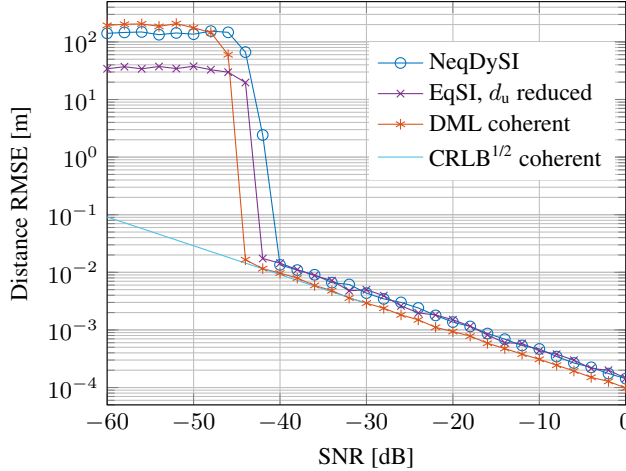


Figure 4.7.: Distance RMSE and CRLB: NeqDySI vs. EqSI

the 5th target) appear at wrong locations, leading to ghost targets. In contrast, NeqDySI is able to detect all targets unambiguously. The sidelobes in the distance-velocity image are at a comparable level to the noise floor and do not disturb the target detection considerably. Nevertheless, the overall noise floor is evidently slightly higher than for EqSI, which is due to the superposition of noise with NeqDySI sidelobes spread over the entire radar image.

Detection accuracy of NeqDySI in the presence of noise

Even though due to high PSL NeqDySI achieves a high dynamic range, its performance in the presence of noise needs further investigation due to its sidelobes adding to noise. Therefore, the root mean square error (RMSE) in the distance estimation is studied for a single target. Fig. 4.7 shows the RMSE for both NeqDySI and EqSI as a function of SNR. As a reference the *deterministic maximum likelihood* (DML) estimator and *Cramer–Rao lower bound* (CRLB) for coherent estimation are presented. For each input SNR value 1000 Monte-Carlo simulations are performed. In this simulation, targets are assumed to be within the reduced unambiguously measurable distance range of the EqSI scheme and no ghost targets occur as in Fig. 4.6a. So, Fig. 4.7 compares only the noise and sidelobe limited detection performance without considering the ghost targets caused by grating lobes.

First of all, from Fig. 4.7 it is evident that both EqSI and NeqDySI do not achieve the CRLB and the performance of coherent ML estimation. This is due to the non-coherent integration of the spatial channels as well as windowing. Both interleaving schemes achieve the same accuracy, but NeqDySI achieves the threshold point, i.e. the point after which a stable detection performance is achieved, around 1 to 2 dB later. In other words, NeqDySI restores the full unambiguous range of distance and velocity with a slight degradation of the detection performance compared to EqSI.

4.4. Optimization of the Interleaving Pattern for Non-Equidistant Interleaving Schemes⁴

Even though the pseudo-random subcarriers interleaving together with non-coherent integration of radar images from all spatial channels results in high PSL values, the interleaving pattern can be optimized for further PSL improvement. The optimization of non-equidistant sampling positions is a topic widely studied in the context of DOA estimation [Ang, 1997; Lange, 2010, 2011], where antenna positions on a linear or planar array represent the spatial sampling points. Since the non-equidistant subcarrier interleaving can be seen for each individual spatial channel as a non-uniform sampling of delay induced complex exponentials, optimization methods used for DOA estimation can be adopted for our optimization problem. Analogously, the optimization of the interleaving pattern for NeqDySI is associated with the array optimization problem for planar arrays. However, our problem has different frame conditions: significantly larger number of samples, sampling in a fixed grid, high dynamic range, etc. Furthermore, since with the current processing methods the detection is performed on the radar image obtained by NCI of the distance-velocity images from all spatial channels, a joint optimization for all Tx channels based on NCI-integrated radar image is required. As this is a high-order non-convex optimization problem, we propose the use of genetic algorithms for this task.

Since genetic algorithms represent a wide and extensively researched field of mathematical optimization, it cannot be covered exhaustively within the scope of this work. Instead, we give a brief overview of the genetic algorithms to facilitate a better understanding of the proposed optimization approach. For more detailed information on genetic algorithms please refer to [Goldberg, 1989; Weise, 2009] and the references therein. Along with the description of optimization methods, we give a problem formulation for the optimization task. Then, we point out the existence of two kinds of sidelobes: the ones due to limited bandwidth of the signal and the ones due to non-equidistant sampling, i.e. subcarrier interleaving. For a high PSL, the first kind of sidelobes has to be suppressed by windowing. Thus, we study the impact of windowing on the optimization of PSL and show that it is sufficient to include it in the optimization as a fixed parameter. Finally, we present some optimization results for both NeqSI and NeqDySI multiplexing schemes.

4.4.1. Genetic Algorithms

Genetic algorithms are optimization methods that belong to the family of evolutionary algorithms. These are biology-inspired optimization algorithms based on principles of Darwinian evolution theory such as natural selection, crossover, mutation and survival of the fittest [Weise, 2009]. Based on these processes a population of individuals is optimized from generation to generation with respect to a cost function in a meta-heuristic manner. That is, based on optimization criteria a set of the fittest candidates, i.e. individuals, drive the evolution of the population into a certain direction, whereas through the mutation probabilistic changes of the population are introduced. This aims to prevent the process from converging to a local minimum, while through the survival of the fittest the population evolves from generation to generation to fit better to the optimization goals. Due to the universal nature of this approach evolutionary algorithms are applicable in a

⁴ Some contributions from this section were partially reported in [Hakobyan, 2017b]. Some of author's own formulations from [Hakobyan, 2017b] are adopted in this section.

wide variety of problems and perform well in many different problem categories [Weise, 2009]. They are especially well suited for optimization problems with unknown fitness landscape, and therefore are a proper choice for optimization of the non-equidistant interleaving pattern for OFDM-MIMO radar.

Genetic algorithms are the class of evolutionary algorithms that use arrays of a fixed data type as genomes, i.e. as set of parameters that define a possible solution [Weise, 2009]. Some sources differentiate a special subtype of genetic algorithms that operates in a search space of real numbers and refer to it as evolution strategy [Weise, 2009; Lange, 2012]. Although in our formulation of the interleaving pattern optimization the genomes are real numbers, we prefer the more general term genetic algorithms to refer to this optimization. In the following we describe the steps of genetic algorithms and our configuration for one-dimensional optimization of the interleaving pattern, i.e. for NeqSI. It can be extended to 2D optimization, i.e. NeqDySI, analogously.

First, an initial population of individuals $\underline{\rho}_x^{(v)}$, $v \in \{1, \dots, \nu\}$ is generated randomly. The elements (genes) of individuals $\underline{\rho}_x^{(v)}$ are random real numbers, which later will be mapped to the subcarrier interleaving pattern described by Φ_p in (4.1). The size of the population is an important parameter for creating enough of diversity to sufficiently cover the search space but at the same time it influences the computation time significantly. Since our optimization task is computationally complex due to the large number of subcarriers, we adapt ν depending on N_c . A typical value used for many of our simulations is $\nu = 1000$.

The objective values of the individuals in the population are computed based on the specified cost function. In our case, the cost function is the PSL of the non-coherently integrated distance profiles, as described in the next section. The PSL of each individual is used as its fitness value, i.e. a value indicating how good a particular solution is. Based on the fitness values of individuals in the population, now the reproduction of a new generation by means of survival of the fittest, crossover and mutation takes place.

We use for reproduction an elitist evolutionary algorithm [Weise, 2009], i.e. a set of the fittest individuals $\underline{\rho}_{x,e}^{(v_e)}$, $v_e \in \{1, \dots, \nu_e\}$ from the current population survives for the next generation. This guarantees that in case the global optimum is discovered during the optimization, the algorithm will converge to that optimum. In our setting, these are the top 5 % individuals, i.e. $\nu_e = 0.05\nu$. Other individuals of the next generation are created by means of crossover and mutation. To this end, first a set of parents is created from the individuals of the current generation, which is commonly referred to as selection. For the latter, many approaches such as truncation selection, random selection, roulette wheel selection, etc. exist [Weise, 2009]. Since we already facilitate the evolution through preservation of elite individuals, for the selection we use the random selection that does not account for the fitness of the individuals in the current population. This keeps the population evolving, while preserving enough diversity between individuals. Denoting the number of children, i.e. individuals of the next generation created by crossover and mutation by ν_c and ν_m , respectively, a total number of parents $\lambda = 2\nu_c + \nu_m$ is sufficient. A higher number of parents can be chosen to create more children, from which only the $\nu - \nu_e$ fittest survive.

After the parent pool $\underline{\rho}_x^{\dot{v}}$, $\dot{v} \in \{1, \dots, \lambda\}$ is created, crossover children are generated via random mixing of the genes between two randomly selected parents. That is, each gene of the child is randomly selected from one of corresponding two genes of its parents. Bearing in mind that the parents are in a random order, for the n -th gene this can be written as

$$\ddot{\rho}_{x,c}^{(v_c)}(n) = \begin{cases} \dot{\rho}_x^{(2v_c-1)}(n) & \text{for } X_c(n) \geq 0 \\ \dot{\rho}_x^{(2v_c)}(n) & \text{for } X_c(n) < 0 \end{cases}, \quad v_c \in \{1, \dots, \nu_c\} \quad (4.5)$$

where X_c denotes a zero-mean random variable used for selecting one of two genes. The proportion of the crossover children to the mutation ones is a configuration parameter. In our setting the number of crossover children is $\nu_c = 0.8\nu$. The rest of individuals of the next population is created via mutation of the remaining parents. For the mutation, a Gaussian distributed zero-mean random variable with a variance σ_x^2 is added to the genes of each parent:

$$\ddot{\rho}_{x,m}^{(v_m)} = \dot{\rho}_x^{(v_m)} + \underline{X}_{x,m}^{(v_m)}, \quad v_m \in \{2\nu_c + 1, \dots, \lambda\}, \quad (4.6)$$

where $\underline{X}_{x,m}^{(v_m)} \in \mathbb{R}^{N_c}$ has *independent identically distributed* (i.i.d.) elements $X_{x,m}^{(v_m)}(n) \sim \mathcal{N}(0, \sigma_x^2) \forall n$. The mutation variance σ_x^2 defines the degree to which the optimization resembles a random walk or a gradient search. A reasonable strategy is to start from a σ_x^2 slightly smaller than the range of the values in the genome $\dot{\rho}_x$ and shrink it over the course of optimization. This resembles a quasi-random walk in the beginning of optimization, such that the probability of converging to a local minimum is low. Shrinking the mutation variance gradually over the course of optimization reduces the probabilistic change of the population, enabling a gradual transformation into a gradient-like optimization.

Finally, the new population is created by merging all three kinds of children:

$$\ddot{\rho}_x^{(v_m)} = \left\{ \dot{\rho}_{x,c}^{(v_c)} \cup \ddot{\rho}_{x,c}^{(v_c)} \cup \ddot{\rho}_{x,m}^{(v_m)} \right\}. \quad (4.7)$$

The optimization comprising the evaluation, selection and reproduction is carried out iteratively until a termination criterion is met. A termination criterion can be reaching of a certain time or iteration limit, finding an individual with a sufficient fitness, or, more meaningfully, the convergence of the algorithm to a certain solution unchanged over numerous iterations. The described optimization cycle of genetic algorithms is summarized in Fig. 4.8.

4.4.2. Formulation of the Optimization Task

To obtain a favorable interleaving pattern, we formulate the choice of the latter as an optimization task with respect to the PSL of the distance-velocity ambiguity function. Since the detection is performed on the radar image resulting from the NCI of the distance-velocity images from all spatial channels, the non-coherently integrated ambiguity function has to be considered. Thus, a joint optimization for all Tx channels is required. In the following, we describe the formulation of the optimization task for NeqSI, i.e. one-dimensional. Its extension to include the velocity dimension, i.e. for NeqDySI, is straightforward.

We represent the interleaving scheme by the interleaving vector $\underline{\Phi} \in \mathbb{N}^{N_c}$ that contains N_c/N_{Tx} samples of each of $1, 2, \dots, N_{Tx}$. $\underline{\Phi}$ indicates which subcarriers belong to which Tx channel. From $\underline{\Phi}$ the selection matrix $\underline{\Phi}_p$ can be obtained with the help of indicator function by $\underline{\Phi}_p = \text{diag}(\underline{\Phi} == p)$, where $(\underline{\Phi} == p)$ yields a vector with ones at the positions where $\underline{\Phi}$ has the value p and zeros elsewhere. For the p -th Tx channel, we denote this vector by $\underline{\Phi}_p$.

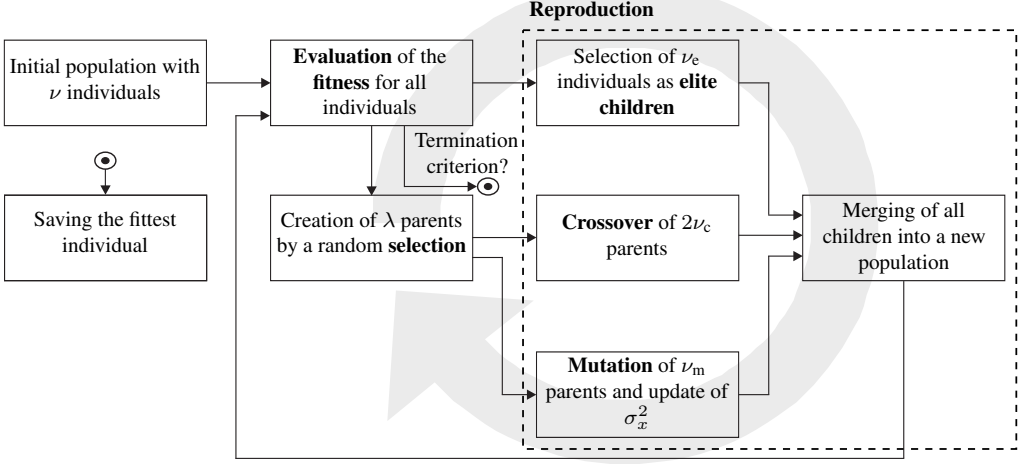


Figure 4.8.: Basic cycle of the genetic algorithms used

The non-coherently integrated ambiguity function in distance is

$$\chi_{\text{NCL},d} = \sum_{p=1}^{N_{\text{Tx}}} |\mathcal{F}^{-1}(\mathbf{w}_{N_c} \Phi_p \cdot \mathbf{1}_{N_c})|^2 = \sum_{p=1}^{N_{\text{Tx}}} |\mathcal{F}^{-1}(\underline{w}_{N_c} \odot \underline{\Phi}_p)|^2, \quad (4.8)$$

where \underline{w}_{N_c} is a column vector containing the diagonal elements of \mathbf{w}_{N_c} , i.e. the vector of the window function in the distance dimension. The continuous inverse Fourier transform \mathcal{F}^{-1} in (4.8) implies that for an accurate PSL calculation the continuous ambiguity function should be considered which is not limited to on-grid values. The PSL is calculated from the ambiguity function as the ratio of the main peak power to that of the highest sidelobe. From (4.8) it is evident that the distance ambiguity function, and thus the PSL depends both on the interleaving pattern $\underline{\Phi}$ as well as on the applied window function \underline{w}_{N_c} . We include the latter into the optimization as a fixed parameter, as we discuss in the next section. The optimization task is thus to maximize the PSL of $\chi_{\text{NCL},d}$ over interleaving pattern $\underline{\Phi}$, while maintaining the unambiguously measurable distance range for each Tx channel:

$$\max_{\underline{\Phi}} \text{PSL}(\chi_{\text{NCL},d}(\underline{\Phi}, \underline{w}_{N_c})) \quad \text{subject to,} \quad d_{u,p} = d_u, \quad (4.9)$$

where $d_{u,p}$ denotes the unambiguously measurable distance range of the p -th Tx antenna, and d_u is the original range before subcarrier interleaving. Note that we do not impose more specific constraints regarding the unambiguous distance range to not unnecessarily restrict the space of possible solutions.

To apply the genetic algorithms presented in Section 4.4.1 for solving the optimization task in (4.9), a mapping of the individuals $\underline{\rho}_x^{(v)}$ to the interleaving pattern $\underline{\Phi}$ is required. We perform this mapping by sorting the genes in $\underline{\rho}_x^{(v)}$ and dividing the entire range of gene values into N_{Tx} intervals with N_c/N_{Tx} elements in each. The scheme describing which gene belongs to which interval is used for assignment of subcarriers to corresponding Tx channels. Consequently, for each individual the PSL of the corresponding interleaving pattern can be calculated according to (4.9), the inverse of which serves as a cost function. That is, the higher the PSL, the lower the cost function, and thus the higher the fitness of the individual. The changes of individuals

during crossover and mutation lead to different interleaving schemes, such that effectively an optimization of PSL over Φ is achieved.

For a practical implementation the constraint in (4.9) can be omitted by defining the cost function as a ratio of the main peak to the next highest value within the original unambiguous distance range and outside the mainlobe. This would lead to a maximum cost in case grating lobes appear in the range of interest, and thus to a minimum fitness.

4.4.3. Effect of Windowing on the PSL of Non-Equidistant Sampling

The ambiguity function in (4.8) exhibits two different sidelobe types: sidelobes due to the subsampling and those due to the limited bandwidth of the measurement signal. To obtain a high PSL, both types of sidelobes have to be considered. Whereas the first type can be optimized by the choice of a favorable interleaving pattern, the second type of sidelobes can be effectively suppressed by windowing — analogous to the sidelobe suppression in case of equidistant sampling. However, the windowing influences the sidelobes due to the subsampling, and thus needs to be considered during the optimization of the interleaving pattern.

As the inclusion of the window function into the optimization would significantly complicate it by increasing its order, we prefer to define a suitable window prior to the optimization and include it into the optimization as a fixed parameter. The analysis below for a particular window type confirms the validity of this approach.

For this study, we choose the Kaiser window due to following reasons: it is parameterizable with a single parameter β , it offers a good trade-off between the mainlobe width and the sidelobe level, and it has a closed-form frequency domain representation that enables efficient interpolation techniques for off-grid peak detection. Similarly, the proposed optimization can be carried out for any other window that is parameterizable and has high enough sidelobe suppression.

We consider the configuration with $N_{Tx} = 4$ and $N_c = 2048$ from Section 4.3.1, and optimize the interleaving pattern for Kaiser window with different β values, as shown in Fig. 4.9. For a reference the PSL in case of EqSI interleaving is shown, since for the latter only the sidelobes due to the limited bandwidth of the signal are present. Evidently, there is a clear optimum at around $\beta = 3.2$ that maximizes the PSL of NeqSI for the given N_c . Whereas a lower β does not suppress the sidelobes due to the limited bandwidth of the signal sufficiently, a higher β reduce the energy of the main peak, which has an adverse effect on PSL. Thus, it can be deduced that the window function has to be chosen such that the sidelobes due to the limited bandwidth of the signal are suppressed below those due to the subsampling. Below this level, however, the sidelobe suppression has to be kept low to minimize the energy reduction of the main peak.

To investigate the sensitivity of the PSL to the application of a window function with parameters different than the ones used for the optimization, we apply a window with different β on an interleaving pattern optimized for $\beta = 3.2$. The latter was found to be optimum for this parametrization (Fig. 4.9). As Fig. 4.9 shows, there is only a minor difference to the case where during both optimization and application the same β is used. This shows that given sufficient sidelobe suppression, it is meaningful to incorporate the window function into the optimization of the interleaving pattern as a fixed parameter.

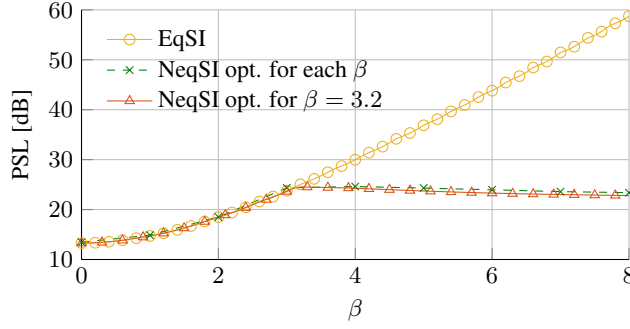


Figure 4.9.: PSL as a function of the β parameter of the used Kaiser window

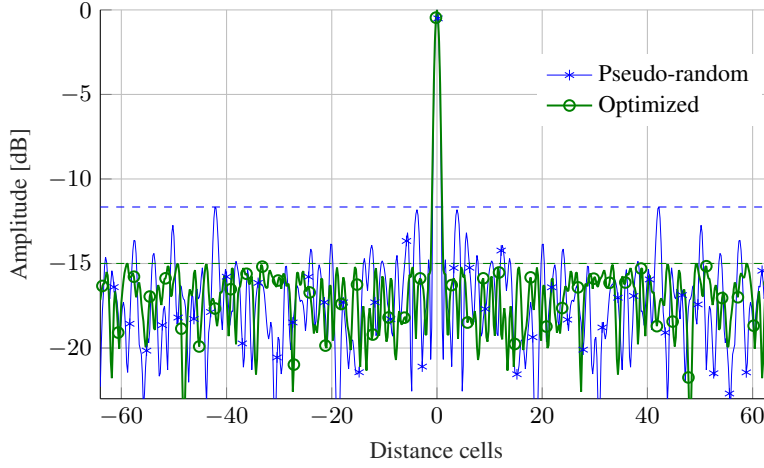


Figure 4.10.: NCI distance ambiguity function for NeqSI, $N_c = 128$, Kaiser window with $\beta = 1.5$

4.4.4. Optimization Results for Non-Equidistant Interleaving Schemes

Below we present some optimization results for the non-equidistant interleaving schemes proposed in this chapter. First, we illustrate the difference of the NCI ambiguity function of an optimized interleaving pattern to that of a pseudo-random one for NeqSI with $N_c = 128$ (Fig. 4.10)⁵. Clearly, the optimization of the interleaving pattern smoothens the sidelobes, resulting in a higher PSL.

Next, the PSL of the ambiguity function is studied for both NeqSI and NeqDySI over different number of subcarriers and OFDM symbols (Fig. 4.11). For both NeqSI (Fig. 4.11a) and NeqDySI (Fig. 4.11b) the reference results are obtained with pseudo-random interleaving; in case of NeqDySI the interleaving pattern changes for each OFDM symbol. The Kaiser window applied for sidelobe suppression is parametrized for each configuration such that it suppresses the sidelobes due to limited bandwidth of the signal below the ones due to subsampling⁶. The results

⁵ The ambiguity function is shown symmetric around zero for the sake of clearness

⁶ For NeqSI with $N_c = 2^i$, $i \in [7, 12]$, the following values are used: $\beta = [1.5, 2.1, 2.5, 2.9, 3.2, 3.7]$. Analogously, for NeqSI with $N_c \times N_{\text{sym}} = 2^i$, $i \in [14, 21]$, the following values are used: $\beta = [4.3, 4.6, 5.5, 5.4, 5.8, 6.2, 6.5, 6.8]$

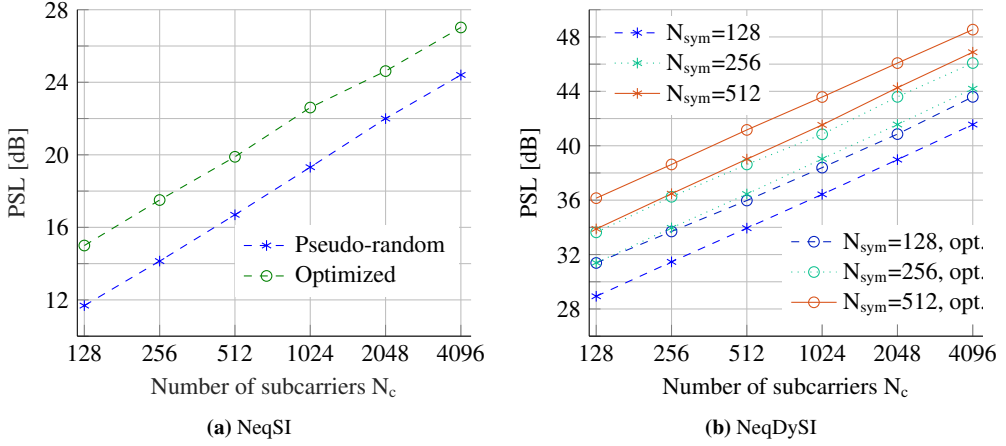


Figure 4.11.: PSL of the NCI ambiguity function for non-equidistant interleaving schemes: pseudo-random (denoted by $*$) vs. optimized (denoted by \circ)

for pseudo-random interleaving which serves as a reference are obtained via 1000 Monte Carlo simulations.

Evidently, for both NeqSI and NeqDySI the proposed optimization yields interleaving patterns with a PSL improved by up to 3.5 dB. Furthermore, it can be observed that even for configurations with a high number of samples a considerable PSL improvement is obtained (Fig. 4.11b). Nevertheless, the higher the number of samples, the smaller is the improvement compared to the pseudo-random scheme. This can be explained by the increasing complexity of the optimization task, which increases the chance for the optimization to converge to a local optimum and not to the global one. The former might, however, be close to the global optimum, and thus, represent a practically “good enough” solution. Also, from Fig. 4.11b it becomes apparent that the PSL depends on the number of samples, regardless of which dimension the samples are in. As an example, the configuration with $N_c = 128$ and $N_{\text{sym}} = 256$ has approximately the same PSL as the one with $N_c = 256$ and $N_{\text{sym}} = 128$.

4.5. Application of Sparse Recovery Methods for OFDM-MIMO Radar

As the multiplexing of Tx channels implies sharing of the available resources, only a part of these resources is available to each channel. In case of multiplexing via non-equidistant interleaving of OFDM subcarriers, a subsampling of the measurement signal takes place in each channel. In recent years, methods for recovery of sparse signals from subsampled data together with techniques for compressed acquisition of the measurement signal emerged into a new research field known as *compressed sensing* (CS)⁷. Based on the assumption that the measurement signal is sparse, i.e. has only a limited number of non-zero components in some representation, the sparse recovery methods aim to reconstruct the original signal from subsampled data. Since the radar scene is typically sparse, i.e. the number of available samples is significantly higher than

⁷ In some publications compressed sensing is referred to as compressive sensing or compressive sampling

the number of targets, these methods are generally applicable for radar signal processing. To overcome the drawback of the increased sidelobes due to the subcarrier subsampling at each spatial channel, we propose to combine the non-equidistant interleaving schemes with CS based signal processing methods. The latter can be seen as a sparse recovery, whereas the former can be considered as compressed acquisition of the measurement signal at each channel.

Since CS is a large and dynamically growing research field, it can be neither covered completely in the scope of this work nor an exhaustive literature survey is possible. Instead, we give in the following an intuitive description of the CS fundamentals and present the most significant and relevant literature sources.

4.5.1. Compressed Sensing Overview

The theoretical foundation of today's digital technology is the *sampling theorem* discovered by Whittaker, Nyquist, Kotelnikov and Shannon and described in their pioneering works on sampling of continuous-time bandlimited signals [Whittaker, 1915; Nyquist, 1928; Kotelnikov, 1933; Shannon, 1949]. These works state that bandlimited continuous-time signals can be perfectly reconstructed from equidistant samples taken with a rate at least twice the highest frequency in the signal (Nyquist rate). These findings enabled a massive digitalization in many areas, resulting in more robust, flexible and cost-efficient sensing and processing systems. As a result of constant growth and increasing sophistication of such systems, in many applications (imaging, video, remote sensing, etc.) sampling at the Nyquist rate leads to massive data loads difficult to process and store, or is even unachievable due to the limitations of ADCs.

To reduce the data volumes which have to be stored, the signals are often compressed. This is especially effective for signals that contain a high amount of redundancy, i.e. have a representation where less data can accurately represent the information content of the signal. Many real world signals such as image, video, speech, etc. have such sparse or compressible representations, which is effectively used for signal compression by schemes such as JPEG. Intuitively, sampling such signals at Nyquist rate and then compressing them digitally seems not to be the optimal approach. A more advantageous approach for sensing of sparse or compressible signals would be to sense them already in a compressed form, i.e. with a lower sampling rate. This idea is at the very core of CS: exploit the additional knowledge about the signal sparsity for compression of the signal already at the sensing stage such that the main information content is preserved. Consequently, CS is means to overcome the Nyquist rate sampling for signals that have a sparse or compressible representation.

Long before this principle has attracted the attention of the signal processing community, first steps in this direction have been done by several researchers. So in the early 1900's Caratheodory showed that under certain conditions a signal comprising of a sum of M sinusoids is uniquely determined by its value at $t = 0$ and any other $2M$ time samples [Caratheodory, 1907, 1911]. Similar results were obtained by Feng, Bresler and Venkataramani for multiband signals in the 1990's in [Feng, 1996; Bresler, 1996; Venkataramani, 1998] and by Vetterli, Marziliano, Blu and Maravic for signals with a finite number of degrees of freedom in the 2000's in [Vetterli, 2002; Maravic, 2005]. Finally, in [Candès, 2006b,d,c,e,a; Donoho, 2006], Candès, Romberg, Tao and Donoho have shown that with the knowledge of the sparsity of the signal it can be exactly recovered from a small set of linear, non-adaptive, compressive measurements, which essentially laid the foundation of the CS field.

Since then, CS has been applied for a wide range of applications such as *medical imaging* [Vasanawala, 2010; Trzasko, 2009; Küstner, 2016], *compressed imaging* [Duarte, 2008; Romberg, 2008] and *spectroscopy* [Arce, 2014], *sub-Nyquist sampling* architectures [Tropp, 2010b; Mishali, 2010, 2011], *channel sensing* [Berger, 2010b; Bajwa, 2010], as well as radar [Baraniuk, 2007b; Herman, 2009; Berger, 2008; Yu, 2010; Anitori, 2013; Bajwa, 2011; Bar-Ilan, 2014]. For radar, most publications motivate the application of CS by two significant improvements: a super-resolution parameter estimation and a compressed data acquisition at a sub-Nyquist rate. Whereas some of these works study the application of sub-Nyquist rate ADCs and super-resolution distance estimation [Baraniuk, 2007b; Herman, 2009; Bajwa, 2011; Bar-Ilan, 2014], others apply CS on the spatial domain — for reduction of number of spatial channels for MIMO radar and sparsity based DOA estimation [Berger, 2008; Yu, 2010]. These concepts typically consider conventional frequency estimation methods for Doppler processing, while other concepts based on subsampling in slow-time and CS based Doppler processing are also known [Lutz, 2014; Cohen, 2015, 2016a].

Since the radar signals are frequency sparse and the processing in all radar dimensions is based on frequency estimation, the application of CS for frequency sparse signals is of high relevance for radar [Duarte, 2010; Baraniuk, 2010; Duarte, 2011, 2013; Gilbert, 2008]. The latter has certain peculiarities such as loss of sparsity in case of spectral leakage, off-grid frequency components, etc. Therefore, some enhancement and adjustment of CS methods, such as assumption of a certain signal structure in addition to sparsity [Duarte, 2011; Baraniuk, 2010], interpolation [Duarte, 2013], etc., were introduced. These ideas served as basis for the SIMFE algorithm we present in Section 4.5.3.

4.5.2. Fundamentals of Compressed Sensing

Below we give a brief intuitive overview of some fundamental principles behind CS. See [Eldar, 2012; Baraniuk, 2007a; Candès, 2008] for more detailed description of CS fundamentals. The principles presented in this section will be described for complex-valued, discrete and finite-dimensional signals, as the radar measurement signal is typically of this kind.

Mathematical preliminaries

We will view the N -samples long signal of interest \underline{x} as a vector in a complex N -dimensional space \mathbb{C}^N . An important measure to describe vectors living in an N -dimensional *vector space* is their ℓ_p *norm*. It is defined for $p \in [1, \infty]$ as

$$\|\underline{x}\|_p = \begin{cases} (\sum_{n=1}^N |x_n|^p)^{\frac{1}{p}} & \text{for } p \in [1, \infty), \\ \max_{n \in [1, N]} |x_n| & \text{for } p = \infty, \end{cases} \quad (4.10)$$

and represents a measure of the signal strength [Davenport, 2010]. It is also used to describe how close two signal vectors in the sense of a certain ℓ_p norm are. An illustration that demonstrates the notion of the norm in \mathbb{R}^2 Euclidean space is given in Fig. 4.12, where the point on the one-dimensional space X with the minimum ℓ_p norm is to be found. This can be imagined as an ℓ_p shape growing from the origin of the coordinate axis until it intersects with the subspace X . The point of intersection \hat{x} will be the point of subspace X with the minimum ℓ_p norm. Clearly, depending on p , the properties of the norm change considerably. In case of $p < 1$, the definition of the norm in (4.10) does not satisfy the triangle inequality, i.e. the norm is non-convex, and

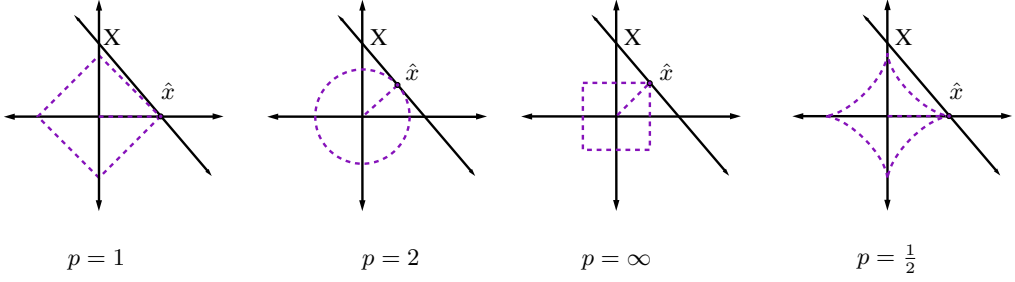


Figure 4.12.: Search of the point $\hat{x} \in X$ in \mathbb{R}^2 with the minimal ℓ_p norm, $p = 1, 2, \infty$, and ℓ_p quasinorm, $p = 0.5$

thus it is a quasinorm. Interestingly, from Fig. 4.12 it can be observed that the norms that are not strictly convex ($p \leq 1$) yield a solution on one of the axes, i.e. a sparse solution. Another notion related both to the norm and sparse signals is the ℓ_0 norm denoted as $\|\underline{x}\|_0 = |\text{supp}(\underline{x})|$, where $\text{supp}(\underline{x}) = \{i : x_i \neq 0\}$ denotes the *support* of \underline{x} , and $|\text{supp}(\underline{x})|$ denotes the *cardinality* of $\text{supp}(\underline{x})$. In other words, $\|\cdot\|_0$ denotes the number of non-zero elements in a vector, and thus is a measure of its sparsity.

Another concept important for CS is the notion of bases. A set of linearly independent vectors $\{\underline{\psi}_n\}_{n=1}^N$ is called a *basis* for an N -dimensional vector space if the vectors in the set span that vector space. This implies that each vector in the space can be uniquely represented as a linear combination of these basis vectors. That is, for any vector \underline{x} in the N -dimensional space there exists a unique length- N vector $\underline{\alpha}$ such that

$$\underline{x} = \underline{\Psi} \underline{\alpha} \quad (4.11)$$

where the $N \times N$ matrix $\underline{\Psi}$ with the columns $\{\underline{\psi}_n\}_{n=1}^N$ denotes the basis. An important special case of a basis is an orthonormal basis, i.e. a basis with unit vectors (columns of $\underline{\Psi}$) that are orthogonal to each other. The advantage of orthonormal bases is that the coefficients $\underline{\alpha}$ can be easily calculated by $\underline{\alpha} = \underline{\Psi}^T \underline{x}$. The importance of vector bases for CS is that many low dimensional signals are not sparse in their signal domain, but have a sparse representation in some other basis.

The concept of basis can be further generalized to arbitrary sized sets of possibly linearly dependent vectors called frames [Eldar, 2012]. That is, a *frame* is a set of vectors $\{\underline{\phi}_n\}_{n=1}^N$ in M -dimensional space, $M < N$, that corresponds to a matrix $\underline{\Phi} \in \mathbb{C}^{M \times N}$. The rows of the frame $\underline{\Phi}$ are linearly independent. For a given signal $\underline{y} \in \mathbb{C}^M$, there exist infinitely many vectors \underline{x} such that $\underline{y} = \underline{\Phi} \underline{x}$. The notion of frame is important for CS and sparse approximation literature, since the matrix that maps the compressed measurement to the signal of interest represents a frame. This matrix is often referred to as *overcomplete dictionary*.

We will use the following notation for the remainder of this chapter. $\mathcal{N}(\underline{\Phi})$ denotes the *nullspace* of the matrix $\underline{\Phi}$. For a set Ω , $|\Omega|$ denotes its cardinality. By $\underline{\Phi}_\Omega$ we denote the $M \times |\Omega|$ matrix obtained by choosing columns of $\underline{\Phi}$ indexed by the set Ω . Based on the definition of frame, we will assume whenever $|\Omega| \leq M$, $\underline{\Phi}_\Omega$ is full rank, and we denote the *Moore-Penrose pseudoinverse* of the latter by $\underline{\Phi}_\Omega^+ = (\underline{\Phi}_\Omega^H \underline{\Phi}_\Omega)^{-1} \underline{\Phi}_\Omega^H$.

Sparse signals

As discussed previously, it is often useful to model signals as vectors living in a certain vector space. However, this modeling generally implies that any arbitrary vector can be a valid signal, whereas the real world signals often obey a certain model. This means, for many classes of signals not all possible vectors represent a valid signal. Thus, the model of the signal contains a priori knowledge about the signal structure that helps to limit meaningfully the vector space the signal resides in. Incorporating the model of a particular signal of interest into its acquisition and processing can increase the effectiveness of the system.

One common signal model that has gained significant attention over the past few years is the signal sparsity. Many real world signals in different fields have a low-dimensional representation that preserves most of the signal information. For instance, image signals are sparse in the wavelet domain, where they have few dominant components and the remaining ones are close to zero. In a certain way the same applies to radar signals: the number of reflections is commonly much smaller than the number of signal samples. Thus, the radar signal is typically sparse in the domains where reflections are compressed into a pulse.

A signal $\underline{x} \in \mathbb{C}^N$ is said to be K -sparse when it has at most K non-zero elements, i.e. $\|\underline{x}\|_0 \leq K$. The same applies for signals that are not sparse by themselves but a basis Ψ exists such that $\underline{x} = \Psi \underline{\alpha}$ and $\|\underline{\alpha}\|_0 \leq K$. Thus, we will refer to \underline{x} as K -sparse bearing in mind that it is sparse in some basis. We further denote the set of all K -sparse signals as

$$\Sigma_K = \{\underline{x} = \Psi \underline{\alpha} : \|\underline{\alpha}\|_0 \leq K\}. \quad (4.12)$$

Signals that have K dominant coefficients and $(N - K)$ small coefficients are said to be compressible and can be approximated to a K -sparse signal by a best K -terms approximation, i.e. thresholding the remaining $(N - K)$ coefficients.

Compressed Sensing

At the core of CS is the compression of signals that have a sparse or compressible representation already at the sensing phase, potentially reducing the cost of signal acquisition [Davenport, 2010]. The sensing system acquires M samples by linear projection of the signal of interest $\underline{x} \in \mathbb{C}^N$ through the sensing matrix $\Phi \in \mathbb{C}^{M \times N}$:

$$\underline{y} = \Phi \underline{x} = \Phi \Psi \underline{\alpha}, \quad (4.13)$$

where $\underline{y} \in \mathbb{C}^M$ is the compressed measurement vector. The matrix Φ performs a dimensionality reduction, i.e. for N much larger than M , it maps the space \mathbb{C}^N of the signal of interest into the space \mathbb{C}^M of the measurement. This means that the problem of recovery of the vector \underline{x} from the measurement \underline{y} is ill conditioned, i.e. infinite number of solutions $\hat{\underline{x}}$ such that $\underline{y} = \Phi \hat{\underline{x}}$ exist. Nonetheless, CS has shown to enable a signal recovery based on the knowledge that \underline{x} lives in or near Σ_K . We will focus on the case $\underline{x} \in \Sigma_K$, since we can always reduce the problem to this by substituting the measurement matrix Φ by $\tilde{\Phi} = \Phi \Psi$. The problem of signal recovery consists of designing *i)* a measurement matrix Φ that preserves the entire information during the *dimensionality reduction*, and *ii)* a recovery algorithm that is able to reconstruct the signal based on the sparsity constraint from an underdetermined equation system. Before we discuss the reconstruction algorithms, let us examine the necessary conditions for the measurement matrix to satisfy our requirements.

In order to be able to recover all sparse signals \underline{x} from the measurement $\Phi \underline{x}$, for any two distinct K -sparse vectors $\underline{x}, \underline{x}' \in \Sigma_K$, it should hold that $\Phi \underline{x} \neq \Phi \underline{x}'$, since otherwise \underline{x} and \underline{x}' are projected into the same measurement \underline{y} and cannot be distinguished. In the latter case $\Phi \underline{x} = \Phi \underline{x}'$, i.e. $\Phi(\underline{x} - \underline{x}') = \underline{0}$, the vector $(\underline{x} - \underline{x}') \in \Sigma_{2K}$ also belongs to $\mathcal{N}(\Phi)$. Thus, the matrix Φ uniquely represents every vector $\underline{x} \in \Sigma_K$ if and only if no vector from Σ_{2K} belongs to $\mathcal{N}(\Phi)$. This condition guarantees that a compressed measurement \underline{y} contains the necessary information for an unambiguous recovery of \underline{x} . That is, in case the signal support $\Omega = \text{supp}(\underline{x})$ is known, a recovery of the signal by $\underline{x} = \Phi_{\Omega}^+ \underline{y}$ is possible. In this case the matrix Φ is said to satisfy the *nullspace property* (NSP) of the order K .

Whereas the NSP guarantees that the recovery of the signal is possible, it implies that the measurement is exact, i.e. contains no noise or other inaccuracies. Thus, for real world applications more practical conditions are required. Such a condition on isometry of the matrices Φ was introduced by Candès and Tao in [Candès, 2005]. A matrix Φ is said to satisfy the *restricted isometry property* (RIP) of order K if a $\sigma_K \in (0,1)$ exists such that

$$(1 - \sigma_K) \|\underline{x}\|_2^2 \leq \|\Phi \underline{x}\|_2^2 \leq (1 + \sigma_K) \|\underline{x}\|_2^2 \quad (4.14)$$

for all $\underline{x} \in \Sigma_K$ [Candès, 2005].

In words, (4.14) can be interpreted as a condition that guarantees that a matrix Φ satisfying a RIP of order K approximately preserves the distances between any pair of K -sparse vectors [Eldar, 2012]. In presence of noise this means that up to a certain amount of noise the stable recovery of any K -sparse signal from the compressed measurement is possible. Clearly, this property has a significant importance for CS, since it provides theoretical guarantees for sparse signal recovery in the presence of noise.

Whereas RIP plays an important role for many recovery algorithms, it is generally difficult to verify whether for a particular matrix Φ it holds. To ensure this, all possible combinations of K columns of the sensing matrix Φ have to be verified to satisfy RIP. This might be very challenging, especially for large matrices. Fortunately, for some types of matrices RIP has been proven to hold with a very high probability. For example, sufficiently large random matrices with i.i.d. elements have been shown to satisfy RIP with a very high probability [Candès, 2006d].

Recovery algorithms

The problem of signal recovery is to reconstruct the length- N and K -sparse vector \underline{x} from the length- M compressed measurement vector \underline{y} and the measurement matrix Φ . Since $M < N$, there are infinitely many vectors \underline{x}' such that $\underline{y} = \Phi \underline{x}'$. In other words, for any vector $\underline{z} \in \mathcal{N}(\Phi)$, it holds $\Phi \underline{z} = \underline{0}$, and thus $\underline{y} = \Phi(\underline{x}' + \underline{z})$. Consequently, the recovery problem can be formulated as a search of the sparsest vector in the $(N - M)$ -dimensional translated nullspace $\mathcal{H} = \mathcal{N}(\Phi) + \underline{z}$ [Baraniuk, 2007a].

The sparse recovery problem can be formulated as an optimization problem of minimum ℓ_0 norm reconstruction:

$$\hat{\underline{x}} = \arg \min_{\underline{x}} \|\underline{x}\|_0 \quad \text{subject to} \quad \Phi \underline{x} = \underline{y}, \quad (4.15)$$

which returns the sparsest solution $\hat{\underline{x}}$ that suits to the measurement \underline{y} . Unfortunately, this is a nonconvex optimization problem, which in the general case is NP-hard, and solving it requires an exhaustive search through all $\binom{N}{K}$ possible sets. This becomes infeasible even for moderate values of N and K .

Since the problem of optimization in (4.15) is the nonconvex ℓ_0 norm, one solution is the *convex relaxation* of the ℓ_0 norm to replace it with the ℓ_1 norm. Then, (4.15) can be written as

$$\hat{\underline{x}} = \arg \min_{\underline{x}} \|\underline{x}\|_1 \quad \text{subject to} \quad \Phi \underline{x} = \underline{y}. \quad (4.16)$$

The property of the ℓ_1 norm to exactly yield the sparsest solution has been known for decades [Beurling, 1938]. Fig. 4.12 illustrates this property in \mathbb{R}^2 space. This convex optimization problem is known as *basis pursuit* (BP) [Chen, 1998a]. A slightly different version of it considers noise and reformulates the constraint in (4.16) as $\|\Phi \underline{x} - \underline{y}\|_2 \leq \epsilon$ with ϵ setting a threshold of how much the solution may diverge from the measurement in the least squares sense. This method finds the sparsest solution that approximately fits to the measurement and is known as *basis pursuit de-noising* (BPDN) [Chen, 1998a]. It can be formulated as an unconstrained optimization problem by

$$\hat{\underline{x}} = \arg \min_{\underline{x}} \frac{1}{2} \|\underline{y} - \Phi \underline{x}\|_2^2 + \lambda \|\underline{x}\|_1, \quad (4.17)$$

where λ is a regularization parameter typically unknown a priori. For a certain λ , the formulations in (4.16) and (4.17) yield the same solution. This formulation represents the problem as an *unconstrained convex optimization*, which can be solved using standard techniques such as gradient based methods or posed as a linear program and solved accordingly (see [Tropp, 2006; Figueiredo, 2007] and the references therein).

Another class of algorithms widely used for sparse recovery are the *greedy algorithms*. At the core of these recovery methods is the iterative approximation of the signal coefficients and support. Whereas some of these algorithms solely rely on iterative identification of the support, more advanced ones try to improve the estimate of the signal coefficients and/or support at each iteration based on the mismatch between the estimate and the measurement. These techniques often provide a practically good performance at feasible computational costs, contrary to the convex optimization methods that generally have a complexity about $\mathcal{O}(N^3)$ [Baraniuk, 2007a]. Some of these techniques even provide performance guarantees similar to the ones of ℓ_1 minimization [Eldar, 2012]. We refer the reader to [Tropp, 2010a; Eldar, 2012] and the references therein for an overview of the greedy algorithms. Below we briefly discuss one of the oldest and simplest greedy methods which many other greedy algorithms are based on — *orthogonal matching pursuit* (OMP) [Mallat, 1993; Pati, 1993].

OMP starts the evaluation by assigning the measurement to the residue vector $\underline{r}^{(0)} \leftarrow \underline{y}$, with “ \leftarrow ” denoting the assignment operator, and iterates until the desired sparse solution is found or another stopping criterion is met. On the first step of iterative evaluation, it finds the best approximation of the measurement with a single component by calculating a very rough estimate $\underline{h}^{(i)} = \Phi^T \underline{r}^{(i)}$ and taking the largest component of $\underline{h}^{(i)}$. The index of $\underline{h}^{(i)}$ is added to the support, after which a joint least squares estimate of the measurement for the signal components in the support is calculated. This estimate is then subtracted from the measurement signal, which yields the residue for the next iteration $\underline{r}^{(i+1)}$. The described process is repeated iteratively to identify the signal support, whereas the joint least squares estimation for all components in the support updates the signal coefficients at each iteration. The latter has the advantage that the impact of new components identified at each iteration on already detected ones is accounted for. The OMP algorithms is formally described in Algorithm 4.1, where the operator $\text{hard}(\underline{h}, k)$ denotes the hard thresholding of \underline{h} that keeps only the strongest k components and sets the rest to zero.

Algorithm 4.1 Orthogonal matching pursuit (OMP)

Input: Φ, y , stopping criterion
Initialization: $\underline{r}^{(0)} \leftarrow y, \underline{x}^{(0)} \leftarrow \underline{0}, \Omega^{(0)} \leftarrow \emptyset, i \leftarrow 0$
1: **while** not converged **do**
2: $\underline{h}^{(i)} \leftarrow \Phi^T \underline{r}^{(i)}$ ▷ Form a rough signal estimate
3: $\Omega^{(i+1)} \leftarrow \Omega^{(i)} \cup \text{supp}(\text{hard}(\underline{h}^{(i)}, 1))$ ▷ Identify and add to the support
4: $\underline{x}^{(i+1)} \leftarrow \Phi_{\Omega^{(i+1)}}^+ y$ ▷ Estimate the coefficients with least squares
5: $\underline{r}^{(i+1)} \leftarrow y - \Phi \underline{x}^{(i+1)}$ ▷ Update the residue
6: **end while**
Output: $\hat{\underline{x}} = \underline{x}^{(i)}$

We want to note that in some CS applications the actual recovery of the signal is not necessarily the aim — the task is rather to solve an inference problem, e.g. estimation of a certain parameter. For radar, we will be concerned with this kind of problem, and the task is essentially frequency estimation. These two problems are, however, very similar in their nature.

Structures beyond sparsity

In many applications, signals exhibit structure beyond what can be expressed by the sparsity model alone. Few examples for such signals are *a)* images, where the wavelet transform tends to cluster the dominant coefficients into a connected rooted subtree, *b)* applications such as surveillance as well as high-resolution radar where the coefficients might appear clustered together, *c)* applications where multiple sparse signals recorded simultaneously exhibit the same support, etc [Eldar, 2012]. It is apparent that this additional structure of the signal can be leveraged during the signal recovery. This can be done by restricting the allowed signal supports to a subset that corresponds to the subspaces in Σ_K which exhibit this structure. By doing so, sensing and recovery methods that are more tailored to the particular application at hand can be developed. The direction of CS that focuses on exploiting the additional structure of sparse signals is known as *structured compressed sensing* (SCS); for an overview of SCS please refer to [Duarte, 2011].

A modeling suitable for capturing the additional signal structure is the representation of the signal space as a union of subspaces. Specifically, let \underline{x} live in one of M possible subspaces $\mathcal{U}_1, \mathcal{U}_2, \dots, \mathcal{U}_M$, then the possible solution space is the union of M subspaces

$$\underline{x} \in \mathcal{U} = \bigcup_{i=1}^M \mathcal{U}_i. \quad (4.18)$$

This modeling allows more general signal structures than the sparse modeling $\underline{x} \in \Sigma_K$ alone. Furthermore, it allows an extension of the discussed concepts to infinite-dimensional representations such as continuous signals [Duarte, 2011]. Two of the simplest types of unions are the structured sparse supports that allow only \mathcal{U}_i subspaces out of all $\binom{N}{K}$ subspaces in $\underline{x} \in \Sigma_K$ [Baraniuk, 2010] and the sparse *union of subspaces* that enables modeling of a block sparsity [Eldar, 2010].

Sparse union models are also applicable for radar signals. One reason why such models are useful is that the radar signals are truly (frequency) sparse in the infinite-dimensional space, i.e. for infinitely long measurements. For a time-limited measurement signal, the signal sparsity is

affected by spectral leakage. This is an important constraint that leads to a coherence between the signal coefficients, which sparsity based processing methods have to account for. As we show in Section 4.5.3, by imposing an additional structure on the signal this issue can be partially compensated for. A further application for structured sparsity models is the multichannel estimation for MIMO radar. For MIMO radar with an aperture smaller than the distance resolution, the measurement vectors of multiple spatial channels have the same support, which leads to the *multiple measurement vector* (MMV) problem; for detail on the latter see [Eldar, 2012].

4.5.3. CS based Distance-Velocity Estimation⁸

As we discussed above, multiplexing of MIMO channels via non-equidistant interleaving schemes can be considered as a subsampling of the radar measurement signal. Inspired by the massive advances in the area of CS, we represent the distance-velocity estimation problem of OFDM-MIMO radar as a sparse estimation problem from compressed measurements. This problem, however, has some specific aspects to consider. First of all, since the detection is commonly performed on the distance-velocity radar image, our estimation task is generally multidimensional. That being said, the computational complexity of the sparse estimation algorithm should be conceivable. Furthermore, measurement signals from multiple spatial channels pose a kind of MMV problem and have to be meaningfully combined for a joint estimation. Finally, since we are dealing with time-limited measurements of frequency sparse signals, an important aspect to consider is the spectral leakage, as it affects the signal sparsity.

Below we present a new CS based multidimensional frequency estimation method we name SIMFE. The proposed method overcomes the limitations of the state-of-the-art CS algorithms both in performance and computational efficiency. Compared to the classical Fourier processing, SIMFE is superior regarding the detection of targets initially masked by sidelobes of more dominant ones. We show that the combination of SIMFE with non-equidistant interleaving schemes enables a high dynamic range in distance-velocity estimation, while maintaining the original unambiguous range and resolution both in distance and velocity for all spatial channels. We describe SIMFE applied to NeqSI multiplexed signals — the extension of it to NeqDySI is straightforward.

Sparse iterative multidimensional frequency estimation (SIMFE)

SIMFE is a multidimensional parameter estimation method designed for frequency sparse signals. To meet the specifics of the particular task at hand, it combines multiple ideas that contribute to its good performance in the task it is designed for. Nevertheless, both the method itself as well as the individual ideas it comprises are applicable for other similar frequency estimation tasks, e.g. other radar problems, channel sensing, etc. In our setup, SIMFE performs a 2D off-grid parameter estimation incorporating off-grid *pseudo-dictionaries* and integrating windowed measurements from multiple channels. Thus, SIMFE substitutes the detection, frequency estimation and frequency interpolation of the conventional radar signal processing.

The OMP algorithm served as a basis for our method. The reason for this choice is its computational efficiency in comparison to, e.g., convex optimization methods. This is critical in our real-time application, especially due to the multidimensional evaluation. We further increase the

⁸ Contributions presented in this section were partially reported in [Hakobyan, 2017b]. Some of author's own formulations from [Hakobyan, 2017b] are adopted in this section.

computational efficiency by formulating the problem such that the CS dictionary is decomposed into two independent dictionaries for columns and rows of the measurement matrix. Note that this is possible only if the signals of the measurement matrix can be decomposed into a product of row and column vectors. This avoids the need for a prohibitively large dictionary, as commonly used for multidimensional CS applications (e.g. [Herman, 2009; Zhang, 2012; Destino, 2016; Steffens, 2016]). This, in turn, enables efficient CS processing for large measurement matrices needed in many real-world applications. Furthermore, since the dictionary decomposition leads to two DFT dictionaries, a further increase in computational efficiency is achieved by the use of 2D-FFTs for transforms between the measurement space and sparse representation instead of large matrix multiplications as in [Herman, 2009; Zhang, 2012; Destino, 2016; Steffens, 2016]. Note that parallel to this work the idea of splitting the CS dictionary for computationally efficient extension of OMP algorithm to 2D in application to pulse-Doppler radar has been proposed in [Cohen, 2015, 2016a].

In CS terms, the distance-velocity estimation problem from non-equidistantly interleaved OFDM-MIMO radar can be represented in the following form:

$$\mathbf{z}_\nu = \mathbf{\Phi}_\nu \mathbf{F}_{N_c} \mathbf{Z}_\nu \mathbf{F}_{N_{\text{sym}}}^{-1}, \quad 1 \leq \nu \leq N_{\text{virt}}, \quad (4.19)$$

where \mathbf{Z}_ν is the sparse representation of the measurement signal in the distance-velocity plane, i.e. the radar image of the ν -th spatial channel (as $\mathbf{z}_{d,v}$ in (3.22)), $\mathbf{\Psi}_d = \mathbf{F}$ and $\mathbf{\Psi}_v = \mathbf{F}^{-1}$ are the DFT dictionaries or bases in distance and velocity dimensions, respectively, $\mathbf{\Phi}_\nu$ is the sensing matrix (as the selection matrix $\mathbf{\Phi}_p$ in (4.1)), and \mathbf{z}_ν is the subsampled measurement matrix of the ν -th spatial channel. $N_{\text{virt}} = N_{\text{Tx}} \times N_{\text{Rx}}$ is the number of virtual antennas of the MIMO radar, and the index of the Tx-Rx antenna pair “ p, q ” is replaced by the corresponding spatial channel index “ ν ”. The task is to estimate the frequency components in \mathbf{Z}_ν .

A fundamental difficulty of CS application on frequency sparse signals is that the sparse representation of the signal (i.e. \mathbf{Z}_ν in (4.19)) is convolved with a certain function (e.g. sinc function) due to the finite time duration of the measurement. In fact, this leads to a non-sparse spectrum due to the spectral leakage, even though the measured signal is frequency sparse. This problem has been identified in some works [Duarte, 2013, 2011], where additional measures and adjustments of CS algorithms were considered. Specifically, in [Duarte, 2013] a peak interpolation is integrated into the iterative hard thresholding algorithm to better estimate off-grid frequency components and treat the spectral leakage. We develop this idea further by incorporating some measures such as off-grid estimation, off-grid pseudo-dictionaries and windowing into our algorithm.

The following steps are performed at each iteration of the algorithm: *a)* Estimation of the dominant frequency component, *b)* peak interpolation for refined, off-grid frequency estimation, *c)* update of the support, *d)* residue update. The algorithm operates iteratively until all dominant frequency components are found. For initialization, each data matrix \mathbf{z}_ν from (4.19) is windowed and assigned as an initial value to the residue \mathbf{R}_ν of the ν -th spatial channel:

$$\mathbf{z}'_\nu = \mathbf{w}_{N_c} \mathbf{z}_\nu \mathbf{w}_{N_{\text{sym}}}, \quad \mathbf{R}_\nu \leftarrow \mathbf{z}'_\nu, \quad (4.20)$$

where the diagonal window matrices \mathbf{w}_{N_c} and $\mathbf{w}_{N_{\text{sym}}}$ are defined as in Chapter 3. Since in slow-time, i.e. over OFDM symbols, equidistant measurements are obtained, it is advantageous to window the rows of the matrix \mathbf{z}_ν with a suitable window $\mathbf{w}_{N_{\text{sym}}}$ to suppress sidelobes in the velocity dimension. The window \mathbf{w}_{N_c} in the distance dimension is chosen according to the guidelines in Section 4.4.

First, a 2D-FFT is performed on the residue \mathbf{R}_ν of each channel:

$$\mathbf{Z}_\nu \leftarrow \mathbf{F}_{N_c}^{-1} \Phi_\nu \mathbf{R}_\nu \mathbf{F}_{N_{\text{sym}}} \quad (4.21)$$

For a joint multichannel estimation of the dominant frequency component, the 2D complex-valued matrices \mathbf{Z}_ν are then integrated non-coherently:

$$\mathbf{Z}_{\text{NCI}} \leftarrow \sum_{\nu=1}^{N_{\text{virt}}} |\mathbf{Z}_\nu|^2. \quad (4.22)$$

Then, the dominant component of \mathbf{Z}_{NCI} has to be found:

$$\{\tilde{\Omega}_d^{(i)}, \tilde{\Omega}_v^{(i)}\} \leftarrow \arg \max_{k,l} \mathbf{Z}_{\text{NCI}}(k,l), \quad (4.23)$$

where the index i indicates the current iteration, k and $\tilde{\Omega}_d^{(i)}$ denote the distance index and that of the dominant component, and similarly l and $\tilde{\Omega}_v^{(i)}$ denote the same for the velocity. Next, the row and column indexes of the detected dominant component $\tilde{\Omega}_d^{(i)}$ and $\tilde{\Omega}_v^{(i)}$ are used for a precise off-grid frequency estimation via an interpolation. This step is essential, since the frequencies in the radar signal are typically not on the FFT grid, and a refined off-grid estimation improves the estimation accuracy as well as minimizes the residue for the next iteration. As we will show in the next section, the accuracy of the interpolation algorithm has a significant influence on the overall performance. In our work, we use a Kaiser window based 3rd order Taylor series interpolation (a version of the method in [Duda, 2011]). The precise position $\{\Omega_d^{(i)}, \Omega_v^{(i)}\}$ of the peak obtained via interpolation is added to the support, i.e. to the set of already detected off-grid frequencies:

$$\Omega_d \leftarrow \Omega_d \cup \Omega_d^{(i)}, \quad \Omega_v \leftarrow \Omega_v \cup \Omega_v^{(i)}. \quad (4.24)$$

Next, new pseudo-dictionaries containing i complex exponentials of the detected frequencies are created in (4.25), and a least squares estimation of the complex amplitudes of those frequencies is performed for each channel in (4.26):

$$\Psi_{\Omega_d} \leftarrow \left[w_{N_c}(n) e^{-j \frac{2\pi}{N_c} \Omega_d(k)n} \right]_{\substack{n=0 \dots N_c-1 \\ k=1 \dots i}} \in \mathbb{C}^{N_c \times i}, \quad (4.25)$$

$$\Psi_{\Omega_v} \leftarrow \left[w_{N_{\text{sym}}}(n) e^{j \frac{2\pi}{N_{\text{sym}}} \Omega_v(k)n} \right]_{\substack{n=0 \dots N_{\text{sym}}-1 \\ k=1 \dots i}} \in \mathbb{C}^{i \times N_{\text{sym}}},$$

$$\mathbf{A}_{\Omega_\nu} \leftarrow (\Phi_\nu \Psi_{\Omega_d})^+ \mathbf{z}'_\nu \Psi_{\Omega_v}^+ \in \mathbb{C}^{i \times i}. \quad (4.26)$$

Note that the least squares amplitude estimation in (4.26) is carried out with the windowed data. Combined with the windowed estimation of the support in (4.20)-(4.21), this limits the influence of the targets on each other, improving generally the estimation performance. This is especially advantageous in configurations where in one dimension uniformly sampled measurements are obtained, e.g. the velocity dimension for NeqSI. Finally, a two-dimensional complex exponential is created for each channel with the complex amplitudes \mathbf{A}_{Ω_ν} from (4.26) and subtracted from the measurement matrix of that channel to update the residue:

$$\mathbf{R}_\nu \leftarrow \mathbf{z}'_\nu - \Psi_{\Omega_d} \mathbf{A}_{\Omega_\nu} \Psi_{\Omega_v}. \quad (4.27)$$

By subtracting the detected 2D complex exponentials from the measurement in each channel, not only the detected peaks, but also the sidelobes generated by these frequencies are canceled out.

This enables a better detection of the remaining weaker frequencies during the next iterations. A similar subtraction is performed in many iterative algorithms such as CLEAN [Tsao, 1988], RELAX [Li, 1996] and Doppler focusing CS recovery [Bar-Ilan, 2014]. The steps (4.21)-(4.27) are performed iteratively, until all frequencies in the measurement data are detected. In fact, the basic idea of such iterative processing is also known from Gram-Schmidt orthogonalization, which many works in digital communication apply for successive interference cancellation [da Silva, 19.04.2016].

Since the estimation of complex amplitudes \mathbf{A}_{Ω_ν} in (4.26) is done for all detected frequencies jointly, the influence of these on each other is accounted for by SIMFE during the amplitude estimation. These amplitude estimates are updated at each iteration, analogous to OMP.

As other iterative algorithms, SIMFE requires the number of targets. Typically the true number of targets is unknown, but often the maximum number of expected targets is known empirically. Thus, the number of targets can be set higher than the true number, and the detected ghost targets can be later discarded during DOA estimation. Alternatively, SIMFE can perform an iterative processing until the residue energy is reduced below a certain threshold, i.e. until all significant components have been found. A further, more advanced approach would be to incorporate a simultaneous order estimation similar to Akaike information criterion (AIC) or Bayesian information criterion (BIC), i.e. introduce an objective function whose maximum or minimum returns the order estimate (see [Stoica, 2004] and the references therein). We consider such methods for model order selection with SIMFE out of scope of this thesis. The SIMFE algorithm is summarized in Algorithm 4.2.

Algorithm 4.2 Sparse iterative multidimensional frequency estimation (SIMFE)

Input: measurement matrices \mathbf{z}_ν , number of targets K , window functions \underline{w}_{N_c} and $\underline{w}_{N_{\text{sym}}}$, sensing matrices Φ_ν

Initialization: $\mathbf{w} = \underline{w}_{N_c} \cdot \underline{w}_{N_{\text{sym}}}^T$, $\mathbf{z}'_\nu = \mathbf{z}_\nu \odot \mathbf{w}$, $\mathbf{R}_\nu^{(0)} \leftarrow \mathbf{z}'_\nu$, $\nu \in [1, N_{\text{virt}}]$, $\Omega_d \leftarrow \emptyset$, $\Omega_v \leftarrow \emptyset$

- 1: **for** $i = 1, \dots, K$ **do**
- 2: $\mathbf{Z}_\nu^{(i)} \leftarrow \mathbf{F}_{N_c}^{-1} \Phi_\nu \mathbf{R}_\nu^{(i-1)} \mathbf{F}_{N_{\text{sym}}}$ ▷ Rough signal estimate
- 3: $\mathbf{Z}_{\text{NCI}}^{(i)} \leftarrow \sum_{\nu=1}^{N_{\text{virt}}} |\mathbf{Z}_\nu^{(i)}|^2$ ▷ Non-coherent integration
- 4: $\{\tilde{\Omega}_d^{(i)}, \tilde{\Omega}_v^{(i)}\} \leftarrow \arg \max (\mathbf{Z}_{\text{NCI}}^{(i)})$ ▷ Search of the dominant component
- 5: $\{\Omega_d^{(i)}, \Omega_v^{(i)}\} \leftarrow \mathbb{T}(\mathbf{Z}_{\text{NCI}}^{(i)}, \tilde{\Omega}_d^{(i)}, \tilde{\Omega}_v^{(i)}, \underline{w}_{N_c}, \underline{w}_{N_{\text{sym}}})$ ▷ Interpolation algorithm
- 6: $\Omega_d \leftarrow \Omega_d \cup \Omega_d^{(i)}, \quad \Omega_v \leftarrow \Omega_v \cup \Omega_v^{(i)}$ ▷ Support update
- 7: $\Psi_{\Omega_d}^{(i)} \leftarrow \mathbb{D}(\Omega_d, \underline{w}_{N_c}), \quad \Psi_{\Omega_v}^{(i)} \leftarrow \mathbb{D}(\Omega_v, \underline{w}_{N_{\text{sym}}})$ ▷ Pseudo- dictionaries
- 8: $\mathbf{A}_{\Omega_\nu}^{(i)} \leftarrow (\Phi_\nu \Psi_{\Omega_d}^{(i)} + \mathbf{z}'_\nu (\Psi_{\Omega_v}^{(i)})^+)$ ▷ Least squares amplitude estimate
- 9: $\mathbf{R}_\nu \leftarrow \mathbf{z}'_\nu - \Psi_{\Omega_d}^{(i)} \mathbf{A}_{\Omega_\nu}^{(i)} \Psi_{\Omega_v}^{(i)}$ ▷ Residue update
- 10: **end for**

Output: Supports Ω_d and Ω_v , complex amplitudes $\mathbf{A}_{\Omega_\nu}^{(i)}$

Note that SIMFE solves the MMV problem by combining the measurements from all spatial channels via NCI for a joint estimation of frequencies, i.e. support. The estimation of signal coefficients, however, is done for each channel individually.

Extension of SIMFE with structured sparsity model

As for most CS algorithms, the practical realization of SIMFE might require additional adjustments to the application at hand [Duarte, 2011] in order to meet the hardware-specific demands and to achieve the desirable performance. Two challenges for SIMFE in practice are the presence of highly correlated frequency components and the mismatch between the frequencies in different spatial channels. The first issue appears when reflections are present whose distance and velocity difference is smaller than the distance and velocity resolution of the radar. In this case, the iterative evaluation will typically process the sum of these reflections as a single reflection, since they cannot be resolved. Thus, the iterative evaluation will approximate the highly correlated frequency components by a single frequency, which can lead to a higher residue left after subtraction. The second effect might occur due to different path lengths at different channels of the radar front-end, or for an aperture size larger than the distance resolution. Since such effects are not modeled by the proposed sparse iterative processing, both issues might affect the estimation performance in terms of dynamic range.

To cope with the described issues, we apply the idea of structured sparsity [Duarte, 2013] on the SIMFE algorithm. Specifically, we set a constraint of limited mutual coherence between the frequencies in the support. That is, if a certain frequency is added to the support, the range of correlated frequencies is excluded from the space of possible solutions. Mathematically this can be expressed as [Duarte, 2013]:

$$\mathcal{T}_{\text{SCS}} = \left\{ \sum_{k=1}^K a_k \underline{e}(d_k \Delta) \quad \text{subject to} \quad d_k \in \{0, \dots, N-1\}, \right. \\ \left. |\langle \underline{e}(d_k \Delta), \underline{e}(d_j \Delta) \rangle| \leq \chi, 1 \leq k \neq j \leq K \right\}, \quad (4.28)$$

where

$$\underline{e}(\omega) = \frac{1}{\sqrt{N}} [1, e^{j\omega}, e^{j2\omega}, \dots, e^{j\omega(N-1)}]^T, \quad (4.29)$$

\mathcal{T}_{SCS} is the structured sparse signal, $\Delta = 2\pi/N$, N is the number of samples, K is the number of frequencies, d_k is the k -th frequency, $\langle \cdot, \cdot \rangle$ is the inner product of two vectors, and χ is the maximal allowed mutual coherence between the frequencies in the signal. Imposing this signal model on the iterative processing, solutions that contain linear combinations only of incoherent frequencies can be obtained, since the solution space is restricted to only incoherent subspaces. This sets a limit on the resolution, while improving the iterative processing performance in terms of dynamic range.

We adjust the proposed SIMFE algorithm with this assumption, which can be formulated as an additional step:

$$\forall k \in [0, N_c) \wedge l \in [0, N_{\text{sym}}), \quad \text{if } \mathbf{Z}_{\text{SCS}}(k, l) > \chi, \\ \text{then } \mathbf{Z}_{\text{NCI}}(k, l) = 0, \quad \text{for } \mathbf{Z}_{\text{SCS}} = \mathbf{F}_{N_c} \mathbf{\Psi}_{\Omega_d} \mathbf{\Psi}_{\Omega_v} \mathbf{F}_{N_{\text{sym}}}^{-1}. \quad (4.30)$$

In words, for all frequencies in the support $\{\Omega_d, \Omega_v\}$, the coherent sets of frequencies in the sparse representation \mathbf{Z}_{NCI} are discarded. To incorporate this model into SIMFE, this additional step in (4.30) has to be included after (4.22).

Computationally efficient realization

As mentioned, SIMFE achieves a high computational efficiency through splitting the CS dictionary into two independent dictionaries and application of FFTs and IFFTs for transforms between the measurement space and sparse representation instead of large matrix multiplications. Nevertheless, its realization in a straightforward manner might still be challenging for real-time implementation in automotive applications due to the computationally expensive transforms between the measurement space and sparse representation at each iteration step. To improve the computational efficiency, a realization is required that bypasses these steps.

To achieve this, the subtraction in (4.27) for the residue update can be performed in the sparse domain, i.e. directly from the radar image \mathbf{Z}_ν . This implies that the residue \mathbf{R}_ν itself is defined in the sparse domain. Accordingly, it has to be initialized with the radar images: $\mathbf{R}_\nu \leftarrow \mathbf{Z}_\nu$, with $\mathbf{Z}_\nu = \mathbf{F}_{N_c}^{-1} \Phi_\nu \mathbf{z}'_\nu \mathbf{F}_{N_{\text{sym}}}$. In this setup, for the residue update in (4.27) the signal to be subtracted has to be transformed to the sparse domain:

$$\mathbf{R}_\nu \leftarrow \mathbf{Z}_\nu - \mathbf{F}_{N_c}^{-1} \Phi_\nu (\Psi_{\Omega_d} \mathbf{A}_{\Omega_\nu} \Psi_{\Omega_v}) \mathbf{F}_{N_{\text{sym}}} \mathbf{F}_{N_{\text{sym}}} \mathbf{F}_{N_c} \mathbf{R}_\nu. \quad (4.31)$$

Now, the transform to the sparse domain in (4.31) can be rewritten in a more efficient form as $(\mathbf{F}_{N_c}^{-1} \Phi_\nu \Psi_{\Omega_d}) \mathbf{A}_{\Omega_\nu} (\Psi_{\Omega_v} \mathbf{F}_{N_{\text{sym}}})$, i.e. the pseudo-dictionaries are first individually transformed to the sparse domain, and then the calculation of the signal to be subtracted is performed. This, in turn, can be efficiently implemented via FFTs and IFFTs. Furthermore, in case the signal kernel in sparse domain has a closed-form representation, the pseudo-dictionaries can be directly generated in the sparse domain, similar to the approach proposed for CLEAN algorithm in [Kulpa, 2008]. Given a window function with a closed-form frequency representation, this is the case in the velocity dimension, since equidistant samples are obtained. Also, provided that the window function is chosen such that the sidelobes in some dimension are suppressed below the noise floor, in this dimension the subtraction can be limited to the samples of the mainlobe only.

The described steps dramatically reduce the computational costs for SIMFE, since computationally expensive matrix multiplications with the large measurement matrix at each iteration are avoided. Instead, equivalent operations are performed on the pseudo-dictionaries which are of a significantly smaller size. This enables real-time implementation feasible for automotive radar — despite the large number of samples and multidimensional frequency estimation problem.

4.5.4. Simulative Analysis

To illustrate the performance of the presented method in combination with NeqSI multiplexing, simulations for four Tx antennas are presented below. As a baseline system the state-of-the-art EqSI approach is considered. The bandwidth of the OFDM radar is 1 GHz with $N_c = 2048$ subcarriers and $N_{\text{sym}} = 512$ symbols. The carrier frequency is $f_c = 77$ GHz. Kaiser windows with $\beta = 3.2$ and $\beta = 7.7$ are used for sidelobe suppression in the distance and velocity dimensions, respectively.

A five-target scenario with targets of different amplitudes is simulated (Table 4.2). Three targets (1,3,4) with considerable amplitude differences are placed in two neighboring velocity cells to show the performance in a challenging case. A white Gaussian noise with power of -10 dB is added to the received signal. The true number of targets is assumed to be known.

Fig. 4.13 shows the non-coherently integrated radar images for the EqSI and NeqSI schemes. The true targets as well as detections for NeqSI are depicted with a 20 dB amplitude offset to

make them visible for targets masked by sidelobes. An interleaving pattern optimized according to Section 4.4 is used for NeqSI.

Clearly, EqSI has grating lobes, which leads to multiple peaks in the distance estimation for a single target, i.e. ambiguities. In contrast, NeqSI enables a full unambiguous distance range, but leads to sidelobes in the distance dimension. This is treated with the help of SIMFE algorithm that is able to detect weak targets masked by sidelobes of more dominant ones (e.g. 3rd and 4th targets). Also targets with a low SNR such as the 5th target are properly detected. In this setup, SIMFE achieves a dynamic range above 50 dB due to its good noise characteristics and ability to handle the sidelobes due to subsampling. Thus, it complements NeqSI, enabling a full unambiguous range in distance estimation and compensating its drawback of reduced PSL.

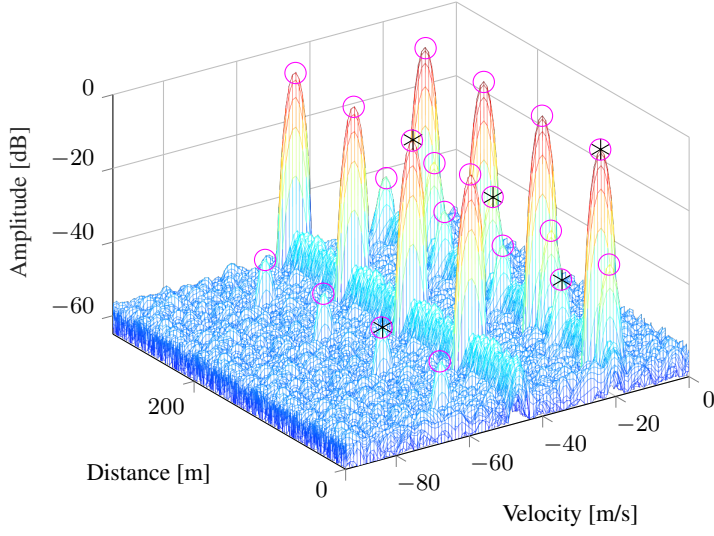
To evaluate the performance of SIMFE quantitatively, we analyze the residue after the detection and elimination of a single frequency component from the signal over different input SNR values (Fig. 4.14). The power ratio between the detected frequency peak and the highest residue peak after the subtraction of this frequency is denoted by the peak-to-residue ratio (PRR). To demonstrate the importance of the interpolation step, results are presented for different interpolation methods. The highest noise peak relative to the signal peak indicates the maximum achievable dynamic range. The results are obtained through 500 Monte-Carlo simulations.

Evidently, without an interpolation the residue after subtraction of the detected frequency is prohibitively high ($\text{PRR} \approx 7$ dB). This demonstrates the drawback of the original OMP algorithm for frequency estimation. The reason for a poor performance is the arbitrary frequencies in the measurement data that are out of the dictionary. Therefore, SIMFE includes an interpolation step and uses pseudo-dictionaries that contain specifically the detected off-grid frequencies. Using a Kaiser window based interpolation with the help of 2nd order Taylor series, a PRR of around 40 dB is achieved. With an interpolation based on 3rd order Taylor series approximation of the Kaiser window, a $\text{PRR} > 70$ dB is obtained for the input $\text{SNR} > 25$ dB. For $\text{SNR} < 25$ dB the residue is lower than the noise peaks, and thus negligible. Note that the lower the SNR, the higher the residue; but for lower SNR values the residue is smaller than the noise peaks and does not limit the dynamic range. For the further performance evaluation the interpolation with 3rd order Taylor series will be considered.

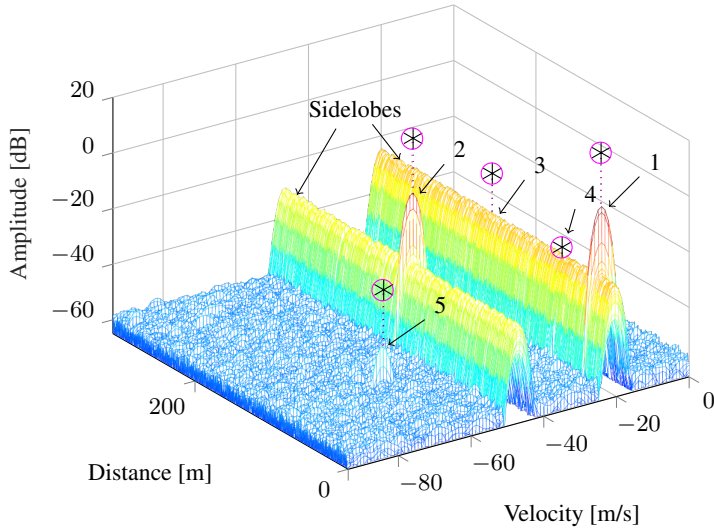
Analogously, Fig. 4.14b illustrates the residue after the subtraction of the detected single frequency for SIMFE with the structured sparsity model (S-SIMFE). The PRR of the latter is increased, since the highest residue is typically left at the position of the mainlobe of the detected frequency, i.e. at the frequencies correlated with the detected one. Since the structured sparsity model excludes this range of frequencies from evaluation, the PRR is further improved. This improvement is, however, achieved at the cost of imposing a resolution limit on frequency estimation. For practical applications, this represents a meaningful trade-off between the resolution and dynamic range, as we will show by means of measurements in Section 6.4. Thus, the following performance evaluation will incorporate the structured sparsity model.

Since in the velocity dimension equidistant measurements are obtained, a full dynamic range can be achieved in velocity estimation (analogous to FFT evaluation). Therefore, the further performance evaluation focuses on the distance estimation, i.e. on targets with different distances in the same velocity cell.

Next, we calculate the RMSE in distance estimation and the probability of detection (hit-rate, P_D) for 3 targets distributed randomly in the same velocity cell over different input SNR values. The



(a) EqSI



(b) NeqSI with SIMFE

Figure 4.13.: Performance of the proposed algorithm in 5 target scenario: * – true position, o – detection

Table 4.2.: Targets in simulation

Targets	1	2	3	4	5
SNR _{in} [dB]	10	5	-20	-30	-35
Distance [m]	18	140	160	60	90.3
Velocity [m/s]	-20.4	-46.5	-20.4	-22.29	-65

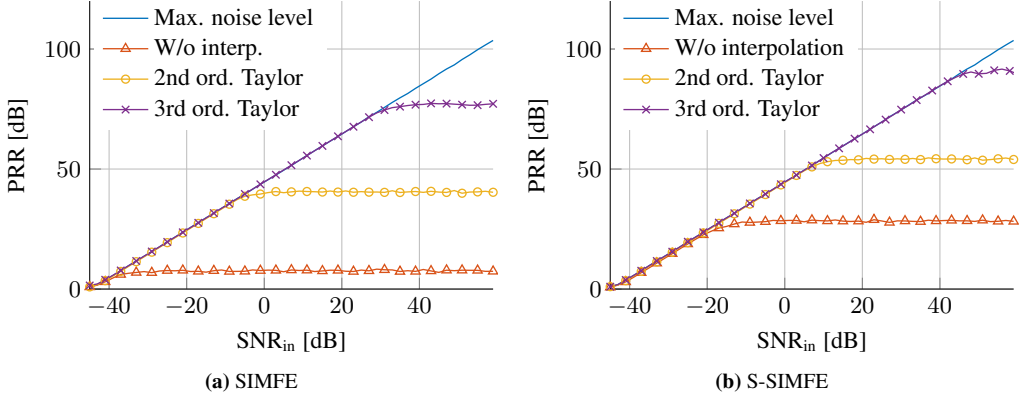


Figure 4.14.: Residue after subtraction of the detected frequency

targets have the same amplitude, and their mainlobes are not overlapping considerably. A target is assumed detected, i.e. a hit, if the detection is within one distance and velocity cell around the true target position. The distance RMSE is calculated only for the detected targets. It is normalized to the size of the distance cell and presented in logarithmic representation in Fig. 4.15. The results for the conventional 2D-FFT processing is shown as a reference. 500 Monte-Carlo simulations are performed for each SNR value to generate the results.

While both algorithms have a comparable probability of detection, S-SIMFE has a better performance for $\text{SNR}_{\text{in}} > 0$ dB. This is due to the fact that during the iterative evaluation the influence of the detected frequencies on each other is taken into account, whereas for FFT evaluation this is not the case.

Furthermore, we analyze the distance RMSE and P_D in presence of two targets with different amplitudes in a noiseless case, in order to investigate how critical the strong amplitude differences are for S-SIMFE (Fig. 4.15b). The results are shown for the weaker target. Evidently, S-SIMFE is able to handle strong amplitude differences. The threshold point (i.e. the point with near to 100 % detections) is achieved at an amplitude difference of about 85 dB. In contrast, the threshold point for FFT evaluation is at around 23 dB amplitude difference, since for higher amplitude differences the weaker target is masked by sidelobes. For FFT processing, also the RMSE is considerably higher, since the weaker target is influenced by the sidelobes of the stronger one.

4.6. Concluding Remarks

In this chapter, the extension of OFDM radar with MIMO technology for improved DOA estimation was discussed. Specifically, the focus was on multiplexing methods that enable operation free of mutual interference for multiple Tx antennas used for MIMO processing. First, we discussed the conventional multiplexing methods and pointed out their advantages and drawbacks. We described the EqSI multiplexing, which is considered to be the state-of-the-art multiplexing method for OFDM radar. EqSI enables simultaneous operation for all Tx antennas utilizing the entire bandwidth, and thus maintains the full distance resolution as well as unambiguous velocity range for all Tx channels. Furthermore, due to the same reason it is superior to the conventional multiplexing schemes in terms of coherence between Tx channels.

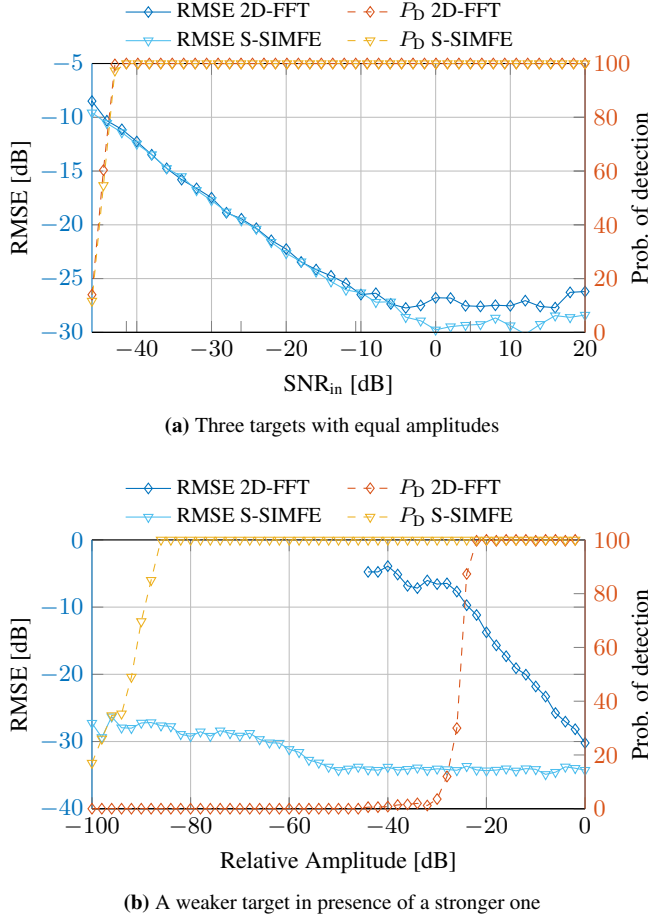


Figure 4.15.: Distance RMSE and P_D for targets in the same velocity cell

EqSI leads, however, to a reduction of unambiguously measurable distance range due to the increased spacing between subcarriers assigned to one Tx channel. To overcome this drawback, we proposed two new multiplexing schemes based on non-equidistant interleaving of subcarriers. The latter enables the original unambiguous range as well as resolution in both distance and velocity dimensions for all MIMO channels.

The first proposed multiplexing method called NeqSI interleaves the OFDM subcarriers non-equidistantly and uses the same interleaving pattern for all OFDM symbols. This can be interpreted as subsampling in the frequency domain, due to which NeqSI leads to increased sidelobes in the distance dimension. To cope with these sidelobes, we proposed a novel frequency estimation method named SIMFE. Based on the sparsity model, the proposed method performs iterative distance-velocity estimation, and is capable of detecting targets masked by sidelobes of more dominant ones. Thus, SIMFE compensates the drawbacks of NeqSI, while maintaining its advantages in terms of unambiguous range and resolution. Furthermore, we introduced a variation of NeqSI called NeqDySI that obtains a significantly higher PSL by varying the interleaving pattern from OFDM symbol to symbol. This leads to a high dynamic range even for the conventional Fourier processing. For both methods, we presented an approach for optimization of the interle-

aving pattern based on genetic algorithms, through which a PSL improvement up to 3.5 dB is obtained.

Based on the above discussion, it can be concluded that due to its multicarrier structure OFDM enables advanced multiplexing schemes for MIMO radar that are superior to the conventional ones in many aspects. EqSI multiplexing is well suited for applications where the requirements on the unambiguous distance range are satisfied. This is, however, not the case for some automotive applications, especially at higher carrier frequencies. Non-equidistant interleaving schemes overcome this drawback of EqSI. NeqSI with SIMFE processing is well suited for applications with targets distributed in the velocity plane, since there the full dynamic range is obtained due to equidistant sampling in slow-time. NeqDySI with Fourier processing is advantageous for applications where targets have SNR below 0 dB. Otherwise, also NeqDySI requires the SIMFE processing to obtain the full dynamic range.

Chapter 5.

Interference Mitigation Techniques for OFDM Radar

The interference between automotive radar systems becomes a major issue with the increasing number of radars integrated in vehicles for comfort and safety functions. Therefore, in the long-term, interference robustness is a vitally important aspect for successful deployment of this sensor type in the automotive area — especially for safety-critical applications. Due to the flexibility available with digital generation of arbitrary radar waveforms, OFDM is believed to have a potential for better interference robustness, achievable with interference-robust waveforms and interference suppression techniques. This chapter addresses the topic of interference for OFDM radar and presents novel approaches for its mitigation or — more preferably — avoidance.

We first analyze the impact of interference on OFDM radar and discuss the effect of signal processing steps on it. Then, we introduce a method for suppression of arbitrary narrowband interference applicable to OFDM radar. Since state-of-the-art radars, typically operating with FMCW modulation, can be regarded as narrowband interferers for a high bandwidth OFDM radar with comparably short duration of OFDM symbols, this method enables interference robustness against existing radar systems. A literature survey for interference mitigation techniques against OFDM interferers as well as for concepts that aim at interference-free coexistence of multiple OFDM radar systems is presented. Finally, to facilitate a high degree of robustness against arbitrary interference types already in the analog domain, we propose the extension of OFDM radar with cognitive features, which enables avoidance of interference by dynamically adapting the transmit signal. We introduce novel methods for adaptation of the Tx signal as well as for efficient spectrum sensing, and highlight the high potential of this topic for future radar systems. Furthermore, we point out that one of the proposed methods based on linear adaptation of the carrier frequency enhances additionally the distance estimation, breaking the link between the radar bandwidth and the distance resolution.

5.1. Influence of Interference on OFDM Radar

Before proceeding to interference mitigation techniques, the impact of interference on estimation performance of OFDM radar needs to be discussed. In our discussion we focus on analysis of the signal in the digital domain, i.e. after analog-to-digital conversion. We assume a proper sampling of the receive signal, i.e. no ADC clipping. The latter has to be facilitated by a suitable system design and parametrization, which shall guarantee that interference does not exceed the dynamic range of the ADC. Since the interfering signal power might be higher than that of the

radar reflections due to the one-way propagation of the former, this is a relevant aspect for the radar receiver design.

For this discussion we consider the classical OFDM radar signal processing described in Section 3.2. Here, we include the interference term into the signal model and describe the influence of the signal processing steps on it. As we already analyzed the noise properties of OFDM radar in Section 3.2.3, we do not consider the noise term in the following. Furthermore, we skip the range migration and Doppler shift terms in the signal model in (3.12) according to the assumptions behind the classical signal processing and for the sake of simplicity. Note that this is not necessary for the interference suppression algorithm in the next section, as it treats each OFDM symbol individually.

Including the interference term into (3.17), for the μ -th OFDM symbol the receive signal is

$$\mathbf{y}_{f,t_s} = \sum_{i=0}^{N_{\text{path}}-1} \bar{a}_i \mathbf{F}_{N_c}^{-1} \mathbf{D}_{N_c}^* (\bar{\tau}_i) \mathbf{s} \mathbf{D}_{N_{\text{sym}}} (\bar{f}_{D_i} \alpha) + \mathbf{v}_{f,t_s}. \quad (5.1)$$

where $\mathbf{v}_{f,t_s} \in \mathbb{C}^{N_c \times N_{\text{sym}}}$ is the matrix of interfering signal, whose columns represent the interference samples for each OFDM symbol. The spectrum \mathbf{y}_{f,t_s} with orthogonal subcarriers is obtained via FFT over each OFDM symbol:

$$\mathbf{y}_{f,t_s} = \mathbf{F}_{N_c} \mathbf{y}_{f,t_s} = \sum_{i=0}^{N_{\text{path}}-1} \bar{a}_i \mathbf{D}_{N_c}^* (\bar{\tau}_i) \mathbf{s} \mathbf{D}_{N_{\text{sym}}} (\bar{f}_{D_i} \alpha) + \underbrace{\mathbf{F}_{N_c} \mathbf{v}_{f,t_s}}_{\mathbf{v}_{f,t_s}}, \quad (5.2)$$

For the interfering signal, the FFT in (5.2) yields the interference spectrum. Hence, in case of narrowband interference, this operation will compress its energy into a narrow range of frequencies. This will lead to a certain separation of the interference energy from that of the signal, which is exploited by the interference suppression algorithm presented in the next section.

After (5.2), a spectral division is performed:

$$\mathbf{z}_{f,t_s} = \mathbf{y}_{f,t_s} \cdot / \mathbf{s} = \sum_{i=0}^{N_{\text{path}}-1} \bar{a}_i \underline{D}_{N_c}^* (\bar{\tau}_i) \cdot \underline{D}_{N_{\text{sym}}}^T (\bar{f}_{D_i} \alpha) + \mathbf{v}_{f,t_s} \cdot / \mathbf{s}. \quad (5.3)$$

Analogous to the case of noise, interference is not amplified through the spectral division if the modulation symbols in \mathbf{s} have unit amplitudes. Since this is favorable regarding the *signal-to-interference ratio* (SIR) in the radar image, it is assumed for the following discussion. In this case, the spectral division influences only the phases of the interfering signal, i.e. $\mathbf{v}_{f,t_s} \cdot / \mathbf{s} = \mathbf{v}_{f,t_s} \odot \mathbf{s}^*$. Thus, given that the radar signal \mathbf{s} and the interference \mathbf{v}_{f,t_s} are not correlated, the spectral division leads to a decorrelation of the interference \mathbf{v}_{f,t_s} over subcarriers. In case the columns of \mathbf{s} are not identical (no RS-OFDM), decorrelation occurs also over OFDM symbols.

Next, the distance profiles \mathbf{z}_{d,t_s} are created via IFFT over subcarriers. Assuming no windowing for the simplicity of representation, this results in

$$\mathbf{z}_{d,t_s} = \mathbf{F}_{N_c}^{-1} \mathbf{z}_{f,t_s} = \sum_{i=0}^{N_{\text{path}}-1} \bar{a}_i \underline{u}_{N_c}^* (\bar{\tau}_i) \cdot \underline{D}_{N_{\text{sym}}}^T (\bar{f}_{D_i} \alpha) + \mathbf{F}_{N_c}^{-1} (\mathbf{v}_{f,t_s} \odot \mathbf{s}^*), \quad (5.4)$$

where $u_{N_c}^*(\bar{\tau}_i)$ is defined as in (3.21). In (5.4), the spectrum of interference \mathbf{v}_{f,t_s} is multiplied elementwise with the complex conjugate spectrum of the radar signal \mathbf{s}^* , and the result is transformed back to the time domain. Evidently, this corresponds to a *circular discrete correlation* of the time signal $\mathbf{x} = \mathbf{F}_{N_c}^{-1}\mathbf{s}$ and the interference \mathbf{v}_{f,t_s} [Hakobyan, 2016c].

Finally, FFT is performed over OFDM symbols. Without windowing, this results in

$$\mathbf{z}_{d,v} = \mathbf{z}_{d,t_s} \mathbf{F}_{N_{\text{sym}}} = \sum_{i=0}^{N_{\text{path}}-1} \bar{a}_i \underline{u}_{N_c}^*(\bar{\tau}_i) \cdot \underline{u}_{N_{\text{sym}}}^T(\bar{f}_{D_i} \alpha) + \mathbf{F}_{N_c}^{-1}(\mathbf{v}_{f,t_s} \odot \mathbf{s}^*) \mathbf{F}_{N_{\text{sym}}}. \quad (5.5)$$

In case modulation symbols (columns of \mathbf{s}) change over slow-time in a non-correlated manner, the FFT in (5.5) will spread the interference over the velocity dimension, since it is decorrelated through the spectral division in (5.3). Contrary to interference, this processing compresses the radar signal into a peak.

The above discussion makes apparent that through the distance processing interference is correlated with the radar Tx waveform, which yields the cross-correlation of these both terms. Thus, assuming the Tx signal is not correlated to interference (e.g. two OFDM radars operating with pseudo-randomly generated, and thus uncorrelated waveforms), this processing will lead to spreading of the interference energy over the distance dimension. Additionally, if the Tx signal changes from OFDM symbol to symbol, the resulting cross-correlation will be different for each symbol, and the Doppler processing in (5.5) will further spread its energy over the velocity dimension. Consequently, taking into account the large number of degree of freedom in terms of waveform choice, OFDM radar with changing symbols potentially achieves a decorrelation of interference over both distance and velocity dimensions (only in the distance dimension in case of RS-OFDM). Since the same processing compresses the energy of each radar reflection into a single distance-velocity cell, a processing gain of signal over interference, i.e. interference suppression, is achieved in both dimensions. Given two uncorrelated waveforms, this processing gain is typically comparable to that for noise, described in Section 3.2.3. Also for interference of a certain deterministic structure such as chirp signals, typically a spreading of energy over the entire radar image is achieved. In contrast to noise, however, in this case the interference floor exhibits a certain structure, as we will see in the next section.

Summarizing, OFDM radar has favorable interference properties due to decorrelation of interfering signal over the distance-velocity plane. Since OFDM enables a large number of degrees of freedom in terms of waveform choice, the probability of interference being strongly correlated to the radar signal is low. Because of this, a significant interference suppression in the radar image is achieved and the probability of ghost targets due to correlated interfering signal is strongly reduced. This is an essential advantage compared to the chirp-sequence radar, for which the probability of chirp interference with a similar slope resulting in ghost targets is comparably high. However, since in case of OFDM radar the receive signal is sampled with the entire bandwidth, no analog pre-filtering of interference residing in the same frequency band is possible, contrary to chirp systems. Therefore, additional interference suppression and avoidance techniques are absolutely essential.

5.2. A Narrowband Interference Suppression Method for OFDM Radar¹

In this section, we present an interference suppression method for OFDM radar that mitigates arbitrary narrowband interferences. An interference is considered as narrowband if its occupied bandwidth during one OFDM symbol is much smaller than that of the OFDM radar. This is the case for an FMCW radar with the same bandwidth as the OFDM radar, but with frequency ramps of a much longer duration (typically in ms range) than an OFDM symbol (typically in μ s range). In this case, the interference affects only a small band of contiguous OFDM subcarriers. This property is used for the interference suppression method presented below. We study the proposed methods with simulations in Section 5.2.2 and verify with measurements in Section 6.5.

5.2.1. Interference Suppression Algorithm

As mentioned, in case of narrowband interference the FFT operation in (5.2) concentrates the interference energy into a narrow range of frequencies, such that a limited number of adjacent subcarriers contain most of the interference energy. The basic idea of the proposed method is to exclude subcarriers strongly corrupted by interference from evaluation, through which a significant amount of interference energy is discarded. Then, the values of excluded subcarriers are recovered by a *forward-backward linear prediction* (FBLP) from the values of neighboring subcarriers.

The proposed interference suppression algorithm operates on each OFDM symbol $\underline{z}_{f,\mu} = [z_{f,\mu}(0), \dots, z_{f,\mu}(N_c - 1)]^T$, $\mu \in [0, N_{\text{sym}})$ in (5.3). With this in mind, the index “f, μ ” will be omitted in the following. The interference suppression is achieved in three steps: interference detection, least-squares estimation of prediction coefficients from unaffected subcarriers and FBLP of the samples affected by interference.

In case of a considerable interference power, the subcarriers occupied by an interfering signal will have a much higher amplitude than the unaffected ones. Thus, these subcarriers can be detected based on their amplitude by an energy detector. They will then be excluded from processing to drop the major part of the interference. For simulations in Section 5.2.2, we use a CFAR based detection of corrupted subcarriers.

However, the exclusion of affected samples from processing by replacement of their values with zeros leads to gaps in frequency samples, which will result in increased sidelobes after the IFFT in (5.4). This might limit the dynamic range in presence of targets with very high SNR. To avoid this limitation, the values of affected subcarriers are recovered from neighboring unaffected subcarriers via linear prediction.

Let us denote the index of the first and the last subcarrier in the band occupied by the detected interference by n_f and n_l , respectively. It is well known that signals consisting of a sum of complex sinusoids such as the desired signal in \underline{z} in (5.3) have a linear dependency between the samples, which can be represented by an *autoregressive* (AR) model [Tufts, 1982; Haykin, 2014].

¹ Contributions presented in this section were partially reported in [Hakobyan, 2016c]. Some of author’s own formulations from [Hakobyan, 2016c] are adopted in this section.

In presence of noise, the set of linear equations describing this dependency can be represented in a matrix form as

$$\underbrace{\begin{bmatrix} z(o-1) & \dots & z(0) \\ \vdots & \ddots & \vdots \\ z(n_f-2) & \dots & z(n_f-o-1) \\ z(n_1+o) & \dots & z(n_1+1) \\ \vdots & \ddots & \vdots \\ z(N_c-2) & \dots & z(N_c-o-1) \end{bmatrix}}_{\mathbf{B}} \cdot \underbrace{\begin{bmatrix} g_{fp}(1) \\ g_{fp}(2) \\ \vdots \\ g_{fp}(o) \end{bmatrix}}_{\underline{g}_{fp}} \approx \underbrace{\begin{bmatrix} z(o) \\ \vdots \\ z(n_f-1) \\ z(n_1+o+1) \\ \vdots \\ z(N_c-1) \end{bmatrix}}_{\underline{b}}, \quad (5.6)$$

where $o > N_{\text{targ}}$ is the assumed order of the system and \underline{g}_{fp} is the vector of forward linear prediction (FP) coefficients. The model order o has to be higher than the maximum number of targets expected. However, o defines the number of adjacent subcarriers necessary for prediction, and thus should not be unnecessarily large. For details on the choice of the system order o please refer to [Haykin, 2014].

A least squares estimate of \underline{g}_{fp} is given by

$$\underline{g}_{fp} = (\mathbf{B}^H \mathbf{B})^{-1} \mathbf{B}^H \underline{b}, \quad (5.7)$$

where the superscript “ H ” denotes the conjugate transpose. In linear prediction notation, (5.7) can be rewritten as

$$\underline{g}_{fp} = \mathbf{R}^{-1} \underline{r}, \quad (5.8)$$

where $\mathbf{R} = \mathbf{B}^H \mathbf{B}$ is the correlation matrix and $\underline{r} = \mathbf{B}^H \underline{b}$ is the correlation vector obtained from the measurement data. Alternatively, the autocorrelation function of \underline{z} is estimated and \underline{g}_{fb} is calculated by the Levinson-Durbin algorithm [Levinson, 1947; Durbin, 1959] which is computationally more efficient than the least squares estimate in (5.8).

According to the theory of optimum linear prediction [Haykin, 2014], the backward prediction (BP) coefficients \underline{g}_{bp} can be obtained from \underline{g}_{fp} with

$$\underline{g}_{bp} = \mathbf{T} \underline{g}_{fp}^*, \quad \mathbf{T} = \begin{bmatrix} 0 & \dots & 1 \\ & \ddots & \\ 1 & \dots & 0 \end{bmatrix}, \quad (5.9)$$

where \mathbf{T} is the permutation matrix that swaps the coefficients of \underline{g}_{fp} . Consecutively, the missing samples of all affected subcarriers are predicted recursively in forward and backward directions:

$$z_{fp}(i_{fp}) = [z(i_{fp}-1), \dots, z(i_{fp}-o)] \cdot \underline{g}_{fp}, \quad (5.10)$$

$$z_{bp}(i_{bp}) = [z(i_{bp}+o), \dots, z(i_{bp}+1)] \cdot \underline{g}_{bp}, \quad (5.11)$$

with $i_{fp} = \{n_f, n_f+1, \dots, n_1\}$ and $i_{bp} = \{n_1, n_1-1, \dots, n_f\}$. Both predictions can be further averaged to obtain a better estimate of the missing samples:

$$z(n_i) = \frac{(z_{fp}(n_i) + z_{bp}(n_i))}{2}, \quad n_i \in [n_f, n_1]. \quad (5.12)$$

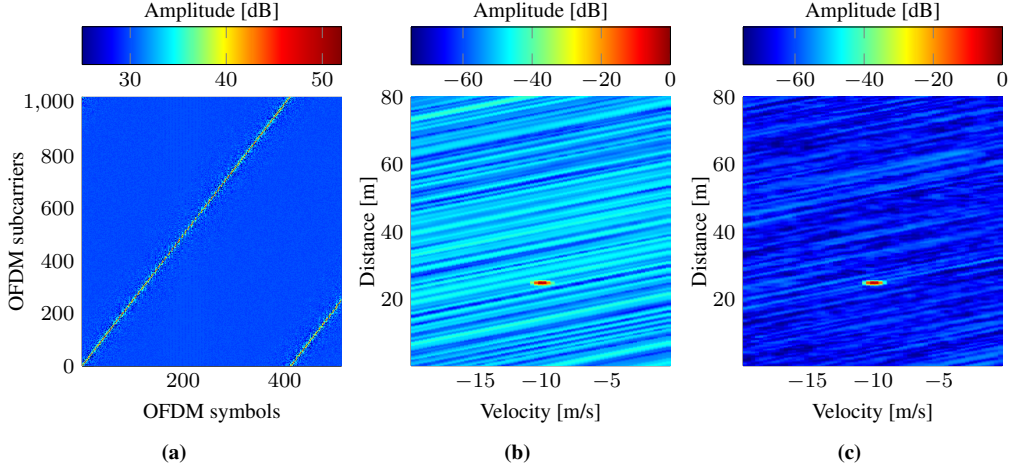


Figure 5.1.: OFDM radar distance-velocity estimation in presence of interference: (a) OFDM signal overlapped with interference, (b) (d,v) image without interference suppression, (c) (d,v) image with interference suppression.

Then, the further OFDM processing steps described in Section 5.1 can be performed.

Even though described for a single band affected by interference, the presented approach can be analogously applied if multiple narrow bands are affected.

5.2.2. Simulative Analysis

In this section, the performance of the proposed algorithm is studied in simulations. An OFDM radar with interference from an FMCW radar at 77 GHz is simulated. Both systems have the same bandwidth of $B = 625$ MHz. For the OFDM radar this bandwidth is shared between $N_c = 1024$ OFDM subcarriers modulated with complex modulation symbols of unit amplitudes and random phases. Chirp duration is $T_{ch} = 5$ ms, whereas with $T_{SRI} = 12.29 \mu s$ and $N_{sym} = 512$ a duration of measurement cycle of $T_{cycle} = 6.3$ ms is achieved for the OFDM radar. Both FMCW and OFDM signals have the same power at the receiver input. A Kaiser window with $\beta = 7.7$ is used for sidelobe suppression for FFTs in (5.4) and (5.5). For the interference suppression, the model order is set to $o = 50$.

This configuration results in detection of 3 to 5 subcarriers affected by the interference for each OFDM symbol. For the detection of those subcarriers a CFAR detector is used. A target at the distance $d = 25$ m and velocity of $v = -10$ m/s is simulated in a noiseless setup. The OFDM signal overlapped by the interfering chirp is shown in Fig. 5.1a, and the radar image without interference suppression is shown in Fig. 5.1b. In this case, a mean SIR of 51.3 dB is achieved, which corresponds to the integration gain of 2D-FFT. Fig. 5.1c shows the radar image with interference suppression. Due to the latter a mean SIR of 64.25 dB is obtained, which corresponds to a 13 dB SIR improvement.

For quantitative performance evaluation of the presented algorithm, the dependency of the mean SIR in the radar image as well as the SIR with respect to the highest interference peak is shown in Fig. 5.2. Furthermore, to demonstrate the need for recovery of the samples affected by

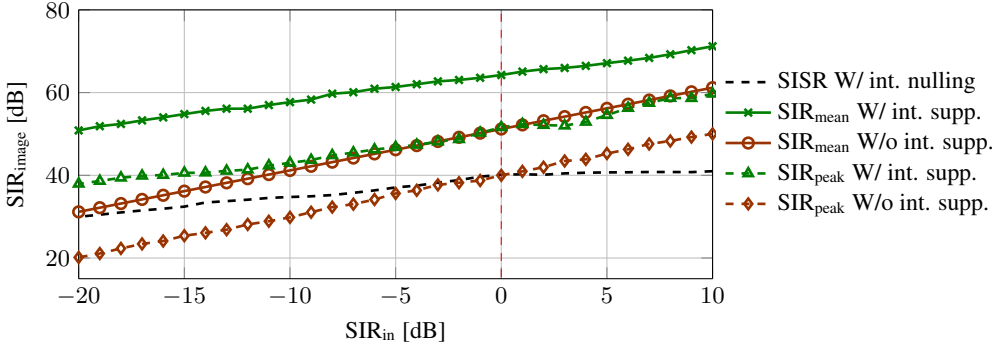


Figure 5.2.: SIR in the radar image over the input SIR

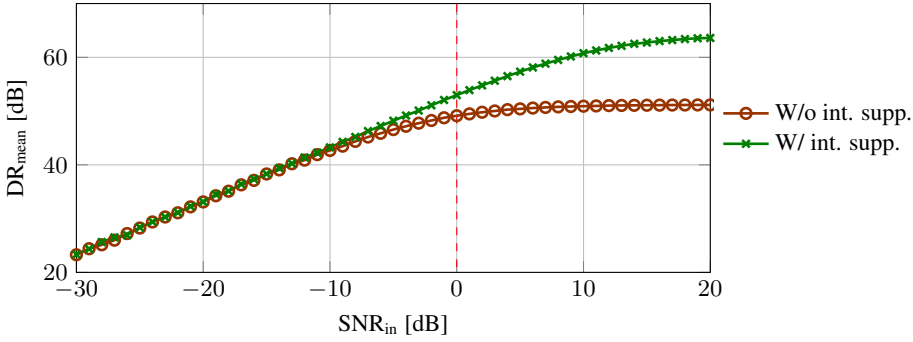


Figure 5.3.: Mean dynamic range in the radar image over the input SNR for $\text{SIR}_{\text{in}} = 0$

interference, the *signal-to-interference-and-sidelobe-ratio* (SISR, the ratio of the main peak power to that of the highest interference or sidelobe) in case of just nulling of the affected samples is shown. Evidently, replacement of the affected subcarrier values with zeros leads to increase of sidelobes, which, depending on SNR, might limit the dynamic range. Thus, a recovery of nulled samples is necessary, especially in case of targets with a high SNR. Clearly, with the proposed method the SIR in the radar image can be further increased by 12–16 dB.

To demonstrate the performance of the proposed algorithm in presence of noise, Fig. 5.3 presents the mean dynamic range (DR_{mean}) over SNR for $\text{SIR} = 0$ dB. The term mean dynamic range refers to the ratio of the highest peak power to the mean power of noise, interference and sidelobes. As Fig. 5.3 shows, in case of a low SNR, i.e. when noise is more significant than interference ($\text{SNR}_{\text{in}} < -10$ dB), the DR is limited by noise. Starting from -15 dB, interference has a visible impact on the DR, and the proposed algorithm obtains an SIR improvement. For $\text{SNR}_{\text{in}} > -7$ dB, without interference suppression the dynamic range is limited almost completely by the interference and no significant DR improvement over increasing SNR is obtained. In this region the proposed algorithm achieves an increase of the DR via interference suppression, which tends asymptotically to the interference suppression in the noiseless case for $\text{SNR}_{\text{in}} > 5$ dB.

Summarizing, the proposed method is effective for suppression of arbitrary narrowband interferences, including interference from state-of-the-art FMCW radars with slow ramps. Through discarding of the subcarriers that are strongly corrupted by interference, a 12–16 dB interference

mitigation can be achieved, which further contributes to the interference robustness of OFDM radar. With the proposed method, the effectiveness of interference mitigation depends on the number of affected subcarriers, i.e. on the bandwidth affected by interference during one OFDM symbol. Thus, it approaches its limits for chirp interference with a large slope (e.g. fast-chirp radar), i.e. when for OFDM radar the interference no longer can be considered as narrowband. Furthermore, it is limited by the factor that due to the FFT-based OFDM demodulation performed with rectangular window not the entire interference energy is compressed into its spectral band due to spectral leakage.

5.3. OFDM Radar Networks and Methods for Mitigation of OFDM Interference

Since OFDM radar has been primarily studied in the context of combination with communication, some research on OFDM radar networks and their interference properties is known in OFDM radar literature [Braun, 2014; Fink, 2012; Sturm, 2011, 2012b, 2013; Sit, 2012b, 2014a,b]. These works will be shortly discussed in the following.

Multi-user OFDM radar networks for radar and communication systems are studied in [Braun, 2014]. The authors provide a performance analysis under the consideration of mutual interference between radar nodes and suggest metrics such as radar network outage probability as a performance metric for OFDM radar networks. As a measure for evenly distributing interference between radar nodes, the use of arbitrary (non-equidistantly) spaced OFDM subcarriers by all radar nodes is proposed. Therefore, for the radar estimation iterative processing methods such as coherent successive target cancellation are considered. The impact of arbitrary spaced subcarriers on the detection performance of OFDM radar is studied in [Fink, 2012].

Also in [Sturm, 2011, 2012b, 2013], a multi-user OFDM radar network is considered. For interference avoidance these works perform equidistant interleaving of OFDM subcarriers between multiple radar sensors. This approach has the advantage that it enables operation of multiple radar sensors with theoretically orthogonal OFDM waveforms, while the classical 2D-FFT processing remains applicable for distance-velocity estimation. However, the drawback here is that only part of the subcarriers is evaluated, even though the entire bandwidth has to be sampled. This results in a reduction of unambiguous distance range, but not the processing gain. Additionally, in a practical application this approach faces challenges due to carrier frequency offsets between the local oscillators (LO) of different radar nodes, resulting in interference. This issue is studied in [Sturm, 2012b, 2013]. Moreover, the authors point out that interference from other OFDM radars has the same impact on the radar image as noise [Sturm, 2011]. That is, it rises only the background noise level but does not lead to false targets. This assumes, however, that both systems are modulated with symbols that carry communication data, i.e. have a pseudo-random character and are uncorrelated.

To further increase the interference robustness of OFDM radar operating in radar networks, an interference cancellation method for signals of other OFDM radar and communications systems is proposed in [Sit, 2012b, 2014a,b]. The idea behind these methods is to demodulate the OFDM radar and communication signals of other radar sensors and subtract them from the received signal. This assumes, of course, that other radars use a known modulation scheme. Moreover, for time and frequency offset detection the interfering signal must contain pilot subcarriers as

well as training OFDM symbols. Based on this known structure, a time and frequency offset detection is performed using an algorithm well known from communications [Schmidl, 1997]. The presented results show a considerable interference suppression achieved with this approach [Sit, 2012b, 2014a,b]. Measurements with an OFDM radar setup to verify the performance of this methods are presented in [Sit, 2016]. A somewhat similar method for cancellation of OFDM interference from DVB-T signals in the context of low-frequency SAR systems has been proposed in [Svensson, 2014].

Unfortunately, all these approaches assume an operation in a network of other OFDM radars, where all radar nodes follow some known convention. However, realistically the frequency bands available for automotive radar will be used by systems which do not necessarily follow some specific convention or use a certain waveform type. This is evident alone from the fact that a large number of radar systems of earlier generations are already deployed in vehicles. Thus, for a high interference robustness achievable in real world application more universal approaches to interference handling are needed. Therefore, in the next section we propose the extension of OFDM radar with cognitive features, such that through environment awareness and dynamical adaptation of the transmit signal more universal interference robustness is achieved.

5.4. Interference-Aware Cognitive OFDM Radar

Cognitive radar is one of the emerging topics in the area of radar that gains increasingly more attention over the past few years. The extension of radar with cognitive features is considered to be a natural development of today’s radar systems [Haykin, 2006]. Indeed, in times when *artificial intelligence* (AI) achieves revolutionary advances [Silver, 2016] in many areas of life, also the radar needs to become more intelligent. The principle behind cognitive radar is the continuous sensing and perception of the radar environment and subsequent adaptation of the transmit signal for optimized radar functionality. Typical applications for this principle are the improvement of the target detection and tracking performance via cognitive adaptation [Huleihel, 2013; Sharaga, 2015; Nijsure, 2015] as well as the interference mitigation between radar and communication systems sharing the same frequency band [Aubry, 2014; Guo, 2015; Manna, 2016; Jakabosky, 2016]. In our work, we aim at extending OFDM radar with cognitive features to mitigate interference from other automotive radar sensors, increasing its interference robustness in a universal manner and already in the analog domain — i.e. by avoidance instead of post-treatment. We point out that due to the high degree of flexibility through digital signal generation and processing, OFDM offers an excellent framework for the cognitive functionality. In what follows, we present some first steps for the research in the area of automotive cognitive radar and highlight its perspectives.

First, we describe the concept of cognitive radar according to the literature, give a state-of-the-art survey of known cognitive radar concepts, and present our vision of cognitive radar in the context of interference mitigation. Based on the latter, we present three main components of cognitive radar: sensing, interpretation and adaptation. In our work we focus mainly on the waveform adaptation and present novel adaptation approaches. Furthermore, we propose a practical method for spectrum sensing that uses the available hardware of the OFDM radar receiver.

5.4.1. Cognitive Radar

Overview

The concept of cognitive radar has first been introduced by Haykin in 2006 [Haykin, 2006]. In his pioneering work, he describes a radar system that is able to *learn* continuously about the environment, *reason* and *adjust* its transmit signal to dynamically optimize its detection and tracking performance. This results in a system with a dynamic closed feedback-loop comprising the transmitter, environment, and receiver. Such a system assumes a receiver that is capable of sensing and reasoning the environment and an adaptive transmitter that has a feedback link from the receiver. According to Haykin, the echo-location system of a bat can be considered as a neurobiological realization of such a cognitive radar.

More recently, a slightly different formulation of cognitive radar based on a *sense-learn-adapt* (SLA) approach has been presented in [Guerri, 2014]. Learning about the environment is achieved based on *knowledge-aided* (KA) supervised training. Also here, the use of cognitive features for improvement of detection and tracking performance is considered. Further applications of cognitive radar aiming at improved detection and tracking based on various optimization metrics were presented in [Sharaga, 2015; Huleihel, 2013; Nijssure, 2015].

Another typical application for cognitive radar is the coexistence with communication systems sharing the same frequency band [Aubry, 2014; Guo, 2015; Manna, 2016; Jakabosky, 2016]. In this setup, typically the communication system is considered the primary user, and radar takes advantage of the spectral opportunities as they arise. For this purpose, primarily two components are needed: a sensing system that is capable of continuously sensing the entire operational spectral band, and a waveform adaptation approach to fit the transmit signal into available spectral slices, along with suitable signal processing methods.

For spectrum sensing, several approaches have been proposed, ranging from straightforward ones such as use of an additional radar sensor for spectrum sensing [Piezzo, 2013] to sophisticated spectrum-blind *modulated wideband converters* (MWC) [Mishali, 2010], and further spectrum sensing methods operating based on CS principles [Stinco, 2014]. Unfortunately, all these systems suffer from high hardware costs due to high-rate ADCs or high number of receive channels needed, as the frequency band of interest is typically large. For the waveform adaptation, an approach based on notching of frequency bands corrupted by interference has been proposed in [Li, 2014], which, however, has a noticeable impact on the radar performance due to the increased sidelobes in distance estimation. Some works on optimization of waveforms with spectral gaps were presented in [He, 2010; Aubry, 2014], which, however, achieve only a limited improvement. A more suitable CS-based processing for a signal composed of several narrow bands has been proposed in [Cohen, 2016b]. Also this approach has its drawbacks compared to conventional radars with no spectral gaps.

Our interpretation of cognitive radar

In our work, we aim at incorporating cognitive features into automotive radar systems to increase their interference robustness. More specifically, we leverage the flexibility provided by OFDM to achieve an interference-robust, fully-digital cognitive OFDM radar. Therefore, expanding upon the definition of cognitive radar by Haykin in [Haykin, 2006], below we give our interpretation of cognitive radar we call interference-aware cognitive radar. It is depicted in Fig. 5.4 and comprises three main components:

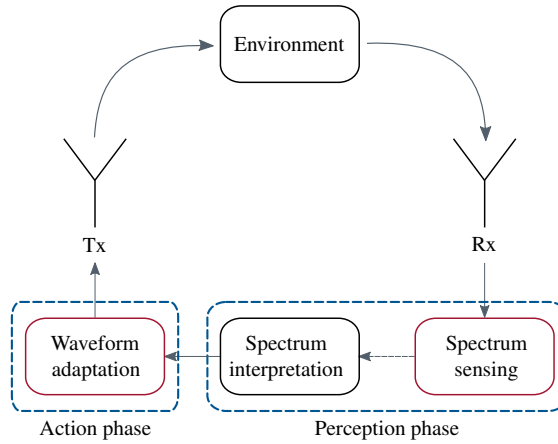


Figure 5.4.: Closed-loop perception-action cycle of cognitive radar

1. **Spectrum sensing** is the process of continuously analyzing the operational spectral band by sampling the received signal and building its spectrum for a subsequent detection of interference from other sensors. Alternatively, this block can directly deliver the spectrum occupancy information, depending on the sensing concept.
2. **Spectrum interpretation** is the block that contains the entire cognitive intelligence of the system. It is responsible for reasoning the information obtained from the spectrum sensing block by means of detection and classification of interfering signals, as well as estimation of various interference parameters. Based on this knowledge, prediction of the interference behavior for the next transmission cycle is performed. This serves as a basis for the choice of an optimal adaptation strategy that is then followed for the next measurement cycle. As typical for many cognitive systems, this block will generally incorporate knowledge from previous measurement cycles as well as further a priori knowledge such as various interference models. In simpler terms, it will have a temporal memory and knowledge-based pattern recognition features. Naturally, this can be further extended by the ability of the system to learn continuously from its own observations. Thus, the spectrum sensing and interpretation blocks are responsible for the perception ability of the cognitive radar, by means of which the radar learns about its immediate environment and decides how to adjust to it.
3. **Waveform adaptation** block comprises possible adaptation methods along with the corresponding signal processing algorithms, as well as the practical realization of the chosen adaptation strategy. It represents the last component of the feedback loop, i.e. implements the action phase. Waveform adaptation methods aim at avoiding interference dynamically based on the available spectral information, while maintaining the radar performance unaffected.

Depending on implementation, this cycle can be repeated either for the entire measurement or for each slow-time sample. However, since typically the waveform adaptation methods are subject to certain constraints posed by the signal processing, often the adaptation strategy needs to be known at the beginning of the measurement cycle. In this case, a prediction of the interference behavior for the duration of the measurement cycle has to be provided by the spectrum interpretation block. In contrast, the spectrum sensing block is required to acquire information continuously, based on

which interference prediction is performed and an adaptation strategy is chosen at the beginning of the new measurement cycle.

Note that with this approach not only the interference robustness of the cognitive radar is improved, but also the interfering system itself experiences less interference. Thus, the cognitive approach leads to better use of the available spectral resources such that overall less interference between systems occurs.

Objectives

In the context of this topic, our main objective is to develop a practical, interference-robust, cognitive OFDM radar system for automotive applications. It must fit into the OFDM radar concept both in terms of hardware and signal processing methods, as well as exploit the flexibility of digital signal generation and processing to obtain a high adaptability.

First of all, the assumption we build upon is that a large frequency band is available for the radar operation (e.g. 77 to 81 GHz frequency band), and the radar is able or prefers to utilize only part of it (e.g. only 500 MHz due to ADC-limitations). Thus, in simple terms the task is to adaptively choose a slice of the large operational frequency band that is most favorable in terms of interference.

Even though the long-term goal should be to achieve interference robustness against all radar types operating in the same frequency band, to reduce the complexity of the task we first focus on chirp interferers, as this is the type of signals most commonly used for automotive applications. The described methods are, however, applicable to a certain extent to other interference types. Furthermore, we focus heavily on the waveform adaptation techniques, as we consider the latter to be the main prerequisite for cognitive radar. To this end, we aim at developing methods that allow adaptability without adversely affecting the radar estimation performance. Moreover, for efficient implementation, adaptation methods which are compatible with the classical OFDM radar signal processing, are preferable. For spectrum sensing, we need techniques that are able to capture and analyze the entire operational band without significant increase of hardware costs due to high-rate ADCs [Piezzo, 2013] or banks of additional hardware equipment [Mishali, 2010]. As to the spectrum interpretation, we do not address this block in the scope of our work, considering it as a promising topic to be studied in future research. Thus, for the discussion of waveform adaptation methods, we assume perfect knowledge of interference parameters.

As we show in the following, OFDM provides means both for efficient spectrum sensing and waveform adaptation, without the need for expensive hardware adjustments. We start our discussion from waveform adaptation methods, as these are the cornerstone of the cognitive radar functionality.

5.4.2. Waveform Adaptation Methods for Cognitive Radar

As mentioned, the state-of-the-art techniques based on notching affected frequency bands or the use of several narrow bands have performance limitations and need sophisticated signal processing methods. Therefore, in our work we choose a different approach for the waveform adaptation that overcomes these drawbacks. Specifically, the waveform adaptation methods presented below cover a smaller frequency band than generally available, and adapt to the spectral conditions by changing the carrier frequency. The adaptation of the carrier frequency can be done either for the complete measurement at once, or for each slow-time sample individually, following

a certain adaptation pattern. Whereas the former is a simple yet effective method that requires no adjustment of the signal processing, the latter allows more flexible adaptation using the same signal processing methods, but needs more specific treatment of estimation parameters.

In terms of hardware changes, both methods are simple to realize — the only adjustment needed is an adaptive LO instead of one with a constant carrier frequency. This can be realized with the help of standard hardware components such as phase-locked loops (PLL) or direct digital synthesizers (DDS). Naturally, also the RF hardware (antennas, mixers, etc.) should also be designed for proper operation in the entire operational band.

In what follows, we consider a 4 GHz operational band in the frequency range 77 to 81 GHz, from which we use a band of 500 MHz at a time. Thus, the adaptive carrier frequency $f_{c,a}$ is varied in the range 77.25 to 80.75 GHz. Furthermore, we choose a parametrization suitable for the classical OFDM radar signal processing (Table 5.1), since the ACDC and APMC methods require the carrier frequency to be constant for the entire measurement cycle, and thus are applicable only to the first adaptation method. To prolong the duration of OFDM symbols to the full duration allowed by the required SRI, we use a somewhat unusual parametrization with a narrower subcarrier spacing than required for the unambiguous distance range. To mitigate the ICI due to the Doppler shift, we only use every fourth subcarrier, i.e. 1024 subcarriers out of 4096. This parametrization obtains lower ICI levels, since typically the largest ICI originates from the neighboring subcarriers. Hence, it enables the full processing gain both with respect to noise and interference, while keeping the Doppler induced ICI lower than for the full spectral occupancy and obtaining a sufficiently large unambiguous distance range.

Table 5.1.: Parametrization for cognitive radar

Modulation parameter	Value	Radar parameter, $f_c = 79$ GHz	Value
Range of $f_{c,a}$	77.25 to 80.75 GHz	d_{\max}	300 m
B	500 MHz	d_u	307.2 m
N_c , all	4096	Δd	0.3 m
N_c , used	1024	v_u	± 95.6 m/s
N_{sym}	256	Δv	0.747 m/s
Δf	122 kHz	G_p	60.2 dB
T	8.192 μ s		
T_{CP}	2 μ s		
T_{SRI}	10.192 μ s		
T_{cycle}	2.6 ms		

5.4.2.1. Carrier Frequency Hopping – Waveform Adaptation

A straightforward approach for adaptation to interference is the adjustment of the carrier frequency for the entire measurement cycle to use a spectral slice free of interference. This can be interpreted as cognitive hopping of the carrier frequency, and thus we name this simple yet effective method *carrier frequency hopping waveform adaptation* (CFH-WA). This method is effective if a spectral slice free of interference is available for the duration of the measurement cycle, i.e. if interference does not occupy the entire operational bandwidth, or for chirps that are slow enough to leave room for OFDM measurement. An example for such adaptation is shown in Fig. 5.5, where interference is avoided by adapting the carrier frequency to 80.6 GHz for the first and to 79.7 GHz for the second measurement cycles.

Since the adaptation is done between measurement cycles, the signal processing is unaffected, and thus needs no further investigation. Furthermore, for CFH-WA both the classical signal processing as well as more advanced processing methods such as ACDC and APMC are applicable. Neglecting the propagation and reflectivity differences, the carrier frequency adaptation affects only the velocity estimation parameters (e.g. v_u , Δv). However, since the bandwidth available for adaptation (4 GHz) is much smaller than the carrier frequency (77 GHz), the difference of velocity parameters due to adaptation is not considerable.

Clearly, CFH-WA is effective if the spectrum is not heavily used, and enough free space for a complete OFDM measurement is available. Nevertheless, in case interference covers the entire operational band such that no room for an OFDM measurement with a constant carrier frequency is left, more advanced adaptation methods are required. In the following we consider methods for adaptation of the carrier frequency during the measurement cycle, study its impact on measurement parameters and propose suitable signal processing methods.

5.4.2.2. Slow-Time Chirp Waveform Adaptation with Variable Symbol Repetition Intervals

To achieve higher adaptability than with CFH-WA, we consider adjustment of the carrier frequency not only between measurement cycles, but also during the measurement, i.e. for each OFDM symbol individually. This requires, however, rethinking of the signal processing algorithms, since through this modification some new effects arise.

First of all, due to the coupling of target distance and carrier frequency (the term $\bar{a}_i = a_i \cdot \exp(-j2\pi f_c \tau_i)$, $\tau_i = 2d_i/c_0$ in (3.12)), the adaptive change of the latter leads to a delay-induced phase term over the slow-time dimension. That is, now the phase progression over slow-time depends both on target velocity and distance. If the carrier frequency is changed arbitrarily, then the phase progression over the slow-time is no longer linear, and frequency estimation methods such as DFT are no longer applicable. The parameter estimation in this case requires different processing methods such as matched filtering, and has, accordingly, different properties. For a linear change of the carrier frequency, however, the distance-induced phase term in slow-time is linear, and thus frequency estimation methods including DFT are applicable. Due to the linear change of carrier frequency, each individual OFDM subcarrier can be considered as a chirp over slow-time, and therefore we name this adaptation method *slow-time chirp waveform adaptation* (STC-WA). This principle of slow-time chirps has been first introduced for fast-chirp radar in [Schoor, 2013] to increase the distance resolution through slow-time–distance coupling. In our work, we adopt this principle for OFDM radar and use it primarily for adaptation in the context of cognitive radar. The improvement of the distance resolution is also obtained in our application and represents an additional benefit. Moreover, in our work we point out the drawback of the original method in terms of reduced velocity resolution and propose a novel solution to this problem based on the use of *variable symbol repetition intervals* (VSRI). The latter substantially improves the estimation performance, maintaining the original velocity resolution and achieving a full improvement of the distance resolution.

Mathematical description of STC-WA

For STC-WA, the adaptive carrier frequency $f_{c,a}$ changes linearly over slow-time:

$$f_{c,a}(\mu) = f_{c,0} + \mu \Delta f_c, \quad \mu \in [0, N_{\text{sym}}) \quad (5.13)$$

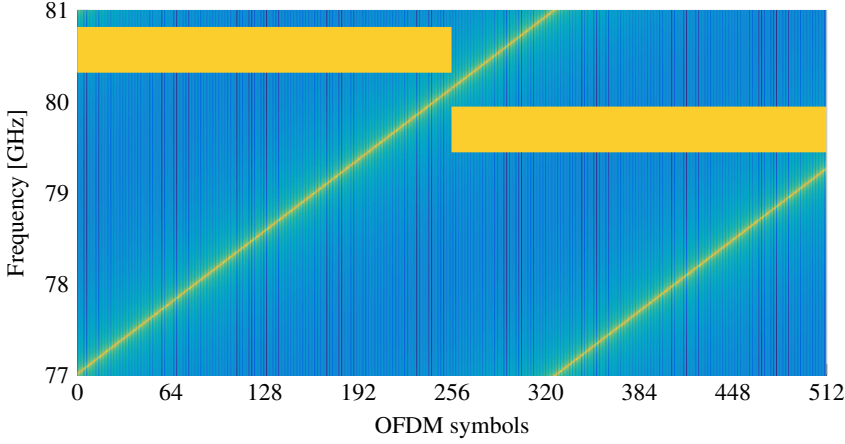


Figure 5.5.: Two consecutive OFDM measurement cycles of CFH-WA; adaptation to chirp interference with a bandwidth $B_{\text{int}} = 4$ GHz, and chirp repetition interval $T_{\text{CRI}} = 2.69$ ms

where $f_{c,0} = f_c - \Delta f_c N_{\text{sym}}/2$ denotes the carrier frequency of the first OFDM symbol, f_c is the (reference) carrier frequency in the middle of the slow-time axis, and Δf_c denotes the carrier frequency step. Note that the latter can be both positive and negative, depending on the slope of the slow-time chirp. We denote the bandwidth of the slow-time chirp, i.e. the sweep of the carrier frequency during the measurement cycle by $B_{\text{STC}} = N_{\text{sym}} \Delta f_c$.

With this modification, the received signal in (3.17) for the μ -th OFDM symbol is

$$y_{\text{tr,ts}}(m, \mu) = \sum_{i=0}^{N_{\text{path}}-1} \frac{a_{i,at}}{\sqrt{N_c}} e^{-j2\pi f_{c,a}(\mu)\tau_i} e^{-j2\pi f_{c,a}(\mu)\gamma_i \mu T_{\text{SRI}}} \sum_{n=0}^{N_c-1} s(n, \mu) \cdot e^{j2\pi \frac{mn}{N_c}} e^{-j2\pi n \bar{\tau}_i}, \quad \mu \in [0, N_{\text{sym}}]. \quad (5.14)$$

Note that in (5.14), the Doppler shift of subcarriers, range and Doppler frequency migration, and Doppler scaling are ignored analogous to the classical OFDM radar signal processing. As (5.14) shows, the change of carrier frequency affects only the two phase terms $\exp(-j2\pi f_c \tau_i)$ and $\exp(-j2\pi f_c \gamma_i t)$ in (3.7). Through the adaptation of the carrier frequency the inner sum in (5.14) is unchanged, and thus the distance estimation is unaffected. Therefore, we skip the steps of distance processing described in Section 3.2 and proceed straight to its result:

$$z_{\text{d,ts}}(k, \mu) = \sum_{i=0}^{N_{\text{path}}-1} a_i u_{N_c}^*(\bar{\tau}_i, k) e^{-j2\pi f_{c,a}(\mu)\tau_i} e^{-j2\pi f_{c,a}(\mu)\gamma_i \mu T_{\text{SRI}}}, \quad k \in [0, N_c], \quad \mu \in [0, N_{\text{sym}}], \quad (5.15)$$

where $z_{\text{d,ts}}$ denotes the distance profiles indexed by k over the slow-time indexed by μ , $u_{N_c}^*(\bar{\tau}_i, k)$ is the k -th element of $\underline{u}_{N_c}^*(\bar{\tau}_i)$ defined as in (3.21) and denotes the result of distance processing for the i -th target in the k -th distance cell. From (5.15) it is apparent that the phase term in slow-time now depends on both distance term τ_i and velocity term γ_i . Substituting (5.13) into (5.15) and denoting $\tilde{a}_i = a_i \exp(-j2\pi f_{c,0} \tau_i)$:

$$z_{d,t_s}(k, \mu) = \sum_{i=0}^{N_{\text{path}}-1} \tilde{a}_i u_{N_c}^*(\bar{\tau}_i, k) e^{-j2\pi \Delta f_c \mu \tau_i} e^{-j2\pi f_{c,0} \gamma_i \mu T_{\text{SRI}}} e^{-j2\pi \Delta f_c \gamma_i \mu^2 T_{\text{SRI}}}, \quad (5.16)$$

$$k \in [0, N_c), \quad \mu \in [0, N_{\text{sym}}).$$

As (5.16) shows, for STC-WA there are three phase terms in slow-time:

1. The first term $\exp(-j2\pi \Delta f_c \mu \tau_i)$ denotes the delay-induced linear phase progression over the slow-time. This term represents additional distance information and is later used to improve the distance estimation.
2. The term $\exp(-j2\pi f_{c,0} \gamma_i \mu T_{\text{SRI}})$ denotes the Doppler-induced linear phase progression over the slow-time and is used for velocity estimation.
3. The third term $\exp(-j2\pi \Delta f_c \gamma_i \mu^2 T_{\text{SRI}})$ is a Doppler-induced quadratic phase progression over the slow-time. This term occurs due to the dependency of the Doppler shift on the carrier frequency. A linearly increasing carrier frequency causes a linear increase of the Doppler frequency, i.e. leads to a Doppler-induced phase change with first and second order terms. In other words, the Doppler frequency now becomes a linear chirp with a slight frequency sweep. This has two consequences for the Doppler spectrum. First of all, the frequency sweep leads to a widening of the peak after the slow-time pulse compression, which we refer to as l -dimension. The widening of the peak in l -dimension, in turn, results in a decreased resolution of both distance and velocity estimations obtained from the slow-time processing, as well as in reduced SNR. Moreover, the frequency sweep results in a different spectral shape; the more the sweep range is, the more its spectral shape diverges from a distinct peak and resembles a chirp spectrum. This can potentially lead to detection of multiple closely-located targets for a single reflection, since the detection algorithm commonly assumes a spectral peak with a distinct maximum.

In contrast to the case with a constant carrier frequency, the frequency of slow-time complex exponentials is now dependent on both distance and velocity. Thus, after the frequency estimation over slow-time, additional processing for resolving the jointly estimated velocity and distance terms is required. For this purpose, the unambiguous distance measurements from fast-time dimension can be used [Schoor, 2013]. Thus, the phase terms from both estimations in fast-time and slow-time are written in an equation system as:

$$\begin{cases} 2\pi \frac{\mu l}{N_{\text{sym}}} = \left(2\pi \left(\Delta f_c \frac{2\hat{d}}{c_0} \mu + f_{c,0} \frac{2\hat{v}}{c_0} \mu T_{\text{SRI}} + \Delta f_c \frac{2\hat{v}}{c_0} \mu^2 T_{\text{SRI}} \right) \right) \mod 2\pi, \\ 2\pi \frac{k n}{N_c} = \left(2\pi n \Delta f \frac{2\hat{d}}{c_0} \right) \mod 2\pi, \end{cases} \quad (5.17)$$

$$k \in [0, N_c), \quad l \in [0, N_{\text{sym}}),$$

where $\hat{d} \in [0, N_c)$ and $\hat{v} \in [0, N_{\text{sym}})$ are the distance and velocity components corresponding to k and l . Given that the distance measurements from fast-time are unambiguous, the modulo operation on fast-time phases can be omitted, and the value of \hat{d} can be substituted into the first equation. When carried out for already detected peak indices (k, l) , solving this equation system yields directly the distances and velocities of the targets. Alternatively, this equation system can be solved for each value of indexes k and l . This can be interpreted as an axis transformation from the orthogonal (k, l) -axis to non-orthogonal (\hat{d}, \hat{v}) axis, as illustrated in Fig. 5.6. To distinguish between the results before and after this transformation, in the following we refer to the former

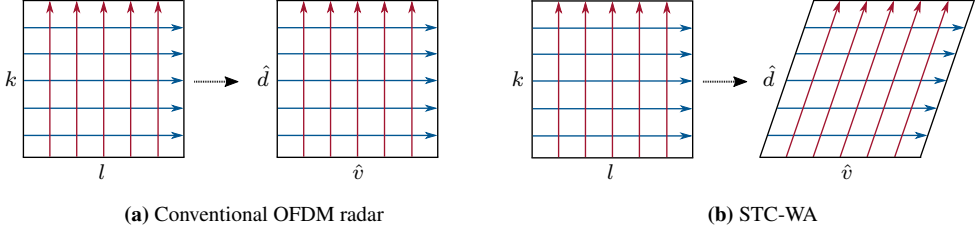


Figure 5.6.: The mapping from (k, l) axis to the (\hat{d}, \hat{v}) radar profile [Armanious, 2016]

as (k, l) space, and the latter is as before referred to as distance-velocity space or (d, v) space. This (k, l) space is the 2D-spectrum resulting from 2D-FFT based signal processing, where the frequencies in l -dimension contain portions both due to distances and velocities of targets. The described axis transformation combines the unambiguous distance estimates from fast-time with high-resolution estimates from slow-time (given that the STC bandwidth is large), and thus obtains an improved unambiguous distance estimate.

The mathematical description of the estimation parameters for STC-WA as well as derivations for quantification of the peak expansion due to the quadratic Doppler term are given in Appendix B.

Extension of STC-WA with VRSI

In the following, we present a novel method for implicit compensation of the quadratic Doppler term in (5.16). The proposed method is based on insertion of variable delays between OFDM symbols such that the SRI is changed adaptively to counteract the change of the carrier frequency. For simplicity of representation, we describe the proposed approach based on slow-time chirps with positive slope only. That is, for $f_{c,a}(\mu) = f_{c,0} + \mu\Delta f_c$, $\mu \in [0, N_{\text{sym}})$, SRI is adapted with

$$T_{\text{SRI},a}(\mu) = T_{\text{SRI}} + T_a(\mu), \quad \mu \in [0, N_{\text{sym}}), \quad (5.18)$$

such that the product of the adaptive carrier frequency $f_{c,a}(\mu)$ and the adaptive SRI $T_{\text{SRI},a}(\mu)$ stays constant for all μ . In (5.18), T_{SRI} is the original SRI without the additional variable delay, and $T_a(\mu)$ denotes the adaptive, linearly changing delay of μ -th OFDM symbol that compensates for the linearly changing carrier frequency. Mathematically, the proposed condition can be expressed as

$$f_{c,a}(\mu)T_{\text{SRI},a}(\mu) = f_{c,\max}T_{\text{SRI}}, \quad \forall \mu, \quad (5.19)$$

with $f_{c,\max} = f_{c,0} + B_{\text{STC}}$. This leads to a reduction of the Doppler-induced phase term to a complex exponential with a constant frequency:

$$e^{-j2\pi f_{c,a}(\mu)T_{\text{SRI},a}(\mu)\gamma_i\mu} = e^{-j2\pi f_{c,\max}T_{\text{SRI}}\gamma_i\mu}, \quad \forall \mu. \quad (5.20)$$

In simple terms, the increase of the carrier frequency is balanced by the decrease of the SRI such that the product of the two stays constant. This can be interpreted as a modification of the signal frequency by adjustment of intervals between the sampling points, i.e. stretching/compression of the discrete-time axis. Substituting (5.19) into (5.18), $T_{\text{SRI},a}(\mu)$ is given as [Armanious, 2016]:

$$T_{\text{SRI},a}(\mu) = \frac{f_{c,\max}}{f_{c,0} + \mu\Delta f_c} T_{\text{SRI}}, \quad \forall \mu, \quad (5.21)$$

The signal processing is not influenced by the adaptive VSRI, i.e. is the same as for STC-WA described above. The velocity estimation parameters are determined by the product of the reference carrier frequency and SRI, and thus are

$$v_u = \frac{c_0}{2f_{c,\max} T_{\text{SRI}}}, \quad (5.22)$$

$$\Delta v = \frac{c_0}{2f_{c,\max} T_{\text{SRI}} N_{\text{sym}}}. \quad (5.23)$$

Thus, the insertion of linear adaptive delays between OFDM symbols enables an implicit compensation of the Doppler-induced quadratic phase term, i.e. leads to a linearization of the Doppler term over slow-time. This maintains the original velocity resolution and obtains full improvement of the distance resolution. Thus, STC-WA with VSRI is advantageous not only for waveform adaptation but also for improving the distance resolution. Concerning the hardware realization, the carrier frequency adaptation can be achieved with the help of adaptive variable-frequency LOs, and the adaptive delays can be introduced digitally. Therefore, both the enhancement of the interference robustness through waveform adaptation as well as improved distance resolution come with no significant increase of hardware costs.

Simulative analysis

In terms of cognitive radar, STC-WA represents a more flexible waveform adaptation method than CFH-WA. In fact, the latter can be considered as a special case of STC-WA with a zero-frequency-step in the slow-time, i.e. $\Delta f_c = 0$. Since for STC-WA the carrier frequency is adapted not only between measurements, but also during the measurement by a linear frequency sweep, it enables a better adaptation to chirp interference, especially if the latter covers the entire operational bandwidth with a moderate chirp repetition interval (CRI). To demonstrate this advantage of STC-WA, a chirp interference covering the entire 4 GHz operational bandwidth with a CRI of $T_{\text{CRI}} = 1.53$ ms is simulated. The OFDM signal is adapted to fit between two consecutive chirps with $\Delta f_c = 13.67$ MHz such that the interference is entirely avoided, as shown in Fig. 5.7.

Clearly, for slow enough interfering chirps STC-WA enables efficient interference avoidance through chirp-like waveform adaptation. Also, for this method it is advantageous to adapt the starting point of the measurement, as this can maximize the available interference-free measurement time. For this purpose, up-to-date spectral information with an update rate corresponding to the SRI of OFDM radar is required, which is the topic of the next section.

To show the impact of STC-WA on the distance-velocity estimation, we study the radar images for a target moving with high velocity. A target with a velocity $v = 60$ m/s at the distance of $d = 60$ m is simulated. The bandwidth of OFDM radar covered by slow-time chirps is $B_{\text{STC}} = 3.5$ GHz, i.e. the frequency band from 77.25 GHz to 80.75 GHz is swept with a step $\Delta f_c = 13.67$ MHz. Simulations are performed in a noiseless setup. As a reference, results for the conventional OFDM radar with a constant carrier frequency of 79 GHz are shown. To demonstrate the improvement for STC-WA through VSRI, we present the radar images both in (k, l) and (d, v) -dimensions.

The (k, l) -image in Fig. 5.8b shows that in case of STC-WA, the target peak is shifted in l -dimension due to the additional distance-induced exponential term in slow-time. Moreover, the peak is widened due to the quadratic Doppler term. This leads to a peak expansion in the (d, v) -image after the axis transformation, as Fig. 5.8d shows. In addition to the peak expansion,

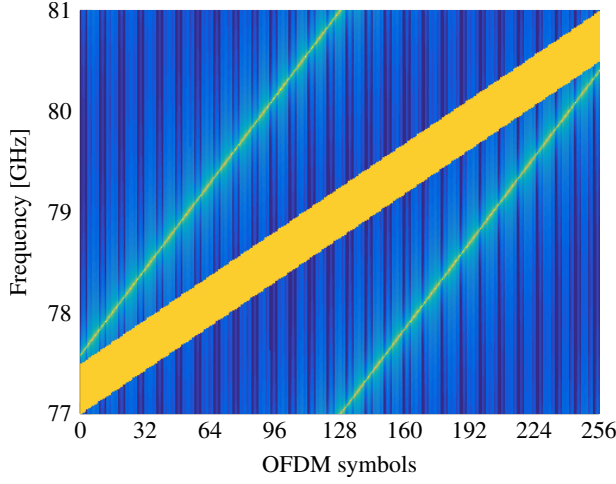


Figure 5.7.: STC-WA applied for avoidance of a chirp interference with $B_c = 4$ GHz and $T_{CRI} = 1.53$ ms. Due to the large bandwidth of interfering chirps, in this scenario STC-WA is more advantageous than CFH-WA

in both (k, l) -space and (d, v) -space the peak shape is changed: it is split into two adjacent peaks — a shape characteristic for a chirp spectrum. The latter is adverse for the radar estimation, since it leads potentially to a detection of two closely spaced targets. Furthermore, through the peak expansion the target SNR is reduced, since the energy is spread over multiple neighboring cells. These adverse effects are avoided by the use of VSRI, as shown in Fig. 5.8e and Fig. 5.8f. Evidently, with VSRI the peak expansion is prevented, resulting in sharp peaks both in (k, l) -image and (d, v) -image. Hence, the original SNR and velocity resolution are maintained, and full improvement of the distance resolution due to the slow-time bandwidth is achieved.

The presented results suggest that not only adaptation to chirp interference is enabled by STC-WA with VSRI, but also the distance resolution is effectively improved due to the use of larger bandwidth in slow-time. It should be noted, however, that the improvement of the distance resolution comes at the cost of shaping the ambiguity into another form: a stretched ellipsis in the distance-velocity space (see. Fig. 5.8f). Note that the sidelobes in distance-velocity space due to the limited bandwidth and measurement time (see. Fig. 5.8d and Fig. 5.8f) are also shaped accordingly along the axis of the ellipsis of target peaks. This is yet advantageous both in the sense that a valuable parameter such as distance resolution is improved without increase of the sampling rate, as well as due to the fact that this form of ambiguity is potentially less adverse due to physical factors.

The adaptivity achievable with STC-WA approaches its limits for chirps with a repetition interval in μs range. To adapt to this kind of interference in scenarios where both CFH-WA and STC-WA are not sufficient, more flexible approaches are required — e.g. arbitrary adaptation of the carrier frequencies for individual OFDM symbols. Such approaches require, however, more sophisticated signal processing methods, since the distance-induced phase term over the slow-time is no longer growing linearly. Even though we do not study such waveform adaptation methods in this work due to limited time, it is worth to note that VSRI is analogously applicable also in case of arbitrary carrier frequency adaptation.

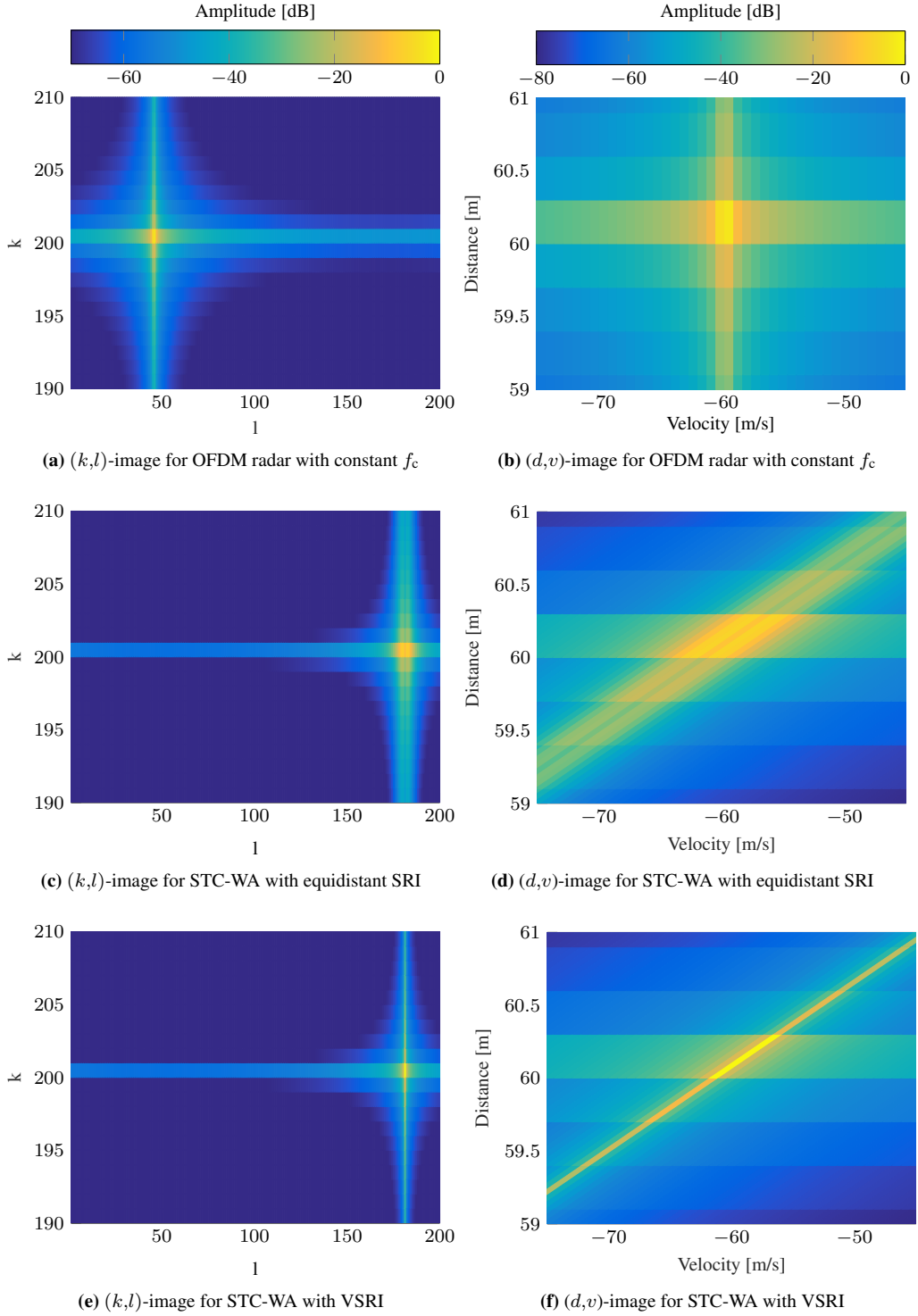


Figure 5.8.: Comparison of STC-WA with equidistant SRI, STC-WA with VSRI, and the classical OFDM radar with constant carrier frequency: target with $v = 60$ m/s and $d = 60$ m, rectangular window (colorbar of (a) applies to (c) and (e), and that of (b) to (d) and (f))

5.4.3. Spectrum Sensing

We define the spectrum sensing as the process of capturing the total available spectral band and scanning for interference. Spectrum sensing enables awareness of the spectral situation, and thus a subsequent adaptation of the radar transmit signal to avoid interference. The challenge for spectrum sensing is the large bandwidth of the potentially available spectral band that needs to be sensed.

In case of sampling at Nyquist rate, sensing of the entire operational band requires ADCs with very high sampling rates. This reflects notably on the system costs, and thus is impractical. An alternative state-of-the-art approach [Mishali, 2010, 2011] considers the problem of blindly sensing multiple narrow bands in a large frequency band, and uses multiple receive paths with sub-Nyquist ADCs for this purpose. The use of multiple sampling paths affects again the system costs. Moreover, the assumption of only a few narrow spectral bands being occupied does not apply to our application. Therefore, to enable efficient spectrum sensing, more practical approaches are required.

In fact, the spectrum sensing module is required to be *i)* cost efficient, *ii)* sense the entire bandwidth, and *iii)* have a high update rate to provide timely and up-to-date spectral information. The accuracy of spectrum sensing, in contrast, is to a large extent of no concern, since only interference detection, and not analysis of its signal is of interest. In what follows, a spectrum sensing technique that overcomes costly hardware demands is introduced, which we name *stepwise spectrum sensing* (SW-SS)². The proposed method is capable of providing spectral information with a high update rate, as required for effective adaptation with CHF-WA and STC-WA.

The SW-SS technique is based on the idea of sensing the entire spectrum in multiple steps, using the hardware available for OFDM radar. The sensing is performed continuously and delivers up-to-date spectral information with an update rate $1/T$, where T is the OFDM symbol duration. For spectrum sensing, we consider the standard hardware architecture of the OFDM radar receiver realized with IQ-sampling (Fig. 5.9). In contrast to the conventional OFDM radar, here we consider a variable frequency LO instead of the stable frequency LO. The former can be realized with the help of PLLs, or in a digital realization, with DDSs. The downconverted signal is filtered with a low pass filter to suppress out-of-band frequency components. The filtered receive signal is then sampled using ADCs at Nyquist rate, which is $f_s = B$ for IQ-sampling. Accordingly, the number of discrete complex samples N_s obtained from one OFDM symbol of a duration T is $N_s = N_c$. In case of real sampling both the ADC-rates and the resulting number of samples are double of that for the IQ-sampling.

The process of sampling for one symbol of OFDM radar is shown in Fig. 5.10a, according to the parametrization considered in Section 5.4.2. The LO is tuned to a stable carrier frequency of $f_c = 79$ GHz; the downconverted receive signal is low pass filtered and sampled with $f_s = 500$ MHz. Accordingly, from one OFDM symbol with a bandwidth of $B = 500$ MHz and a duration of $T = 8.192 \mu\text{s}$, $N_s = 4096$ complex samples are obtained.

For spectrum sensing in the context of cognitive OFDM radar, however, an approach that allows sampling of a significantly larger bandwidth — preferably in the same time interval T — is

² The principle of sequentially sensing subbands of a large spectral band is known from some other applications such as cognitive radio (see e.g. [Bkassiny, 2012])

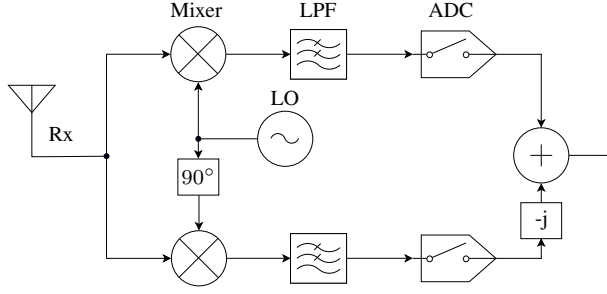


Figure 5.9.: Hardware architecture of an OFDM receive channel with IQ-sampling. LFP denotes the low pass filter

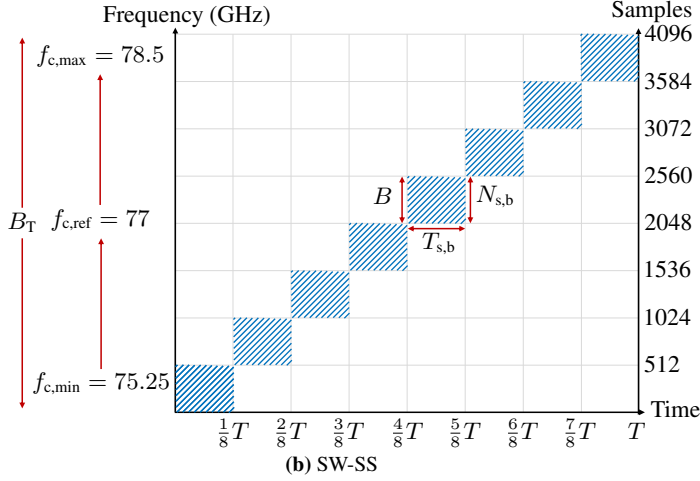
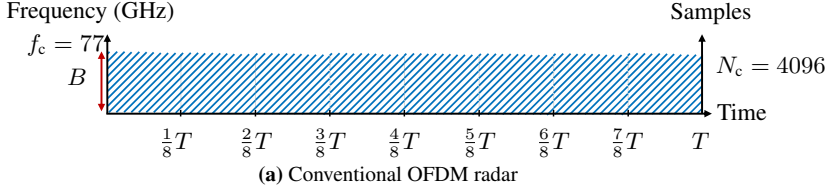


Figure 5.10.: Sampling and building of the spectrum: (a) Conventional OFDM radar vs. (b) SW-SS [Armanious, 2016]

required. We denote the total operational bandwidth to be sensed by $B_T = N_b B$, where N_b is the factor between the OFDM radar bandwidth B and the total bandwidth to be sensed B_T . The straightforward approach of sampling the entire operational band at Nyquist rate results in ADC rates often unachievable or too expensive (e.g. IQ-sampling ADCs with 4 Gs/s sampling rate for $B_T = 4$ GHz). To overcome this, we take advantage of the fact that the resolution and accuracy of the spectrum reconstruction are not primarily of interest for cognitive radar — in the first place, information about the spectrum occupancy is of relevance. Consequently, a coarse estimation of the spectrum is sufficient for our application. Therefore, the approach we propose operates at the same ADC-rates as already used for OFDM radar, and senses the entire operational frequency band by shorter observations of each spectral slice. More specifically, the operational spectral band is divided into N_b slices, and each slice of a bandwidth B is sensed at a time for a time duration T/N_b . This stepwise sensing of a large spectral band leads to a more coarse spectral

estimate, since each spectral slice is observed for a shorter time $T_b = T/N_b$. During the symbol duration T , the carrier frequency is stepped through all frequency slices, and each slice is sampled with $f_s = B$, resulting in N_c/N_b samples for each slice. Hence, the overall number of samples obtained during the OFDM symbol duration T stays the same as for conventional OFDM radar, i.e. BT .

This approach is illustrated in Fig. 5.10b for parameters $B_T = 4\text{ GHz}$, $B = 500\text{ MHz}$, and $N_b = 8$. From each 500 MHz spectral slice, 512 samples are obtained. Since the observation time for each slice is reduced by $N_b = 8$, also the spectral resolution is reduced by the same factor. Once signals of all spectral slices are sampled, the spectrum for the entire 4 GHz band is obtained via FFTs of each slice and concatenation of these into a single frequency spectrum. Then, the positions of occupied frequencies can be detected by an energy detector, e.g. a CFAR algorithm. That is, if the energy at some frequency exceeds a certain threshold, this frequency is marked as occupied. Finally, based on this the spectrum sensing block yields an occupancy grid for the entire spectrum with an update rate $1/T$. This enables up-to-date spectral awareness required for waveform adaptation.

Note that the stepwise sensing approach does not cover the entire time-frequency space for the operational band B_T and time duration T , but only a part of it, such that each spectral slice is sensed at a time. Whereas theoretically this might lead to a missed detection of interference present in the operational band but not intersecting with the sensing pattern, in practice this issue is irrelevant, since the sensing is switching between the spectral slices much faster than the potential interference signal is changing. Due to this reason the probability of missing interference because of the stepwise sensing is very low. It can be further reduced by the choice of the sensing pattern, e.g. random patterns instead of the linearly increasing steps shown in Fig. 5.10b.

SW-SS will typically be realized in the form of an additional receive path dedicated solely to spectrum sensing. This path needs to have a dedicated variable frequency LO, since the available LO is used for radar functionality and is dedicated to waveform adaptation. This can also be implemented as a stable frequency LO tuned to some reference frequency and used for both functions, in addition to which for both waveform adaptation and spectrum sensing two separate DDSs are used. Furthermore, since for spectrum sensing the requirements for the ADC in terms of number-of-bits are less strict, for this additional channel more cost-efficient ADCs with lower resolution can be used. Thus, in terms of hardware components SW-SS requires only an additional receive path and dedicated variable frequency LO.

In summary, SW-SS represents an efficient method for coarse spectrum sensing with a high update rate. It requires hardware components already available for OFDM radar, and can be realized with moderate hardware expenses in the form of an additional receive channel.

5.5. Concluding Remarks

In the long term, interference robustness is a major issue for automotive radar that increasingly gains importance due to the growing number of radar sensors. OFDM radar offers a large degree of flexibility due to digital signal generation and processing, and thus has a potential for a better interference robustness than the conventional radar systems with analog modulation. Specifically, the large number of degrees of freedom for the waveform choice increases to a great extent the probability for the radar signal being uncorrelated with the interference. As a consequence, such

interference has a noise-like impact on OFDM radar, i.e. it increases the overall noise floor but does not lead to ghost targets. In this regard, OFDM radar has a major advantage compared to the state-of-the-art radars operating with linear frequency chirps, since for the latter the chance of correlated interference due to similar slopes is higher. However, in contrast to FMCW and chirp-sequence radars, for OFDM radar no methods for analog filtering of interference residing in the same frequency band exist, and thus methods for additional interference mitigation are required.

For suppression of arbitrary narrowband interferences, we proposed an algorithm based on exclusion of corrupted OFDM subcarriers and recovery of their values with the help of linear prediction methods. This interference suppression technique is applicable also to interference from state-of-the-art FMCW radars with slow ramps, and thus is of high relevance to OFDM radar. Next, we discussed the approaches known from the literature for interference robustness between OFDM radar systems operating in networks as well as methods for suppression of OFDM interference.

Finally, to increase the interference robustness of OFDM radar in a universal manner, we proposed the notion of interference-aware cognitive radar comprising three main blocks: spectrum sensing, spectrum interpretation and waveform adaptation. We focused in our work primarily on the last block and proposed two waveform adaptation methods: CFH-WA and STC-WA. Since the latter is based on linearly increasing carrier frequency over slow-time, it effectively covers larger bandwidth and thus improves additionally the distance resolution. However, it leads to a second-order Doppler term, which has an adverse effect on the detection performance. To overcome this drawback, we proposed the use of VSRI, which implicitly compensates the quadratic Doppler term. For spectrum sensing, we proposed a practical method that enables sensing of a large bandwidth with a high update rate using the available OFDM radar hardware components.

Chapter 6.

OFDM-MIMO Radar Prototype and Experimental Validation of the Proposed Methods

In this chapter, a prototypical realization of an OFDM-MIMO radar at 24 GHz is presented. The constructed radar prototype serves two purposes: *i*) to confirm experimentally the feasibility of OFDM as a modulation for high-performance automotive radar, and *ii*) to provide a platform for experimental validation of the proposed algorithms. Compared to OFDM radar realizations known in the literature [Sturm, 2012b; Pfeffer, 2014, 2015], the presented prototype is superior in several essential aspects: *a*) it realizes a bandwidth of 625 MHz per OFDM symbol, *b*) achieves a dynamic range above 60 dB in distance-velocity estimation, *c*) uses MIMO for improved DOA estimation realized with a patch antenna array, and *d*) achieves an update rate for the entire radar measurement below 1 s, enabling measurements in dynamically changing scenarios. In the following, the hardware setup as well as the baseband signal processing of the realized OFDM-MIMO radar prototype is described, followed by measurement results to demonstrate the radar performance. Then, the distance-velocity estimation algorithms presented in Chapter 3, multiplexing methods and SIMFE algorithm proposed in Chapter 4, and interference mitigation methods described in Chapter 5 are validated experimentally using measurements with the presented OFDM-MIMO radar prototype.

6.1. Description of the System Prototype¹

The OFDM-MIMO radar system prototype is realized at 24 GHz based on discrete high-frequency components and laboratory devices. The choice of the operational frequency band is dictated by the availability of RF components and devices. Although the target frequency band for the considered automotive OFDM radar is at 77 GHz, for the purposes of validation of the system performance and the proposed signal processing methods, a prototype operating at 24 GHz is analogously applicable. The system is designed to facilitate a high degree of flexibility in terms of configuration of radar parameters, such that different digital radar concepts can be directly implemented and tested. For this purpose, the system employs large digital resources in terms of digital signal generation as well as high-rate sampling and digital signal processing. The system prototype comprises the following main components:

¹ Contributions of this section have been partially reported in [Hakobyan, 2016f]. Some of the author's own formulations in [Hakobyan, 2016f] are adopted in the text. The antenna design was carried out by a co-author.

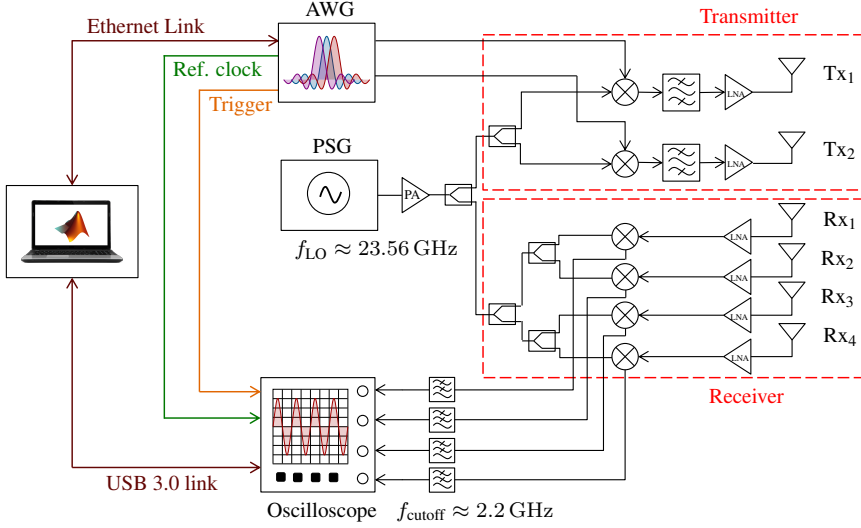


Figure 6.1.: Block diagram of the OFDM-MIMO radar prototype

- Arbitrary waveform generator (AWG) Tektronix AWG70002A
- RF signal generator Agilent PSG-L series E8244A
- A 6-channel RF-front-end that realizes 2×4 MIMO channels and is built of modular components including power amplifier (PA), power dividers, mixers, band pass filters (BPF), a patch antenna array, low noise amplifiers (LNA), and low pass filters (LPF).
- Oscilloscope Keysight Infiniium S-Series MSOS404A
- Computer with Matlab software

The block diagram of the system prototype is presented in Fig. 6.1 and a photograph of it in an anechoic chamber is shown in Fig. 6.2.

At the Tx path, the OFDM signal samples for both Tx channels are synthesized digitally at the intermediate frequency (IF) of 937.5 MHz using Matlab and then loaded into the AWG via an Ethernet link. The AWG generates the predefined OFDM waveform with a bandwidth of 625 MHz (or less) and sampling rate of 25 GS/s. In simple terms, the AWG realizes the function of the DAC with 10 bit resolution. Since two AWG outputs are used to generate signals of two Tx channels, for both Tx channels real and not IQ-signals are generated by the AWG. These signals are up-converted to the carrier frequency of 24.5 GHz with passive single-sideband (SSB) mixers by mixing with a carrier signal at 23.5625 GHz. The carrier signal is generated by the PSG that operates as an LO. A tunable BPF with 1 GHz passband at the center frequency of 24.5 GHz is used to filter out the lower sideband of the SSB mixers. The resulting RF signal is amplified with LNAs and is fed to Tx antennas. For a sinusoidal signal, the achieved transmit power at the input of the Tx antennas is ≈ 8 dBm.

A series feed MIMO patch antenna array with a focused beam in elevation and a wide beam in azimuth is used [Hakobyan, 2016f]. The patch antennas are optimized for a bandwidth of 1 GHz around the center frequency of 24.5 GHz and have a gain of 13 dBi. The spacing between two adjacent Rx antennas is $1.4\lambda_c$ and the spacing between two Tx antennas is $2.1\lambda_c$, with λ_c denoting the wavelength of the carrier signal. The antennas are placed such that according to the

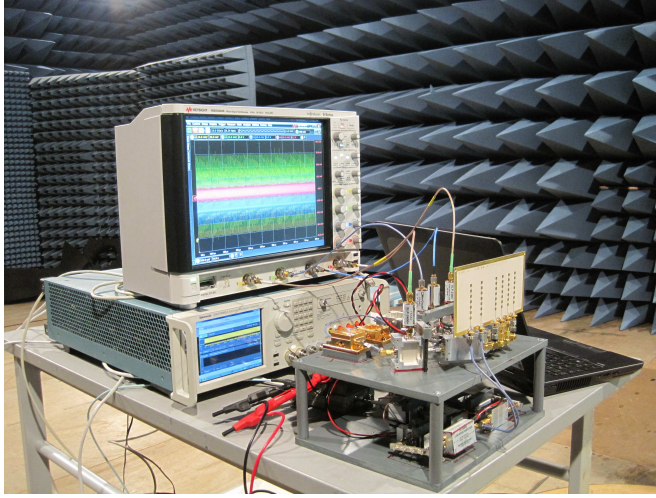


Figure 6.2.: Photo of the OFDM-MIMO radar prototype in an anechoic chamber [Hakobyan, 2016f]

MIMO principle the gaps between Rx antennas are filled with virtual antennas to obtain a spacing of $0.7\lambda_c$. The resulting antenna array allows for unambiguous DOA estimation in azimuth at the range of $\pm 45^\circ$.

At the receive path, signals from the Rx antennas are amplified with the help of LNAs and down-converted to the IF with passive SSB mixers by mixing with the carrier signal from the PSG. A low pass filter with a cut-off frequency of 2.2 GHz is used at the input of the oscilloscope for reduction of high frequency noise. The resulting signal at each of the four receive paths is sampled by the four-channel oscilloscope at a frequency at least twice the highest frequency of the received IF signal (typically sampled at 5 GHz). Finally, the sampled signal is acquired from the oscilloscope through a USB 3.0 link, and the entire radar signal processing is carried out in Matlab.

The sampling at a high rate is dictated by the real sampling at IF and by the fixed sampling frequencies the oscilloscope can operate at. In this setup, the oscilloscope operates as a 10 bit ADC. The start of the sampling is initiated by a trigger signal from the AWG. To this end, two options are available: either to capture the entire measurement cycle after the first trigger enable signal, or to capture each OFDM symbol individually as the trigger enable for each symbol is received. The latter enables more efficient memory usage when CP is used or breaks between OFDM symbols are included. To synchronize the clocks between the AWG and the oscilloscope, a 10 MHz reference clock signal from AWG is fed to the oscilloscope.

Since the received signal is sampled at IF (typically at $f_{IF} = 937.5$ MHz) with a sampling frequency beyond the Nyquist rate (typically at 5 GHz), first a digital IF-demodulation and baseband signal processing is needed to obtain the complex-valued baseband signal at Nyquist rate. For this purpose, the signal is down-converted digitally to baseband via a multiplication with a carrier signal of the intermediate frequency. The baseband signal is then filtered with a zero-group-delay *half-band filter* (HBF) with a stopband suppression of 80 dB to eliminate the second sideband and out-of-band noise. A decimation with a factor of two is performed to reduce the sampling rate. Since in the used setup the sampling frequency f_s is a multiple of the bandwidth, the last two steps are performed iteratively f_s/B times until the sampling rate is

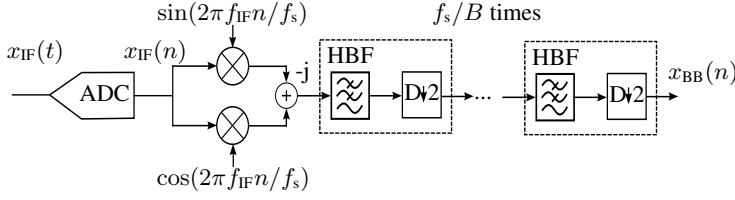


Figure 6.3.: Block diagram of the OFDM-MIMO radar prototype [Hakobyan, 2016f]

reduced down to the Nyquist rate. The basic principle of the baseband signal processing including the IF-demodulation is shown in Fig. 6.3, where $x_{IF}(n)$ denotes the sampled real-valued IF-signal, $x_{BB}(n)$ is the complex-valued baseband signal at Nyquist rate, and n is the sample index.

Note that the described baseband signal processing does not take advantage of the sampling at a higher rate to improve the input SNR, in order to keep the results of the prototype comparable to a real world realization with a Nyquist rate sampling. Furthermore, it should be noted that the actual implementation for the prototype is a computationally efficient equivalent of the described processing.

The subsequent signal processing for distance-velocity estimation is carried out as described in Chapter 3. The distance-velocity images of different spatial channels are integrated non-coherently, followed by detection with an OS-CFAR [Rohling, 1983] performed on the NCI distance-velocity image. For the detected peaks, the complex amplitudes from spatial channels are fed to the DOA estimation, which is performed through digital beamforming with a conventional Bartlett beamformer [Bartlett, 1950]. After the DOA estimation, a target list with distances, velocities and DOAs of the detected targets is obtained at the output of the radar processing.

As typical for radar systems, for accurate DOA estimation phase calibration of the spatial channels is required. In our setup, we perform a DOA-independent phase calibration using phases of spatial channels measured for a predefined target (corner reflector) with a DOA of 0° . Furthermore, to ensure that targets at all spatial channels have the same distance index, a distance calibration is required due to the modular setup with comparably long cables. This is done by measuring the delay differences in spatial channels and circular shifting of the time signals in each spatial channel by a number of samples corresponding to its delay.

Despite the massive data loads² generated due to the sampling at a high rate, an update rate below 1 s is achieved by implementation of some signal processing steps on the graphics processing unit (GPU) as well as due to processing in multiple threads for data acquisition, signal processing, and visualization of results. These three threads are running in parallel with a one cycle delay — with an update rate of the slowest thread.

The remainder of this chapter provides measurements both for performance verification of the radar prototype as well as for the validation of the signal processing methods and radar concepts proposed in this work. For each measurement scenario, a parametrization suited to the purpose of the measurement is used; all measurements are performed at carrier frequency of 24.5 GHz.

² For the configuration in Table 6.1, the data acquired from all four Rx channels for one measurement cycle are approximately 268 MB

Table 6.1.: Parametrization for the OFDM-MIMO radar measurements in an anechoic chamber

Modulation parameters	CP-OFDM	RS-OFDM
B	625 MHz	625 MHz
N_c	2048	2048
$\Delta f = B/(N_c \gamma)$	≈ 76.3 kHz	≈ 76.3 kHz
$T = 1/\Delta f$	≈ 13.1 μ s	≈ 13.1 μ s
$T_{\text{SRI}} = T + T_{\text{CP}}$	≈ 14.74 μ s	≈ 13.1 μ s
N_{sym}	455	512
$T_{\text{cycle}} = N_{\text{sym}} T_{\text{SRI}}$	6.7 ms	6.7 ms
Radar parameters	CP-OFDM	RS-OFDM
$d_u = c_0/(2\Delta f \gamma N_{\text{Tx}})$	≈ 245.75 m	≈ 245.75 m
$v_u = \pm c_0/(4f_c T_{\text{SRI}})$	$\approx \pm 207$ m/s	$\approx \pm 234$ m/s
$\Delta d = c_0/(2B)$	0.24 m	0.24 m
$\Delta v = c_0/(2f_c T_{\text{meas}})$	≈ 0.91 m/s	≈ 0.91 m/s

6.2. Measurements for Performance Verification of the System Prototype

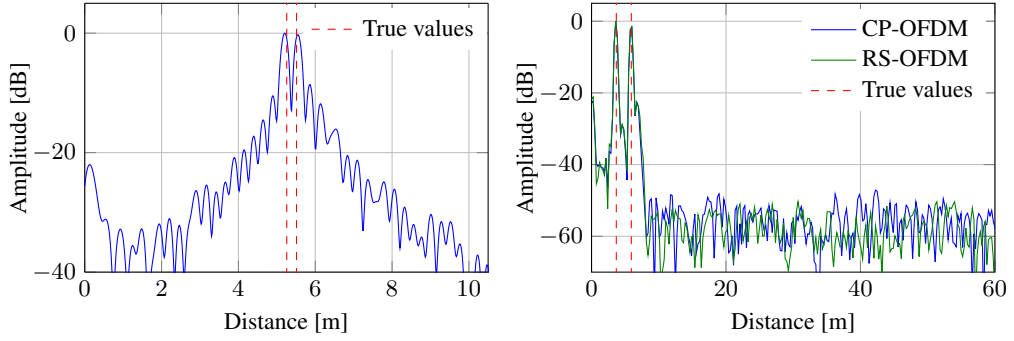
For performance verification, radar measurements both in an anechoic chamber as well as in a road scenario are carried out. For these measurements, the conventional OFDM radar signal processing described in Section 3.2 is used. OFDM subcarriers are modulated with complex modulation symbols of equal amplitude and random phase in order to keep the performance representative for the general case without PAPR optimization. The two Tx channels are multiplexed via EqSI, with each using half of the subcarriers. These measurements are to confirm the system performance of the radar prototype as well as to demonstrate both the suitability and the practical feasibility of OFDM for high-end automotive radar applications.

6.2.1. Measurements in an Anechoic Chamber³

For the measurements presented below, the configuration given in Table 6.1 is used. This table includes two slightly different parametrizations for RS-OFDM and CP-OFDM operation modes, since the former omits CP, and thus achieves shorter SRI. The total measurement time is kept the same for both CP-OFDM and RS-OFDM modes to allow a meaningful comparison. The duration of the CP for CP-OFDM matches to the unambiguously measurable distance range. As in Section 5.4.2, due to SNR considerations zero-subcarriers are added in between the used ones, resulting effectively in an extension of the OFDM symbol duration by a factor $\gamma = 4$.

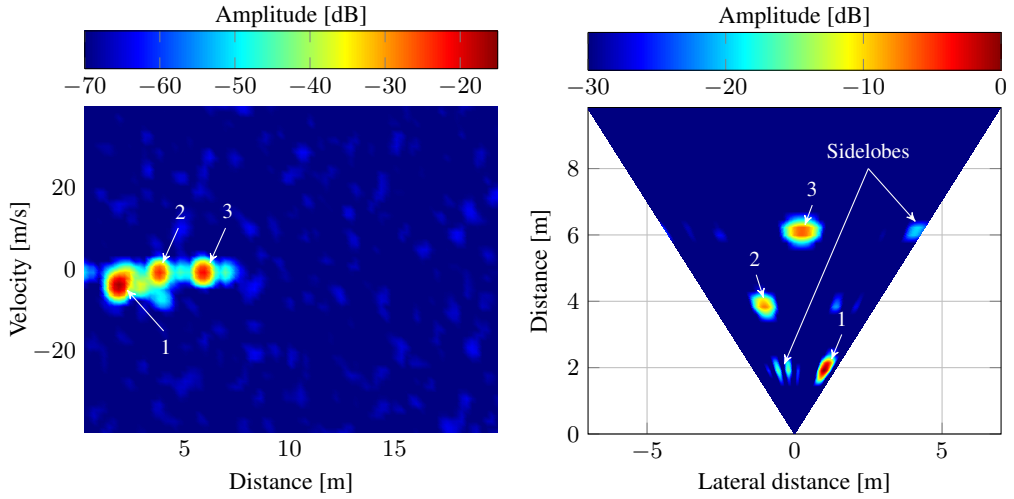
To verify the theoretically achievable distance resolution, measurements with two closely located stationary targets were carried out. Two corner reflectors of the same size were placed at the distance of 5.493 m and 5.748 m, i.e. with a distance difference of 25.5 cm. The result of the

³ Contributions of this section have been partially reported in [Hakobyan, 2016f]. Some of the author's own formulations in [Hakobyan, 2016f] are adopted in the text.



(a) Distance measurement of two closely placed targets (rectangular window) (b) Zero-Doppler cut of the distance-velocity image for two stationary targets: CP-OFDM vs. RS-OFDM

Figure 6.4.: Distance estimation for stationary targets in an anechoic chamber



(a) Distance-velocity radar image

(b) Distance and DOA measurements represented in a distance-lateral-distance image

Figure 6.5.: Radar measurements in a three-target scenario; two stationary and one slowly moving targets in an anechoic chamber

distance estimation with a single OFDM symbol and rectangular window is shown in Fig. 6.4a. Clearly, the targets are resolved distinctly in the distance dimension, which confirms the distance resolution theoretically achievable for the given bandwidth. Note that if a window function other than rectangular is used, the distance resolution is reduced accordingly.

To compare the performance of RS-OFDM and CP-OFDM, the zero-Doppler cut of the distance-velocity image for both operation modes is presented in Fig. 6.4b. Two targets at the distances of 3.9 m and 6.12 m are measured; for sidelobe suppression a Kaiser window with $\beta = 7$ is used in both distance and velocity dimensions. Fig. 6.4b shows that in addition to the increased unambiguous velocity range obtained by omitting CP (see Table 6.1), RS-OFDM achieves a slightly higher SNR due to integration of more OFDM symbols in the same measurement time. For moderate CP duration, however, this SNR improvement is not essential when considered on

a logarithmic scale.

To demonstrate the system performance in distance-velocity estimation, a scenario with two stationary targets from Fig. 6.4b and a slowly moving target with a velocity of approximately -3 m/s at around 2 m was measured with RS-OFDM (Fig. 6.5a). In this scenario, the dynamic range achieved in the distance-velocity radar image is above 50 dB (Kaiser window, $\beta = 7$). The distance and DOA estimation for this scenario is presented in Fig. 6.5b in a distance-lateral-distance representation.

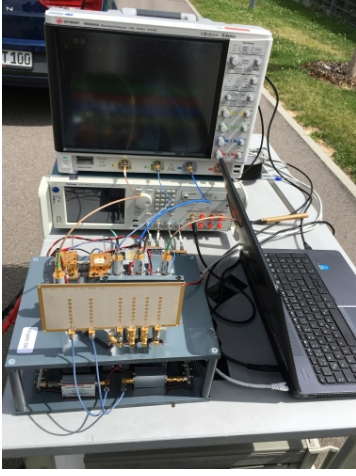
6.2.2. Measurements in a Road Scenario

To verify the system performance in a real life scenario, measurements of a car driving towards the radar in a road scenario are carried out (Fig. 6.6). The configuration used for these measurements is given in Table 6.2. To obtain a high velocity resolution with moderate number of OFDM symbols, the SRI is set to $36 \mu\text{s}$, which results in an unambiguous velocity range of $\approx 170 \text{ m/s}$, i.e. $\pm 85 \text{ m/s}$. Due to the memory limitations of the oscilloscope, however, considerably shorter OFDM symbols are used with CP: $T \approx 3.28 \mu\text{s}$.

Fig. 6.7a shows the distance-velocity image of the measured scenario. The car moving towards the radar is at around 33 m , moving with a velocity around -13.5 m/s . A Kaiser window with $\beta = 7$ is used for sidelobe suppression. Detection is performed with OS-CFAR, which is configured such that only few dominant targets are detected. Detections are plotted additionally on the radar image as red stars to enable a clear representation of the measured scenario. Stationary targets — mainly buildings — can be seen in the zero-velocity cell, whereas the car moving towards the radar is clearly distinguished as several reflections at the distances of 32 m to 36 m with a velocity around -13.5 m/s . The colorbar limit matches to the amplitude of the highest peak, i.e. internal coupling at around 30 dB . Clearly, the dynamic range determined through the highest peak and the noise floor is above 80 dB . Note that as opposed to the Fig. 6.5a, no suppression of the peak induced by the crosstalk (direct coupling between the radar antennas) is performed in this measurement, and the highest peak is the one induced by the crosstalk. Regardless of the fact that in Fig. 6.7a the dynamic range is determined by the crosstalk, it shows the ability of OFDM radar to achieve a high dynamic range in the distance-velocity estimation.

To show the DOA estimation capabilities of the radar prototype, the distance-lateral-distance image is presented in Fig. 6.7b (often referred to as range-cross-range representation). The results of the DOA estimation with a conventional Bartlett beamformer together with the distance values are transformed into the lateral-distance. This is done for all velocity cells, which are then projected into a single 2D-image via NCI — similar to the NCI of the distance-velocity radar images for improved detection performance. To compensate the amplitude differences in the distance dimension, the results are normalized to the signal energy for each distance cell. Albeit not entirely representative of the radar detection, this results in a realistic visual representation of the radar measurements in the spatial domain. Also in this representation, detections of the dominant targets are plotted for the clarity of visual representation. Both stationary targets on the left side of the road as well as the car driving towards the radar are clearly distinguishable in this image.

The presented measurements demonstrate the high performance of the constructed OFDM-MIMO radar prototype in distance-velocity estimation. This confirms experimentally the suitability of OFDM as a modulation for high-performance radar applications. Furthermore, the DOA



(a) OFDM-MIMO radar prototype



(b) The measured road scenario

Figure 6.6.: Photos of the measurement setup (scenario, radar prototype) during outdoor measurements

Table 6.2.: Parametrization for the OFDM-MIMO radar measurements in an road scenario

Modulation parameters	Values	Radar parameters	Values
B	625 MHz	$d_u = c_0 / (2\Delta f \gamma N_{Tx})$	≈ 245.75 m
N_c	2048	$v_u = \pm c_0 / (4f_c T_{SRI})$	$\approx \pm 85$ m/s
$\Delta f = B/N_c$	≈ 305.2 kHz	$\Delta d = c_0 / (2B)$	0.24 m
$T = 1/\Delta f$	≈ 3.28 μ s	$\Delta v = c_0 / (2f_c T_{meas})$	≈ 0.33 m/s
T_{SRI}	≈ 36 μ s		
N_{sym}	512		
$T_{cycle} = N_{sym}T_{SRI}$	≈ 18.5 ms		

measurements with the MIMO principle prove the applicability of OFDM subcarrier interleaving as a multiplexing method for MIMO radar. Such multiplexing has a major advantage in terms of simultaneous measurements for all Tx channels which cover the same bandwidth, since this enables a high degree of coherence between the Tx channels, and thus accurate MIMO radar processing.

6.3. Experimental Validation of the Proposed Distance-Velocity Estimation Algorithms

6.3.1. Validation of ACDC in a Road Scenario⁴

For validation of the ACDC based processing described in Section 3.3, measurements in a road scenario are carried out. Analogous to the road measurements in the previous section, the target of

⁴ Contributions of this section have been partially reported in [Hakobyan, 2017a]. Some of the author's own formulations in [Hakobyan, 2017a] are adopted in the text.

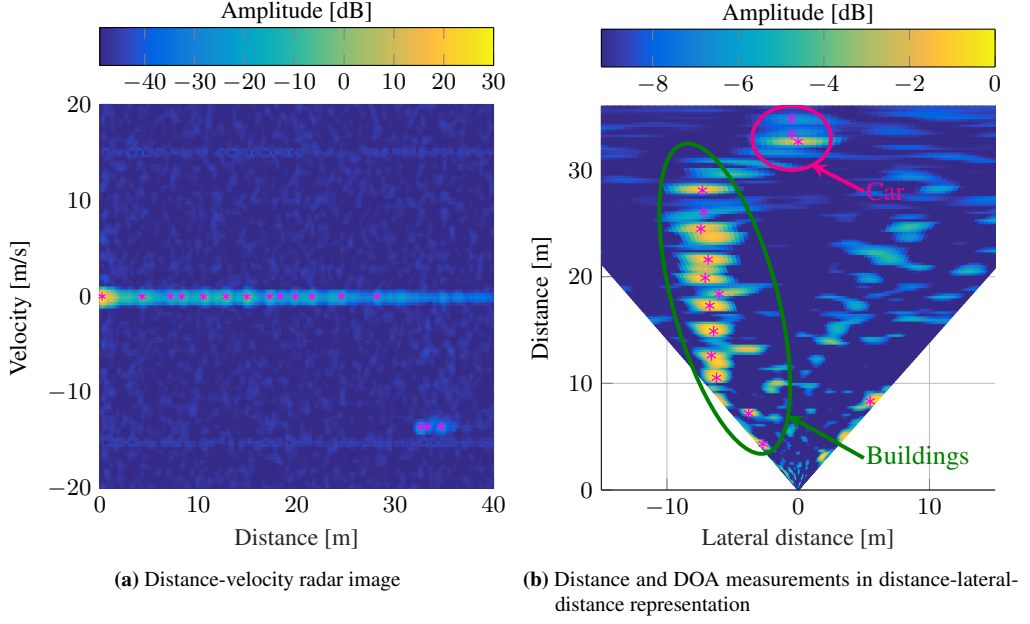


Figure 6.7.: Radar measurements in the road scenario from Fig. 6.6

Table 6.3.: OFDM radar parametrization for experimental validation of ACDC based processing

Modulation parameters	Values	Radar parameters	Values
B	75 MHz	$d_u = c_0/(2\Delta f)$	16 384 m
N_c	8192	$v_u = \pm c_0/(4f_c T_{\text{SRI}})$	$\approx \pm 28$ m/s
$\Delta f = B/N_c$	9.16 kHz	$\Delta d = c_0/(2B)$	2 m
$T = 1/\Delta f$	109 μ s	$\Delta v = c_0/(2f_c T_{\text{meas}})$	0.219 m/s
N_{sym}	128		
$T_{\text{SRI}} = T$	109 μ s		
$T_{\text{meas}} = N_{\text{sym}} T_{\text{SRI}}$	13.98 ms		

interest is a car driving towards the radar prototype (see Fig. 6.6). The latter is configured such that the measured target leads to a significant Doppler shift of OFDM subcarriers. The parametrization used for the measurements is presented in Table 6.3. For this measurement, only one transmit and one receive channel is used, which considerably reduces the data loads and enables a high update rate. Due to the fact that at 24 GHz the Doppler effect is considerably less than that at the target frequency of 77 GHz, the radar bandwidth is restricted to $B = 75$ MHz to achieve a tight subcarrier spacing. With $N_c = 8192$ subcarriers a subcarrier spacing $\Delta f \approx 9.16$ kHz is obtained. The target drives towards the radar with a velocity $v \approx -68.4$ km/h ≈ -19 m/s, which results in a Doppler shift of $f_D \approx 3.1$ kHz, i.e. $\tilde{f}_D = f_D/\Delta f \approx 0.34$. The radar operates in RS-OFDM mode with modulation symbols that have unit amplitudes and random subcarrier phases.

The distance-velocity radar image for the ACDC based processing of the measured scenario is shown in Fig. 6.8b and compared to that of the classical OFDM radar processing shown in Fig. 6.8a. At the time of the measurement the target is at the distance of around 17 m. Due to

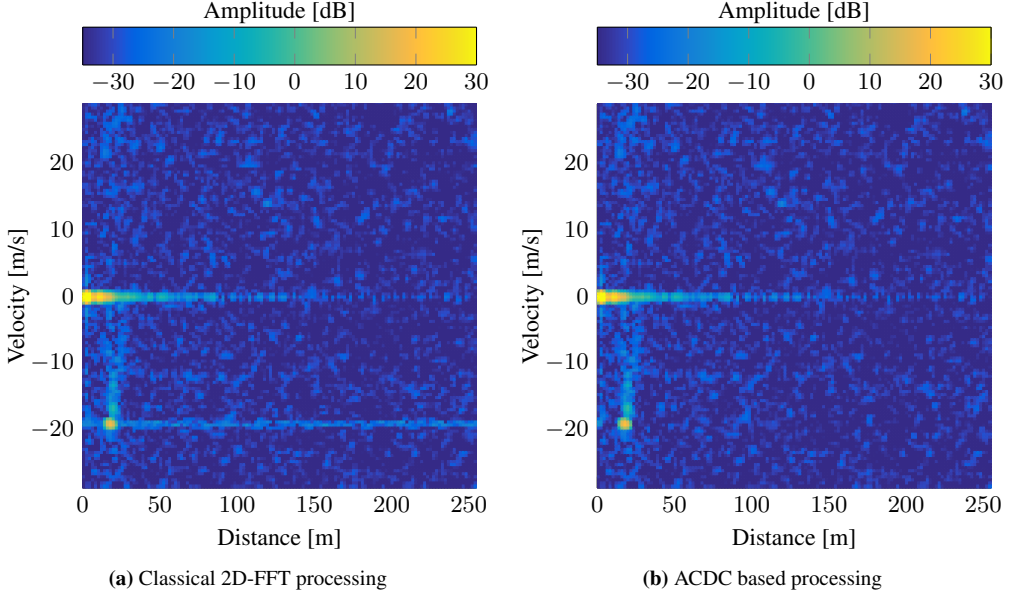


Figure 6.8.: Radar image for a car moving with $v \approx 19$ m/s (Kaiser window with $\beta = 7$)

Table 6.4.: OFDM radar parametrization for experimental validation of ACMC based processing

Modulation parameters	Values	Radar parameters	Values
B	625 MHz	$d_u = c_0/(2\Delta f)$	491.5 m
N_c	2048	$v_u = \pm c_0/(4f_c T_{\text{SRI}})$	$\approx \pm 40$ m/s
$\Delta f = B/N_c$	≈ 305.2 kHz	$\Delta d = c_0/(2B)$	0.24 m
$T = 1/\Delta f$	≈ 3.28 μ s	$\Delta v = c_0/(2f_c T_{\text{meas}})$	0.158 m/s
T_{SRI}	77 μ s		
N_{sym}	512		
$T_{\text{meas}} = N_{\text{sym}} T_{\text{SRI}}$	39.4 ms		

the low distance resolution of $\Delta d = 2$ m, most reflections from the target are compressed into a single peak. Reflections from stationary targets are concentrated in the velocity cell $v = 0$. Clearly, ICI occurs in case of the classical processing caused by the Doppler shift, which is concentrated in the velocity cell of the target due to repeating OFDM symbols. This leads to the bright trace in the target velocity cell stretching over the distance cells. In contrast, ACDC compensates the Doppler shift of the target, enabling an ICI free processing. As a result, no trace resulting from ICI is present, i.e. no reduction of the dynamic range occurs. Moreover, the peak power in case of ACDC is ≈ 1.7 dB higher, since the whole energy of the reflection is concentrated in the peak and not spread in the form of ICI. Consequently, the results show a high dynamic range of more than 60 dB (difference between the strongest peak and noise), limited solely by the noise level.

The performed measurements verify the effectiveness of ACDC in solving the Doppler sensitivity issue of OFDM. ICI due to the Doppler shift is avoided by a scenario-independent Doppler compensation with ACDC, which enables a full concentration of the signal energy into a single

peak. As a result, a Doppler independent performance with a high dynamic range and SNR is achieved for any number of targets within the unambiguously measurable velocity range.

6.3.2. Validation of ACMC in a Road Scenario

Analogous to the validation of the ACDC method, the performance of ACMC processing presented in Section 3.4 is verified with measurements in the same road scenario (Fig. 6.6). For this measurement, a corner reflector with 10 m^2 RCS is mounted additionally on the vehicle roof above the driver seat to obtain a reflection concentrated strongly in a single distance cell. This aims to enable a better visual distinction of the migration effects and their compensation. Also here, only one transmit and one receive channel is used. The radar parametrization is adapted such that the target movement during the measurement leads to a considerable range and Doppler frequency migration (Table 6.4). To achieve this, the SRI is stretched to $77 \mu\text{s}$ by adding long breaks between the $3.28 \mu\text{s}$ long OFDM symbols, i.e. $\alpha = T_{\text{SRI}}/T = 23.5$. With 512 OFDM symbols, this results in a measurement cycle duration of 39.4 ms , while the short OFDM symbols enable moderate data rates and thus a high update rate. Due to the breaks between OFDM symbols CP-OFDM is used. Modulation symbols have unit amplitudes and random phases.

The vehicle representing the target of interest is moving towards the radar with a velocity $v \approx -22 \text{ m/s} \approx -79 \text{ km/h}$ and is at a distance of 14 m to 19 m at the time of the measurement. With the given configuration, this target velocity leads to a range and Doppler frequency migration of around 3.5 cells during one measurement cycle. The distance profiles over the slow-time for the conventional FFT processing and for ACMC based processing are shown in Fig. 6.9a and Fig. 6.9c, respectively. For these images the stationary targets are removed for the clarity of representation. The effect of the range migration is clearly visible in Fig. 6.9a, where the peaks in the distance profiles migrate over multiple distance cells. The corresponding distance-velocity radar image in Fig. 6.9b demonstrates clearly the smearing of target peaks due to the migration effects. In contrast, the distance profiles over slow-time for the ACMC based processing in Fig. 6.9c exhibit no range migration, and the entire reflection energy is concentrated in a single cell. The migration compensation is distinctly recognizable, especially for the reflection from the corner reflector at around 16 m . Consequently, the radar image for ACMC based processing in Fig. 6.9d exhibits no smearing of the target peaks. For the corner reflector, the energy of the reflection is focused into a single peak with a width (resolution) corresponding to the radar bandwidth and the measurement time. Note that no windowing is performed (rectangular window) for the images in Fig. 6.9, in order to isolate the migration effects from the peak widening due to the windowing.

The presented measurements confirm that ACMC based processing achieves a resolution beyond the limits of the classical processing through the compensation of the range and Doppler frequency migration effects. This enables furthermore a coherent integration of measurement samples over a considerably longer measurement duration, which yields a higher processing gain, and thus a larger dynamic range. In this measurement, the amplitude difference for the corner reflector in the radar images from the ACMC and the classical processing is more than 7 dB — a significant difference for the radar detection.

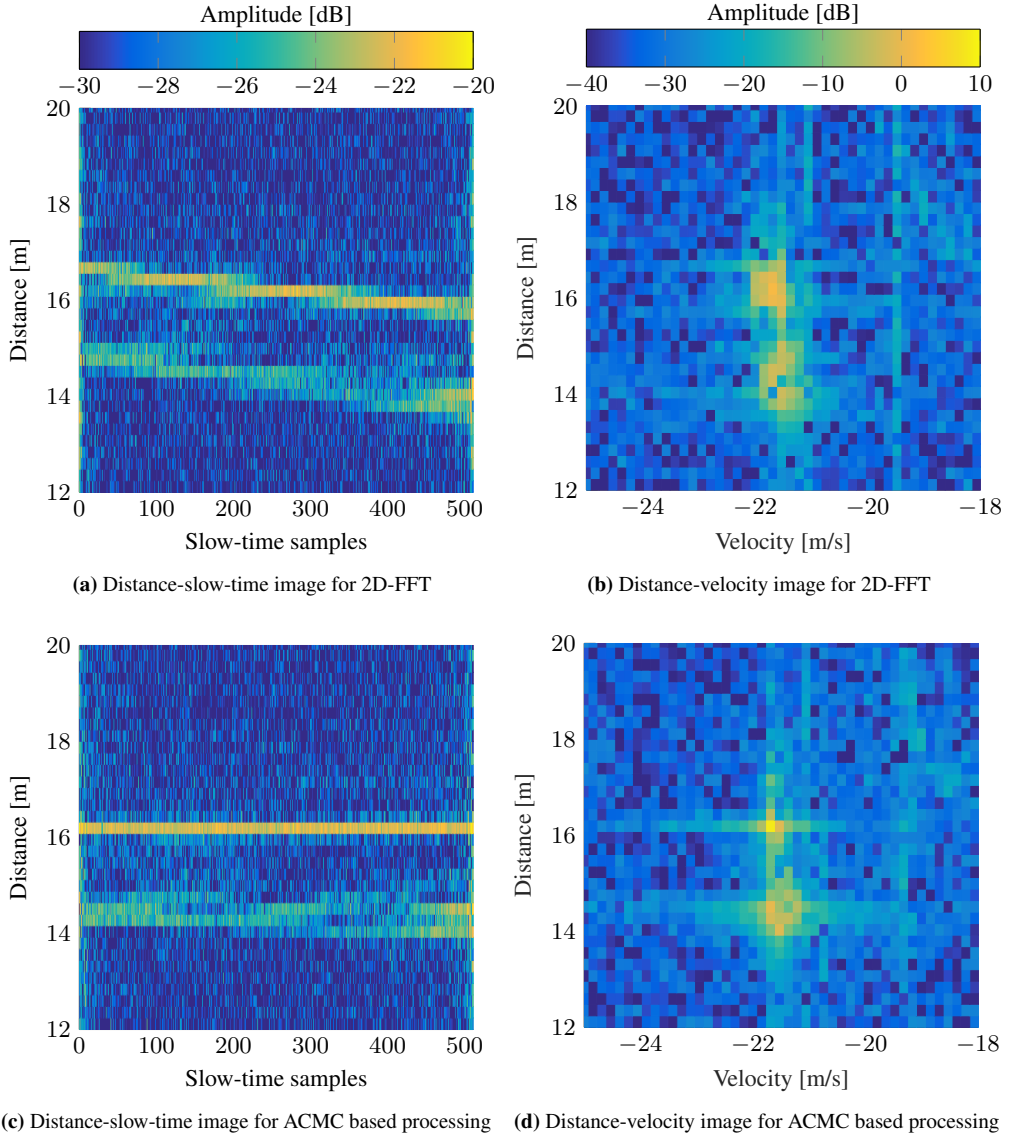


Figure 6.9.: Measurement results for experimental validation of the ACMC method and comparison to the classical FFT processing: the range and Doppler frequency migrations are compensated by ACMC (rectangular window, colorbar of (a) applies also to (c), and that of (b) also to (d)). The distinct single reflection at around 16 m originates from the corner reflector mounted on the roof of the vehicle and the remaining reflections are primarily from the vehicle front part

6.4. Experimental Validation of the Proposed Multiplexing Methods for OFDM-MIMO Radar⁵

Below, measurements for experimental validation of the multiplexing methods proposed in Chapter 4 are presented. Specifically, the NeqDySI multiplexing with the classical 2D-FFT processing and the NeqSI multiplexing with SIMFE processing are validated experimentally with measurements in an anechoic chamber. Since for these multiplexing methods a velocity-dependent performance validation is not primarily of interest, measurements are performed with stationary targets. Table 6.5⁶ presents the parametrization used for measurements with both NeqDySI and NeqSI. For both multiplexing methods, the specific interleaving scheme used for measurements is optimized with the approach described in Section 4.4.

6.4.1. Validation of the NeqDySI Multiplexing

For the measurements below, $N_{Tx} = 2$ Tx antennas are multiplexed via NeqDySI using $N_c = 2048$ subcarriers and $N_c = 512$ OFDM symbols. The interleaving pattern optimized for a Kaiser window with $\beta = 6.5$ in both dimensions achieves a PSL of around 46.7 dB in the non-coherently integrated ambiguity function. CP-OFDM is used for this measurement, the changing interleaving pattern prohibits the use of RS-OFDM.

Three corner-reflectors are located at the distances of 2.2 m, 3.9 m and 6.1 m. The radar images of all spatial channels from 2 Tx and 4 Rx antennas are processed with the classical OFDM radar processing and integrated non-coherently. Fig. 6.10 presents the resulting distance-velocity image. All three targets are clearly distinguishable. In this measurement, a dynamic range of around 46 dB and a ratio of the highest peak to the noise and sidelobe floor of around 54 dB is obtained with the conventional Fourier processing, which conforms with the simulation results in Section 4.3.2.

The measurement results confirm the ability of NeqDySI to obtain a high PSL by spreading the sidelobes of non-equidistant interleaving both in the distance and velocity dimensions. Clearly, the combination of NeqDySI with the conventional signal processing is advantageous in case all targets in the measurement have input SNR below 0 dB, i.e. in case the dynamic range of the radar image is primarily limited by the noise floor. In the opposite case, alternative processing methods such as SIMFE can be used to increase the dynamic range based on sparse signal processing. The latter is validated with measurements in the following in combination with the NeqSI multiplexing.

6.4.2. Validation of the NeqSI Multiplexing with SIMFE Processing

In an analogous setup as above, measurements for verification of the NeqSI multiplexing (Section 4.3.1) and the SIMFE processing (Section 4.5.3) are carried out. The interleaving pattern used for NeqSI is analogously optimized for $N_c = 2048$ subcarriers and $N_{Tx} = 2$ Tx antennas for a Kaiser window with $\beta = 3.4$. The resulting interleaving pattern exhibits a PSL of 26.78 dB. The measurements from all spatial channels are jointly evaluated by SIMFE.

⁵ Contributions of this section have been partially reported in [Hakobyan, 2016d, 2017b]. Some of the author's own from [Hakobyan, 2016d, 2017b] are adopted in the text.

⁶ Note that this parametrization is configured for the performance validation of the proposed multiplexing methods and is not intended for automotive radar

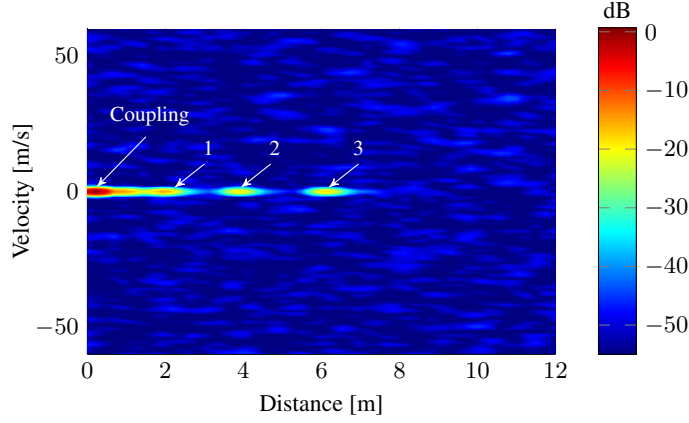


Figure 6.10.: Distance-velocity measurement with a NeqDySI multiplexed OFDM-MIMO radar in an anechoic chamber: three corner reflectors represent the targets

Table 6.5.: Parametrization for the OFDM-MIMO radar measurements with both NeqDySI and NeqSI

Modulation parameters	Values	Radar parameters	Values
B	625 MHz	$d_u = c_0/(2\Delta f\gamma)$	≈ 491.5 m
N_c	2048	$v_u = \pm c_0/(4f_c T_{\text{SRI}})$	$\approx \pm 832$ m/s
$\Delta f = B/N_c$	≈ 305.2 kHz	$\Delta d = c_0/(2B)$	0.24 m
$T = 1/\Delta f$	≈ 3.28 μ s	$\Delta v = c_0/(2f_c T_{\text{meas}})$	≈ 1.6 m/s
T_{CP}	0.4 μ s		
$T_{\text{SRI}} = T + T_{\text{CP}}$	≈ 3.68 μ s		
N_{sym}	512		
$T_{\text{cycle}} = N_{\text{sym}} T_{\text{SRI}}$	≈ 1.9 ms		

Three corner-reflectors are placed at the distances of 2.3 m, 3.8 m and 5.5 m. Besides the existing true targets, the coupling between antennas appears as a stationary target peak in the distance-velocity image at the distance of about 0 m. Since only stationary targets are involved in the measurement, we focus on the zero-Doppler cut of the distance-velocity radar image that is shown in Fig. 6.11. Clearly, the strong internal coupling leads to high sidelobes that mask the weaker targets — e.g. the farthest target is masked completely. The sidelobes are at around 27 dB below the main peak of the strongest target, as expected from simulations.

During the first iteration of SIMFE, the internal coupling is detected as a target and subtracted from the radar image. This eliminates the peak of the internal coupling as well as part of its sidelobes from the measurement signal. However, since the coupling is not a single peak due to physical difference of the cable lengths and crosstalk between antennas, the subtraction still leaves a residue that is especially high at the position of its mainlobe. Therefore, we deploy the structured sparsity model described in Section 4.5.3 to handle such effects. In fact, as the measurement shows, such modelling does not truly correspond to the actual structure of the measurement signal. Nevertheless, it impacts the search space of the sparse solution, and thus facilitates a better recovery of the signal. The effect of structure based evaluation is shown in Fig. 6.11 by the nulled values at the position of the internal coupling after the first iteration. After four iterations (including the one for coupling), all three targets are detected correctly, even

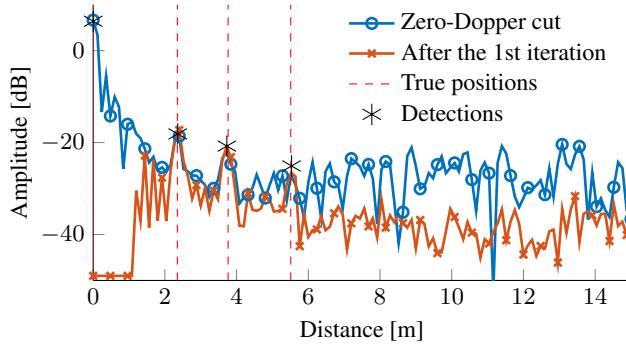


Figure 6.11.: Zero-Doppler cut for a 3-target scenario processed with SCS-SIMFE

though the last true target at 5.5 m was initially masked completely by the sidelobes of more dominant frequency components.

The measurement presented above verifies the properties of the NeqSI multiplexing in terms of increased sidelobes in the distance dimension. The PSL of the measurement confirms the results obtained from simulation. Furthermore, the presented measurement verifies the ability of the SIMFE algorithm to detect weak targets masked entirely by sidelobes. Hence, this confirms the property of SIMFE processing to complement the drawback of NeqSI multiplexing in terms of increased sidelobes, enabling a MIMO radar concept that maintains all the radar parameters (resolution and unambiguous range in velocity and distance) unchanged. At the same time, the presented measurement indicates the need of this multiplexing scheme for a realization with a low internal coupling to simplify the detection of zero-Doppler targets. Finally, the practicability of the structured sparsity model in overcoming the real life imperfections of a particular realization is confirmed.

6.5. Experimental Validation of the Proposed Interference Mitigation Techniques

6.5.1. Validation of the Proposed Narrowband Interference Suppression Method⁷

To verify the performance of the narrowband interference suppression method presented in Section 5.2, OFDM radar measurements corrupted by chirp interference are carried out in an anechoic chamber. One of two transmitters of the OFDM radar prototype is programmed to transmit an FMCW signal and represents an interferer for the other Tx antenna operating as OFDM radar transmitter. Except for the carrier frequency at 24.5 GHz, the configuration used for the measurements is the same as for the simulations in Section 5.2.2 — both for OFDM radar as well as FMCW interferer (see Fig. 5.1a). Two stationary targets (corner reflectors) at the distance of 4.7 m and 6.4 m are present in the measurement. The interfering signal arrives at the OFDM radar receiver via reflection from the measured targets as well as through the direct coupling due

⁷ Contributions of this section have been partially reported in [Hakobyan, 2016c]. Some of the author's own from [Hakobyan, 2016c] are adopted in the text.

to the crosstalk between antennas. Due to the latter, interference has a higher input power than the OFDM radar signal.

Fig. 6.12 shows the distance-velocity radar images of the measured scenario processed with the conventional OFDM radar signal processing. The result without interference suppression presented in Fig. 6.12a has a mean SIR of ≈ 48 dB and a peak SIR of 38.7 dB. This is in accordance with the results of simulations in Section 5.2.2. Interference is spread over in the distance-velocity space, which enables an interference suppression determined by the processing gain of the system as well as the cross-correlation between the OFDM radar signal and the interference. However, the floor in Fig. 6.12a exhibits a clear structure, since unlike noise, FMCW interference is a signal of deterministic form. An increased mean SIR of ≈ 58.8 dB and a peak SIR of 48.96 dB is obtained through interference suppression with the proposed method, as shown in Fig. 6.12b. This corresponds to ≈ 11 dB improvement of the mean SIR, which largely agrees with the simulation results. After interference suppression, the interference level is reduced down to the noise floor, such that no significant dynamic range limitation due to interference occurs.

The measurement presented above confirms both the ability of OFDM radar signal processing to suppress interference by spreading it in the distance-velocity space as well as the effectiveness of the proposed interference suppression method against narrowband interferences (e.g. slow FMCW chirps). Furthermore, the measurements show the robustness of the presented method against multipath propagation of interference, since the interfering signal arrives at the receiver through multiple paths: over the direct coupling and via reflection from targets.

6.5.2. Verification of the Waveform Adaptation Properties of STC-WA for Cognitive Interference Avoidance

To show experimentally the ability of STC-WA to adapt to interference by cognitively avoiding it and to investigate the effect of such adaptation on the distance-velocity estimation, measurements with the OFDM-MIMO radar prototype for adaptation with STC-WA are presented below. Since the carrier frequency of the radar prototype at 24 GHz does not facilitate measurements with STC-WA that would exhibit a significant peak expansion due to the quadratic Doppler term (see Section 5.4.2) for any realistically achievable velocity, we restrict our experiments to evaluation of static scenarios in an anechoic chamber. That is, we do not study experimentally the benefits of VSRI for STC-WA, and focus instead on the adaptation properties of the latter. In a similar manner as in the previous section, one of the transmit channels of the radar prototype is programmed to generate the interfering signals, while the second one operates as an OFDM radar transmitter. The adaptation of the carrier frequency is carried out digitally — by adapting the IF at which the transmit signal is generated by the AWG. For this measurement, we exceed slightly the specifications of different hardware components⁸ of the prototype, operating in a wider band than the system is designed for. This is, however, not substantial for the sake of this measurement, since the targets are in a short distance and have a sufficiently high power.

The parameters used for this measurement are as follows: a bandwidth of $B = 312.5$ MHz is covered by $N_c = 2048$ subcarriers of unit amplitudes and random phases. For one measurement cycle $N_{\text{sym}} = 512$ CP-OFDM symbols with SRI of $T_{\text{SRI}} = T + T_{\text{CP}} = 1.25T = 8.192 \mu\text{s}$ are used, such that a measurement cycle duration of $T_{\text{cycle}} \approx 4.2$ ms is achieved. The carrier

⁸ Specifically, the passband frequency range of the BPF, the frequency range antennas are optimized for, etc.

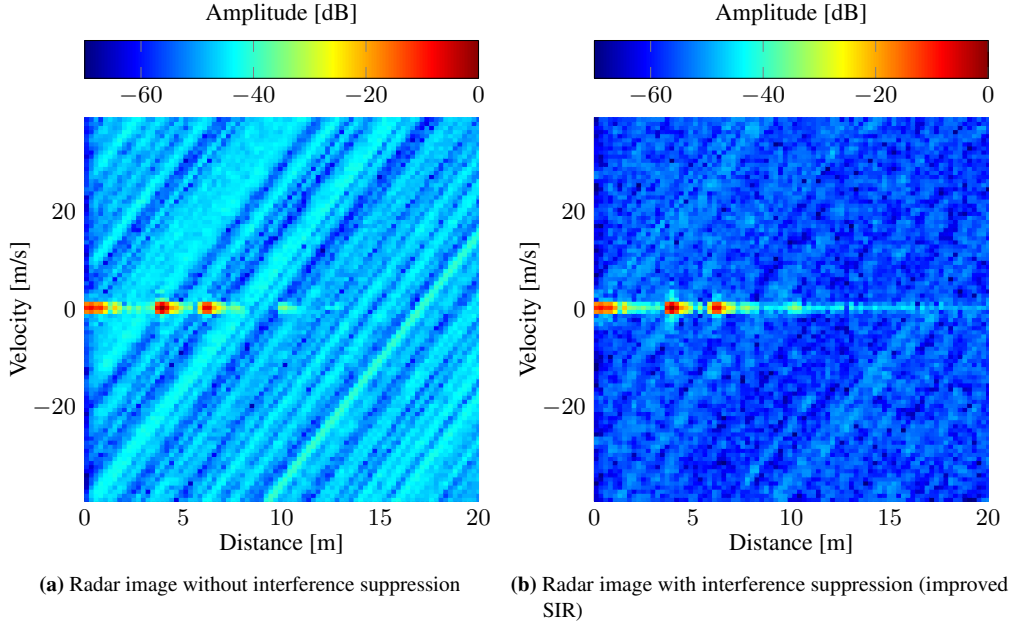
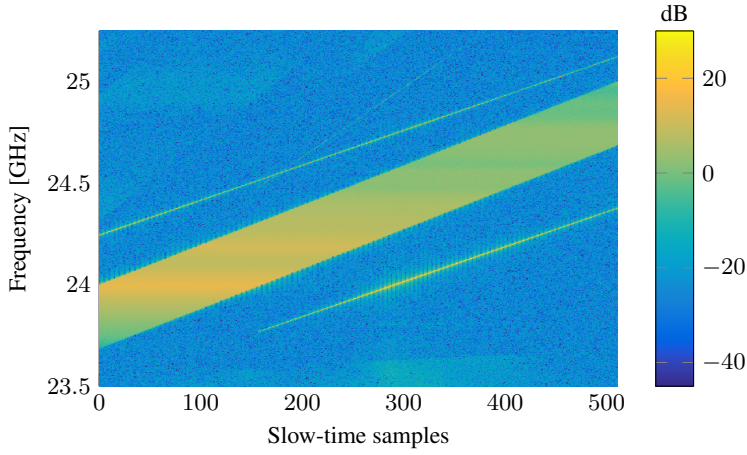


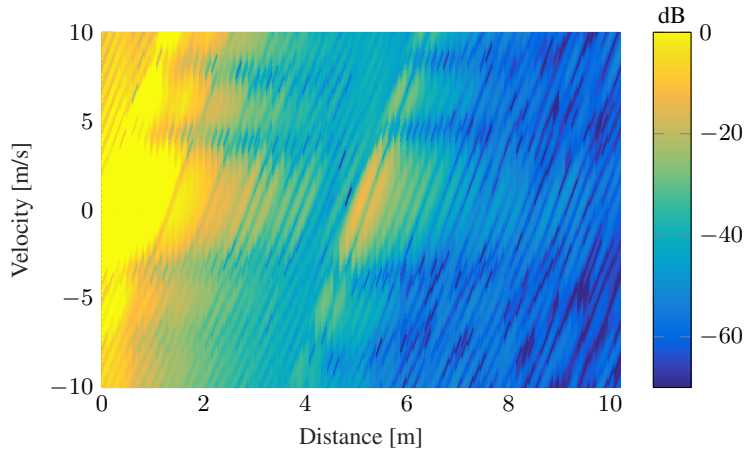
Figure 6.12.: Distance-velocity measurements of two targets in an anechoic chamber in case of chirp interference

frequency of the first OFDM symbol is about 23.85 GHz, and for each subsequent OFDM symbol the carrier frequency is increased linearly with a step $\Delta f_c \approx 1.95$ MHz such that over the measurement cycle a slow-time bandwidth of $B_{\text{STC}} = 1$ GHz is covered. The interference comprises two chirps of the same slope, covering a bandwidth of 1 GHz in 5 ms. The first chirp starts with a frequency of 24.24 GHz at the beginning of the measurement cycle, whereas the second chirp starts at 23.77 GHz with a time delay of 1.3 ms. That is, the OFDM measurement is fitted with STC-WA between two FMCW signals such that interference from them is avoided entirely. The spectrum over slow-time containing both the OFDM signal and chirp interference is captured by the oscilloscope at the receiver of the radar prototype and is shown in Fig. 6.13a. Clearly, given that knowledge about the spectral occupancy is available, such an adaptation with STC-WA represents efficient means for avoiding interference. This waveform adaptation method is most suitable for avoidance of interference from FMCW radars.

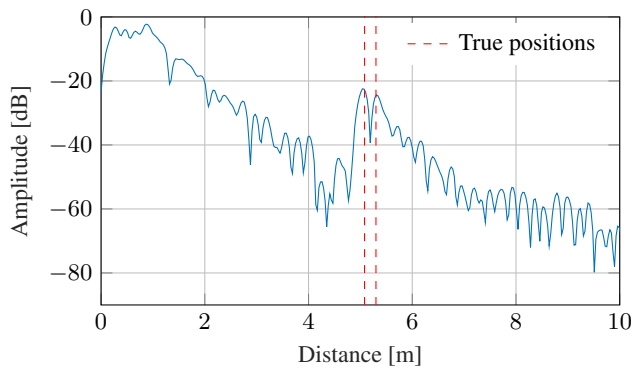
Next, the influence of such adaptation on the distance-velocity estimation performance needs to be investigated. Since with STC-WA effectively a larger bandwidth is covered through the linearly changing carrier frequency of the subsequent OFDM symbols, scenarios with closely positioned targets are of relevance for the performance analysis of STC-WA. Hence, in our experiments we measure two closely positioned corner reflectors that have a distance difference far below the original OFDM radar resolution. These two targets are placed at the distances of 5.08 m and 5.3 m, i.e. with a distance difference of 22 cm, whereas the original radar resolution corresponding to its bandwidth is 48 cm. The distance-velocity radar image for this measurement is shown in Fig. 6.13b. Since with STC-WA the distance information is obtained from both fast-time and slow-time measurements, the target peaks appear in the form of rotated ellipses in the two-dimensional space. Also the sidelobes follow the same pattern.



(a) Measured spectra over the OFDM symbols (two interfering chirps)



(b) Distance-velocity radar image for two targets located at a distance below the original radar resolution (rectangular window)



(c) Zero-Doppler cut of the radar image from (b): targets can be clearly resolved in distance (rectangular window, DC-offset compensation)

Figure 6.13.: Measurements with OFDM radar prototype adaptive with STC-WA to interference

To show clearly the radar resolution in the distance dimension, the zero-Doppler slice of the distance-velocity image in Fig. 6.13b is presented in Fig. 6.13c. The distance resolution corresponding to the OFDM radar bandwidth does not allow a resolution of the measured targets. However, the slow-time bandwidth of 1 GHz covered by the sweep of the carrier frequency is significantly larger than the bandwidth covered by a single symbol, and thus enables clear resolution of the targets in distance, as Fig. 6.13c shows.

The measurements presented above confirm both the ability of STC-WA to adapt to interference in the context of cognitive interference avoidance as well as the improvement of the distance resolution obtained due to a larger bandwidth effectively covered by the radar. However, to be fair it has to be noted that the improvement of the distance resolution owes to the fact that the shape of the peaks is changed to a stretched rotated ellipsis. That is, some combinations of closely located distances and velocities along the axis of this ellipsis are now more difficult to resolve. This is, however, physically more acceptable, e.g. for resolving stationary targets that have the same velocity and different distances. Moreover, given that a different slope of the slow-time chirp is used for the next measurement cycle, the axis of the ellipsis will be rotated, and the unfavorable distance-velocity combinations are more likely to be resolved.

6.6. Concluding Remarks

In this chapter, an OFDM-MIMO radar prototype operating at 24 GHz has been presented. The constructed prototype has several features superior to the state-of-the-art OFDM radar prototypes: a large bandwidth, MIMO technology realized as a single patch antenna array, as well as high update rates. Due to these aspects, it is suitable for measurements in an automotive radar application. The performance of the radar prototype in distance, velocity and DOA estimation has been studied with measurements. Depending on the configuration, the radar prototype achieves a dynamic range of 50 dB to 80 dB in distance-velocity estimation, which demonstrates the feasibility of OFDM as a modulation scheme for high-performance radar applications. The DOA measurements in a real world scenario with moving targets confirmed another important feature of OFDM in the context of MIMO radar: subcarrier interleaving for multiplexing of Tx antennas enables a high coherence between measurements from different Tx channels. This owes to the fact that measurements of Tx channels using the same bandwidth are carried out simultaneously. In fact, this is an essential advantage for MIMO radar processing, since it facilitates a phase relationship between Tx channels dependent only on DOA, and thus enables accurate DOA estimation with the MIMO principle.

The signal processing methods and radar concepts proposed in this work have been validated experimentally based on measurements with the presented OFDM-MIMO radar prototype. Measurements in a road scenario with a car moving towards the radar prototype were used to verify the performance of the ACDC and APMC methods presented in Chapter 3. The measurements confirmed the ability of these methods to prevent degradation of the radar performance due to Doppler shift and migration effects. Then, the proposed NeqDySI and NeqSI multiplexing methods for OFDM-MIMO radar have been validated with measurements in an anechoic chamber. These measurements have additionally confirmed the ability of the SIMFE algorithm to detect targets masked entirely by sidelobes of the NeqSI multiplexing, and thus validated the simulation results of both multiplexing schemes and the SIMFE algorithm presented in Chapter 4. Finally, measurements in the presence of interference have been carried out to validate the narrowband

interference suppression method as well as the STC-WA waveform adaptation method proposed in Chapter 5. Both measurements confirmed the simulation results, suggesting that a high interference robustness can be achieved with OFDM radar by means of interference suppression as well as cognitive interference avoidance. Additionally, the impact of STC-WA on the radar estimation has been studied, which has confirmed its ability to effectively increase the distance resolution.

Chapter 7.

Conclusions

7.1. Summary of Key Contributions

Motivated by the need for high-performance automotive radar sensors, this work aimed at development of concepts and algorithms for a high-end digital automotive radar operating with OFDM waveforms. Owing to the digital signal generation and processing, OFDM radar provides a large degree of flexibility and adaptability in terms of waveform choice as well as radar operation is general. Based on these properties of OFDM radar, new concepts were developed in this work that achieve high radar performance in many respects. Building upon the solid foundation of the known work on OFDM radar, this thesis makes novel contributions to three major fields of OFDM radar: *i*) signal processing algorithms for distance-velocity estimation that obtain a performance beyond that of the conventional OFDM radar signal processing, *ii*) novel multiplexing methods and corresponding signal processing algorithms for OFDM-MIMO radar, and *iii*) interference mitigation techniques for OFDM radar for high interference robustness.

As a basis for the signal processing algorithms proposed in this work, we introduced a novel and rigorous signal model for OFDM radar. Based on this signal model, the limitations of the conventional OFDM radar signal processing become apparent. To overcome these shortcomings, we introduced advanced signal processing algorithms that compensate several adverse effects. First, the ACDC method for compensation of the Doppler shift in a scenario independent manner was proposed. The high performance as well as the new perspectives of ACDC in terms of more advantageous parametrization were shown in simulations. This method overcomes the Doppler sensitivity of OFDM radar — a major issue specific to OFDM modulation. The second proposed processing method, APMC, prevents performance degradation due to range and Doppler frequency migration. With APMC, the target movement is compensated during the Doppler processing by the use of a special kernel that implicitly accounts for the target movement during the measurement. Consequently, no performance degradation due to the migration effects occurs, and a simultaneous distance and velocity resolution beyond the limits of the conventional Fourier based processing is achieved. As both algorithms are highly computationally efficient, their real-time implementation for automotive radar is feasible. In fact, to obtain a performance beyond the limits of the conventional processing, such algorithms with more sophisticated modeling of the measurement signal become indispensable.

As MIMO radar is an established technology for automotive radar, the second major topic studied in this work was the multiplexing methods for extension of OFDM radar with MIMO. To emphasize the advantage of OFDM modulation for MIMO radar, we first discussed the conventional multiplexing methods, pointing out the advantages and shortcomings of each

method. We then presented the state-of-the-art EqSI multiplexing, which enables a simultaneous operation of multiple Tx antennas covering the same bandwidth. Since this multiplexing has a drawback in terms of reduced unambiguous distance range that becomes unaffordable for some applications, we proposed the NeqSI and NeqDySI multiplexing schemes that overcome this shortcoming. To obtain favorable interleaving patterns, we introduced an optimization approach based on genetic algorithms for joint maximization of the PSL of the distance-velocity ambiguity function. To further compensate the drawback of non-equidistant interleaving in terms of reduced PSL, we formulated the distance-velocity estimation problem as a frequency estimation problem from subsampled data. Based on this, we introduced the SIMFE algorithm that enables detection of targets masked entirely by sidelobes due to non-equidistant interleaving. Simulation results have shown the ability of this approach to achieve a high dynamic range as well as to maintain the original radar parameters at each MIMO channel despite multiplexing.

The next topic addressed in this thesis was the interference robustness of OFDM radar. We started from analyzing the effect of the OFDM radar signal processing steps on interference. Due to the large variety of OFDM waveforms, it exhibits favorable interference properties, as its signals are likely to be uncorrelated with the interference. This is a major advantage compared to the traditional radar systems that have higher risk of correlation between their signal and interference. To further increase the interference robustness of OFDM radar, we introduced an interference suppression method effective towards arbitrary narrowband interference. This method is especially valuable for OFDM radar due to the fact that the signals of commercially available FMCW radars represent narrowband interference for OFDM radar. We then introduced the concept of interference-aware cognitive OFDM radar — an approach that has high potential in terms of interference mitigation for future radar systems. We formulated the idea of cognitive OFDM radar for dynamic interference avoidance based on spectral awareness, and made some first steps in this field. Specifically, we proposed waveform adaptation methods based on change of the carrier frequency. We extended the STC-WA method with variable symbol repetition intervals that linearize the Doppler shift, preventing performance degradation. The effectiveness of these methods for interference avoidance was confirmed with simulations. In addition, we pointed out the added benefit of the STC-WA method in terms of improved distance resolution, which owes to the fact that during the adaptation effectively a larger bandwidth is covered.

To demonstrate the feasibility of OFDM-MIMO radar for high-performance automotive applications, an OFDM-MIMO radar prototype at 24 GHz was constructed in this work. Real world measurements, both in an anechoic chamber as well as in a road scenario were carried out to validate the performance of the proposed signal processing methods and radar concepts. The measurements confirmed the performance obtained in simulations, proving the practicability of the proposed methods for real world application.

The obtained results suggest that despite the increased hardware requirements (e.g. sampling rates, linearity requirements, etc.), OFDM radar offers novel features due to the large degree of flexibility and is suitable for high-end automotive radar applications. Key points in this respect are its interference properties, multiplexing possibilities for MIMO radar, as well as its adaptability that leaves room for further novel features.

7.2. Outlook

The presented work indicates that in some respects, complete and practical solutions for OFDM radar are already available. For example, sophisticated algorithms for OFDM-based distance-velocity estimation suitable for high-performance radar applications have been developed in this work. In many other aspects, however, there is a need as well as potential for subsequent research. In what follows, we present some suggestions for future research on the topic of digital automotive radar.

One major research topic that would complement this work from the hardware perspective is the analysis of realization aspects of digital OFDM radar. To this end, derivation of more specific requirements on the OFDM radar hardware (e.g. ADCs, DACs, PAs, etc.) from the specified performance requirements would be of great interest. Here, the properties of the radar application and the radar signal processing in particular need to be taken into account. Whereas in this work we have experimentally shown the feasibility of OFDM radar for real world applications based on a prototypical realization, such analysis would facilitate meaningful statements on the hardware cost of a practical realization.

As for improving the cost-efficiency of OFDM radar, research that focuses on efficient implementations with less hardware resources could deliver a valuable contribution to its further commercial realization. One such approach presented in this thesis, albeit serving a different purpose, is the STC-WA method that allows a high distance resolution with a comparably low bandwidth, i.e. sampling rate. Analogously, methods for compression of OFDM measurements to reduce the amount of data to be acquired and processed are of a great interest.

For multiplexing of MIMO channels, the combination of orthogonal codes with OFDM should be investigated. There are few publications that considered this for SAR applications, and as we previously pointed out, Doppler shift is a major concern for the orthogonality of codes. However, a combination of ACDC based processing with code multiplexed OFDM-MIMO radar could overcome this drawback. This would enable the simultaneous use of all subcarriers by all Tx antennas. As for MIMO radar with non-equidistant interleaving, more sophisticated sparsity based frequency estimation methods than the one introduced in this work would be of interest.

We consider the work on interference-aware cognitive radar presented in this thesis to represent the first steps into this novel topic. Thus, we believe the adaptive and cognitive interference avoidance has a large potential still to be explored. All three building blocks of cognitive radar leave room for future research. Particularly, methods for more flexible waveform adaptation as well as spectrum interpretation are of great interest. For the latter, machine learning methods could be a promising approach, as they may enable an end-to-end solution from the spectrum sensing to the choice of an adaptation strategy. As for the waveform adaptation, methods that allow more dynamic adaptation within the measurement cycle are of a high relevance.

Appendix A.

ACMC Description Based on a Frequency Domain Signal Model

To return to the continuous time and frequency model, the DFT and IDFT operations in (3.49) are substituted with Fourier and inverse Fourier transforms, and the discrete time and frequency indexes — $m = tN_c/T$ and $n = f/\Delta f$ — are substituted with continuous ones. Thus, for the μ -th OFDM symbol (3.49) can be rewritten as

$$\begin{aligned}
 Y(f, \mu) &= \sum_{i=0}^{N_{\text{path}}-1} \bar{a}_i \mathcal{F} \left(e^{j2\pi f_{D_i} t} \mathcal{F}^{-1} \left(e^{-j2\pi \tau_i f} s(f) \sigma(f - f_n) e^{-j2\pi f \gamma_i \mu \alpha T} e^{j2\pi \bar{f}_{D_i} \alpha \mu} \right) \right) \\
 &= \sum_{i=0}^{N_{\text{path}}-1} \bar{a}_i e^{j2\pi \bar{f}_{D_i} \alpha \mu} \mathcal{F} \left(e^{j2\pi f_{D_i} t} \mathcal{F}^{-1} \left(s(f) \sigma(f - f_n) e^{-j2\pi f T(\bar{\tau}_i + \gamma_i \mu \alpha)} \right) \right) \quad (\text{A.1}) \\
 &= \sum_{i=0}^{N_{\text{path}}-1} \bar{a}_i e^{j2\pi \bar{f}_{D_i} \alpha \mu} \mathcal{F} \left(x_\mu(t - T(\bar{\tau}_i + \gamma_i \mu \alpha)) e^{2\pi f_{D_i} t} \right) = \sum_{i=0}^{N_{\text{path}}-1} \bar{a}_i e^{j2\pi \bar{f}_{D_i} \alpha \mu} \\
 &\quad \cdot X(f - f_{D_i}) e^{-j2\pi(f - f_{D_i})T(\bar{\tau}_i + \gamma_i \mu \alpha)}, \quad 0 \leq n < N_c, \quad 0 \leq \mu < N_{\text{sym}},
 \end{aligned}$$

where $Y(f, \mu)$ is the received μ -th OFDM symbol in the frequency domain, \mathcal{F} and \mathcal{F}^{-1} denote the Fourier and inverse Fourier transforms, respectively, $x_\mu(t)$ denotes the μ -th OFDM symbol in the time domain as in (3.3), and $X(f)$ is the μ -th OFDM symbol in the frequency domain:

$$\begin{aligned}
 X(f) &= \mathcal{F}(x(t)) = \int_{-\infty}^{\infty} x(t) e^{-j2\pi f t} dt = \frac{1}{\sqrt{N_c}} \sum_{n=0}^{N_c-1} s(n) \int_0^T e^{-j2\pi(f - f_n)t} dt \\
 &= \frac{1}{\sqrt{N_c}} \sum_{n=0}^{N_c-1} s(n) T e^{-j\pi(f - f_n)T} \text{sinc}(\pi T(f - f_n)), \quad (\text{A.2})
 \end{aligned}$$

with

$$\text{sinc}(z) = \begin{cases} \sin(z) / z & \text{for } z \neq 0 \\ 1 & \text{for } z = 0 \end{cases}. \quad (\text{A.3})$$

For a discrete time signal, the integral in (A.2) is replaced with a finite sum, which results in a Dirichlet kernel $\mathcal{D}_{N_c}(\pi T(f - f_n))$ instead of the sinc function in (A.2) defined as

$$\mathcal{D}_N(z) = \frac{\sin(Nz)}{\sin(z)}. \quad (\text{A.4})$$

For a discrete frequency grid $f = n'\Delta f$, $0 \leq n' < N_c$, (A.1) can be rewritten as

$$Y(n', \mu) = Y(f, \mu) \Big|_{f=n'\Delta f} = \sum_{i=0}^{N_{\text{path}}-1} \bar{a}_i e^{j2\pi \bar{f}_{D_i} \alpha \mu} X(n\Delta f - f_{D_i}) e^{-j2\pi(n' - \bar{f}_{D_i})\bar{\tau}_i} \cdot e^{-j2\pi n' \gamma_i \mu \alpha} e^{j2\pi \bar{f}_{D_i} \gamma_i \mu \alpha}, \quad 0 \leq n' < N_c, \quad 0 \leq \mu < N_{\text{sym}}. \quad (\text{A.5})$$

Consequently, for the n' -th frequency point the Doppler processing with ACMC is:

$$Y(n', l) = \sum_{\mu=0}^{N_{\text{sym}}-1} Y(n', \mu) w_{N_{\text{sym}}}(\mu) e^{j2\pi n' \hat{\gamma}(l) \mu \alpha} e^{-j2\pi \frac{l\mu}{N_{\text{sym}}}} = \sum_{i=0}^{N_{\text{path}}-1} \bar{a}_i X(n\Delta f - f_{D_i}) \cdot e^{-j2\pi(n' - \bar{f}_{D_i})\bar{\tau}_i} \sum_{\mu=0}^{N_{\text{sym}}-1} w_{N_{\text{sym}}}(\mu) e^{j2\pi \mu \left(\bar{f}_{D_i} \alpha (1 + \gamma_i) - \frac{l}{N_{\text{sym}}} \right)} \cdot e^{-j2\pi \mu \alpha n' (\gamma_i - \hat{\gamma}(l))}, \quad 0 \leq n' < N_c, \quad 0 \leq l < N_{\text{sym}}. \quad (\text{A.6})$$

The first exponential term in the inner sum leads to a maximal integration gain for

$$l = \bar{f}_{D_i} \alpha (1 + \gamma_i) N_{\text{sym}} = \gamma_i f_c T \alpha (1 + \gamma_i) N_{\text{sym}}. \quad (\text{A.7})$$

Taking into account $\gamma_i = 2v_i/c_0$ and $v_i \ll c_0$, the second γ_i can be ignored, i.e. $(1 + \gamma_i) \approx 1$. With $\hat{\gamma}(l)$ being

$$\hat{\gamma}(l) = \frac{2\hat{v}(l)}{c_0} = \frac{2l\Delta v}{c_0} = \frac{l}{f_c T_{\text{cycle}}}, \quad (\text{A.8})$$

for l as in (A.7) the last exponential term has in its argument

$$\gamma_i - \hat{\gamma}(l) = \gamma_i - \frac{l}{f_c T_{\text{cycle}}} = \gamma_i - \frac{\gamma_i f_c T \alpha N_{\text{sym}}}{f_c T_{\text{cycle}}} = 0. \quad (\text{A.9})$$

Hence, for the Doppler cell index l corresponding to the Doppler of the i -th target \bar{f}_{D_i} , the inner sum yields a maximum for all n' , since the migration term is compensated entirely. Thus, the following processing will be migration-free.

To investigate the effect of ACMC for an arbitrary $l_i = \gamma_i f_c T_{\text{cycle}}$, the argument of the exponential terms in the inner sum is reformulated as:

$$j2\pi \mu \left(\bar{f}_{D_i} \alpha - \frac{l}{N_{\text{sym}}} \right) - j2\pi \mu \alpha n' (\gamma_i - \hat{\gamma}(l)) = j2\pi \mu \left(\gamma_i f_c T \alpha - \frac{l}{N_{\text{sym}}} - \alpha n' \left(\frac{l_i - l}{f_c T_{\text{cycle}}} \right) \right) = j2\pi \mu \frac{(l_i - l)}{N_{\text{sym}}} \left(1 - \frac{f_{n'}}{f_c} \right) = j2\pi \mu \frac{(l_i - l)}{N_{\text{sym}}} \eta(n') \quad (\text{A.10})$$

Consequently, the inner sum in (A.6) yields a peak for $l \approx l_i$, $0 \leq l < N_{\text{sym}}$, i.e. at the mainlobe of the resulting Doppler spectrum. Since $f_{n'}/f_c \ll 1$, the migration term left after ACMC is negligible, i.e. $\eta(n') \approx 1 \forall n'$. Hence, the inner sum in (A.6) is

$$\sum_{\mu=0}^{N_{\text{sym}}-1} w_{N_{\text{sym}}}(\mu) e^{j2\pi \mu \left(\bar{f}_{D_i} \alpha - \frac{l}{N_{\text{sym}}} \right)} e^{-j2\pi \mu \alpha n' (\gamma_i - \hat{\gamma}(l))} \approx \sum_{\mu=0}^{N_{\text{sym}}-1} w_{N_{\text{sym}}}(\mu) e^{j2\pi \mu \left(\bar{f}_{D_i} \alpha - \frac{l}{N_{\text{sym}}} \right)} = u_{N_{\text{sym}}}(\bar{f}_{D_i} \alpha, l), \quad 0 \leq l < N_{\text{sym}} \quad (\text{A.11})$$

Appendix B.

Estimation Parameters of STC-WA

In the following, some derivations for the radar parameters resulting from extension of OFDM radar with slow-time chirps according to STC-WA are presented. Since through this modification the estimation in fast-time is unaffected, we focus primarily on the properties of slow-time estimation. To this end, we study the distance and velocity estimation parameters, along with the influence of the second-order Doppler term on the estimation performance.

From (5.16), the DFT processing in slow-time results in a full coherent integration for the phase

$$\frac{l}{N_{\text{sym}}} = \left(\Delta f_c \frac{2\hat{d}}{c_0} + f_{c,0} \frac{2\hat{v}}{c_0} T_{\text{SRI}} + \Delta f_c \frac{2\hat{v}}{c_0} \mu T_{\text{SRI}} \right) \mod 1, \quad (\text{B.1})$$

which is the simplified form of the first equation in (5.17). Since the exponential terms on the right hand side of (B.1) are processed jointly, the estimation parameters are determined by all of these terms. Thus, we will study each term individually to decouple their influence on each other. Consequently, to derive solely the distance estimation parameters resulting from the slow-time processing, we first consider the static case, i.e. $\hat{v} = 0$. In this case, (B.1) can be rewritten as

$$\frac{l}{N_{\text{sym}}} = \left(\Delta f_c \frac{2\hat{d}}{c_0} \right) \mod 1, \quad (\text{B.2})$$

From (B.2), the distance estimation parameters in slow-time can be directly derived, analogous to those in the fast-time:

$$d_{\text{u,STC}} = \frac{c_0}{2\Delta f_c}, \quad (\text{B.3})$$

$$\Delta d_{\text{STC}} = \frac{c_0}{2\Delta f_c N_{\text{sym}}} = \frac{c_0}{2B_{\text{STC}}}. \quad (\text{B.4})$$

Note that whereas (B.3) follows directly from the definition of modulo operation, (B.4) is obtained by setting $l = 1$.

Analogously, to investigate the velocity estimation parameters, we consider $\hat{d} = 0$:

$$\frac{l}{N_{\text{sym}}} = \left(\frac{2\hat{v}}{c_0} T_{\text{SRI}} (f_{c,0} + \mu \Delta f_c) \right) \mod 1, \quad (\text{B.5})$$

Since the slow-time index μ remains in the phase term, no l exists for which (B.5) holds for all μ . This causes the spectral shape different from that of a stable frequency. As the frequency sweep is centered around $f_c = f_{c,0} + \Delta f_c N_{\text{sym}}/2$, the center of the spectral shape is at

$$\frac{l}{N_{\text{sym}}} = \left(\frac{2\hat{v}}{c_0} T_{\text{SRI}} f_c \right) \mod 1, \quad (\text{B.6})$$

which means that, ignoring the change of the spectral shape, the velocity estimation parameters v_u and Δv stay unchanged.

Next, we study the peak expansion due to the quadratic Doppler term in (B.1) and derive formulas for its quantification. These formulas are to determine the scale to which a resolution degradation takes place. First, we study the expansion in l -dimension measured in DFT cells. Since for the peak expansion the sweep of the term $\exp(\Delta f_c \mu T_{\text{SRI}} 2\hat{v}/c_0)$ is relevant, we substitute the value of μ by N_{sym} for the following calculations to obtain the full sweep. Thus, from (B.1) the peak expansion in l -dimension denoted by ε_1 is

$$\varepsilon_1 = \frac{2\hat{v}}{c_0} T_{\text{SRI}} \Delta f_c N_{\text{sym}}^2 = \frac{2\hat{v} T_{\text{cycle}} B_{\text{STC}}}{c_0}. \quad (\text{B.7})$$

Note that ε_1 describes additionally the peak expansion in DFT cells both in the distance and velocity dimensions, which can be easily proven based on the derivations given below. Using the relationship between the indexes l and \hat{v} given by $\hat{v} = l\Delta v = c_0 l / (2f_c N_{\text{sym}} T_{\text{SRI}})$, the peak expansion ε_1 can be translated into the velocity dimension:

$$\varepsilon_v = \frac{c_0 \varepsilon_1}{2f_c N_{\text{sym}} T_{\text{SRI}}} = \frac{\hat{v} B_{\text{STC}}}{f_c}. \quad (\text{B.8})$$

where ε_v denotes the peak expansion in the velocity dimension measured in [m/s]. Evidently, $\varepsilon_v/\Delta v = \varepsilon_1$, i.e. ε_1 describes the peak expansion in the velocity dimension measured in DFT cells. Analogously, the peak expansion in the distance dimension is

$$\varepsilon_d = \frac{c_0 \varepsilon_1}{2N_{\text{sym}} \Delta f_c} = \frac{2\hat{v} T_{\text{cycle}} B_{\text{STC}} c_0}{2N_{\text{sym}} \Delta f_c c_0} = \hat{v} T_{\text{cycle}}. \quad (\text{B.9})$$

where ε_d denotes the peak expansion in the distance dimension measured in [m]. Also in the distance dimension, the peak expansion measured in DFT cells is $\varepsilon_d/\Delta d_{\text{STC}} = \varepsilon_1$.

Bibliography

- Ang, C., See, C., and Kot, A. Optimization of array geometry for identifiable high resolution parameter estimation in sensor array signal processing. *Information, Communications and Signal Processing, 1997. ICICS., Proceedings of 1997 International Conference on*, 3:1613–1617, 1997.
- Anitori, L., Maleki, A., Otten, M., Baraniuk, R. G., and Hoogeboom, P. Design and analysis of compressed sensing radar detectors. *IEEE Transactions on Signal Processing*, 61(4):813–827, Feb 2013.
- Arce, G. R., Brady, D. J., Carin, L., Arguello, H., and Kittle, D. S. Compressive coded aperture spectral imaging: An introduction. *IEEE Signal Processing Magazine*, 31(1):105–115, Jan 2014.
- Armanious, K. Implementation of cognitive functions for high interference-robustness with OFDM radar. Master’s thesis, University of Stuttgart, 2016.
- Aubry, A., Maio, A. D., Piezzo, M., Naghsh, M. M., Soltanalian, M., and Stoica, P. Cognitive radar waveform design for spectral coexistence in signal-dependent interference. In *2014 IEEE Radar Conference*, pages 474–478, May 2014.
- Bajwa, W. U., Haupt, J., Sayeed, A. M., and Nowak, R. Compressed channel sensing: A new approach to estimating sparse multipath channels. *Proceedings of the IEEE*, 98(6):1058–1076, June 2010.
- Bajwa, W. U., Gedalyahu, K., and Eldar, Y. C. Identification of parametric underspread linear systems and super-resolution radar. *IEEE Transactions on Signal Processing*, 59(6):2548–2561, June 2011.
- Balanis, C. A., editor. *Antenna theory – Analysis and design*. John Wiley & Sons, 2nd edition, 1997.
- Bar-Ilan, O. and Eldar, Y. C. Sub-Nyquist radar via Doppler focusing. *IEEE Transactions on Signal Processing*, 62(7):1796–1811, April 2014.
- Baraniuk, R. Compressive sensing [lecture notes]. *Signal Processing Magazine, IEEE*, 24(4): 118–121, July 2007a.
- Baraniuk, R. and Steeghs, P. Compressive radar imaging. In *Radar Conference, 2007 IEEE*, pages 128–133, April 2007b.
- Baraniuk, R. G., Cevher, V., Duarte, M. F., and Hegde, C. Model-based compressive sensing. *IEEE Transactions on Information Theory*, 56(4):1982–2001, April 2010.
- Bartlett, M. S. Periodogram analysis and continuous spectra. *Biometrika*, 37(1-2):1, 1950.

- Berger, C. R., Zhou, S., Willett, P., Demissie, B., and Heckenbach, J. Compressed sensing for OFDM/MIMO radar. In *2008 42nd Asilomar Conference on Signals, Systems and Computers*, pages 213–217, Oct 2008.
- Berger, C. R., Demissie, B., Heckenbach, J., Willett, P., and Zhou, S. Signal processing for passive radar using ofdm waveforms. *IEEE Journal of Selected Topics in Signal Processing*, 4 (1):226–238, Feb 2010a.
- Berger, C. R., Wang, Z., Huang, J., and Zhou, S. Application of compressive sensing to sparse channel estimation. *IEEE Communications Magazine*, 48(11):164–174, November 2010b.
- Beurling, A. Sur les intégrales de Fourier absolument convergentes et leur application à une transformation fonctionnelle. In *In Proc. Scandinavian Math. Congress, Helsinki, Finland*, 1938.
- Bkassiny, M., Jayaweera, S. K., Li, Y., and Avery, K. A. Wideband spectrum sensing and non-parametric signal classification for autonomous self-learning cognitive radios. *IEEE Transactions on Wireless Communications*, 11(7):2596–2605, July 2012.
- Bluestein, L. A linear filtering approach to the computation of discrete Fourier transform. *IEEE Transactions on Audio and Electroacoustics*, 18(4):451–455, Dec 1970.
- Braun, M. *OFDM radar algorithms in mobile communication networks*. PhD thesis, Karlsruhe Institute of Technology, 2014.
- Bresler, Y. and Feng, P. Spectrum-blind minimum-rate sampling and reconstruction of 2-D multiband signals. In *Proceedings of 3rd IEEE International Conference on Image Processing*, volume 1, pages 701–704 vol.1, Sep 1996.
- Candès, E. Compressive sampling. In *Proc. Int. Congress of Math., Madrid, Spain*, 2006a.
- Candès, E. J. and Romberg, J. Quantitative robust uncertainty principles and optimally sparse decompositions. *Foundations of Computational Mathematics*, 6(2):227–254, 2006b.
- Candès, E. J. and Tao, T. Decoding by linear programming. *IEEE Transactions on Information Theory*, 51(12):4203–4215, Dec 2005.
- Candès, E. J. and Tao, T. Near-optimal signal recovery from random projections: Universal encoding strategies? *IEEE Transactions on Information Theory*, 52(12):5406–5425, Dec 2006c.
- Candès, E. J. and Wakin, M. B. An introduction to compressive sampling. *IEEE Signal Processing Magazine*, 25(2):21–30, March 2008.
- Candès, E. J., Romberg, J., and Tao, T. Robust uncertainty principles: exact signal reconstruction from highly incomplete frequency information. *IEEE Transactions on Information Theory*, 52 (2):489–509, Feb 2006d.
- Candès, E. J., Romberg, J. K., and Tao, T. Stable signal recovery from incomplete and inaccurate measurements. *Communications on Pure and Applied Mathematics*, 59(8):1207–1223, 2006e.
- Cao, Y. h., Xia, X. g., and Wang, S. h. IRCI free colocated MIMO radar based on sufficient cyclic prefix OFDM waveforms. *IEEE Transactions on Aerospace and Electronic Systems*, 51(3): 2107–2120, July 2015.

- Caratheodory, C. Über den Variabilitätsbereich der Koeffizienten von Potenzreihen, die gegebene Werte nicht annehmen. *Math. Ann.*, 64:95–115, 1907.
- Caratheodory, C. Über den Variabilitätsbereich der Fourier'schen Konstanten von positiven harmonischen Funktionen. *Rend. Circ. Mat. Palermo*, 32:193–217, 1911.
- Chang, R. W. Synthesis of band-limited orthogonal signals for multichannel data transmission. *The Bell System Technical Journal*, 45(10):1775–1796, Dec 1966.
- Chen, S., Donoho, D., and Saunders, M. Atomic decomposition by basis pursuit. *SIAM J. Sci. Comp.*, 20(1):33–61, 1998a.
- Chen, V. C. and Ling, H. Joint time-frequency analysis for radar signal and image processing. *IEEE Signal Processing Magazine*, 16(2):81–93, Mar 1999.
- Chen, V. C. and Qian, S. Joint time-frequency transform for radar range-Doppler imaging. *IEEE Transactions on Aerospace and Electronic Systems*, 34(2):486–499, Apr 1998b.
- Chen, X., Guan, J., Liu, N., and He, Y. Maneuvering target detection via Radon-fractional Fourier transform-based long-time coherent integration. *IEEE Transactions on Signal Processing*, 62(4):939–953, Feb 2014.
- Cohen, D. and Eldar, Y. C. Reduced time-on-target in pulse Doppler radar: Slow time domain compressed sensing. In *2016 IEEE Radar Conference (RadarConf)*, pages 1–4, May 2016a.
- Cohen, D., Dikopoltsev, A., and Eldar, Y. C. Extensions of sub-Nyquist radar: Reduced time-on-target and cognitive radar. In *2015 3rd International Workshop on Compressed Sensing Theory and its Applications to Radar, Sonar and Remote Sensing (CoSeRa)*, pages 31–35, June 2015.
- Cohen, D., Dikopoltsev, A., Ifraimov, R., and Eldar, Y. C. Towards sub-Nyquist cognitive radar. In *2016 IEEE Radar Conference (RadarConf)*, pages 1–4, May 2016b.
- da Silva, M. M. and Monteiro, F. A., editors. *MIMO Processing for 4G and Beyond: Fundamentals and Evolution*. CRC Press, 19.04.2016.
- Davenport, M. A. *Random Observations on Random Observations: Sparse Signal Acquisition and Processing*. PhD thesis, Rice University, 2010.
- Destino, G., Saloranta, J., Juntti, M., and Nagaraj, S. Robust 3D MIMO-OFDM channel estimation with hybrid analog-digital architecture. In *Signal Processing Conference (EUSIPCO), 2016 24th European*, 2016.
- Donnet, B. J. and Longstaff, I. D. Combining MIMO radar with OFDM communications. In *2006 European Radar Conference*, pages 37–40, Sept 2006.
- Donoho, D. L. Compressed sensing. *IEEE Transactions on Information Theory*, 52(4):1289–1306, April 2006.
- Duarte, M. and Baraniuk, R. G. Recovery of frequency-sparse signals from compressive measurements. In *Allerton Conference on Communication, Control, and Computing*, pages 599–606, Monticello, IL, Sep. 2010.
- Duarte, M. and Baraniuk, R. G. Spectral compressive sensing. *Applied and Computational Harmonic Analysis*, 35(1):111–129, Jul. 2013.

- Duarte, M. and Eldar, Y. Structured compressed sensing: From theory to applications. *Signal Processing, IEEE Transactions*, 59(9):4053–4085, Sept. 2011.
- Duarte, M. F., Davenport, M. A., Takbar, D., Laska, J. N., Sun, T., Kelly, K. F., and Baraniuk, R. G. Single-pixel imaging via compressive sampling. *IEEE Signal Processing Magazine*, 25(2):83–91, March 2008.
- Duda, K. DFT interpolation algorithm for Kaiser-Bessel and Dolph-Chebyshev windows. *IEEE Transactions on Instrumentation and Measurement*, 60(3):784–790, March 2011.
- Durbin, J. Efficient estimation of parameters in moving-average models. *Biometrika*, 46:306–316, 1959.
- Eldar, Y. and Kutyniok, G., editors. *Compressed Sensing: Theory and Applications*. Cambridge University Press, 2012.
- Eldar, Y. C., Kuppinger, P., and Bolcskei, H. Block-sparse signals: Uncertainty relations and efficient recovery. *IEEE Transactions on Signal Processing*, 58(6):3042–3054, June 2010.
- Feng, P. and Bresler, Y. Spectrum-blind minimum-rate sampling and reconstruction of multiband signals. In *1996 IEEE International Conference on Acoustics, Speech, and Signal Processing Conference Proceedings*, volume 3, pages 1688–1691 vol. 3, May 1996.
- Figueiredo, M. A. T., Nowak, R. D., and Wright, S. J. Gradient projection for sparse reconstruction: Application to compressed sensing and other inverse problems. *IEEE Journal of Selected Topics in Signal Processing*, 1(4):586–597, Dec 2007.
- Fink, J. and Jondral, F. K. Comparison of OFDM radar and chirp sequence radar. In *2015 16th International Radar Symposium (IRS)*, pages 315–320, June 2015a.
- Fink, J. and Jondral, F. K. A numerical comparison of chirp sequence versus OFDM radar waveforms. In *2015 IEEE 82nd Vehicular Technology Conference (VTC2015-Fall)*, pages 1–2, Sept 2015b.
- Fink, J., Braun, M., and Jondral, F. K. Effects of arbitrarily spaced subcarriers on detection performance in OFDM radar. In *2012 IEEE Vehicular Technology Conference (VTC Fall)*, pages 1–5, Sept 2012.
- Franken, G. E. A., Nikookar, H., and Genderen, P. V. Doppler tolerance of OFDM-coded radar signals. In *2006 European Radar Conference*, pages 108–111, Sept 2006.
- Garmatyuk, D. and Schuerger, J. Conceptual design of a dual-use radar/communication system based on OFDM. In *MILCOM 2008 - 2008 IEEE Military Communications Conference*, pages 1–7, Nov 2008.
- Garmatyuk, D., Schuerger, J., Morton, Y. T., Binns, K., Durbin, M., and Kimani, J. Feasibility study of a multi-carrier dual-use imaging radar and communication system. In *Radar Conference, 2007. EuRAD 2007. European*, pages 194–197, Oct 2007.
- Garmatyuk, D., Schuerger, J., and Kauffman, K. Multifunctional software-defined radar sensor and data communication system. *IEEE Sensors Journal*, 11(1):99–106, Jan 2011.
- Gassier, G., Chabriel, G., Barrère, J., Briolle, F., and Jauffret, C. A unifying approach for disturbance cancellation and target detection in passive radar using OFDM. *IEEE Transactions on Signal Processing*, 64(22):5959–5971, Nov 2016.

- Gilbert, A. C., Strauss, M. J., and Tropp, J. A. A tutorial on fast Fourier sampling. *IEEE Signal Processing Magazine*, 25(2):57–66, March 2008.
- Goldberg, D. E. *Genetic Algorithms in Search, Optimization and Machine Learning*. New York: Addison-Wesley, 1989.
- Guerci, J. R., Guerci, R. M., Ranagaswamy, M., Bergin, J. S., and Wicks, M. C. Cofar: Cognitive fully adaptive radar. In *2014 IEEE Radar Conference*, pages 0984–0989, May 2014.
- Guo, X. Radar interference suppression based on spectrum notching and compressive sensing data recovery. In *IEEE 5th Asia-Pacific Conference on Synthetic Aperture Radar (APSAR)*, 2015.
- Hakobyan, G. Verfahren zum Betreiben einer OFDM-Radarvorrichtung, DE patent, DE102015222043, 2015a.
- Hakobyan, G. Radarvorrichtung und Verfahren zur Abstands- und Geschwindigkeitsschätzung von Objekten,, DE patent, DE102015218538, 2015b.
- Hakobyan, G. and Steinlechner, S. Verfahren zum Betreiben einer Radarvorrichtung, DE patent, DE102015210454, 2015c.
- Hakobyan, G. and Steinlechner, S. Method for operating a radar apparatus, US patent, US20160172658, 2016a.
- Hakobyan, G. and Yang, B. A novel OFDM-MIMO radar with non-equidistant subcarrier interleaving and compressed sensing. In *2016 17th International Radar Symposium (IRS)*, pages 1–5, May 2016b.
- Hakobyan, G. and Yang, B. A novel narrowband interference suppression method for OFDM radar. In *2016 24th European Signal Processing Conference (EUSIPCO)*, pages 2230–2234, Aug 2016c.
- Hakobyan, G. and Yang, B. A novel OFDM-MIMO radar with non-equidistant dynamic subcarrier interleaving. In *2016 European Radar Conference (EuRAD)*, pages 45–48, Oct 2016d.
- Hakobyan, G. and Yang, B. A novel inter-carrier-interference free signal processing scheme for OFDM radar. *IEEE Transactions on Vehicular Technology*, 2017a.
- Hakobyan, G. and Yang, B. OFDM-MIMO radar with optimized waveforms based on non-equidistant subcarrier interleaving and genetic algorithms. *IEEE Transactions on Aerospace and Electronic Systems*, 2017b.
- Hakobyan, G., Armanious, K., and Schoor, M. Radarsystem mit variabler Trägerfrequenz, DE patent, DE102016221947, 2016e.
- Hakobyan, G., Girma, M., Li, X., Tammireddy, N., and Yang, B. Repeated symbols OFDM-MIMO radar at 24 GHz. In *2016 European Radar Conference (EuRAD)*, pages 249–252, Oct 2016f.
- Han, S. H. and Lee, J. H. An overview of peak-to-average power ratio reduction techniques for multicarrier transmission. *IEEE Wireless Communications*, 12(2):56–65, April 2005.
- Haykin, S. Cognitive radar: a way of the future. *IEEE Signal Processing Magazine*, 23(1):30 – 40, 2006.

- Haykin, S. *Adaptive Filter Theory, 5th edition*. Pearson, 2014.
- He, H., Stoica, P., and Li, J. Waveform design with stopband and correlation constraints for cognitive radar. In *2010 2nd International Workshop on Cognitive Information Processing*, pages 344–349, June 2010.
- Herman, M. A. and Strohmer, T. High-resolution radar via compressed sensing. *IEEE Transactions on Signal Processing*, 57(6):2275–2284, June 2009.
- Hong, S., Brand, J., Choi, J. I., Jain, M., Mehlman, J., Katti, S., and Levis, P. Applications of self-interference cancellation in 5G and beyond. *IEEE Communications Magazine*, 52(2): 114–121, February 2014.
- Huang, P., Liao, G., Yang, Z., Xia, X. G., Ma, J. T., and Ma, J. Long-time coherent integration for weak maneuvering target detection and high-order motion parameter estimation based on Keystone transform. *IEEE Transactions on Signal Processing*, 64(15):4013–4026, Aug 2016.
- Huang, P., Liao, G., Yang, Z., Xia, X. G., Ma, J., and Zheng, J. Ground maneuvering target imaging and high-order motion parameter estimation based on second-order Keystone and generalized Hough-HAF transform. *IEEE Transactions on Geoscience and Remote Sensing*, 55(1):320–335, Jan 2017.
- Huleihel, W., Tabrikian, J., and Shavit, R. Optimal adaptive waveform design for cognitive MIMO radar. *IEEE Transactions on Signal Processing*, 61(20):5075 – 5089, 2013.
- Jakabosky, J., Ravenscroft, B., Blunt, S. D., and Martone, A. Gapped spectrum shaping for tandem-hopped radar/communications cognitive sensing. In *2016 IEEE Radar Conference (RadarConf)*, pages 1–6, May 2016.
- Jun, W., Shouhong, Z., and Zheng, B. On motion compensation for weak radar reflected signal detection. In *6th International Conference on Signal Processing, 2002.*, volume 2, pages 1445–1448 vol.2, Aug 2002.
- Kotelnikov, V. On the carrying capacity of the ether and wire in telecommunications. In *Izd. Red. Upr. Svyazi RKKA (Moscow)*, 1933.
- Kulpa, K. The CLEAN type algorithms for radar signal processing. In *2008 Microwaves, Radar and Remote Sensing Symposium*, pages 152–157, Sept 2008.
- Küstner, T., Würslin, C., Gatidis, S., Martirosian, P., Nikolaou, K., Schwenzer, N., Schick, F., Yang, B., and Schmidt, H. MR image reconstruction using a combination of compressed sensing and partial Fourier acquisition: ESPReSSo. *IEEE Transactions on Medical Imaging*, 35(11):2447–2458, Nov 2016.
- Lanari, R. A new method for the compensation of the SAR range cell migration based on the chirp z-transform. *IEEE Transactions on Geoscience and Remote Sensing*, 33(5):1296–1299, Sep 1995.
- Lange, O. *Optimierung von Antennenarrays zur verbesserten Richtungsschätzung für automobile Radarsysteme*. PhD thesis, University of Stuttgart, 2012.
- Lange, O. and Yang, B. Array geometry optimization for direction-of-arrival estimation including subarrays and tapering. In *2010 International ITG Workshop on Smart Antennas (WSA)*, pages 135–142, Feb 2010.

- Lange, O. and Yang, B. Antenna geometry optimization for 2D direction-of-arrival estimation for radar imaging. In *2011 International ITG Workshop on Smart Antennas*, pages 1–8, Feb 2011.
- Lellouch, G. *Waveform Design and Processing Techniques in OFDM radar*. PhD thesis, University of Cape Town, 2015.
- Lellouch, G., Pribic, R., and van Genderen, P. Wideband OFDM pulse burst and its capabilities for the Doppler processing in radar. In *2008 International Conference on Radar*, pages 531–535, Sept 2008a.
- Lellouch, G., Tran, P., Pribic, R., and van Genderen, P. OFDM waveforms for frequency agility and opportunities for Doppler processing in radar. In *2008 IEEE Radar Conference*, pages 1–6, May 2008b.
- Levanon, N. Multifrequency radar signals. In *Radar Conference, 2000. The Record of the IEEE 2000 International*, pages 683–688, 2000a.
- Levanon, N. Multifrequency complementary phase-coded radar signal. *IEE Proceedings - Radar, Sonar and Navigation*, 147(6):276–284, Dec 2000b.
- Levanon, N. and Mozeson, E. Multicarrier radar signal - pulse train and CW. *IEEE Transactions on Aerospace and Electronic Systems*, 38(2):707–720, Apr 2002.
- Levinson, N. The Wiener RMS (root mean square) error criterion in filter design and prediction. *J. Math. Phys.*, 25(4):261–278, 1947.
- Li, J. and Stoica, P. Efficient mixed-spectrum estimation with applications to target feature extraction. *IEEE Transactions on Signal Processing*, 44(2):281–295, Feb. 1996.
- Li, X., Hu, Z., Qiu, R. C., Wu, Z., Browning, J. P., and Wicks, M. C. Demonstration of cognitive radar for target localization under interference. *IEEE Transactions on Aerospace and Electronic Systems*, 50(4):2440–2455, October 2014.
- Li, Y., Zeng, T., Long, T., and Wang, Z. Range migration compensation and Doppler ambiguity resolution by Keystone transform. In *2006 CIE International Conference on Radar*, pages 1–4, Oct 2006.
- Lutz, S., Ellenrieder, D., Walter, T., and Weigel, R. On fast chirp modulations and compressed sensing for automotive radar applications. In *Radar Symposium (IRS), 2014 15th International*, pages 1–6, 2014.
- Mallat, S. G. and Zhang, Z. Matching pursuits with time-frequency dictionaries. *IEEE Transactions on Signal Processing*, 41(12):3397–3415, Dec 1993.
- Manna, M. L., Monsurro, P., Tommasino, P., and Trifiletti, A. Adaptive spectrum controlled waveforms for cognitive radar. In *IEEE Radar Conference (RadarConf)*, May 2016.
- Maravic, I. and Vetterli, M. Sampling and reconstruction of signals with finite rate of innovation in the presence of noise. *IEEE Transactions on Signal Processing*, 53(8):2788–2805, Aug 2005.
- Mishali, M. and Eldar, Y. C. From theory to practice: Sub-Nyquist sampling of sparse wideband analog signals. *IEEE Journal of Selected Topics in Signal Processing*, 4(2):375–391, April 2010.

- Mishali, M. and Eldar, Y. C. Sub-Nyquist sampling. *IEEE Signal Processing Magazine*, 28(6): 98–124, Nov 2011.
- Nijssure, Y., Kaddoum, G., and Leung, H. Cognitive chaotic UWB-MIMO radar based on nonparametric Bayesian technique. *IEEE Transactions on Aerospace and Electronic Systems*, 51(3):2360 – 2378, 2015.
- Nyquist, H. Certain topics in telegraph transmission theory. *Trans. AIEE*, 47(2):617–644, 1928.
- Ochiai, H. and Imai, H. On the distribution of the peak-to-average power ratio in OFDM signals. *IEEE Transactions on Communications*, 49(2):282–289, Feb 2001.
- Oppenheim, A. V. and Schaffer, R. W. *Discrete-Time Signal Processing*. Prentice-Hall, third edition edition, 2009.
- Paichard, Y. OFDM waveforms for multistatic radars. In *2010 IEEE Radar Conference*, pages 1187–1190, May 2010.
- Pati, Y., Rezaifar, R., and Krishnaprasad, P. Orthogonal matching pursuit: recursive function approximation with applications to wavelet decomposition. *Signals, Systems and Computers, 1993. 1993 Conference Record of The Twenty-Seventh Asilomar Conference*, 1:40–44, Nov 1993.
- Peled, A. and Ruiz, A. Frequency domain data transmission using reduced computational complexity algorithms. In *Acoustics, Speech, and Signal Processing, IEEE International Conference on ICASSP '80.*, volume 5, pages 964–967, Apr 1980.
- Perry, R. P., DiPietro, R. C., and Fante, R. L. SAR imaging of moving targets. *IEEE Transactions on Aerospace and Electronic Systems*, 35(1):188–200, Jan 1999.
- Perry, R. P., DiPietro, R. C., and Fante, R. L. Coherent integration with range migration using Keystone formatting. In *2007 IEEE Radar Conference*, pages 863–868, April 2007.
- Pfeffer, C., Feger, R., Jahn, M., and Stelzer, A. A 77-GHz software defined OFDM radar. In *2014 15th International Radar Symposium (IRS)*, pages 1–5, June 2014.
- Pfeffer, C., Feger, R., and Stelzer, A. A stepped-carrier 77-GHz OFDM MIMO radar system with 4 GHz bandwidth. In *2015 European Radar Conference (EuRAD)*, pages 97–100, Sept 2015.
- Piezzo, M., Maio, A. D., Aubry, A., and Farina, A. Cognitive radar waveform design for spectral coexistence. In *IEEE Radar Conference (RadarCon13)*, 2013.
- Rabiner, L. R., Schaffer, R. W., and Rader, C. M. The chirp z-transform algorithm and its application. *The Bell System Technical Journal*, 48(5):1249–1292, May 1969.
- Rambach, K. *Direction of arrival estimation using a multiple-input-multiple-output radar with applications to automobiles*. PhD thesis, University of Stuttgart, 2016.
- Rambach, K. and Yang, B. Colocated MIMO radar: Cramer-Rao bound and optimal time division multiplexing for DOA estimation of moving targets. In *2013 IEEE International Conference on Acoustics, Speech and Signal Processing*, pages 4006–4010, May 2013.
- Reiher, M. and Yang, B. On the occurrence of ghost targets in linear FMCW radar: A worst case study. In *2008 International Radar Symposium*, pages 1–4, May 2008.

- Richards, M. The Keystone transformation for correcting range migration in range-Doppler processing. Technical report, 2014a.
- Richards, M. *Fundamentals of Radar Signal Processing*. McGraw-Hill, New York, 2nd edition, 2014b.
- Rohling, H. Radar CFAR thresholding in clutter and multiple target situations. *Aerospace and Electronic Systems, IEEE Transactions on*, AES-19(4):608–621, July 1983.
- Romberg, J. Imaging via compressive sampling. *IEEE Signal Processing Magazine*, 25(2):14–20, March 2008.
- Schmidl, T. M. and Cox, D. C. Robust frequency and timing synchronization for OFDM. *IEEE Transactions on Communications*, 45(12):1613–1621, Dec 1997.
- Schoor, M. *Hochauflösende Winkelschätzung für automobile Radarsysteme*. PhD thesis, University of Stuttgart, 2010.
- Schoor, M. and Kirsch, A. Verfahren zur zyklischen Messung von Abständen und Geschwindigkeiten von Objekten mit einem FMCW-Radarsensor, DE patent, DE 102013200404 A1, July 2013.
- Schroeder, M. Synthesis of low-peak-factor signals and binary sequences with low autocorrelation (corresp.). *IEEE Transactions on Information Theory*, 16(1):85–89, January 1970.
- Sen, S. *Adaptive OFDM radar for target detection and tracking*. PhD thesis, Washington University in St. Louis, 2010.
- Sen, S. PAPR-constrained Pareto-optimal waveform design for OFDM-STAP radar. *IEEE Transactions on Geoscience and Remote Sensing*, 52(6):3658–3669, June 2014.
- Sen, S. and Nehorai, A. Adaptive OFDM radar for target detection in multipath scenarios. *IEEE Transactions on Signal Processing*, 59(1):78–90, Jan 2011.
- Shannon, C. Communication in the presence of noise. *Proc. Institute of Radio Engineers*, 37(1): 10–21, 1949.
- Sharaga, N., Tabrikian, J., and Messer, H. Optimal cognitive beamforming for target tracking in MIMO radar/sonar. *IEEE Journal of Selected Topics in Signal Processing*, 9(8):1440 – 1450, 2015.
- Silver, D., Huang, A., Maddison, C. J., Guez, A., Sifre, L., van den Driessche, G., Schrittwieser, J., Antonoglou, I., Panneershelvam, V., Lanctot, M., Dieleman, S., Grewe, D., Nham, J., Kalchbrenner, N., Sutskever, I., Lillicrap, T., Leach, M., Kavukcuoglu, K., Graepel, T., and Hassabis, D. Mastering the game of go with deep neural networks and tree search. *Nature*, 529:484–503, 2016.
- Sit, Y. L. *MIMO OFDM radar-communication system with mutual interference cancellation*. PhD thesis, Karlsruhe Institute of Technology (KIT), 2017.
- Sit, Y. L. and Zwick, T. MIMO OFDM radar with communication and interference cancellation features. In *2014 IEEE Radar Conference*, pages 0265–0268, May 2014a.
- Sit, Y. L. and Zwick, T. MIMO OFDM radar networks: Inter- & intra-system interference handling. In *2014 Asia-Pacific Microwave Conference*, pages 1318–1320, Nov 2014b.

- Sit, Y. L., Sturm, C., Baier, J., and Zwick, T. Direction of arrival estimation using the MUSIC algorithm for a MIMO OFDM radar. In *2012 IEEE Radar Conference*, pages 0226–0229, May 2012a.
- Sit, Y. L., Sturm, C., and Zwick, T. One-stage selective interference cancellation for the OFDM joint radar-communication system. In *2012 The 7th German Microwave Conference*, pages 1–4, March 2012b.
- Sit, Y. L., Nguyen, T. T., Sturm, C., and Zwick, T. 2D radar imaging with velocity estimation using a MIMO OFDM-based radar for automotive applications. In *2013 European Radar Conference*, pages 145–148, Oct 2013.
- Sit, Y. L., Nuss, B., Basak, S., Orzol, M., and Zwick, T. Demonstration of interference cancellation in a multiple-user access OFDM MIMO radar-communication network using USRPs. In *2016 IEEE MTT-S International Conference on Microwaves for Intelligent Mobility (ICMIM)*, pages 1–4, May 2016.
- Skolnik, M. *Radar Handbook*. McGraw-Hill, New York, 3rd edition, 2008.
- Steffens, C., Yang, Y., and Pesavento, M. Multidimensional sparse recovery for MIMO channel parameter estimation. In *Signal Processing Conference (EUSIPCO), 2016 24th European*, 2016.
- Stinco, P., Greco, M., Gini, F., and Manna, M. L. Compressed spectrum sensing in cognitive radar systems. In *IEEE International Conference on Acoustics, Speech and Signal Processing (ICASSP)*, pages 81 – 85, 2014.
- Stoica, P. and Selen, Y. Model-order selection: a review of information criterion rules. *IEEE Signal Processing Magazine*, 21(4):36–47, July 2004.
- Sturm, C. *Gemeinsame Realisierung von Radar-Sensorik und Funkkommunikation mit OFDM-Signalen*. PhD thesis, Karlsruhe Institute of Technology, 2012a.
- Sturm, C. *Gemeinsame Realisierung von Radar-Sensorik und Funkkommunikation mit OFDM-Signalen*. PhD thesis, KIT, 2012b.
- Sturm, C. and Wiesbeck, W. Waveform design and signal processing aspects for fusion of wireless communications and radar sensing. *Proceedings of the IEEE*, 99(7):1236–1259, July 2011.
- Sturm, C., Zwick, T., and Wiesbeck, W. An OFDM system concept for joint radar and communications operations. In *Vehicular Technology Conference, 2009. VTC Spring 2009. IEEE 69th*, pages 1–5, April 2009.
- Sturm, C., Sit, Y., Braun, M., and Zwick, T. Spectrally interleaved multi-carrier signals for radar network applications and multi-input multi-output radar. *Radar, Sonar & Navigation, IET*, 7(3):261–269, March 2013.
- Svensson, D., McKelvey, T., and Hellsten, H. DVB-T interference cancellation in radar signal processing. In *2014 International Radar Conference*, pages 1–6, Oct 2014.
- Tigrek, F. *A Processing technique for OFDM-modulated wideband radar signals*. PhD thesis, TU Delft, 2010a.

- Tigrek, R. F. and Genderen, P. V. Compensation of range migration for cyclically repetitive Doppler-sensitive waveform (OFDM) . *IEEE Transactions on Aerospace and Electronic Systems*, 46(4):2118–2123, Oct 2010b.
- Tigrek, R. F., de Heij, W. J. A., and van Genderen, P. Solving Doppler ambiguity by Doppler sensitive pulse compression using multi-carrier waveform. In *Radar Conference, 2008. EuRAD 2008. European*, pages 72–75, Oct 2008.
- Tigrek, R. F., de Heij, W. J. A., and van Genderen, P. Multi-carrier radar waveform schemes for range and Doppler processing. In *2009 IEEE Radar Conference*, pages 1–5, May 2009.
- Tigrek, R. F., Heij, W. J. A. D., and Genderen, P. V. OFDM signals as the radar waveform to solve Doppler ambiguity. *IEEE Transactions on Aerospace and Electronic Systems*, 48(1): 130–143, Jan 2012.
- Trees, H. L. V. *Optimum array processing. Part IV of detection, estimation and modulation theory*. Wiley, 2002.
- Tropp, J. A. Just relax: convex programming methods for identifying sparse signals in noise. *IEEE Transactions on Information Theory*, 52(3):1030–1051, March 2006.
- Tropp, J. A. and Wright, S. J. Computational methods for sparse solution of linear inverse problems. *Proceedings of the IEEE*, 98(6):948–958, June 2010a.
- Tropp, J. A., Laska, J. N., Duarte, M. F., Romberg, J. K., and Baraniuk, R. G. Beyond Nyquist: Efficient sampling of sparse bandlimited signals. *IEEE Transactions on Information Theory*, 56(1):520–544, Jan 2010b.
- Trzasko, J. and Manduca, A. Highly undersampled magnetic resonance image reconstruction via homotopic ℓ_0 -minimization. *IEEE Transactions on Medical Imaging*, 28(1):106–121, Jan 2009.
- Tsao, J. and Steinberg, B. D. Reduction of sidelobe and speckle artifacts in microwave imaging: the CLEAN technique. *IEEE Transactions on Antennas and Propagation*, 36(4):543–556, Apr 1988.
- Tufts, D. W. and Kumaresan, R. Estimation of frequencies of multiple sinusoids: Making linear prediction perform like maximum likelihood. *Proceedings of the IEEE*, 70(9):975–989, Sept. 1982.
- Vasanawala, S., Alley, M., Hargreaves, B., Barth, R., J.M., P., and Lustig, M. Improved pediatric MR imaging with compressed sensing. *Radiology*, 256(2):607–616, 2010.
- Venkataramani, R. and Bresler, Y. Further results on spectrum blind sampling of 2D signals. In *Proceedings 1998 International Conference on Image Processing. ICIP98*, volume 2, pages 752–756 vol.2, Oct 1998.
- Vetterli, M., Marziliano, P., and Blu, T. Sampling signals with finite rate of innovation. *IEEE Transactions on Signal Processing*, 50(6):1417–1428, Jun 2002.
- Weinstein, S. and Ebert, P. Data transmission by frequency-Division multiplexing using the discrete Fourier transform. *IEEE Transactions on Communication Technology*, 19(5):628–634, October 1971.
- Weise, T. *Global Optimization Algorithms – Theory and Application*. 2009.

- Whittaker, E. On the functions which are represented by the expansions of the interpolation theory. *Proc. Royal Soc. Edinburgh*, 35:181–194, 1915.
- Wu, X. H., Kishk, A. A., and Glisson, A. W. MIMO-OFDM radar for direction estimation. *IET Radar, Sonar Navigation*, 4(1):28–36, February 2010.
- Xia, X., Zhang, T., and Kong, L. MIMO OFDM radar IRCI free range reconstruction with sufficient cyclic prefix. *IEEE Transactions on Aerospace and Electronic Systems*, 51(3): 2276–2293, July 2015.
- Xu, J., Yu, J., Peng, Y. N., and Xia, X. G. Radon-Fourier transform for radar target detection, I: Generalized Doppler filter bank. *IEEE Transactions on Aerospace and Electronic Systems*, 47 (2):1186–1202, April 2011.
- Xu, J., Xia, X. G., Peng, S. B., Yu, J., Peng, Y. N., and Qian, L. C. Radar maneuvering target motion estimation based on generalized Radon-Fourier transform. *IEEE Transactions on Signal Processing*, 60(12):6190–6201, Dec 2012.
- Yu, Y., Petropulu, A. P., and Poor, H. V. MIMO radar using compressive sampling. *IEEE Journal of Selected Topics in Signal Processing*, 4(1):146–163, Feb 2010.
- Zhang, J., Zhu, D., and Zhang, G. Adaptive compressed sensing radar oriented toward cognitive detection in dynamic sparse target scene. *IEEE Transactions on Signal Processing*, 60(4): 1718–1729, April 2012.
- Zhang, T., Xia, X. G., and Kong, L. IRCI free range reconstruction for SAR imaging with arbitrary length OFDM pulse. *IEEE Transactions on Signal Processing*, 62(18):4748–4759, Sept 2014.